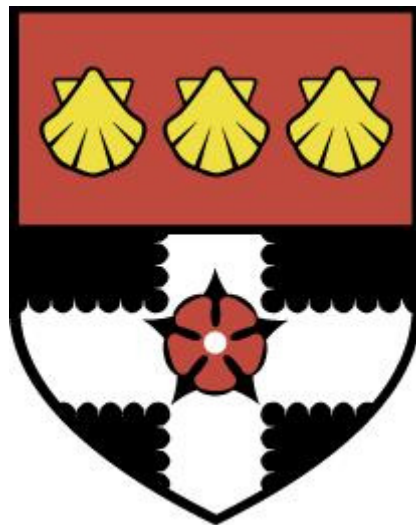


UNIVERSITY OF READING

Department of Meteorology



**The intraseasonal variability of the
Indian summer monsoon: Dynamics,
thermodynamics and
land-atmosphere-ocean interactions**

KARL JOHAN BIN JOHARI CHAN

A thesis submitted for the degree of Doctor of Philosophy

January 2020

DECLARATION

I confirm that this is my own work and that the use of all material from other sources has been properly and fully acknowledged.

Karl Johan Bin Johari Chan

ABSTRACT

The Indian summer monsoon rainfall accounts for approximately 80% of the annual-mean rainfall over India. The intraseasonal variability (ISV) of rainfall affects the agricultural sector and the livelihoods of over one billion people. The ISVs are dominated by the 30-60 days northward-propagating boreal summer intraseasonal oscillation (BSISO) between the eastern equatorial Indian Ocean (EEqIO) and India. This thesis evaluates the break-to-active transition with a focus on the dynamics, thermodynamics and land-ocean-atmosphere interaction in the propagation and strength of the BSISO.

A novel method for identifying break-to-active transition is created by applying an objective criterion to active and break events based on rainfall observations. The northward propagation of BSISO rainfall and convection is accurately captured in the composites of the transition. This method also removes the assumption that all breaks transition to active conditions.

Dynamic and thermodynamic analyses of the northward propagation using reanalysis are associated with moist and unstable anomalies originating from the EEqIO. ISV in SST and surface turbulent fluxes is consistent with air-sea coupling effect. Moisture budgets suggest that the transition to an active phase may originate in atmospheric dynamics and air-sea coupling over the northern Bay of Bengal.

The land-atmosphere coupling (LAC) over India is diagnosed to identify its influence on the transition. LAC is regionally dependent and is significant over northwestern India. Over central India, the transition may be supported by both LAC and atmospheric dynamics. A coupling metric is used to quantify the LAC strength over India during the break-to-active transition, confirming these observations.

The role of air-sea coupling in predicting the break-to-active transition is identified using 7-day initialised forecasts from an uncoupled and two coupled models. The uncoupled model outperforms the coupled models for the northward propagation and active-phase rainfall. However, the performance deteriorates in all models at longer forecast lead times such that the active phase is delayed and shortened. While air-sea coupling maintains the SST-convection phase relationship, it may not be important for predicting transition at short lead times.

ACKNOWLEDGEMENTS

I want to thank my supervisors—Andy Turner and Nick Klingaman—both whom I am eternally indebted to for giving me their time, encouragement and most importantly, patience during my thesis. Their inputs, suggestions and comments in the writing of the thesis have been very valuable. Andy and Nick continue to be my most significant source of inspiration to further my career in meteorology. I also appreciate their straightforward and honest approach during our weekly meeting, without which, would not have pushed me to better myself. My scientific reasoning and writing have also greatly improved under their guidance. I have always been fueled by the motto of my alma mater, Monash University, during my bachelor's degree which says “I am still learning”. To that, my supervisors have pushed and inspired me to always continue learning, and I owe it to them.

Secondly, I would like to thank my family, who have also supported me through my degree and PhD. Their random messages and photos of my pets to me provided a distraction during times of difficulties in the past 4 years. Being away for years at a time is undoubtedly difficult for my parents as I have been told.

I would also like to thank my colleagues, who have helped me through some tough times. The distraction in the office was also appreciated, with discussions on both meteorology related and non-meteorology related topics, more so for the latter.

My Monitoring Committee members, Richard Allan and Matthew Owens, provided a casual setting during our meetings. I would like to thank them for their valuable inputs during our meetings.

Lastly, I acknowledge and is grateful for the many organisations for the use of their datasets. The Indian Meteorological Department provided the daily gridded all India Rainfall. The European Centre for Medium-Range Weather Forecast provided the ERA-Interim reanalysis product. The NOAA/Earth System Research Laboratory Physical Sciences Division for their interpolated outgoing longwave radiation data. TropFlux provided the sea surface temperature and surface turbulent heat fluxes. Finally, I am thankful for Nick's assistance in providing the forecast outputs for chapter 6.

Contents

DECLARATION	I
ABSTRACT	II
ACKNOWLEDGEMENTS	III
TABLE OF CONTENTS	IV
LIST OF FIGURES	VII
LIST OF TABLES	XIV
LIST OF ACRONYMS	XV
1 INTRODUCTION	1
1.1 Motivation	1
1.2 Aims of the thesis	7
1.3 Outline of thesis	9
2 SCIENTIFIC BACKGROUND	11
2.1 The Indian summer monsoon basic state	11
2.2 The interannual variability of the Indian summer monsoon	15
2.3 Intraseasonal variability of the Indian summer monsoon	25
2.3.1 The BSISO and link to active/break Indian monsoon	25
2.3.2 Theory and mechanisms for the BSISO	27
2.3.2.1 Land surface fluxes	27
2.3.2.2 Dynamic theories	27
2.3.2.3 Ocean-atmosphere interactions	32
2.4 Land-atmosphere interaction	36
2.5 Motivation	41
3 THE BREAK-TO-ACTIVE TRANSITION OF THE INDIAN SUMMER MONSOON	43
3.1 Purpose of the chapter	43
3.2 Datasets and methods	45
3.2.1 Atmospheric data	46
3.3 Choice of active-break index	46
3.4 Criteria for a break-to-active transition	48
3.5 Verification of the break-to-active transition	50
3.6 The composite break-to-active transition	51
3.6.1 Rainfall	52
3.6.2 Outgoing-longwave radiation	54
3.7 Summary and discussion	55
4 THE BREAK-TO-ACTIVE TRANSITION OVER THE NORTHERN BAY OF BENGAL IN REANALYSIS	57
4.1 Introduction	57

4.2	Datasets and Methods	59
4.2.1	ERA-Interim	59
4.2.2	TropFlux	59
4.2.3	Atmospheric moisture budget analysis	60
4.2.4	Case study: The 2016 break-to-active transition	61
4.3	Thermodynamics of the break-to-active transition	62
4.3.1	Mixing ratio anomalies	62
4.3.2	Equivalent potential temperature anomalies	64
4.4	Air-sea turbulent fluxes and SST in the break-to-active transition	65
4.4.1	SST	65
4.4.2	Surface turbulent fluxes	67
4.5	Moisture budget analysis of the break-to-active transition over the northern Bay of Bengal	69
4.6	Case study: The 2016 break-to-active transition	72
4.6.1	Rainfall and OLR	72
4.6.2	Thermodynamics	74
4.6.3	Air-sea fluxes and SST	76
4.7	Summary and Discussion	78
5	LAND-ATMOSPHERE COUPLING DURING THE BREAK-TO-ACTIVE TRANSITION OVER INDIA	83
5.1	Purpose of the chapter	83
5.2	Datasets and methods	86
5.2.1	ERA-Interim and ERA-Interim/Land	87
5.2.2	Moisture budget analysis	88
5.2.3	Land-atmosphere coupling metrics	88
5.3	The break-to-active transition over India	90
5.3.1	Soil moisture and surface turbulent fluxes	90
5.4	Thermodynamics of the break-to-active transition over India	94
5.4.1	Mixing ratio anomalies	94
5.4.2	Equivalent potential temperature anomalies	96
5.4.3	Moisture budget	97
5.5	Land-atmosphere coupling strength	100
5.6	Summary and Discussion	103
6	FORECASTING THE 2016 BREAK-TO-ACTIVE TRANSITION - THE ROLE OF AIR-SEA COUPLING	107
6.1	Purpose of the chapter	107
6.2	Model and data	109
6.2.1	Model description	109
6.2.1.1	The atmosphere-only model	110
6.2.1.2	The coupled model	110
6.2.1.2.1	The mixed layer MC-KPP model	110
6.2.1.2.2	The fully dynamic NEMO model	111
6.2.2	Model experiment design	111

6.2.3	Observation and reanalysis data	112
6.3	Verification of the 2016 break-to-active rainfall in forecasts	112
6.3.1	Observations	112
6.3.2	NWP model	113
6.3.3	KPP	115
6.3.4	NEMO	118
6.4	Northward propagation in the forecasts	119
6.5	Role of air-sea coupling in forecasts	122
6.5.1	Hovmöller diagram of SST and LHF	122
6.5.2	NBoB area-average	125
6.6	Thermodynamics of the break-to-active transition in forecasts	129
6.7	Summary and discussion	132
7	CONCLUSIONS	136
7.1	Summary of key findings	136
7.1.1	A novel method for identifying break-to-active transition	136
7.1.2	Possible mechanism(s) for the break-to-active transition	137
7.1.3	Variability of land-atmosphere coupling in the break-to-active transition .	139
7.1.4	Unraveling the role of air-sea coupling during the break-to-active transition in models	141
7.2	Limitations and caveats	143
7.3	Future work	146
	REFERENCES	148

List of Figures

1.1	Map of India and the adjacent oceans depicting the elevation (m, filled contour) and the JJAS climatological (1979-2015) mean-sea-level pressure (hPa, contour lines) obtained from ERA-Interim. Elevation greater than 600m is shaded in grey, with the solid purple line outlining the Tibetan Plateau (approximately 3000m). The red dashed lines represent the climatological (or normal) position of the monsoon trough.	2
1.2	Time series of observed daily all-India rainfall (mm/day) from the India Meteorological Department's gridded rainfall dataset. The long-term 1979-2015 climatology is illustrated by the black line. The blue and red line denotes rainfall for the 2002 and 2009 monsoon season respectively.	4
2.1	Monthly mean monsoon precipitation (mm/day) and 850 hPa winds (m/s) for 1979-2008 for (a) boreal winter (December-February) and (b) boreal summer (June-September). The precipitation was obtained from the Global Precipitation Climatology Project (GPCP; Adler et al., 2003; Huffman et al., 2009), while the winds were taken from the ERA-Interim Renalysis dataset (Dee et al., 2011a). . .	12
2.2	The monsoon rainfall isochrones for the normal (dashed red) and 2016 (solid green) onset date of the 2016 southwest monsoon retrieved from the Indian Meteorological Department's website at http://www.imd.gov.in/pages/monsoon_main.php	13
2.3	Timeseries of interannual All-India Summer Monsoon Rainfall for the period 1871-2017 based on a homogeneous rainfall dataset from 306 rain gauges developed by the Indian Institute of Tropical Meteorology. The year-to-year El Niño and La Niña conditions identified based on the Oceanic Niño Index are indicated by red and blue circles, respectively. The figure was retrieved from http://mol.tropmet.res.in/monsoon-interannual-timeseries/	15
2.4	Schematics of the three phases of the El Niño-Southern Oscillation: (a) neutral phase, (b) El Niño phase and (c) La Niña retrieved from the National Oceanic and Atmospheric Administration's website at https://www.noaa.gov/climate	16
2.5	The (a) active and (b) break phase rainfall anomalies for the period 1979-2015 from the India Meteorological Department gridded rainfall (Rajeevan et al., 2006), overlaid with 850 hPa winds obtained from ERA-Interim. The active and break days were determined using an index described by Rajeevan et al. (2010). The stippling represents significance at the 95% confidence level using a Student's T-test.	26

2.6	A schematic of the idealized northward propagating boreal summer intraseasonal oscillation similar to Klingaman (2008) based on studies by Wang and Xie (1997), Lawrence and Webster (2002), Jiang et al. (2004) and DeMott et al. (2014) and Guo et al. (2011). The numbered boxes and the arrows illustrated the position and propagation direction of convection, respectively. Black arrows represent eastward propagation associated with Kelvin-Rossby wave packets and red arrows show westward propagation of convection as Rossby waves.	28
2.7	A schematic of the easterly shear mechanism obtained from Jiang et al. (2004) in their Fig. 10	29
2.8	The soil moisture and corresponding evaporation regimes as in Seneviratne et al. (2010), based on the Budyko (1963) framework. EF denotes the evaporative fraction, and EF_{max} represents the maximum evaporative fraction value.	36
2.9	A conceptual soil moisture precipitation coupling and feedback loop framework from Seneviratne et al. (2010). The coloured arrow indicates the feedback process: blue arrow represents positive feedback and red arrow indicates negative feedback.	38
3.1	Mean 1979-2015 rainfall (mm/day) over India for JJAS. The black highlighted box is the core monsoon zone (CMZ, 65-88°E, 18-28°N) as previously defined in Mandke et al. (2007) and Rajeevan et al. (2010).	47
3.2	Example of the standardised rainfall anomaly during June-September 1979 averaged over the CMZ. The blue and red colour bars represent the active and break days, respectively. Active (break) days were selected when the standardised rainfall anomaly was above (below) +1 (-1) for at least three consecutive days. The data used are from the IMD gridded rainfall dataset.	48
3.3	Phase space representation of the BSISO mode for all 24 transition events for 1979-2015, separated into eight defined regions. The dot represents the mid-point of the break while the cross indicates the mid-point of the active phase. Transitions within the unit circle are considered to signify weak BSISO activity. The BSISO index is based on Kikuchi et al. (2012)	51
3.4	The break-to-active composite rainfall anomalies (shading, mm/day) and 850 hPa wind anomalies (vectors, m/s). The (a) 0% and (i) 100% represent the mid-points of the break and active phases, respectively, while the transition phase ranges between (b-h) 12.5% and 87.5%. The stippling represents significance at the 95% confidence level using a Student's t-test. The rainfall data used was obtained from the IMD gridded rainfall and wind data from ERA-Interim.	53

3.5	The break-to-active composite OLR anomalies (shading, W/m^2). The (a) 0% and (i) 100% represent the mid-points of the break and active phases respectively, while the transition phase ranges between (b-h) 12.5% and 87.5%. The stippling represents significance at the 95% confidence level using a Student's t-test. The data used were obtained from the NOAA/ESRL PSD website.	54
4.1	The standardised rainfall anomaly (SRA) time-series for the 2016 Indian summer monsoon season. The red and green bars denote the break and active phase, respectively. A single transition event was identified, satisfying the criteria presented in Chapter 3. The mid-point of the break phase is on 20th July, while the mid-point of the active phase is on 5th August. The length of the transition is 16 days. The time-series was obtained from the IMD website at http://www.imd.gov.in/pages/monsoon_main.php	61
4.2	Zonally-averaged break-to-active transition composite of mixing ratio anomalies (g/kg) overlaid with vertical and meridional wind anomalies (m/s). Climatology was calculated using a 1979-2015 period. The dashed lines represents the freezing level. The stiplings represent significance at the 95% confidence level using a Student's T-Test. Datasets were retrieved from ERA-Interim.	63
4.3	As in Fig. 4.2 but for equivalent potential temperature (θ_e) anomalies.	64
4.4	The break-to-active transition of SST anomalies ($^{\circ}C$). Data and climatology were obtained from TropFlux for the period 1979-2015. The stipplings represent significance at the 95% confidence level using a Student's T-Test.	66
4.5	The break-to-active transition composite of surface latent heat flux anomalies (Wm^{-2}) overlaid with 10m wind speed anomalies (m/s). Data and climatology were obtained from TropFlux for the period 1979-2015. The stipplings represent significance at the 95% confidence level using a Student's T-Test. Positive values represent fluxes into the atmosphere.	67
4.6	Similar to Fig. 4.5 but for surface sensible heat flux anomalies (Wm^{-2})	68
4.7	The break-to-active transition of precipitation (P), evaporation (E), vertically-integrated moisture flux divergence ($\nabla \cdot \vec{u}q$) and its corresponding zonal ($\partial(uq)/\partial x$) and meridional ($\partial(vq)/\partial y$) components, column-integrated moisture tendency ($\partial q/\partial t$) and residual. The moisture budget was calculated using ERA-Interim reanalysis for 1979-2015 averaged over the northern Bay of Bengal (10-17 $^{\circ}N$, 85-92 $^{\circ}E$). Units: mm/day.	70

4.8	The break-to-active composite for vertically integrated moisture convergence (shading, mm/day), and vertically integrated zonal and meridional moisture flux (vectors, kg/m/s) for selected break-to-active transition panels. The red box represents the Bay of Bengal region used for the moisture budget analysis. Positive contour values represent moisture convergence.	71
4.9	The break-to-active transition of rainfall and 850 hPa wind anomalies for the 2016 case study period. The rainfall dataset were obtained from IMD and the 850 hPa horizontal winds were retrieved from ERA-Interim. The climatology was calculated from the 1979-2015 period.	73
4.10	The break-to-active transition of OLR anomalies for the 2016 case study period obtained from the NOAA/ESRL PSD website. The climatology was calculated from the 1979-2015 period.	74
4.11	Zonally-averaged (85-90°E) break-to-active transition composites of atmospheric thermodynamic and circulation variables. The panels show (a-e) mixing ratio anomalies (g/kg) overlaid with vertical and meridional wind anomalies, (f-j) θ_e anomalies for the 2016 case study. The dashed line marks the freezing level. The stippling represents significance at the 95% confidence level using a Student's t-test. The data was obtained from ERA-Interim. The climatology was calculated from the 1979-2015 period.	75
4.12	The break-to-active transition composites of (panels a-e) SST , (panels f-j) LHF (Wm^{-2}) and (panels k-o) SHF ($^{\circ}C$) anomalies during the 2016. Overlaid in panels f-o are the total 10m wind speed anomalies (ms^{-1}). The solid and dashed lines represents positive and negative total wind speed anomalies respectively. Positive surface fluxes values represent upwards into the atmosphere. Data obtained from TropFlux.	77
4.13	Schematic illustrating the possible mechanisms for the break-to-active transition.	80
5.1	Diagram illustrating the southeast-to-northwest endpoints (black solid line), labeled as A and B respectively for the thermodynamic cross-section analysis. The red and blue boxes represent the area used in the moisture budget analysis in §5.4.3, representing central India (20-27°N, 73-83°E) and northwestern India (25-30°N, 67-75°E), respectively. The contoured lines represent the JJAS climatology (1979-2010) of volumetric soil moisture (0-7 cm) over the Indian subcontinent obtained from ERA-Interim/Land.	87

5.2	The break-to-active transition composites of (a-e) soil moisture anomalies, (f-j) latent heat flux anomalies overlaid with 10m total wind speed anomalies and (k-o) sensible heat flux anomalies. The fluxes are defined as positive upwards. The labels 0% and 100% represents the break and active phase mid-point, respectively, while labels 25%, 50% and 75% represents the transition phase. Additionally, the stippling represents significance at the 95% confidence level using a Student's T-test.	90
5.3	The radiation budget over (a) central India (20-27°N, 73-83°E) and (b) northwestern India (25-30°N, 67-75°E) during the break-to-active transition. The radiation budget terms are surface net shortwave radiation (<i>SSR</i>), surface net thermal radiation (<i>STR</i>), surface latent heat flux (<i>LHF</i>), surface sensible heat flux (<i>SHF</i>) and the ground heat flux (<i>G</i>) as residual. The radiation budget was calculated using ERA-Interim/Land reanalysis for 1979-2010. The fluxes are defined as positive upwards. Units: Wm^{-2}	92
5.4	The Pearson's correlation across the 19 composite events between soil moisture and LHF (black) and between soil moisture and SHF (red) averaged over central India (solid line) and northwestern India (dashed line) in the composite break-to-active transition. The labels 0% and 100% represents the mid-point of the break and active phase, respectively, while labels 25%, 50% and 75% represents the transition phase.	93
5.5	The northwest (B) to southeast (A) vertical cross-section of mixing ratio anomalies (g/kg) and wind anomalies (m/s) during the break-to-active transition. Data were obtained from ERA-Interim reanalysis for the period 1979-2010. The wind vectors represent horizontal winds relative to the transect line shown on Fig. 5.1, such that a horizontal vector represents flow parallel to the transect. The dashed lines marks the freezing level, $T=0^{\circ}C$	95
5.6	Similar to Fig. 5.5 but for equivalent potential temperature anomalies. The green line represents the rainfall anomalies obtained from the IMD gridded rainfall dataset.	96
5.7	The moisture budget over (a) central India (20-27°N, 73-83°E) and (b) northwestern India (25-30°N, 67-75°E) during the break-to-active transition. The moisture budget terms are precipitation (<i>P</i>), evaporation (<i>E</i>), vertically-integrated moisture flux divergence ($\nabla \cdot \vec{u}q$), column-integrated moisture tendency ($\partial q/\partial t$) and the residual. The moisture budget was calculated using ERA-Interim reanalysis for 1979-2010. Note the difference in magnitude of the moisture budget between central India and northwestern India. Units: mm/day.	98

5.8	(a-e) Terrestrial coupling index (TCI) for soil moisture and latent heat flux (LHF), with positive LHF values representing upward fluxes and (f-j) the corresponding atmospheric coupling index (ACI) based on latent heat flux to 2m specific humidity (2mQ) during the break-to-active transition. Panel (k-o) shows the ACI for lifted condensation level height (LCL). Units are in Wm^{-2} , g/kg and m, respectively. The numbered contour line shows the standard deviation of LHF, 2mQ and LCL respectively.	101
5.9	Schematic for the break-to-active transition mechanisms over central India based on the results in this chapter. Size of the arrows depicts the strength of mechanism.	103
5.10	Similar to Fig. 5.9 but over north-western India.	105
6.1	The 2016 break-to-active precipitation anomalies from observations (panels a-c) and NWP at forecast lead day of +1 (panels d-f), +4 (panels g-i) and +7 (panels j-l). The panels on the left and right represent the active and break phase, while the middle panels indicate the transition phase. Overlaid in each panels are the 850 hPa horizontal wind anomalies obtained from ERA-Interim (panels a-c) and from the NWP (panels d-l).	114
6.2	(a) Pattern correlation coefficient (PCC) and (b) root-mean-square error (RMSE) of the 2016 break-to-active transition between the observation and three different configurations of the NWP model at different forecast lead time. The three configurations are: the uncoupled NWP (green line), the coupled KPP (red line) and the coupled NEMO (blue line). The observation used is the IMD merged satellite-gauge dataset. The correlations and RMSE were calculated by taking the mean from each day during the 2016 break-to-active transition (e.g., 20th July - 5th August 2016) over the domain $5^{\circ}S-35^{\circ}N, 60^{\circ}E-95^{\circ}E$	116
6.3	Similar to Fig. 6.1, but for the coupled KPP.	117
6.4	Difference between NEMO and KPP at forecast lead day of +1 (panels a-c), +4 (panels d-f) and +7 (panels g-i).	119
6.5	Time-latitude Hovmöller plots of OLR anomalies for (a) observations, (b-d) NWP, (e-g) KPP and (h-j) NEMO during the 2016 break-to-active transition averaged between 80° and $90^{\circ}E$. Only forecasts with a lead day of +1, +4 and +7 are shown for brevity. The black solid line represents the northward propagation of active phase convection. The pattern correlation and root-mean square error against the observations for each models are also shown. Observations are the Uninterpolated OLR data provided by the NOAA/OAR/ESRL PSD, Boulder, Colorado, USA, from their website at https://www.esrl.noaa.gov/psd/	120

6.6	Time-latitude Hovmöller plots of sea surface temperature (shading, °C) and surface latent heat flux (contour, Wm^{-2}) anomalies for (a) observations, (b-d) NWP, (e-g) KPP and (h-j) NEMO during the 2016 break-to-active transition averaged between 85° and 95°E. Only forecasts with a lead day of +1, +4 and +7 are shown for brevity. The pattern correlation and root-mean square error for each models against the observations are also shown. The observations were obtained from TropFlux for both sea surface temperature and latent heat flux. . .	123
6.7	The area-average of the 2016 break-to-active transition anomalies of rainfall (blue line, mm/day), SSTs (red line, °C), LHF (magenta line, mm/day), 10m wind speeds (green, m/s) averaged over the NBoB domain (15°-23°N, 80°-95°E) in observations.	125
6.8	Similar to Fig. 6.7 but for the +1 day forecast for (a) NWP, (b) KPP and (c) NEMO. The top most panel illustrates the observations.	126
6.9	Similar to Fig. 6.7 but for the +7 day forecast for (a) NWP, (b) KPP and (c) NEMO. The top most panel illustrates the observations.	128
6.10	The pressure-latitude composite specific humidity anomalies (g/kg) averaged between 85°-95°E in (a-c) observations and in NWP at (d-f) +1 day, (g-i) +4 day and (j-l) +7 day forecast. Observations were obtained from ERA-Interim. . .	130
6.11	The pressure-latitude composite specific humidity anomalies (g/kg) averaged between 85°-95°E in (a-c) observations and in the KPP at (d-f) +1 day, (g-i) +4 day and (j-l) +7 day forecast. Observations were obtained from ERA-Interim. . .	131

List of Tables

3.1	Dates for mid-point of break and active days, and their transition length for all 24 transition events during 1979-2015. The criterion for a break-to-active transition is that the transition must occur within 30 days. The mean, median and standard deviation of the transitions are also provided.	49
6.1	The forecast models used for the 2016 break-to-active transition prediction. GA6.1 = Met Office Global Atmosphere 6.1; NEMO = Nucleus for European Modelling of the Oceans; MC-KPP = Multi-Column K Profile Parameterisation. . .	110

LIST OF ACRONYMS

Acronym or Abbreviation	Definition
θ_e	Equivalent Potential Temperature
2mQ	Two-metre Specific Humidity
AGCM	Atmosphere-Only General Circulation Model
AIR	All-India Rainfall
AVHRR	Advanced Very-High Resolution Radiometer
BoBBLE	Bay of Bengal Boundary Layer Experiment
BOBMEX	Bay of Bengal Monsoon Experiment (Bhat et al., 2001)
BSISO	Boreal Summer Intraseasonal Oscillation
CAM4	Community Atmospheric Model, version 4
CAM5	Community Atmospheric Model, version 5
CESM	Community Earth System Model
CFS	Climate Forecast System (NCEP)
CI	Central India
CMT	Cumulus Momentum Transport
CMZ	Core Monsoon Zone
CTP-HI	Convective Triggering Potential-Humidity Index
ECHAM4	Hamburg Atmospheric Model, version 4
ECMWF	European Centre for Medium-range Weather Forecasting
EEOF	Extended Empirical Orthogonal Function
EEqIO	Eastern Equatorial Indian Ocean
ENSO	El Niño-Southern Oscillation
EQUINOO	Equatorial Indian Ocean Oscillation
ET	Evapotranspiration
FOAM	Met Office Forecast Ocean Assimilation Model
GA6.1	Met Office Global Atmosphere 6.1
GCM	General Circulation Model
GDP	Gross Domestic Product
GDP	Gross Domestic Product
GFS	Global Forecast System (NCEP)
GLACE	Global Land-Atmosphere Coupling Experiment
GLACE2	Global Land-Atmosphere Coupling Experiment, version 2
HadCM3	Hadley Centre Coupled Model, version 3
IMD	India Meteorological Department
INCOMPASS	Interaction of Convective Organisation and Monsoon Precipitation,

	Atmosphere, Surface and Sea
IOD	Indian Ocean Dipole
ISMR	Indian Summer Monsoon Rainfall
ISO	Intraseasonal Oscillation
ITCZ	Inter Tropical Convergence Zone
JASMINE	Joint Air-Sea Monsoon Experiment (Webster et al., 2002)
JJAS	June-September, inclusive
LAC	Land-Atmosphere Coupling
LCL	Lifting Condensation Level
LHF	Latent Heat Flux
MC-KPP	Multi-Column K Profile Parameterisation
MCZ	Maximum Cloud Zone
MJO	Madden-Julian Oscillation
NASA	National Aeronautics and Space Administration (U.S.A)
NCAR	National Centers for Atmospheric Research (U.S.A)
NCEP	National Centers for Environmental Prediction (U.S.A)
NEMO	Nucleus for European Modelling of the Oceans
NWI	Northwestern India
NWP	Numerical Weather Prediction
OLR	Outgoing Longwave Radiation
OSTIA	Operational Sea-surface Temperature and sea ice Analysis
PBL	Planetary Boundary Layer
PUM	Portable Unified Model
SC	Shallow Convection
SHF	Sensible Heat Flux
SM	Soil Moisture
SM-P	Soil moisture-Precipitation
SRA	Standardised Rainfall Anomaly
SST	Sea Surface Temperature
TBO	Tropospheric Biennial Oscillation
TMI	Tropical Rainfall Measure Mission Microwave Imager
TRMM	Tropical Rainfall Measuring Mission
UK FAAM	UK Facility for Airborne Atmospheric Measurements
WNP	Western North Pacific
WRF	Weather Research and Forecast

Chapter 1:

INTRODUCTION

1.1 Motivation

The Indian region receives about 80% of its annual rainfall (Mooley and Parthasarathy, 1984; Webster et al., 1998; Basu, 2007; Krishnan et al., 2009) during the summer monsoon season (June-September, JJAS hereafter), directly affecting the lives of over one billion people. The year-to-year variations in the Indian summer monsoon rainfall (ISMR) bear significant impacts on agricultural production, water resources, power generation, food security and various sectors of society. It is estimated that the agricultural sector accounts for 23% of India's gross domestic product (GDP) and employs 59% of the country's workforce (World Travel & Tourism Council, 2017). Furthermore, 60% of the crops in India are rain-fed, supporting approximately 40% of the population (Reddy and Syme, 2015). Thus, monsoon rainfall is essential for the Indian agricultural sector. Besides the agricultural sector, the timing and onset of the ISMR exert a significant impact on water storage in India. For example, a late monsoon onset in June 2019 resulted with water shortages in Chennai, India's sixth-largest city, after four of its reservoirs ran dry (Patel, 2019). Additionally, water availability also affects India's electricity generation via hydroelectricity, which accounts for 13% of its total power capacity (International Hydropower Association, 2018).

The Indian monsoon is often described as the seasonal reversal in atmospheric circulation and precipitation associated with the asymmetric heating of the ocean and land over the tropics. In the summer months, the maximum solar insolation shifts north of the equator over the Indo-Gangetic Plain (Fig. 1.1). The intense heating over the Indian landmass and the Tibetan Plateau forms a large-scale temperature and pressure gradient between India and the equatorial Indian Ocean to the south. As a result, the southeast trade winds cross into the Northern Hemisphere and are deflected to the east by the Coriolis force together with the East African topography, forming the southwest Indian monsoon winds. These

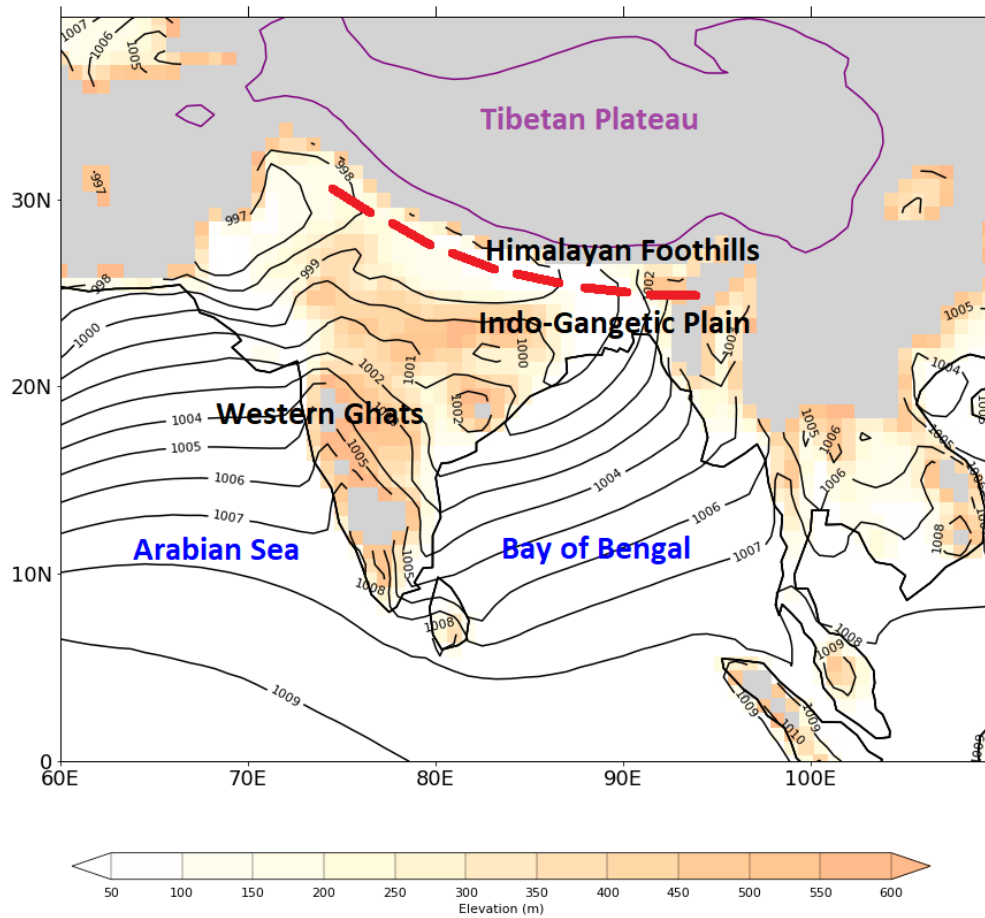


Figure 1.1: Map of India and the adjacent oceans depicting the elevation (m, filled contour) and the JJAS climatological (1979-2015) mean-sea-level pressure (hPa, contour lines) obtained from ERA-Interim. Elevation greater than 600m is shaded in grey, with the solid purple line outlining the Tibetan Plateau (approximately 3000m). The red dashed lines represent the climatological (or normal) position of the monsoon trough.

moisture-rich winds flow towards India, acting as the primary source of summer monsoon precipitation. Due to the fact that the thermal contrast between the land and ocean is the fundamental force driving the monsoon, climate change is expected to increase the Indian monsoon precipitation. According to the Intergovernmental Panel on Climate Change's fifth assessment report, simulations from climate models project an approximate 5% to 15% increase in total monsoon rainfall over India. This increase is chiefly attributed to a warmer Indian Ocean, which amplifies the land-thermal contrast, thereby increasing the amount of moisture transported towards India (Christensen et al., 2013).

Traditionally, the monsoon is often hypothesised as a large land-sea breeze as a result of the meridional temperature gradient between ocean and landmass. Implicitly, this suggests that higher ISM rainfall is associated with stronger temperature gradient while lower ISM rainfall is linked to weaker temperature gradient. However, studies such as Kothawale and Rupa Kumar (2002) and Gadgil (2018) have shown that stronger monsoons were found to be

correlated with weaker land-ocean thermal contrast. This led to some researchers to postulate the Intertropical Convergence Zone (ITCZ) as a modern theory for the Indian monsoon (Gadgil, 2003; Schneider et al., 2014; Gadgil, 2018). In this theory, the manifestation of the monsoon is associated with the seasonal (northward) migration of the ITCZ which forms over the southern equatorial Indian Ocean during the boreal winter. Several major characteristics of the ISM were observed to have the important dynamical characteristics of the ITCZ over the Indian monsoon region during boreal summer. An example is the occurrences of an ITCZ with strong ascent throughout the troposphere over the Indian summer monsoon region. The migration of the ITCZ is controlled by the variations in the cross-equatorial atmospheric energy transport in response to the inter-hemispheric temperature contrast. In general terms, the ITCZ migrates towards the warmer hemisphere (Adam et al., 2016). For instance, Schneider et al. (2014) found that northward migration of the ITCZ towards the Northern Hemisphere occurred when the Southern Hemisphere was 1.2-1.5 K cooler.

During a monsoon season, however, the ISMR is heterogeneous. Variability in rainfall occurs at intraseasonal timescales, characterised by “active” and “break” periods. The rainfall intensity during active and break phases depend on the location of the monsoon trough. The monsoon trough is an elongated belt of a low-pressure zone that is parallel to the Himalayan foothills located northwest of India as illustrated in 1.1. In the active phase, the monsoon trough and the associated enhanced rainfall are situated over central India. In the break, weak or no rainfall is present over central India, and increased rainfall is located over the Himalayan foothills when the monsoon trough shifts northwards to its normal position along the Himalayas (Krishnamurthy and Shukla, 2000; Rajeevan et al., 2006, 2010).

Drought years over India are associated with prolonged break events (Bhat, 2006; Joseph et al., 2009; Neena et al., 2011). Fig. 1.2 illustrates the all-India rainfall (AIR) of two prominent drought years in 2002 (solid blue line) and 2009 (solid red line), along with the long-term climatology (dashed black line). The 2009 drought event was attributed to two extended break periods: one in early June and another between late July and early August when the AIR was significantly below the long-term climatology. The break phase in June resulted in a rainfall deficit of 47% below the June average, affecting 59% of the country, while the second break phase between July-August caused a 27% deficit in August mean rainfall (Neena et al., 2011). Another significant drought event in 2002 was ascribed to an extended break in July, leading to a rainfall deficit of 56% below the July mean, which caused a 21.5% deficit in the seasonal mean (Bhat et al., 2001). The drought triggered a loss of 24 million tonnes of food crops and a 1% fall in India's GDP (Gadgil et al., 2003). Accurate prediction of the ISMR and its intraseasonal variability are therefore essential not only for disaster mitigation but also for the agricultural sector and economy of India. Also, better knowledge and representation in models of the mechanisms driving intraseasonal variability are essential to improve sub-seasonal to

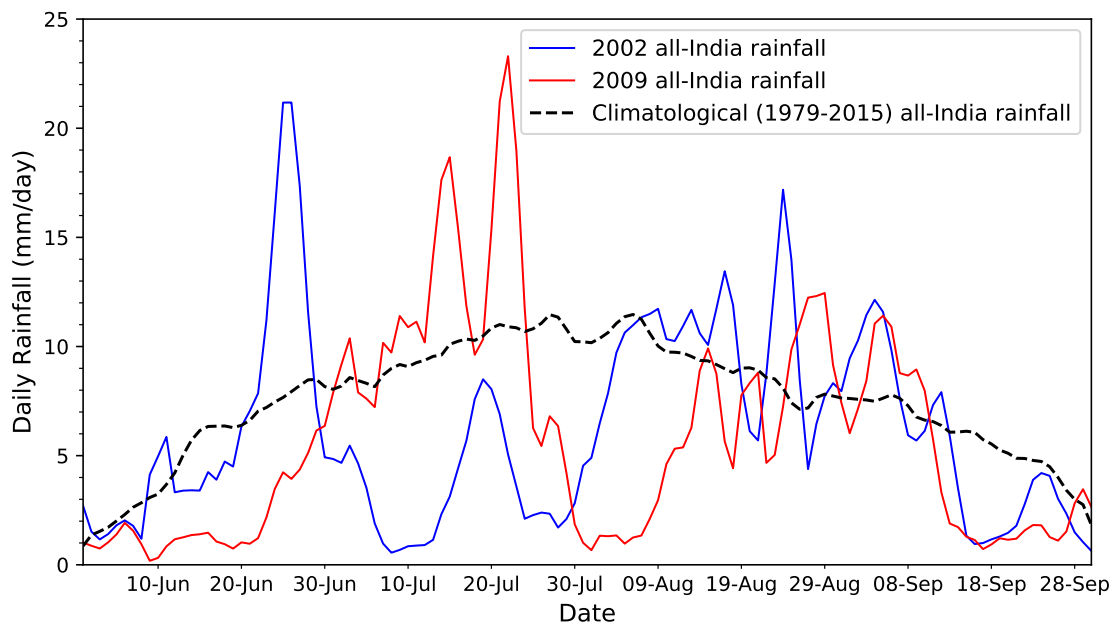


Figure 1.2: Time series of observed daily all-India rainfall (mm/day) from the India Meteorological Department's gridded rainfall dataset. The long-term 1979-2015 climatology is illustrated by the black line. The blue and red line denotes rainfall for the 2002 and 2009 monsoon season respectively.

seasonal forecasting (Kim and Kang, 2008; Lee et al., 2015).

The active-break cycles of monsoon precipitation over the northern Bay of Bengal (NBoB) and India are modulated by a northward propagating intraseasonal oscillation frequently referred to as the boreal summer intraseasonal oscillation (BSISO hereafter, e.g., Webster et al. 1998; Krishnamurthy and Shukla 2000; Rajeevan et al. 2006, 2010; Pai et al. 2016). In the tropics, the largest source of intraseasonal variability (30-60 days) was discovered in the early studies of Madden and Julian (1971, 1972), commonly known as the Madden-Julian oscillation (MJO). The MJO is characterised by a predominantly eastward-propagating, large-scale regions of enhanced and suppressed convection, observed primarily over the equatorial Indian and Pacific Oceans. The MJO is mainly active over the equator during boreal winter. In contrast, during the Indian summer monsoon, the MJO-related features exhibit a pronounced northward propagating component originating from the eastern equatorial Indian Ocean and an off-equatorial westward component over the western North Pacific (Yasunari, 1979; Wang et al., 2005b; DeMott et al., 2013). The boreal summer MJO is also referred to as the BSISO.

There have been various studies attempting to understand the mechanisms governing the northward-propagating BSISO. The coupling between land surface heat fluxes and the low-level atmosphere over the Indian subcontinent was identified as a potential mechanism responsible for northward propagation (Webster, 1983; Taylor, 2008; Barton et al., 2019), as discussed in §2.2.2.1. The northward propagation may be facilitated by the surface moisture and heat fluxes destabilising the planetary boundary layer (PBL) north of convection, leading

to a northward shift in convection. Later studies have favoured atmospheric dynamics (Lawrence and Webster, 2002; Jiang et al., 2004; Kang et al., 2010) as the underlying mechanism responsible for the northward propagation. However, some studies have disputed whether internal atmospheric dynamics alone can sustain the northward propagation, as will be discussed in more detail in §2.2.2.2. Additionally, interactions between the ocean and the atmosphere have also been suggested to promote northward propagation. Studies using a combination of observations, reanalysis and models hypothesised that the northward propagation of convection from the eastern equatorial Indian Ocean lags warm sea surface temperature (SST) anomalies to the north (Vecchi and Harrison, 2002; Kemball-Cook and Wang, 2001; Roxy and Tanimoto, 2007; Klingaman et al., 2008b).

In addition to observational studies on the BSISO, models have been used to understand its processes. However, the current modeling and forecasting capability for the space-time characteristics of the BSISO remains limited as the magnitude and intensity of the northward propagation are underestimated (Sperber and Annamalai, 2008; Sabeerali et al., 2013; Lee et al., 2015; Fang et al., 2017b,c). Atmospheric general circulation models (GCMs) had some success in simulating intraseasonal oscillation but suffer from deficiencies such as exhibiting a weak northward propagation. In contrast, studies based on atmosphere-ocean coupled models (Kemball-Cook and Wang, 2001; Fu et al., 2003) showed that they produced an improved and more realistic (and stronger) BSISO compared to AGCMs, indicating that air-sea coupling is necessary for the BSISO. Yet, the ability of AGCMs to simulate the northward-propagating BSISO, albeit weaker, may further suggest that internal atmospheric dynamics is mainly responsible for driving the BSISO, with the support of air-sea coupling (Fu et al., 2003; Fu and Wang, 2004a; DeMott et al., 2014). In general, the lack of consensus between the uncoupled and coupled experiments suggest that the role of air-sea coupling on the northward propagation is still not well understood. More importantly, this further emphasises the lack of agreement on the physical mechanisms explaining the strength and propagation of the BSISO.

Besides ocean-atmosphere interaction, there is also a lack of research on the role of land-atmosphere interactions in the intraseasonal variability of the ISM (Bellon, 2011). Soil moisture is perhaps the most significant indicator of the land surface state. Soil moisture also plays an important role in the energy cycle by partitioning the surface sensible and latent heat fluxes (or evapotranspiration) into the atmosphere. Through the water cycle, evapotranspiration changes may modify atmospheric moisture and temperature, stability (convection and cloud formation) and more importantly, precipitation (Beljaars et al., 1996; Betts et al., 1996; Koster et al., 2000; Taylor, 2008; Lorenz et al., 2015). Yet, it remains unclear how the spatio-temporal evolution of soil moisture and its subsequent feedback may modify (if any) the atmosphere on the intraseasonal timescales such as the active/break phase transition.

Efforts to further understand how land and oceanic surface processes influence the atmosphere during the Indian summer monsoon was undertaken in 2016 with the Interaction of Convective Organisation and Monsoon Precipitation, Atmosphere, Surface and Sea (INCOMPASS) and the Bay of Bengal Boundary Layer Experiment (BoBBLE) field campaign. The INCOMPASS field campaign combined measurements obtained from the UK Facility for Airborne Atmospheric Measurements (UK FAAM) aircraft, ground and upper-air instrumentation (surface flux towers and radiosondes). The unprecedented use of the UK FAAM aircraft provided a unique opportunity to perform flight sorties covering the pre-monsoon and monsoon period over locations with distinct precipitation gradients, for example, between the wet northeast India and the dry northwest India. The objectives of INCOMPASS are to understand how the land-surface properties, thermodynamic and dynamic forcings on intraseasonal timescales influence the characteristics of the monsoon rainfall ranging from kilometres to country-wide spatial scales (Turner et al., 2019). Furthermore, the BoBBLE field campaign in the southern Bay of Bengal was organised with the aim of developing high-quality in situ observational datasets to improve the understanding of the ocean-atmosphere interaction processes and ocean dynamics of the Indian monsoon and its intraseasonal variability. While there have been many previous field experiments such as the Joint Air-Sea Monsoon Interaction Experiment and the Bay of Bengal Monsoon Experiment, these campaigns were focused on the northern Bay of Bengal. BoBBLE fills the gap on understanding the sensitivity of the Indian monsoon to the physical processes over the southern Bay of Bengal, using a combination of ocean gliders and Argo floats during the peak monsoon period (Vinayachandran et al., 2018). Overall, results from the INCOMPASS and BoBBLE field experiment will provide new insight into the influence of ocean-atmosphere and land-atmosphere coupling on the Indian summer monsoon.

The intraseasonal variability of Indian summer monsoon can have devastating impacts on the socio-economic welfare of nearly 1.3 billion people, as seen in 2002 and 2009. The ability to accurately forecast the timing of the active and break events is vital to mitigate the negative impacts on the country's economy, food security, water resources and most importantly, the lives of the people. The ability to overcome these issues lies in the predictive skills for these events in models. However, the deficiency in the models is linked to the poor representation and understanding of the physical mechanisms governing active/break events and their transition. While past and recent studies have focused their attention on studying composite active and break events (Annamalai and Slingo, 2001; Krishnamurthy and Shukla, 2000; Rajeevan et al., 2006; Krishnamurthy and Shukla, 2007; Rajeevan et al., 2010), very few have looked at these processes as a transition from one phase to another. Many of these studies assume implicitly or explicitly that all active (break) phases transition towards a break (active) phases after a period of time. Attempting to understand the processes driving

the intraseasonal variability of the ISM based on this premise could lead to an inaccurate representation of the mechanisms in models, and thus, misrepresenting the active/break phases. Also, the transition between active/break phases is arguably more important to predict than the states themselves.

In addition, recent BSISO modelling studies focus on simulating and forecasting the active/break phases in climate and forecast models, but very few have looked at forecasting the transition from a break phase to an active phase (or vice versa). Therefore, the central aspect of this thesis is to understand the physical mechanisms, such as the thermodynamic properties and the large-scale circulation governing the transition over the oceanic and land region associated with the BSISO. Furthermore, recent studies have shown that air-sea coupling may influence the strength and propagation of the BSISO, yet it remains unclear if ocean-atmosphere and land-atmosphere interaction are essential for the break-to-active transition. An improved understanding of the physical mechanism(s) may further improve the representation of the physical process of models in simulating and forecasting not just active/break events, but the BSISO as a whole. Therefore, this thesis aims to investigate the issues mentioned above in both observations and atmosphere-only and coupled forecast models. The importance of air-sea coupling during the transition will be further revealed by comparing the forecast of the 2016 break-to-active transition event in initialised uncoupled and coupled forecast models. The case for investigating the 2016 transition event was selected as both INCOMPASS and BoBBLE campaign were being conducted during this period, which provided an opportunity to link the findings in this thesis with those from the field campaigns.

1.2 Aims of the thesis

The focus of this thesis is to understand the transition from a break to an active phase during the Indian summer monsoon. The motivation for investigating the break-to-active transition rather than the active-to-break transition is due to the lower predictability of the transition to an active phase, which will be discussed in greater detail in §3.4. Previous studies (Bhat et al., 2001; Vecchi and Harrison, 2002; Vialard et al., 2012; Govardhan et al., 2017) have related the revival of an active phase to the warming of the lower atmosphere, which increases the instability and the subsequent convection originating from the eastern equatorial Indian Ocean. Furthermore, the convection and associated rainfall show pronounced intraseasonal variability and are strongly coupled to the upper ocean processes in the NBoB. Therefore, this thesis seeks first to examine the intraseasonal variability by focusing on the processes controlling the break-to-active transition over the NBoB. Additionally, a case study on the break-to-active transition during the 2016 Indian monsoon will also be analysed. The research campaign from INCOMPASS and BoBBLE allows us to use 2016 as the focal point for the case

study.

1. How is the break-to-active transition manifested over the NBoB?

- (a) **What are the dynamic and thermodynamic properties of the atmosphere during the transition?**
- (b) **How are surface turbulent fluxes and SSTs modulated on intraseasonal time-scales?**
- (c) **What are the dominant mechanism(s) associated with the break-to-active transition?**
- (d) **How similar are individual events compared to the average/composite events?**

Secondly, I proceed to examine the break-to-active transition over India with the focus on studying how land surface processes may influence the dynamics, thermodynamics and land-atmosphere coupling of the transition. Furthermore, understanding the changes in the land-atmosphere coupling strength will provide an outlook on the importance of localised land-atmosphere coupling on short timescales, compared to other factors such as the large-scale circulation during the break-to-active transition.

2. How do regional land-atmosphere processes influence the break-to-active transition over India?

- (a) **How do land surface properties change during the break-to-active transition?**
- (b) **What are the thermodynamic properties of the atmosphere during the transition?**
- (c) **How does land-atmosphere coupling strength evolve during the transition?**
- (d) **How important is the local land-atmosphere coupling compared to the large-scale processes in the break-to-active transition?**

Finally, this thesis will investigate whether air-sea coupling plays a role in the space-time characteristics of the break-to-active transition over the NBoB by comparing forecast output from an uncoupled and two coupled models. Ultimately, this chapter aims to identify if the inclusion of air-sea coupling in a coupled model improves the prediction on short timescale (<20 days) processes such as the break-to-active transition.

3. How is the break-to-active transition represented in numerical weather prediction (NWP) forecasts under a variety of coupling configuration?

- (a) **Can NWP simulations forecast the northward-propagating BSISO during a transition?**
- (b) **Do intraseasonal SST, and surface heat fluxes influence the characteristics of the northward propagation and resulting rainfall variability?**
- (c) **Does the inclusion of air-sea coupling improve the prediction of a**

break-to-active transition?

- (d) **What is the sensitivity of the break-to-active forecast skill in the coupled model to the representation of ocean dynamics?**

1.3 Outline of thesis

In Chapter 2, a detailed description of the Indian monsoon, its variability and mechanisms will be explored. The basic state of the India monsoon is discussed in §2.1, followed by a brief examination of its interannual variability in §2.2. The majority of the focus in this thesis is dedicated to examining its intraseasonal variability (§2.3). The link between the intraseasonal variability and the active-break cycle is established in §2.3.1. Additionally, the theories and mechanisms for the BSISO are reviewed in the past and recent literature in §2.3.2. Specifically, the land-surface fluxes (§2.3.2.1); dynamic theories (§2.3.2.2); and of particular interest to the aim of this thesis, the ocean-atmosphere interaction (§2.3.2.3). The influence of land-atmosphere interaction (§2.4) will expand upon the land surface fluxes theories by providing an overview of feedback between the land surface state and the atmosphere in past studies.

Chapter 3 introduces the concept of a break-to-active composite, a novel method to investigate the revival of the active phase based on observations and reanalysis datasets (§3.2). The choice of the index to identify individual active and break events is presented in §3.3. The motivation and criteria for identifying break-to-active transition events are discussed in §3.4, and its northward-propagation is verified in a BSISO index representing the strength and propagation of individual transition events (§3.5). The evolution of rainfall and atmospheric fields is investigated in the break-to-active composite in order to understand the general dynamics of the transition over the Indian monsoon region (§3.6).

Next, having established the transition over a broader region in Chapter 3, the composites introduced in the previous chapter will be combined with observations and reanalysis (§4.3) to study the break-to-active transition over the northern Bay of Bengal. The potential mechanism(s) governing the break-to-active transition is investigated by examining the evolution of the thermodynamic properties of the atmosphere. Furthermore, the evolution of surface flux and SST anomalies during the transition are also examined in §4.4. The moisture budget analysis of the NBoB (§4.5) will further assist with determining the dominant mechanism between local ocean surface processes and large-scale circulation. These composite events are also compared to the transition in a case study on the 2016 Indian monsoon to determine their similarities (or lack thereof) to an individual transition event (§4.6).

The break-to-active transition over the Indian land surface is investigated in Chapter 5 by analysing the land surface variability and land-atmosphere coupling strength in reanalysis §5.2. The two-legged land-atmosphere coupling metrics are described in §5.2.3, which are capable of quantifying the coupling strength over India. To study the break-to-active transition over India, the land surface properties (§5.3.1) and thermodynamics (§5.4) of the transition are evaluated using similar break-to-active composites in previous chapters. To distinguish the role of local land-atmosphere coupling and large-scale circulation during the revival of the active phase, a moisture budget over regions indicating strong intraseasonal signals will be analysed (§5.4.3). The role of localised land-atmosphere coupling during the break-to-active transition over India is revealed, and discussed in §5.5.

Chapter 6 builds upon the 2016 break-to-active case study by investigating the transition in an atmosphere-only and two coupled NWP models. The description and configuration of the models and their differences will be discussed (§6.2.1). To investigate the effect of the representation of air-sea coupling, the break-to-active transition composite from the uncoupled model is compared against the coupled models (§6.3–§6.6). These comparisons will reveal if air-sea coupling is a necessary condition for northward propagation and the associated break-to-active transition. Further, the sensitivity of the transition to ocean dynamics is also considered by comparing two coupled models: one without ocean dynamics representation and the other with ocean dynamics. The results on the inclusion of air-sea coupling in forecasting the break-to-active transition in 2016 are discussed in §6.7.

Chapter 7 will provide a synthesis of the key findings of this thesis and how the results may improve our understanding of the potential mechanisms governing the intraseasonal variability of the Indian summer monsoon (§7.1). The limitations of this thesis are also discussed (§7.2), and suggestions for future work will also be explored (§7.3),.

Chapter 2:

SCIENTIFIC BACKGROUND

This chapter describes the basics of the Indian summer monsoon and its variability on interannual and intraseasonal scales. In particular, §2.1 reviews the physics governing the Indian monsoon. The relationship between the seasonal cycle of insolation and the large-scale circulation on the monsoon is reviewed. The interannual aspects of the Indian monsoon and its teleconnection with El Niño-Southern Oscillation (ENSO) and other slowly varying forcings is discussed in §2.2. The main focus of this thesis is to understand the intraseasonal variability of the northward propagating BSISO (§2.3). The link between the BSISO and the active/break cycle of the ISM is discussed in detail in §2.3.1. In, §2.3.2 the leading theories for its generation, such as land surface fluxes (§2.3.2.1), internal atmospheric dynamics (§2.3.2.2) and air-sea interaction (§2.3.2.3) are discussed. Finally, §2.4 builds upon §2.3.2.1, highlighting the role of land-atmosphere interaction in the intraseasonal variability of the Indian monsoon. Lastly, §2.5 summarises the motivation of this thesis in the context of the scientific background.

2.1 The Indian summer monsoon basic state

The fundamentals of the monsoon are the seasonal reversal in large-scale atmospheric circulation and the corresponding changes in precipitation associated with the asymmetric heating of ocean and land surface over the tropics (Li and Yanai, 1996; Webster et al., 1998; Trenberth et al., 2000). The asymmetric heating creates a meridional temperature gradient between the Indian subcontinent and the equatorial Indian Ocean, owing to the higher heat capacity of oceans compared to land. Ocean temperatures are therefore comparatively stable, while land temperatures fluctuate faster in response to the intense solar heating.

In March, the solar maximum moves north from the equator. As a consequence, the Indian subcontinent and the adjacent Tibetan Plateau warm up rapidly, owing to the higher elevation of the Tibetan Plateau ($\approx 4500\text{m}$). The significant heating of the atmosphere above creates an area of low pressure. In contrast, to the south, the equatorial Indian Ocean is

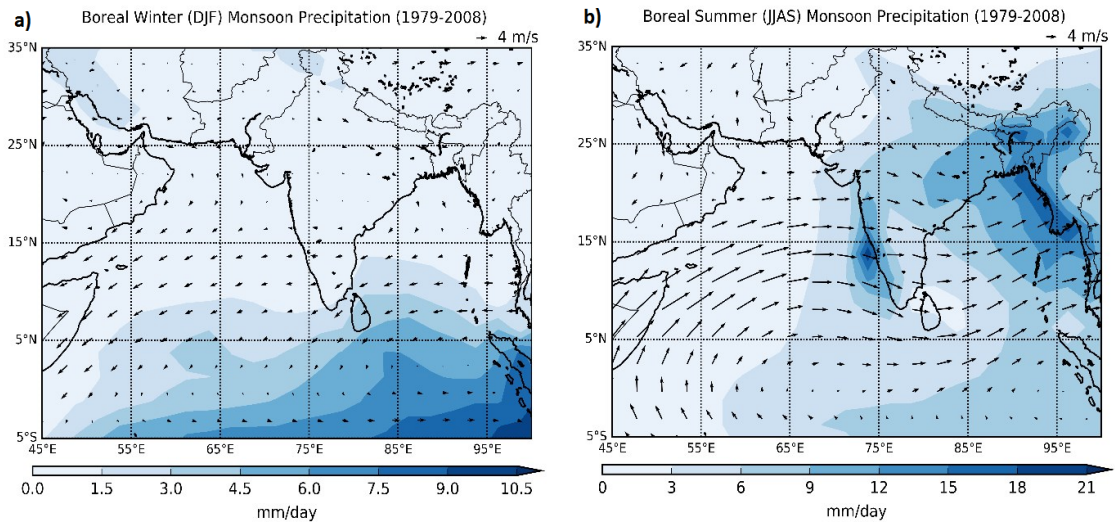


Figure 2.1: Monthly mean monsoon precipitation (mm/day) and 850 hPa winds (m/s) for 1979–2008 for (a) boreal winter (December–February) and (b) boreal summer (June–September). The precipitation was obtained from the Global Precipitation Climatology Project (GPCP; Adler et al., 2003; Huffman et al., 2009), while the winds were taken from the ERA-Interim Reanalysis dataset (Dee et al., 2011a).

comparatively cooler, and a high-pressure zone develops, forming the meridional temperature and pressure gradient between the land and ocean. As a result, a cross-equatorial flow is generated at the surface, which together with the upper-tropospheric cross-equatorial return flow and the Coriolis force forms the distinct C-shape of the Indian summer monsoon winds. The cross-equatorial wind or the Somali Jet contains moisture evaporated from the Indian Ocean (Arabian Sea and Bay of Bengal), which supplies moisture for the Indian monsoon rainfall. Consequently, the southwest Indian summer monsoon in Figure 2.1b forms over the Indian subcontinent in June. The winds converge into the mountainous region of the Western Ghats along the west coast of India, where substantial rainfall is generated due to orographic lifting. The winds continue eastward towards the Bay of Bengal and then turn north around a low-pressure feature called the monsoon trough. The monsoon trough shown in Fig. 1.1, is defined as a belt of a low-pressure roughly parallel to the Himalayan foothills in the northwest-southeast direction. As the wind converges towards the Himalayas, the large rainfall amounts there is due to the orography effect.

Recently, the India Meteorological Department (IMD) has adopted a new set of criterion based on rainfall and large-scale circulation to define the monsoon onset (Pai and Nair, 2009): (a) if rainfall of 2.5 mm or more is observed in 14 stations over the southern tip of India, the monsoon onset over Kerala will be declared on the next day as long as (b) westerly winds are maintained up to 600 hPa in the region 0° – 10° N and 55° – 80° E, (c) zonal wind speeds are between 15–20 knots at 925 hPa in the region 5° – 10° N and 70° – 80° E and (d) OLR values are below 200 Wm^{-2} in the region 5° – 10° N and 70° – 75° E.

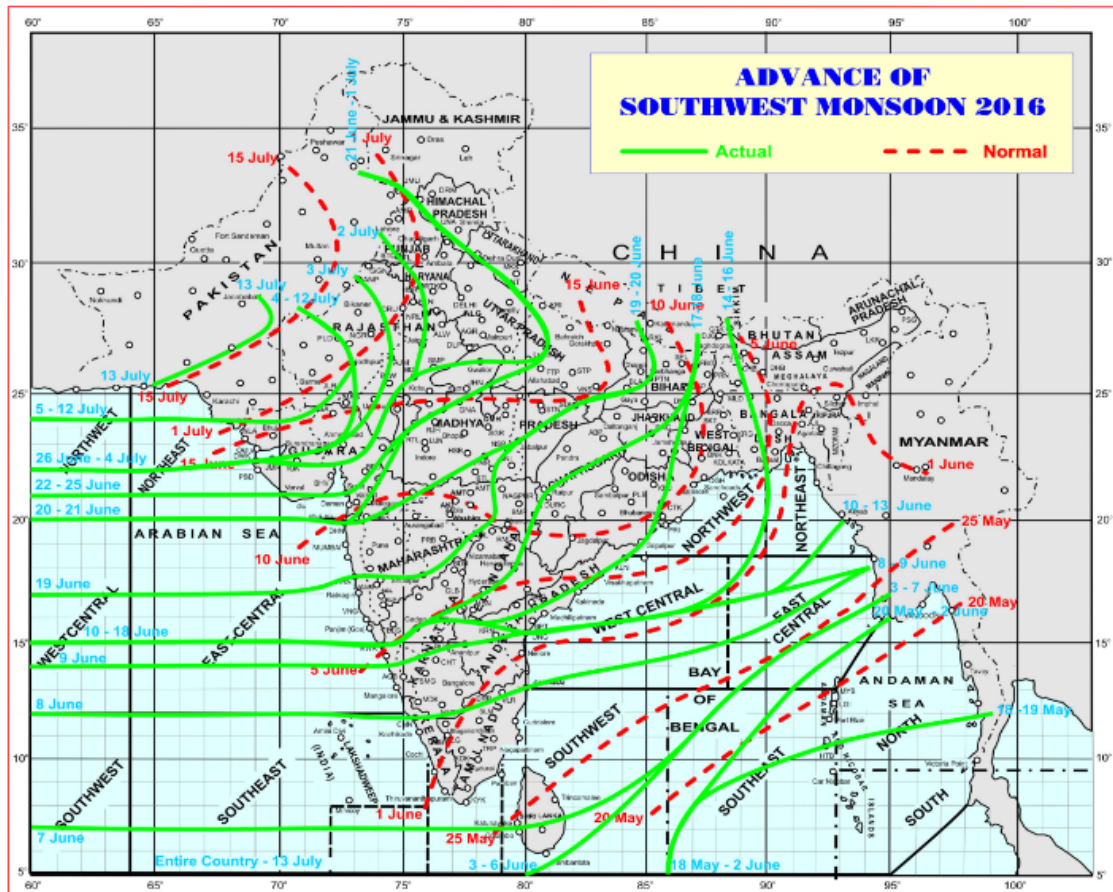


Figure 2.2: The monsoon rainfall isochrones for the normal (dashed red) and 2016 (solid green) onset date of the 2016 southwest monsoon retrieved from the Indian Meteorological Department's website at http://www.imd.gov.in/pages/monsoon_main.php.

The monsoon has a general southeast to northwest seasonal propagation illustrated by the rainfall isochrones in Figure 2.2 for the 2016 season (solid green) in comparison to climatological dates (dashed red). The climatological Indian monsoon onset date over Kerala is 1st June. The interannual standard deviation of the monsoon onset is approximately eight days (Krishnamurthy and Shukla, 2000; Chevuturi et al., 2019). By 15th July, the monsoon covers much of India before retreating from northwest India at the beginning of September. In 2016 however, the southwest monsoon (solid green line) onset was declared over Kerala on 8th June, seven days after its climatological onset date. The monsoon advanced rapidly to the north in the subsequent two days over 15°N, followed by a hiatus over northwestern India due to a weaker Arabian Sea branch. However, a stronger Bay of Bengal branch supported the advance of the monsoon over northeastern India between 10th and 18th June. Thereafter, the monsoon continued to propagate rapidly as it covers the entire subcontinent by 13th July (against the normal date of 15th July).

The rainfall distribution (Figure 2.1b) over India is spatially heterogeneous. The majority of the mean JJAS rainfall occurs in the: a) west coast of India due to the orographic effect of the

Western Ghats, b) central India, c) the northeast, near the foothills of the Himalayas due to the monsoon trough and d) the northern Bay of Bengal. Conversely, rainfall is sparse in southeast India due to the rain shadow caused by the Western Ghats, as well as northwestern India due to the shorter monsoon season there (Raju et al., 2005; Joseph et al., 2006; Moron and Robertson, 2014). Furthermore, the rainfall during intraseasonal active and break periods is associated with variations in the position of the monsoon trough, which will be discussed in §2.3 in greater detail. During the break, the monsoon trough shifts northwards over northeast India and the Himalayan foothills where intense rainfall is observed. Conversely, drier conditions over central, northern and the west coast of India are observed. The opposite is seen for the active phase when the monsoon trough is situated over central India.

Several observational and modelling studies have investigated monsoon onset mechanisms. Krishnamurti et al. (2012) used a combination of observational and the Advanced Research Weather and Forecasting Model datasets for the first 25 days after Indian monsoon onset to study its propagation characteristics. Their results revealed that the progressive evapotranspiration due to moistening of soil moisture by stratiform rains approximately 100 km north of the onset region enhances the development and progression of deep convection. Additionally, Parker et al. (2016) used the ERA-Interim reanalysis dataset for the period 1979-2014 to relate the southeast-northwest advance of the monsoon to the interplay between moist convection and mid-level dry intrusions. The descending northwesterly dry intrusions originate from the Thar Desert, and extend towards the southeast coast of India. The authors found that pre-monsoon rainfall and the wetting of the land surface over southeast India moistens the low-level troposphere via evaporation. The low-level troposphere destabilises and shallow cumulus clouds are formed. Detrainment, the transfer of moisture from cumulus clouds into the surrounding atmosphere, causes the atmospheric column to moisten and destabilise further, favouring deep convection. As the monsoon progresses, the mid-level dry layer shoals towards the northwest by the continuous moistening from below, and consequently, allows the convection to propagate northwestwards. The propagation mechanism of Parker et al. (2016) was subsequently identified by Menon et al. (2018) in hindcast simulations of the Met Office Global Seasonal Forecast System 5. These studies suggest the importance of shallow convection in transferring moisture from the boundary layer to the free troposphere. Evaporation from land-atmosphere interactions and horizontal moisture convergence by the large-scale circulation are thus essential for the progression of the monsoon onset.

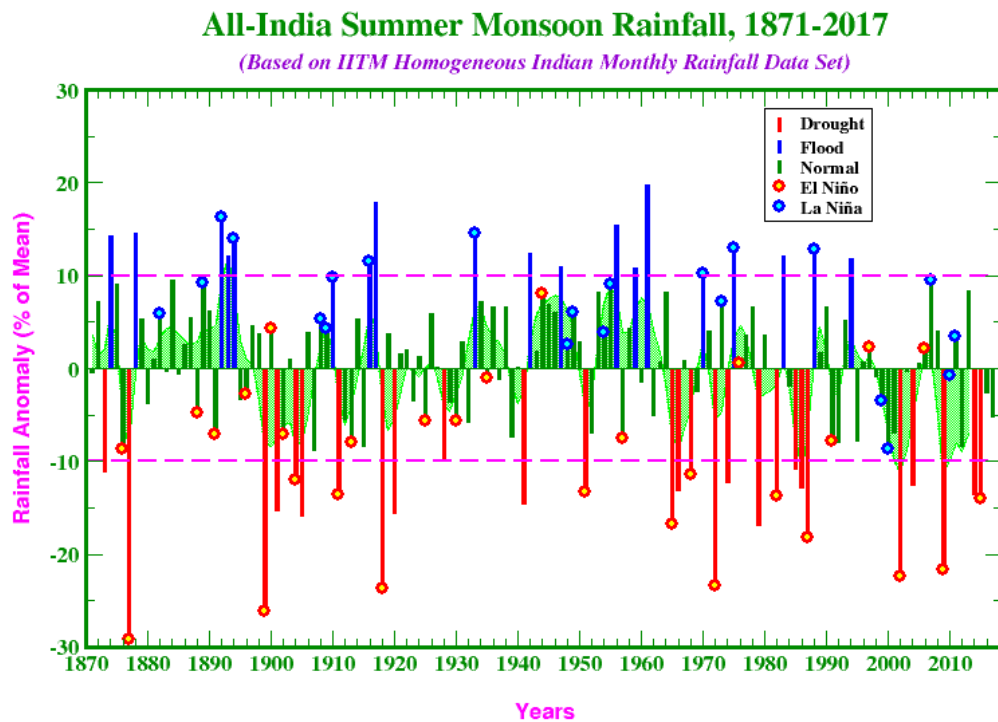


Figure 2.3: Timeseries of interannual All-India Summer Monsoon Rainfall for the period 1871-2017 based on a homogeneous rainfall dataset from 306 rain gauges developed by the Indian Institute of Tropical Meteorology. The year-to-year El Niño and La Niña conditions identified based on the Oceanic Niño Index are indicated by red and blue circles, respectively. The figure was retrieved from <http://mol.tropmet.res.in/monsoon-interannual-timeseries/>

2.2 The interannual variability of the Indian summer monsoon

Long-term assessments of the ISMR have shown that the interannual standard deviation (Fig. 2.3) is about 10% to 20% of the mean (Kucharski and Abid, 2017). Prediction of these variations several months in advance has socio-economic benefits, especially in the agricultural sector in terms of planning strategies and optimum crop production. Additionally, the total seasonal rainfall can be thought of as the sum of a slowly varying predictable component relating to the large-scale forcing, and to the number of active and break events as discussed by Krishnamurthy and Shukla (2000, 2007) and (Turner and Hannachi, 2010). Charney and Shukla (1981) had earlier suggested that the seasonally persisting component of Indian monsoon rainfall anomalies were forced by these slowly varying boundary conditions. Thus, predictability may arise from these boundary forcings (e.g. sea surface temperature, soil moisture and snow cover) and the atmospheric response to these forcings (Goddard et al., 2001; Rajeevan et al., 2012; Johnson et al., 2017; Chevuturi et al., 2019).

For instance, large variability in the magnitude of tropical sea surface temperature (SST) anomalies located in the tropics are intimately linked to the ENSO and is the most significant

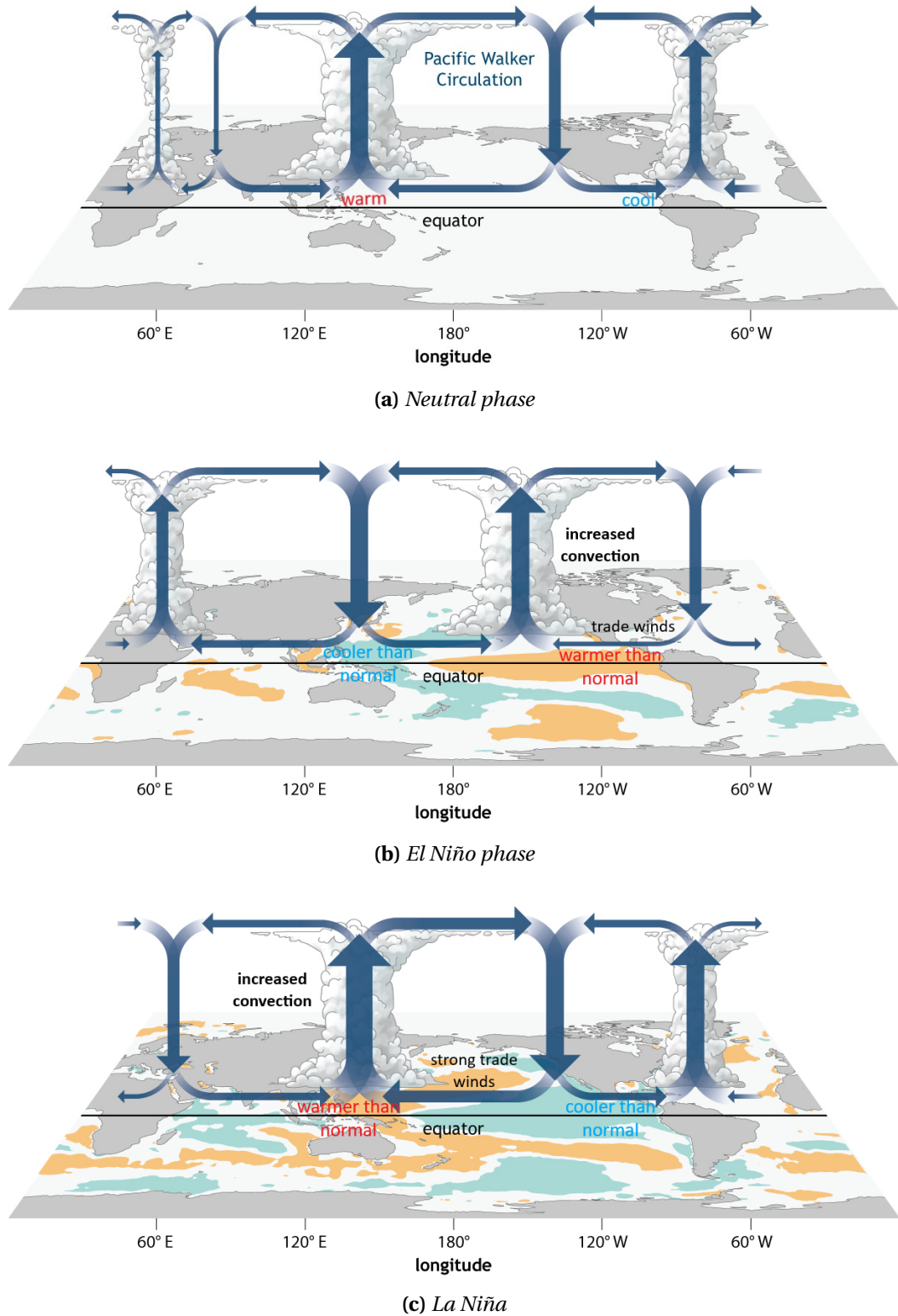


Figure 2.4: Schematics of the three phases of the El Niño-Southern Oscillation: (a) neutral phase, (b) El Niño phase and (c) La Niña retrieved from the National Oceanic and Atmospheric Administration's website at <https://www.noaa.gov/climate>

source of predictability for the Indian monsoon (Webster et al., 1998; Barimalala et al., 2012; Shukla and Huang, 2016). The Indian monsoon precipitation is influenced by the Walker Cell, which in turn is coupled to the SSTs in the underlying ocean over the tropical equatorial Pacific

Ocean and the Maritime Continent (Bjerknes, 1969).

The Walker Cell is a longitudinal circulation across the equatorial Indo-Pacific and is the result of a difference in surface pressure and temperature between the western and eastern tropical Pacific Ocean. Normally, the tropical western Pacific is warm and wet with a low-pressure system and the cool and dry eastern Pacific lie under a high-pressure system. This forms an east-to-west pressure gradient, and causes the surface trade to flow westwards, from high pressure in the eastern Pacific to low pressure in the western Pacific. The circulation is complete in the upper-troposphere as the winds move from the west-to-east.

During the neutral ENSO phase (Fig. 2.4a), the surface trade winds associated with the Walker circulation flow westward across the equatorial Pacific Ocean. The wind exerts stress on the ocean surface, resulting in a westward current. Warm SSTs in the western Pacific result with heat and moisture transport into the lower atmosphere, generating atmospheric convection. Subsequently, the convection causes precipitation over Australia. The resultant drier air then flows eastwards (and westwards), which then sinks over the equatorial eastern Pacific. The pattern of air rising in the west and sinking in the east with the westward-moving air at the surface is referred to as the Walker Circulation. Furthermore, the surface trade winds also cause surface waters in the equatorial eastern Pacific to diverge as a result of Ekman pumping. This divergence causes the upwelling of deep cold ocean water to the surface at the equator and is associated with dry conditions and cold SSTs there.

During El Niño (Fig. 2.4b), the trade winds of the Walker circulation weaken or even reverses, resulting in the warmer than normal SST to move towards the central and eastern tropical Pacific Ocean. The warm SST and the associated convection may also be enhanced by the deepening of the thermocline over central and eastern Pacific, suppressing the upwelling of cooler ocean water. The convection and precipitation subsequently migrate to the east of the Maritime Continent towards the central and eastern Pacific, which brings wetter conditions over countries such as Peru and Ecuador. In contrast, cooler than normal SSTs are now observed over the western tropical Pacific Ocean resulting in drier conditions over Australia and the Maritime Continent.

As for La Niña conditions (Fig. 2.4c), intensification of the Walker circulation results with stronger trade winds. Warmer than normal SSTs are accumulated further west over the Maritime Continent. The subsequent convection strengthens which increases the precipitation over northern Australia. Concomitantly, cooler than normal SSTs due to stronger upwelling are observed across the central and eastern tropical Pacific Ocean as the thermocline shifts towards the surface. Dry conditions now prevail over central and eastern equatorial Pacific.

Through the extensive studies on the relationship between the ISM and ENSO (Ashok

et al., 2003, 2004; Maity and Nagesh Kumar, 2006; Turner et al., 2007; Kucharski and Abid, 2017; Roy et al., 2019), two distinct mechanisms are identified by which the sea surface temperatures over the eastern equatorial Pacific may influence the monsoon rainfall. The first is through the interaction between the equatorial Walker circulation and the regional Indian monsoon Hadley circulation. The other is through the extratropics and upper atmosphere. Put it simply, drought years are usually associated with El Niño, while excess rainfall years are linked to La Niña. In broad terms, ENSO-related tropical Pacific SST affects the Indian summer monsoon through the modulation of the zonal circulation associated with the Walker circulation. During El Niño for instance, the eastward shift of the Walker Circulation and decreased equatorial divergence over the tropical Indian Ocean causing changes in the large-scale zonal circulation. Consequently, the anomalous convergence in the tropical Indian Ocean modulates the cross-equatorial meridional (local Hadley) circulation associated with the Indian monsoon, forming an anomalous divergence over the India which results in a drier than normal ISM.

Furthermore, previous studies have identified different types of El Niño : (1) the traditional/canonical East Pacific El Niño and (2) the Modoki/Central Pacific El Niño (Larkin and Harrison, 2005; Ashok et al., 2007; Yu and Kao, 2007). Kumar et al. (2006b) also suggests reduction in ISM rainfall is greater during the Modoki El Niño compared to the canonical El Niño. This is because the Modoki El Niño is associated with negative rainfall anomalies over the Indian subcontinent, whereas the canonical El Niño is linked with rainfall deficit along the monsoon trough. During the canonical El Niño, the climatological Walker circulation shifts to the eastern Pacific Ocean which results with enhanced low-level convergence over the equatorial Indian Ocean. Due to mass continuity, anomalous subsidence and suppressed convection generated over the Indian continent weakens the monsoon rainfall. As for the El Niño Modoki, the SSTs are characterised by a tripolar SST pattern; warmer than normal SSTs in the central Pacific are flanked by colder than normal SSTs in the eastern Pacific and equatorial Indian Ocean region. This generally weakens the land-ocean thermal gradient between India and the western equatorial Indian Ocean, which subsequently weakens monsoon cross-equatorial flow. As a result, drought-like conditions are observed over the ISM region. Additionally, Dandi et al. (2019) further showed that the weak monsoon rainfall over India during strong El Niño Modoki years is linked to the western North Pacific (WNP) circulation. Anomalous cyclonic circulation located over the WNP induces a strong westerly wind and moisture divergence, and thus, negative rainfall anomalies over south India. Generally, drought conditions over India coincide with El Niño conditions. This is observed when the rainfall anomalies are below -10% of the mean as depicted by the red bars in Fig. 2.3. Furthermore, Pillai and Chowdary (2016) also found that there are more number break phases (2-3 times) and last longer (10-15 days) during El Niño periods.

The opposite is observed during La Niña as the enhancement of the existing subsidence shifts over the central-eastern Pacific and enhance convection forms over the Maritime Continent. As a result, the stronger ascending limb of Walker circulation located over the Indian sector strengthens, which enhance the ISM rainfall. Aneesh and Sijkumar (2018) used observation data to show that La Niña years favour above normal ISM rainfall due to stronger low-level jet over the Arabian Sea and India, as well as weaker westerlies over northwestern India during the pre-1980 period. In combination, the stronger low-level jet and weaker westerlies create an anomalous cyclonic circulation over central India. This anomalous cyclonic circulation leads to stronger convection and rainfall over the region. Therefore, La Niña conditions (blue bars) act to enhance Indian monsoon rainfall and are generally associated with flooding (blue circles) over India. Furthermore, in the post-1980 period, they found that the number of active monsoon rainfall days are reduced. Due to warming of the Indian Ocean, the anomalous cooling over the western equatorial Indian Ocean is reduced, and the land-thermal sea contrast is small, thus, weakening the Indian monsoon. However, it is not always the case that El Niño and La Niña is associated with suppressed and enhanced monsoon rainfall, respectively. For example, one of the strongest El Niño in the 20th century during 1997-98 is only associated with a rainfall anomaly of 4-5% above its long term mean, and no drought conditions were recorded (Krishnamurthy and Goswami, 2000; Kumar et al., 2006a). The severe drought in 2002 was only associated with a weak to moderate El Niño (Bhat, 2006).

Alternative to the Walker and Hadley circulation connection, Ju and Slingo (1995) suggested that drier than normal ISM is associated with increased tropospheric westerlies. This is attributed to the latitudinal shift of the subtropical westerly jet over the Indian region due to anomalous equatorial Pacific SST. Furthermore, drought years during El Niño have been attributed to interaction between meridionally propagating Rossby wave with the subtropical westerlies which generates anomalous quasi-stationary highs in the subtropics and lows in the extratropics. The Rossby wave emanation was shown to have originated from ENSO forcing regions in AGCMs by Krishnan et al. (1998). Additionally, ENSO may also affect the meridional tropospheric gradient over the Indian subcontinent, effectively modulating the strength and duration of the ISM (Goswami and Xavier, 2003).

The Indian Ocean Dipole (IOD) is the Indian Ocean equivalent of the Pacific ENSO (Hameed et al., 1999; Webster et al., 1999; Yamagata et al., 2003, 2013). The IOD is characterised by a zonal dipole in equatorial Indian Ocean SST, with variability on an interannual timescale: the IOD measures differences in SSTs between the western pole in the Arabian Sea (western Indian Ocean) and an eastern pole in the eastern Indian Ocean south of Indonesia. A positive IOD is associated with a cooling of the eastern pole and warming over the western pole. In contrast, a negative IOD phase is associated with a warming of the eastern pole and cooling

over the western pole. Similar to ENSO, the IOD is a coupled ocean-atmosphere phenomenon. An IOD event typically manifests during early summer, matures during September–November and terminates by January. Additionally, the IOD can be classified into two distinct types associated with the ENSO: 1) a normal IOD which occurs concurrently with ENSO and 2) an independent IOD which occurs without ENSO (Sun et al., 2015). In the normal-type IOD, the weakening of the Walker circulation over the eastern tropical Indian Ocean induces easterly wind anomalies near Indonesia during an El Niño. The low-level winds push warmer than normal SSTs towards the western pole. In addition, the easterlies near Indonesia are associated with cooler SST anomalies through anomalous upwelling. Thus a positive IOD manifests over the Indian Ocean (Allan et al., 2001; Baquero-Bernal et al., 2002; Yu and Lau, 2005; Wang and Wang, 2014).

However, other studies have found that some IOD events have occurred independently of ENSO (Webster et al., 1999; Ashok et al., 2003; Yamagata et al., 2003). Yang et al. (2015) evaluated the contribution of ENSO forcing to the IOD based on the Pacific Ocean-Global Atmosphere model simulation experiment. Their study showed that two-thirds of the IOD variance was due to internal variability in the absence of ENSO. In relation to the Indian monsoon, the positive phase of the IOD is associated with enhanced precipitation, while the negative IOD phase suppressed Indian monsoon rainfall. In the positive IOD phase, a temperature difference across the tropical Indian Ocean with cooler than normal water in the east and warmer than normal water in the west are observed. This reduces convection and results with anomalous subsidence and divergence at the lower-troposphere over the eastern pole. To the north, over the Bay of Bengal, low-level convergence is seen due to mass continuity. In combination, the anomalous convergence-divergence pattern over the eastern Indian Ocean sector amplifies the meridional monsoon circulation and thus, enhances precipitation over India. For example, positive IODs during 1994 and 1997 were associated with stronger monsoon rainfall associated with enhanced convection which strengthens moisture convergence over the Indian subcontinent. On the other hand, a negative IOD phase, for instance, during 2016 resulted in a deficiency in rainfall over the southwest region over India. Cooler (warmer) SST anomalies resulted in enhanced subsidence (convection) over the western (equatorial) equatorial Indian Ocean. The stronger than normal subsidence over the western Indian Ocean extended towards the southern/southwestern parts of India, inhibiting convection. As a result of the suppressed convection, negative rainfall anomalies and drought conditions prevailed, including a rainfall deficiency of 66% over Kerala (Sreelekha and Babu, 2019).

Despite advancements in our understanding of the ISMR and its variability, the seasonal prediction of the Indian monsoon remains a difficult task (Krishnamurthy, V. and Shukla, J., 2011). Forecasting the Indian monsoon rainfall was first attempted by H. F. Blanford,

using a statistical model based on antecedent Himalayan snow cover (Blanford, 1884). Next, through the pioneering efforts of Gilbert Walker, a model was developed to forecast the monsoon based on statistical correlations with global atmosphere-ocean-land parameters (Walker, 1923, 1924). Following the approach of Gilbert Walker, during the period 1988-2002, the IMD issued long-range operational forecasts (three months before) of the monsoon rainfall using empirical models based on a 16-parameter power regression and parametric model (Rajeevan et al., 2007). Examples of these parameters include the Southern Oscillation Index (March to May), South Indian Ocean SST (February and March), Arabian Sea SST (January and February), Central India SST (May), Eurasian (December) and Himalayan (January to March) Snow Cover. While the model was able to forecast monsoon rainfall qualitatively, it failed to predict extreme events such as the drought in 2002. The AIR for 2002 saw a seasonal rainfall deficit of 21.5%, yet, IMD predicted 2002 to be a “normal” monsoon season. After 2002, improvements were made by introducing two additional models, similar to the pre-2002 power regression and parametric model but with reduced parameters (8 and 10 parameters). Further improvements by IMD were taken by introducing a two-stage forecast approach: an initial forecast stage in mid-April and an updated forecast at the end of June. Despite accurately forecasting a normal monsoon season for 2003 and 2005, the new models failed to forecast the drought in 2004 (seasonal deficit of 9%), similar to that of 2002. This suggests that statistical models have limitations in the prediction of extreme monsoon seasons (Rajeevan et al., 2007; Sahai et al., 2008). In fact, the official operational forecast of monsoon rainfall for 1989-2012 based on IMD statistical models showed a correlation of -0.12 when compared against the observed AIR. The negative forecast skill was attributed to its failure to accurately forecast four (1994, 2002, 2004 and 2009) extreme events, as well as with limited ability to identify new sources of Indian monsoon predictability as a result of global warming such as development of the central-Pacific El Nino-Southern Oscillation, the rapid deepening of the Asian Low and the strengthening of North and South Pacific Highs during boreal spring (Wang et al., 2015a). When these predictors were included in a physical-empirical model, Wang et al. (2015a) showed an improved forecast skill of 0.51 for 1989–2012 Indian monsoon season.

Since there are limitations in statistical models, an alternative method was developed based on dynamical advanced general circulation models (GCMs). Using a multi-model ensemble (MME) seasonal prediction framework, Rajeevan et al. (2012) showed an improved correlation (0.45) in the seasonal forecasts, issued in May, for AIR between 1860-2005, when compared to correlations (0.28) from a previous MME study by Palmer et al. (2004). However, the strong correlation is still below the potential limit of Indian monsoon predictability of 0.65, which was obtained in experiments using AGCMs (Krishna Kumar et al., 2005; Kucharski and Abid, 2017). As discussed previously, the Indian monsoon interannual variability is modulated by slowly varying predictable forcing such as the ENSO. Thus, if models can

accurately simulate such forcings and their teleconnections (Turner et al., 2005; Turner and Slingo, 2011), then these models may achieve high prediction skill. Gadgil and Srinivasan (2011) used five atmospheric GCMs under the Seasonal Prediction of the Indian Monsoon project to predict the Indian summer monsoon rainfall for the period 1985 to 2004. Two sets of experiments were conducted: the first set of experiment assessed the maximum potential skill (e.g., perfect model experiment) of the models in simulating the 1985-2004 Indian monsoon seasons. The AGCMs were forced using observed (May-September) SSTs, similar to those in the Atmospheric Model Intercomparison Project (Gates et al., 1999). In the second set of experiments, five monsoon seasons (1987, 1988, 1994, 1997 and 2002) were simulated by forcing the models with persisted SST anomalies from April for May-September. The reason for conducting two different simulations was to identify the association of Indian monsoon precipitation with ENSO and Equatorial Indian Ocean Oscillation (EQUINOO). The EQUINOO is the oscillation whereby convection/precipitation is enhanced over the western equatorial Indian Ocean and suppressed over the eastern equatorial Indian Ocean; it is the atmospheric component of the IOD (Gadgil et al., 2004; Vishnu et al., 2019). A positive phase of the EQUINOO enhances Indian monsoon precipitation. Their results from the first set of experiments showed the Portable Unified Model-Hadley Centre (PUM) model performed the best in simulating the sign of the ISMR anomalies, while the NCEP seasonal forecast model had the highest skill in predicting extremes in the monsoon during 1985-2004. The poor accuracy in the other models was attributed to a strong sensitivity of the AGCMs to ENSO and failure to represent the relationship between ISMR and the EQUINOO. Additionally, in the second experiment, a weaker ENSO forcing and persisted April SST anomalies over the Pacific were used. The analysis of the 1994 season, for example, showed that the PUM and NCEP models simulated the observed (positive) sign of the ISMR anomaly, which was attributed to the models' ability to represent the link between EQUINOO and the monsoon rainfall correctly when ENSO forcing is weaker. Their results also suggest that the lack of air-sea feedbacks in AGCMs could lead to a poor simulation of the ENSO-monsoon teleconnection (Wang et al., 2005a; Bracco et al., 2007).

Saha et al. (2016) used the coupled NCEP Climate Forecast System (CFSv2) to explore the potential predictability of the summer monsoon rainfall at different lead months. The maximum potential predictability of rainfall was observed at two months lead time with a correlation of 0.65, which was attributed to the ability of the CFSv2 to capture the ENSO-monsoon rainfall relationship. An accurate representation of the ENSO-monsoon relationship was also found by Turner et al. (2005) using climate simulations of the Met Office Hadley Centre coupled model version 3 (HadCM3). An initial run of the HadCM3 showed that while the mean characteristics of the Asian summer monsoon were simulated well, significant errors in the equatorial Pacific SST existed. These errors were primarily observed in the SSTs,

low-level winds and precipitation which were associated with a poor representation of the ENSO-monsoon teleconnection in the equatorial Pacific. After applying ocean-surface heat flux adjustments to the HadCM3 model for the equatorial Indian and the Pacific Ocean in the model, their results showed an improved monsoon-ENSO teleconnection. This improvement was mainly due to a better representation of the east Pacific SSTs such that the warmest SSTs along the equator were shifted further east during El Niño periods.

While ENSO has a period of 3-7 years, modes with shorter biennial (2-3 year) variability may also influence the interannual variability of the monsoon rainfall. One such phenomenon is the Tropospheric Biennial Oscillation (TBO), which is defined as a system in which relatively strong monsoon rainfall years are followed by relatively weak monsoon rainfall in the subsequent years and vice versa (Meehl, 1987, 1994; Meehl and Arblaster, 2002b; Wang and Yu, 2018). A TBO is considered "more biennial" when these interannual transitions are more frequent (Meehl and Arblaster, 2002b). Additionally, these studies have proposed coupled atmosphere-land-ocean feedbacks over the Indo-Pacific region as a probable mechanism to explain the TBO. The coupled atmosphere-land-ocean mechanism can be divided into a biennial atmosphere-ocean mechanism and a biennial atmosphere-land mechanism. In the local atmosphere-ocean coupling, the initially positive SST anomalies throughout the tropical Indian Ocean enhance local convection, which strengthens the westerly mean monsoon winds which were confirmed in observations and GCM experiments by Meehl and Arblaster (2002a). The strong westerly wind then cools the SSTs through evaporation and mixing in the upper ocean in the same season. Consequently, the cooler SST anomalies weaken the convection and thus, the Indian monsoon rainfall in the subsequent year through the delayed feedback between SSTs and the atmosphere due to the long ocean "memory". Similarly, in the atmosphere-land coupling, soil moisture is analogous to SSTs such that, saturated soil during strong monsoon seasons leads to a cooler land surface. This reduces the land-sea thermal gradient and weakens the summer monsoon westerly flow. As a result, the evaporation and moisture convergence are reduced, which reduces convection and monsoon strength. In order for the biennial oscillation to be completed, the anomalies of the opposite sign in both atmosphere-ocean and atmosphere-land coupling during the weaker monsoon must lead to conditions that enhance the monsoon in the following year. In brief, the biennial variations are associated with the interaction between the monsoon rainfall and the tropical Indian and Pacific Ocean SSTs and the south Asian land surface (Chang and Li, 2000; Meehl and Arblaster, 2002a; Meehl et al., 2003; Li et al., 2006; Zheng et al., 2008).

Soil moisture also exerts a substantial control on the interannual variability of the Indian monsoon. Soil moisture anomalies contribute to land-surface temperature anomalies through latent and sensible heat flux anomalies. Soil moisture has a long memory, ranging from weeks to months, that can also influence surface energy balance and acts as a source

of predictability at seasonal time scales through land-atmosphere feedback (Seneviratne et al., 2010). Soil moisture plays a vital role in the energy cycle by partitioning the surface turbulent fluxes (surface sensible and latent heat flux) to the atmosphere (Koster et al., 2004; Dirmeyer, 2006; Dirmeyer et al., 2014). Studies on the soil moisture-precipitation relationship, however, are limited due to the lack of soil moisture data. Douville et al. (2001) used soil moisture derived from a seasonal (JJAS) simulation over a two year period to study the soil moisture-precipitation link. Their study found that wet soil anomalies over northern India increased local rainfall due to the increase in evaporation. However, this relationship was confined to northern India. Over the Indian continent as a whole, the sensitivity of precipitation to soil moisture is weak since an increased in evapotranspiration is balanced by a decreased in moisture convergence. Therefore, the weak feedback between soil moisture and precipitation is due to the competition between evaporation and moisture convergence. Similarly, Asharaf et al. (2012) used the Consortium for Small-Scale Modelling initialised each year on April for the period 1989-2008 to study the soil-moisture precipitation feedback during the summer monsoon. They confirmed that a positive seasonal soil moisture-precipitation feedback exists over India, such that high pre-monsoon soil moisture increased the southwest monsoon rainfall; this feedback was stronger over northern India. Complex feedbacks between soil moisture and precipitation exist over India, which suggests that the soil moisture-precipitation feedback may be regionally dependent (Douville et al., 2001; Koster et al., 2000; Seneviratne et al., 2010). A detailed analysis of soil moisture and its link to the LAC will be discussed in §2.4.

Besides soil moisture, winter/spring Eurasian snow cover also affects Indian monsoon rainfall on interannual time scales. Blanford (1884) and Walker (1910) were the first to identify a negative correlation between winter/spring Himalayan snow cover and Indian monsoon rainfall. Prior to the monsoon, dry winds originating from the Himalayas flow over wetter soil which evaporated the moisture. The monsoon rainfall is subsequently weakened due to the reduction in the local source of moisture. Additionally, snow cover may persist from winter to late spring over the Himalayas at higher altitude (Halder and Dirmeyer, 2017). The anomalous heavy snow cover during spring may modulate the LAC through delayed snowfall-atmospheric stability feedback over the Himalayas/Tibetan Plateau. This process is similar to the Blandford-type mechanism whereby the extensive snow cover reduces the surface sensible heat and longwave fluxes into the atmosphere, which reduces heating of the troposphere over the Tibetan Plateau. The reduced heating results in a weaker meridional land-ocean thermal contrast, resulting in a weaker Indian summer monsoon. Turner and Slingo (2011) used simulations from HadCM3 to show that variability in snow cover accounts for 50% of the sensible heat fluxes variability over the Tibetan Plateau. Therefore, the snow-monsoon relationship is a negative feedback: the Indian summer monsoon is weaker

when there is more extensive snow cover in Eurasia and is stronger when the snow cover is less extensive (Turner and Slingo, 2011; Saha et al., 2013). However, the monsoon-snow cover teleconnection has been weakening since 1990, as shown in Zhang et al. (2019) using long-term (1967-2015) snow and rainfall observations. Due to global warming, the decline in spring Eurasian snow cover means that it can no longer regulate mid-tropospheric temperature. In fact, the disappearing monsoon-snow cover teleconnection prompted the IMD to remove snow cover as a predictor for its long-range Indian summer monsoon forecast (Fasullo, 2004).

2.3 Intraseasonal variability of the Indian summer monsoon

The Indian summer monsoon (ISM) rainfall also exhibits significant variability on intraseasonal time scales (Webster et al., 1998; Krishnamurthy and Goswami, 2000; Goswami et al., 2006).

2.3.1 The BSISO and link to active/break Indian monsoon

A characteristic feature of the summer monsoon rainfall is the manifestation of wet and dry phases, each lasting approximately 2-3 weeks. (Webster et al., 1998; Rajeevan et al., 2006, 2010). This intermittent rainfall behaviour is frequently referred to as “active” and “break” phases. The active and break cycles of the summer monsoon over India are characterised by the northward propagation of organised convection and rainfall, originating from the equatorial Indian Ocean. This dominant oscillatory mode has a period of 30-60 days, with a preferred period of 40 days (Gadgil, 1990; Annamalai and Sperber, 2005; Lau et al., 2012). The main characteristics of an active period (Fig. 2.5a) are the presence of cyclonic vorticity, a decrease in surface pressure along the monsoon trough region, and strengthening of the low-level Somali jet. Also, increased rainfall is observed over the Indian west coast (Western Ghats), northeastern and central parts of India (Krishnamurthy and Shukla, 2007; Krishnamurthy and Achuthavarier, 2012). However, during the break phase (Fig. 2.5b), the low-level jet weakens and the monsoon trough shifts north to the foothills of the Himalayas followed by enhanced precipitation. Consequently, rainfall in most of India, particularly in northern and central India, reduces considerably.

The active and break phases of the ISM are attributed to the northward propagation of organised convection from the equatorial Indian Ocean towards India with a propagation speed of 1° latitude per day (Yasunari, 1979, 1980; Sikka and Gadgil, 1980; Annamalai and Slingo, 2001; Wang et al., 2005a; Lau et al., 2012). Using satellite-derived cloudiness data, Yasunari (1979, 1980) first discovered a pronounced northward propagation of clouds and

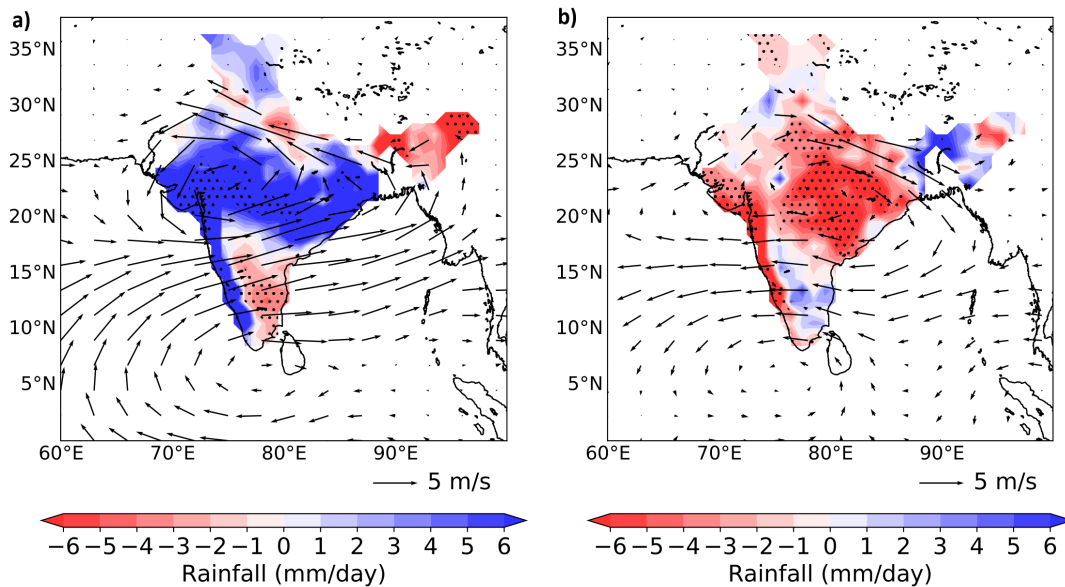


Figure 2.5: The (a) active and (b) break phase rainfall anomalies for the period 1979-2015 from the India Meteorological Department gridded rainfall (Rajeevan et al., 2006), overlaid with 850 hPa winds obtained from ERA-Interim. The active and break days were determined using an index described by Rajeevan et al. (2010). The stippling represents significance at the 95% confidence level using a Student's *T*-test.

convection on intraseasonal scales from the equator to around 30°N over the Indian Ocean sector. The shift in cloudiness is associated with the northward movement of the ITCZ cloud band. Yasunari (1979, 1980) also discovered that the northward propagating mode is initiated by eastward-propagating cloud disturbances developing over the equatorial ocean. Sikka and Gadgil (1980) found two connected maximum cloud zones (MCZ) along Indian longitudes (70°- 90°E) during boreal summer: one along 15°N and the other near the equator that is anti-correlated, such that when one is present, the other is absent. Rajeevan et al. (2012) also found similar convective cloud zone patterns, which propagated northwards from the equator towards India, using a satellite-derived OLR dataset. These observations suggest that the large-scale intraseasonal circulation is asymmetric about the equator in boreal summer, as supported by Kemball-Cook and Wang (2001).

The BSISO and MJO share similar oscillatory periods of 30-60 days, which led some to question whether the northward propagating BSISO is associated with the eastward propagating MJO. The boreal winter ISO (or the MJO) shows predominantly eastward propagation along the equator, while the BSISO also exhibits eastward and northward propagation over the Indian region (Annamalai and Sperber, 2005; Wang et al., 2005b; Sharmila et al., 2013; DeMott et al., 2014; Wang et al., 2018a), and northward/northwestward propagation over the western North Pacific region (Kemball-Cook and Wang, 2001; Yun et al., 2008, 2010; Qi et al., 2019). Wang and Rui (1990) proposed that this propagation is independent of the eastward propagating MJO. However, applying a lagged regression technique to a

25-year OLR and circulation reanalysis dataset, Lawrence and Webster (2002) discovered that of the 54 intraseasonal oscillations (ISOs) identified, 78% of the cases exhibited both northward propagation towards India and eastward propagation towards the western Pacific Ocean. The remainder, or 22%, of the cases, showed independent but stunted northward propagation. In general, the scientific consensus is that the BSISO and MJO are the same systems. The BSISO is merely the summertime manifestation of the MJO and is characterised by a stronger northward propagation and larger meridional scale together with weaker eastward propagation (Salby and Hendon, 1994).

2.3.2 Theory and mechanisms for the BSISO

There have been several mechanisms to explain the northward-propagating BSISO. The influence of land surface fluxes on the BSISO is explored in §2.3.2.1, while a detailed discussion of the land-atmosphere interaction in the Indian monsoon is reviewed in the next section (§2.4). The dynamical theories are also discussed in §2.3.2.2, and the role of air-sea interaction is discussed in §2.3.2.3.

2.3.2.1 Land surface fluxes

Early studies by Webster (1983) offered land-atmosphere interaction as a mechanism for the BSISO. Webster (1983) hypothesised that the northward movement of convection is a consequence of land surface heat fluxes over central India into the atmospheric boundary layer.

The increased solar radiation received at the surface due to clear-sky conditions during the break phase enhances the heating of the boundary layer by sensible heat flux. Consequently, the heating destabilises the lower atmosphere ahead of the convection zone, leading to a northward shift in the active phase convection from the Bay of Bengal towards India. Observations, however, indicate that the most robust northward propagation exists too far south over the NBoB instead of the land. This does not, however, suggest that land surface fluxes are not significant for the northward propagation from the ocean to land. Land-atmosphere feedback may be important when the active phase convection is near the Indian subcontinent (approximately 20°N), as will be discussed in §2.4.

2.3.2.2 Dynamic theories

Dynamic theories then became the focus of research on the northward propagating mode of the BSISO. Wang and Xie (1997) simulated northward propagation using a shallow-water model, leading them to hypothesise Rossby wave emanation from the eastward propagating

equatorial Kelvin-Rossby wave packet originating from the western equatorial Indian Ocean, as a driver for northward propagation. The Rossby wave emanation was associated with equatorial convection of the mean Hadley cell circulation. As convection propagates eastward (Fig. 2.6, boxes 1-2) from the Indian Ocean to the Pacific, the Rossby waves cause the convection to orient in a northwest-southeast tilted band (Fig. 2.6, boxes 2-3). This appears as a northward propagation to an observer at a fixed point, as the system continues moving eastward. The Rossby wave hypothesis was subsequently supported by Lawrence and Webster (2002), who showed that a large proportion of northward propagating ISOs toward the Indian subcontinent also exhibit eastward propagation towards the western Pacific Ocean. However, the hypothesis fails to explain the independent northward propagation found by Wang and Rui (1990).

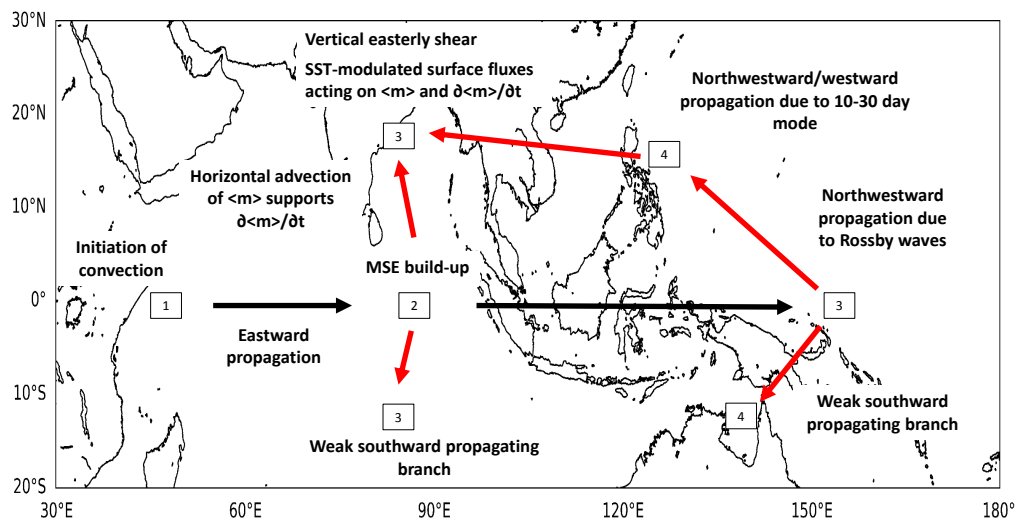


Figure 2.6: A schematic of the idealized northward propagating boreal summer intraseasonal oscillation similar to Klingaman (2008) based on studies by Wang and Xie (1997), Lawrence and Webster (2002), Jiang et al. (2004) and DeMott et al. (2014) and Guo et al. (2011). The numbered boxes and the arrows illustrated the position and propagation direction of convection, respectively. Black arrows represent eastward propagation associated with Kelvin-Rossby wave packets and red arrows show westward propagation of convection as Rossby waves.

Jiang et al. (2004) suggested that the northward propagating BSISO is associated with the combination of vertical easterly shear (due to the summer mean monsoon flow) and moisture-convection feedback (Fig. 2.6, boxes 2-3). Their studies applied a 2.5-layer atmospheric model on an f plane to exclude the Rossby wave emanation mechanism of Wang and Xie (1997) and Lawrence and Webster (2002). In the presence of vertical shear, the coupling between barotropic and baroclinic modes in the free atmosphere induces upper-level baroclinic divergence, and subsequent low-level moisture convergence in regions

north of 5°N. The coupling of the barotropic mode to the baroclinic mode is achieved through the mean vertical easterly shear acting on the meridional gradient of baroclinic divergence, based on the relationship in Eq. 2.1. The variables with subscript + (-) represent the barotropic (baroclinic) mode. The variables D , ζ and \bar{u}_T represent divergence, vorticity and vertical shear of the mean zonal flow respectively.

$$\frac{\partial \zeta_+}{\partial t} \propto \bar{u}_T \frac{\partial D_-}{\partial y} \quad (2.1)$$

$$\frac{\partial D_+}{\partial t} \propto f_0 \zeta_+ \quad (2.2)$$

In the easterly shear mechanism, as shown in Fig. 2.7 from Jiang et al. (2004), in response to the convective heating and maximum vertical wind in the middle troposphere, convergence forms in the lower troposphere and divergence in the upper troposphere (Fig. 2.7a). The maximum positive baroclinic divergence is collocated with the convection centre such that $\frac{\partial D_-}{\partial y} < 0$ is found to the north of convection (Fig. 2.7b). In the presence of easterly shear (Fig. 2.7c), a positive (negative) barotropic vorticity is induced to the north of convection based on Eq. 2.1.

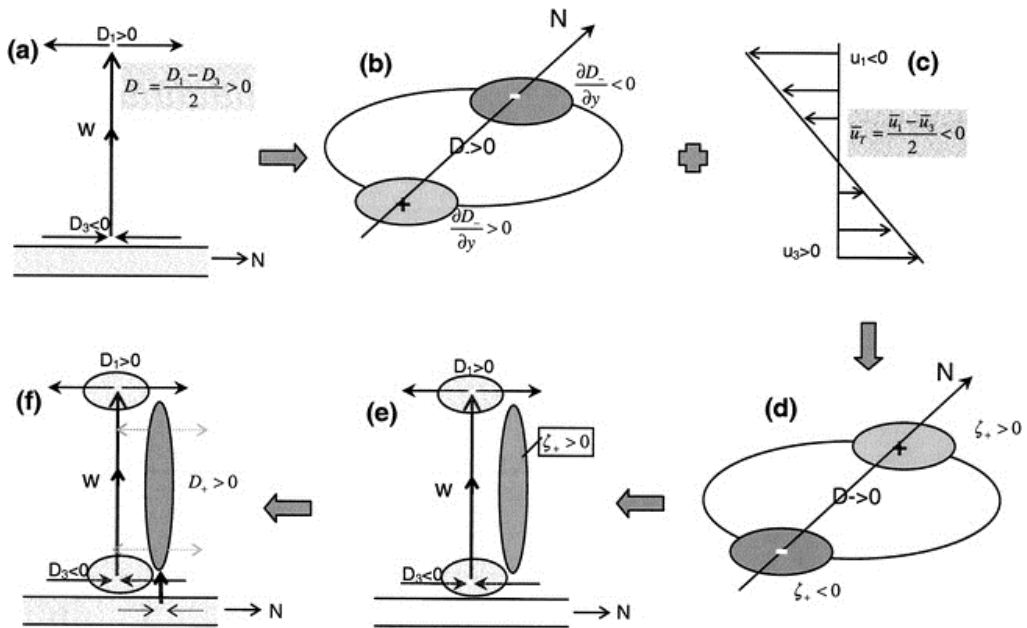


Figure 2.7: A schematic of the easterly shear mechanism obtained from Jiang et al. (2004) in their Fig. 10

Consequently, the barotropic vorticity may induce barotropic divergence in the upper-troposphere (Fig. 2.7d–e) to the north of the convection over the Northern Hemisphere ($f_0 > 0$) through Eq. 2.2. Additionally, upper-level divergence results in boundary layer convergence. The convergence favours enhanced moisture convergence and convective

heating to the north, which leads to the northward propagation of the convective centre by the conservation of mass (Fig. 2.7f). Nearer to the equator, the northward movement of convective heating is supported by the northward displacement of moisture advection due to two proposed mechanisms: (1) the boundary layer moisture advection by the summer mean southerly wind and (2) moisture advection by the intraseasonal wind acting on the mean meridional moisture gradient over the eastern Indian Ocean. Their study highlights that the BSISO may manifest without the atmospheric wave effects and that the vertical easterly shear can also lead to northward propagation. Drbohlav and Wang (2005) further supported the case for internal atmospheric dynamics by using a zonally-symmetric two-dimensional model similar to that used in Wang and Xie (1997) but a zonally averaged version. Their results suggest that northward propagation in their model was triggered by upper tropospheric barotropic divergence due to the vertical advection of easterly vertical wind shear, leading to moisture convergence in the planetary boundary layer north of the convection. Additionally, Bellon and Sobel (2008a,b) demonstrated that meridional advection of anomalous baroclinic vorticity by the mean monsoon flow could induce further upper-level baroclinic vorticity north of the convective heating based on an idealised aquaplanet model. The vorticity subsequently creates boundary layer moisture convergence leading to the northward propagation of advection, similar to Jiang et al. (2004).

Besides internal atmosphere dynamics, Kang et al. (2010) used an ocean-atmosphere coupled general circulation model (GCM) to simulate 20-year ISO precipitation during boreal summer. Their study emphasises the role of convective momentum transport (CMT) in the northward propagating BSISO. The CMT is the vertical redistribution of atmospheric momentum through convective mixing processes. An axially symmetric model was used to diagnose the role of CMT. As shown in their Fig. 3, low-level convergence to the north of convection was induced by a secondary meridional mixing associated with the CMT in regions with vertical easterly shear. The convection transports easterly momentum in the lower troposphere and westerly momentum in the upper troposphere by the large vertical easterly shear of the mean monsoon. These momentum tendencies are balanced by a secondary meridional circulation and the Coriolis force. Subsequently, anomalous southerly and northerly winds are induced in the lower and upper troposphere, respectively. As a result, northward propagation formed due to anomalous meridional winds which induced lower-tropospheric convergence and upper-tropospheric divergence to the north of the convection. The model with CMT managed to simulate the northward propagating pattern of the ISO well, compared to the model without CMT. Kang et al. (2010) results affirm the finding of Jiang et al. (2004), and further suggest that vertical wind shear alone is not sufficient for northward propagation.

The eastward and northward propagation was simulated by Li et al. (2016) using the

Community Earth System Model (CESM) under different model configurations. Under the CESM, five experiments were simulated for 50 years: one atmosphere-only model simulation with the Community Atmosphere Model version 4 (CAM4), two coupled model simulations with CAM4 and Community Atmosphere Model version 5 (CAM5) as the atmospheric component at low resolution, and two simulations using coupled CAM4 and CAM5 but at higher resolution. All simulations showed weaker northward propagation compared to observations during the boreal summer. However, the CAM5 simulations showed slight improvements compared to the uncoupled CAM4 and coupled CAM4 simulations. Similarly, in the boreal winter, the eastward propagation was better simulated in the coupled CAM5 models than in the coupled CAM4 models, while the atmosphere-only CAM4 model showed a standing oscillation. The standing oscillation in the atmosphere-only CAM4 simulation was attributed to the non-propagating moisture anomalies. Whereas, the coupled CAM5 simulation with an improved shallow convection scheme accurately simulates the spatial distribution of shallow convection. The better representation of the low-level moisture processes associated with the shallow convection resulted in a more realistic eastward propagation even at coarser resolutions. Additionally, the phase speed of the eastward propagation was comparable to the observations in the coupled CAM5 model at a higher resolution. Li et al. (2016) also speculated that the eastward propagation during winter is sensitive to air-sea coupling, while northward propagation is influenced by atmospheric dynamics as supported by Sharmila et al. (2013). This suggests that the eastward and northward propagation have distinct mechanisms. Furthermore, the northward propagation in the atmosphere-only model was attributed to a better representation of internal atmospheric dynamics such as the improved CMT in CAM5, as well as the shallow convection scheme (Kang et al., 2010).

Recently, Liu et al. (2018) performed two simulations using the ECHAM4 GCM to identify the role of detrainment from shallow convection (SC) in the BSISO. The control experiment with a standard detrainment rate produced a realistic northward BSISO propagation. By comparison, when the detrainment rate was lowered, the BSISO became stationary. The weak SC resulted in a drier lower and middle troposphere prohibiting deep convection growth. This highlights the importance of moisture detrainment in creating favourable conditions for convective activity north of the existing deep convection.

The BSISO is also linked to the dynamics and thermodynamics of the ISM. In earlier work on the Indian monsoon onset, Parker et al. (2016) and Menon et al. (2018) found that the spatial progression of the Indian monsoon onset is affected by the presence of extratropical dry-air intrusions based on observations and models as was previously discussed. The influence of dry-air intrusions has also been documented during break events (Krishnan et al., 2000; Bhat, 2006; Krishnamurti et al., 2010). For instance, during the 2002 drought over India, Bhat

(2006) suggested that the prolonged break phase was associated with a dry-air intrusion from the deserts over the cooler surface near the eastern Arabian Sea, that suppressed localised convection through increased static stability which prevented cumulonimbus development. Krishnamurti et al. (2010) also suggested that the dry spell in 2009 was associated with West Asian desert air intrusions into central India. Krishnan et al. (2009) used a 20-year simulation of the high-resolution Japan Meteorological Agency model forced with climatological SST to study the monsoon-midlatitude teleconnection. The simulated droughts in the model were attributed to a prolonged monsoonal break event on intraseasonal time-scales, associated with extratropical dry-air intrusions originating from the adjacent desert. During the break, suppressed convection and anomalous divergence over India induces a Rossby wave response, with the associated cyclonic anomalies extending to the west over central Asia, and the Indo-Pakistan region in the mid- and upper troposphere. The cyclonic anomalies are held in place by a stagnant blocking ridge over east Asia which may be associated with an eastward shift of upper-tropospheric anticyclone. As a result, cold air advection from mid-latitude westerlies cool the mid- and upper-troposphere. These dry and cold anomalies decrease the meridional temperature gradient over the Indian subcontinent, and subsequently, the increased stability and weakened convection, resulting in a weaker monsoon.

2.3.2.3 Ocean-atmosphere interactions

In recent years, ocean-atmosphere interactions have been given much attention as a potential mechanism for the BSISO. Many researchers have attempted to diagnose this process, with early research by Krishnamurti et al. (1988) based on in-situ and satellite-derived observations. Their study discovered that surface variables such as SSTs, winds, surface latent and sensible heat fluxes show variability on intraseasonal scales. Subsequently, multiple field campaigns were performed to document the relationship between air-sea fluxes and the BSISO. The Bay of Bengal Monsoon Experiment (BOBMEX, Bhat et al. 2001), the Joint Air-Sea Monsoon Experiment (JASMINE, Webster et al. 2002) and more recently the Bay of Bengal Boundary Layer Experiment (BoBBLE, Vinayachandran et al. 2018) have all shown variations in SSTs during active and break phases of the ISM. For example, during the BoBBLE campaign in 2016, an increase in SST from 28° to 29.5°C was observed over the southern Bay of Bengal after a break phase. The warming was attributed to high solar radiation and lower latent heat flux, which is consistent with the break phase. The calm and cloudless conditions enhanced the surface net heat flux into the ocean, leading to warming. This variation of 1.5°C between break and active phase was also observed during JASMINE and from buoy data during BOBMEX. Furthermore, the existence of intraseasonal SSTs over the Bay of Bengal was shown by Premkumar et al. (2000) and Sengupta and Ravichandran (2001) based on observations from moored buoys during the 1998 summer monsoon. The variation in SST anomalies was

shown to be a response to the surface net heat flux anomalies associated with variations in cloud cover and surface wind speed on intraseasonal scales. Kemball-Cook and Wang (2001) also found that the northward propagation was linked with the localised warming of SSTs and the subsequent destabilisation of the atmospheric column north of active convection, highlighting the role of air-sea interaction.

Furthermore, intraseasonal SST anomalies over the NBoB are associated with the active/break monsoon (Vecchi and Harrison, 2002; Duvel and Vialard, 2007; Klingaman et al., 2008b; Roxy and Tanimoto, 2012). Observation studies have also shown a near-quadrature relationship between SST and convection anomalies, such that warm SST anomalies lead enhanced convection and precipitation by ten days (Woolnough et al., 2000; Vecchi and Harrison, 2002; Duvel and Vialard, 2007; Klingaman et al., 2008b; Roxy and Tanimoto, 2012). Vecchi and Harrison (2002) used satellite-based Tropical Rain Measuring Mission (TRMM) Microwave Imager (TMI) SSTs to show a delay in maximum warming (cooling) over the NBoB during the break (active) phase by approximately ten days, with average SST changes between phases was approximately 0.3°-1.0°C. Their results were corroborated by Klingaman et al. (2008b) using the TMI SST dataset. Vialard et al. (2012) further showed that surface heat flux anomalies are the main driver for the intraseasonal SST fluctuations. Using observational data, they showed that the NBoB has larger surface heat flux variations of 25 Wm⁻² compared to the Arabian Sea. Over the NBoB, the surface heat flux forcing accounts for 89% of the SST variability in the NBoB. Furthermore, 60% of the heat flux variation is due to shortwave radiation and 40% due to latent heat flux. An ocean general circulation model, the Modular Ocean Model version 4, further supports the dominant role of the heat flux variations, with a 90% contribution over the NBoB. A sensitivity experiment was conducted by varying different physical processes on SST variability such as solar and non-solar heat fluxes obtained from the control experiment for the period 1996-2005, which confirmed their findings from observations. These results highlight the SST-convection coupling via the SST-wind-evaporation relationship hypothesised by Vecchi and Harrison (2002): the warming of the SSTs to the north is related to the increased downward solar radiation due to the lack of clouds and reduced evaporation by the reduction of surface wind speed.

Recently, Gao et al. (2019) examined the oceanic feedback to the BSISO by determining the modulation of surface fluxes and moist static energy (MSE) by SST on intraseasonal scales using reanalysis datasets (box 2-3 in Fig. 2.6). This approach is based on a similar framework to DeMott et al. (2016) for the MJO. In order to study the SST effect on the BSISO convection, an analysis of the budget of column-integrated MSE ($\langle m \rangle$) and its time rate of change ($\partial \langle m \rangle / \partial t$) was made. The variables $\langle m \rangle$ and $\partial \langle m \rangle / \partial t$ represent the maintenance and propagation of the BSISO, respectively, both of which are affected by intraseasonal SST-modulated sensible and latent heat fluxes. Their results reveal that convection associated with the BSISO is

in-phase with $\langle m \rangle$ over the Indian Ocean. The horizontal advection of $\langle m \rangle$ is the main driver of $\partial\langle m \rangle/\partial t$. Towards the Bay of Bengal, the meridional advection of $\langle m \rangle$ is the highest contributor to the horizontal advection of $\langle m \rangle$. The zonal advection of $\langle m \rangle$ also contributes to the propagation, albeit with a weaker amplitude. During the active convection over the eastern equatorial Indian Ocean, anomalous southeasterly transport of maximum climatological $\langle m \rangle$ located over South Asia towards the southern Bay of Bengal, which leads to the enhancement of convective activity over the equatorial Indian Ocean. The enhanced $\langle m \rangle$ north of the convection then supports northward propagation of the BSISO convection. Analysis of the intraseasonal SST variability of $\langle m \rangle$ and $\partial\langle m \rangle/\partial t$ also showed substantial contribution by SST-modulated surface fluxes over the central Indian Ocean and Bay of Bengal. In fact, warm SST and positive SST-modulated flux anomalies are found to the northeast and always lead convection, such that intraseasonal SST contributes to 20% of $\partial\langle m \rangle/\partial t$ over the equatorial Indian Ocean. In general, the results of Gao et al. (2019) suggest that intraseasonal SST can support the propagation of convection over the BSISO domain. However, intraseasonal SST variability by itself is sufficient to support propagation but not on its own. An additional mechanism such as the internal atmosphere dynamics is required to drive the majority of the BSISO propagation. This indicates that the intraseasonal SST variability may support, but may not be essential for the propagation of the BSISO.

However, it is still unclear if the SSTs are a passive response to atmospheric forcing, or active in influencing the northward propagating BSISO. Early studies to simulate the BSISO utilised AGCMs to study the northward propagation. Analysis of 10 AGCMs by Waliser et al. (2003) concluded that all models were unable to exhibit the spatial-temporal patterns of intraseasonal rainfall over the equatorial Indian Ocean when compared to observations. The shortcoming was attributed to the weekly SST forcing in the model, which could not accurately represent the intraseasonal SST-rainfall relationship. Fu et al. (2003) investigated the sensitivity of coupling between SST and BSISO in the Indian Ocean by using the ECHAM4 AGCM forced with daily and monthly mean SSTs. The SSTs were obtained from a coupled simulation between ECHAM4 as the atmospheric component and a tropical upper-ocean model (Wang et al., 1995) as the ocean component. In the coupled simulations, the spatiotemporal pattern of the BSISO over the Indian Ocean domain was simulated. However, the uncoupled simulations failed to reproduce the BSISO signal. The weaker northward propagation in the uncoupled model forced with daily SSTs was attributed to warm SSTs collocated with convection, whereas in observations, the warm SSTs were associated with regions with weak convection, clear skies and intense solar insolation.

Similarly, Klingaman et al. (2008a) used the Hadley Centre Atmospheric Model (HadAM3) forced with high-frequency SSTs to confirm the results from Fu et al. (2003). The SSTs used were the Operational Sea Surface Temperature and Sea Ice Analysis product from the United

Kingdom National Centre for Ocean Forecasting. Their results showed that the northward propagation was simulated better when HadAM3 was forced with daily SSTs, compared to 5-day means and monthly mean SSTs. However, their results also showed an error in the phase relationship between SSTs and convection. The heaviest rainfall was collocated with warm SSTs, which is in contrast to observations in which strong convection lead cooler SSTs. The error in the phase relationship in Klingaman et al. (2008a) was hypothesised to be due to the lack of feedback of convection on the intraseasonal SSTs. Mandke et al. (2013) also showed similar results using an atmosphere-only and an atmosphere-ocean slab coupled model from the PUM version 4.5 for 11 years. The coupled model initialised with high-frequency SST showed northward propagation from the EEqIO to the NBoB, which was absent in the atmosphere-only PUM forced with monthly SSTs. In general, SST variability on daily time scales in coupled and atmosphere-only models results in the improved simulation of the northward propagating BSISO over the Indian domain.

Next, Kemball-Cook et al. (2002) compared coupled and uncoupled versions of the ECHAM4 and showed that the uncoupled model was able to simulate a northward propagating signal, although the spatial characteristics and phase speed were unrealistic compared to the coupled simulation. They suggested that air-sea interaction is important to organise and intensify the BSISO. Wang et al. (2009) analysed northward propagating BSISO signals using the coupled National Centers for Environmental Prediction (NCEP) Climate Forecast System (CFS) and its atmospheric component, the NCEP Global Forecast System (GFS). The 30-day forecasts were made for five strong BSISO cases during June-September for the period 2005-2007. The atmosphere-only forecast showed northward propagation from the equator to 15°N, in the first 15 days, after which the signal weakened. In contrast, the northward propagation in the coupled GFS was more realistic when compared to observations, and persisted through the 30-day forecast. Subsequently, Sharmila et al. (2013) used a coupled CFSv2 and GFS model, to analyse the relative role of ocean-atmosphere coupling in the northward propagation. The northward propagation in CFSv2 was from the equator towards the Indian subcontinent. However, the GFS simulation showed a stationary signal over India.

In summary, previous studies using observations and models discussed the importance of air-sea coupling during the BSISO life cycle. These studies have shown feedbacks between SSTs and atmospheric convection through surface fluxes may be important in supporting the propagation of the BSISO, aside from the internal atmospheric dynamics. In models, the application of high-frequency SSTs in the atmosphere-only model may show northward propagation; however, there are limitations in representing the physical SST-rainfall relationship which points towards the lack of air-sea coupling. Furthermore, while air-sea coupling important for climate model simulations, its influence on the intraseasonal variability in initialised numerical weather prediction (NWP) forecast requires further work

since it is unclear if air-sea coupling is important for short-scale forecasts.

2.4 Land-atmosphere interaction

The influence of land-atmosphere coupling (LAC) on the ISM was briefly discussed in §2.3.2.1 and is considered to be an important mechanism for the Indian monsoon. Webster (1983) highlighted the control of land surface variability on the overlying atmospheric properties: land surface anomalies such as soil moisture and vegetation can influence the atmosphere through dynamic, thermodynamic and hydrological processes (Zeng and Yuan, 2018a). Through the water cycle, ET changes may influence properties of the atmospheric state such as moisture and temperature, stability (e.g., lifting condensation level, planetary boundary layer height, convection and cloud formation) and more importantly, precipitation (Beljaars et al., 1996; Betts et al., 1996; Koster et al., 2000; Taylor, 2008; Lorenz et al., 2015).

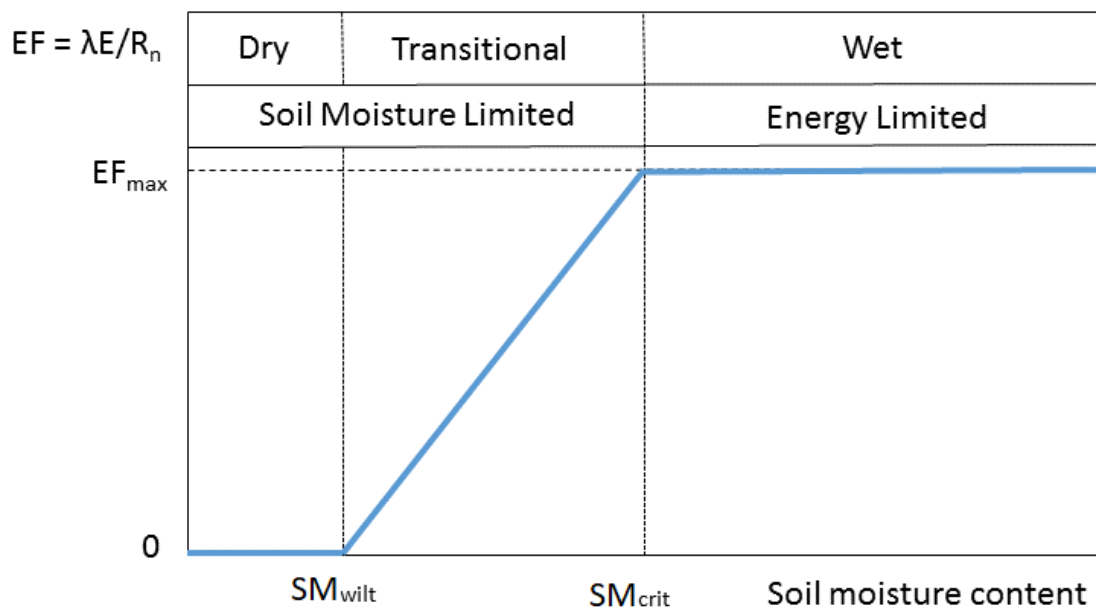


Figure 2.8: The soil moisture and corresponding evaporation regimes as in Seneviratne et al. (2010), based on the Budyko (1963) framework. EF denotes the evaporative fraction, and EF_{max} represents the maximum evaporative fraction value.

In an attempt to understand the extent to which soil moisture can affect atmospheric processes and precipitation, the Global Land-Atmosphere Coupling Experiment (GLACE, Koster et al. (2004, 2006)) was conducted to quantify the global LAC strength in models during the boreal summer. Despite the differences between the 12 models used, a distinct feature was observed: several geographical “hot-spots” of strong LAC, where soil moisture exerts a significant control on atmospheric processes and precipitation via the coupled soil moisture-precipitation feedback (SM-P). In the SM-P feedback, soil moisture influences precipitation via feedbacks with land surface evapotranspiration. However, Seneviratne et al.

(2010) and Halder et al. (2018) argue that the SM-P path is very difficult to characterize due to having both positive and negative feedback paths, and their relationship remains unclear (processes A and B in Fig. 2.8). Understanding the SM-P feedback is important since anomalies in soil moisture may influence the atmosphere on time scales ranging from weeks to months (Koster and Suarez, 2004; Ashfaq et al., 2017). The soil moisture memory at these time scales makes it an important source of predictability for sub-seasonal to seasonal forecasting (Dirmeyer, 2006).

Furthermore, these “hot-spot” regions were located in transitional zones between dry and wet climates. Central India was identified as one of the “hot-spots” of LAC (Koster et al., 2010; Seneviratne et al., 2006), such that positive correlations between soil moisture and evapotranspiration may contribute to precipitation. However, regions with negative correlations also exist. Furthermore, the findings from GLACE confirm the Budyko (1963) framework by defining evapotranspiration regimes as a function of soil moisture (Koster et al., 2004; Seneviratne et al., 2006, 2010) as shown in Fig. 2.8. The evapotranspiration regimes, are defined as either a soil moisture-limited or energy-limited ET regime, characterised by the evaporative fraction ($EF = \lambda E / R_n$). In an energy-limited regime, ET is independent of soil moisture content provided that the SM lies above a given critical SM (SM_{crit}) value such that surface net radiation controls evaporation. In contrast, below the SM_{crit} threshold, soil moisture availability strongly constrains evapotranspiration (soil moisture-limited regime). Below the wilting point (SM_{wilt}), no evapotranspiration can occur. It is apparent from Fig. 2.8 that the transitional climate region ($SM_{wilt} \leq SM \leq SM_{crit}$) is characterised by strong LA coupling where ET feedback in to the atmosphere, such as those seen over central India (Koster et al., 2006). In the dry ($SM \leq SM_{wilt}$) and wet ($SM \geq SM_{crit}$) climatic region, soil moisture has no influence on evapotranspiration. It is worth noting, however, that some of the models showed weak or no coupling. For instance, the Hadley Centre atmosphere model showed the weakest coupling strength among the 12 GLACE AGCMs over the global hot-spot regions, including central India (Lawrence and Slingo, 2005).

A conceptual framework for the SM-P feedback is illustrated in Fig. 2.9: process (A) represents the feedback between soil moisture and evapotranspiration; (B) the feedback between evapotranspiration and precipitation; (C) the feedback between precipitation and subsequent soil moisture. In relationship A, the blue arrow refers to positive feedback whereby an increase in soil moisture leads to an increase in evapotranspiration, which can be found in transitional climate zones as depicted in Fig. 2.8. Concomitantly, the increase in evapotranspiration results in a decrease in soil moisture, forming a negative feedback. Therefore, in order for the soil moisture-precipitation feedback to remain positive, the increased evapotranspiration must be balanced by the increase in precipitation. Next, relationship C is relatively straight-forward, whereby the increase in precipitation leads to an

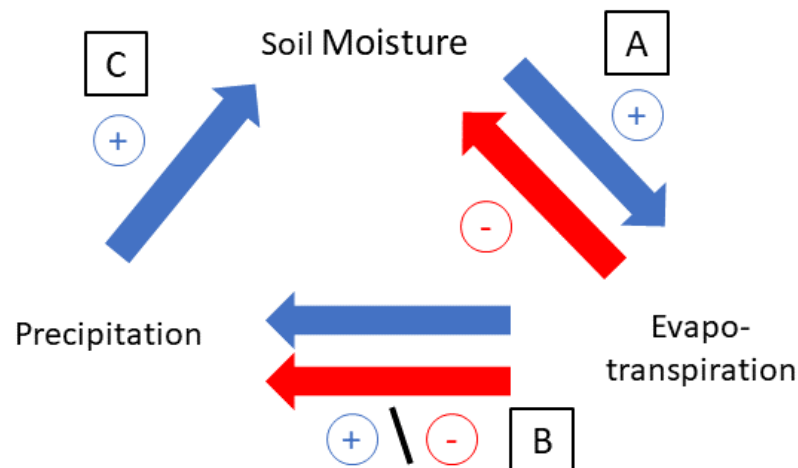


Figure 2.9: A conceptual soil moisture precipitation coupling and feedback loop framework from Seneviratne et al. (2010). The coloured arrow indicates the feedback process: blue arrow represents positive feedback and red arrow indicates negative feedback.

increase in soil moisture. However, once the soil is saturated, any excess rainfall will result in surface runoff. Lastly, relationship B is more complex and has the highest uncertainty in the soil moisture-precipitation feedback loop, as briefly discussed in §2.1. In principle, two distinct cases exist in relationship B and the soil moisture-precipitation feedback: a wet-soil (positive feedback) and dry-soil (negative feedback) case, both of which may lead to enhanced precipitation. Both of these will be addressed below.

In the case of the wet soil regime, soil moisture may increase evapotranspiration and moisture flux into the planetary boundary layer: the abundance of moisture results in enhanced convection and precipitation under wet soil conditions. Several studies have attempted to demonstrate positive feedback between soil moisture and precipitation. Findell and Eltahir (1997) used a 14-year (1981-1994) soil moisture dataset over Illinois and identified a positive correlation ($r^2 > 0.4$) between initial soil moisture conditions in May and subsequent rainfall in mid-June. D’Odorico and Porporato (2004) used the similar soil moisture data but for 1981-2004 to demonstrate that antecedent soil moisture is strongly correlated ($r^2 > 0.87$) to the frequency of rainfall and not the rainfall amount ($r^2 \approx 0$), in contrast to the findings of Findell and Eltahir (1997). While many studies considered localised precipitation recycling process, Pal and Eltahir (2001) used a modified version of the National Center for Atmospheric Research’s (NCAR) regional climate model to the study the influence of late spring/summer soil moisture on the planetary boundary layer and subsequently, precipitation based on radiative feedbacks. Their results found that anomalously high soil moisture increases net surface radiation in the presence of denser vegetation and darker soil, both of which reduce the soil albedo. Consequently, the enhanced net surface radiation further increased the flux of moist static energy into the planetary boundary layer. The effect of moist static energy is to

reduce the boundary layer height and increase the magnitude of moist static energy per unit mass of air, both of which lead to enhanced convective activity. While their study was based over the midwestern United States, the results may provide an insight into how pre-monsoon soil moisture may influence monsoon rainfall over India.

Furthermore, Tuinenburg et al. (2011) applied a convective triggering potential (CTP)-humidity (HI) index framework to a one-dimensional slab model forced with atmospheric soundings from 1975-2009 across India, to diagnose the sensitivity of soil moisture to convective precipitation (strong positive feedback). The CTP-HI index shows that during the monsoon season, a strong association between the wetland surface and large triggering potential was observed over India about 20% of the time. During the pre-monsoon season, however, the strong positive feedback was only confined to the south and east of India. The feedbacks over the south and east India were hypothesised to be associated with irrigation in these regions, which may increase local precipitation. To confirm this, Tuinenburg et al. (2011) used precipitation data from 1969-2004 during the pre-monsoon period (three weeks before the monsoon onset) and showed that pre-monsoon precipitation was higher over the region with large-scale irrigation than over non-irrigated regions. Precipitation associated with the positive soil moisture-precipitation feedback accounts for 3% of the total annual rainfall over India.

However, dry soil conditions may also directly enhance local precipitation via sensible heat flux through the local heating of the boundary layer. The heating destabilises the atmospheric column and amplifies convective activity. Additionally, sensible heating may also affect convective instability by setting up a local boundary-layer convergence. Lingbin Yang and Zhao (2018) investigated the soil moisture-precipitation feedback based on the Koster et al. (2004) framework by calculating the correlation between soil moisture and evapotranspiration (coupling A in Fig. 2.9), evapotranspiration and precipitation (coupling B in Fig. 2.9) and precipitation and soil moisture (coupling C in Fig. 2.9) using observational data. Their results suggest that both positive and negative soil moisture-precipitation feedbacks were present over land, with positive feedbacks being more dominant. However, the negative feedback is non-negligible as 43.8%, and 40.2% of the identified negative soil moisture-precipitation feedback occurred in the arid and humid climate zones, respectively. In regions with a distinct soil moisture gradient, enhanced convection can be generated over the drier region as shown in a study by Frye and Mote (2010a) over the Southern Great Plains. However, Frye and Mote (2010b) noted that the initiation of convection over dry soil was more frequent only when the synoptic conditions were favourable, such as large convective available potential energy, unstable environment and weak convective inhibition. A comparable pattern was noted in the latest case study during the 2016 monsoon onset during the INCOMPASS field campaign. Using aircraft observations to study the response of the boundary layer to irrigation

and antecedent rainfall, Barton et al. (2019) discovered that the deep convection developed over drier soil moisture in the presence of strong soil moisture gradients.

Shukla and Mintz (1982) used the Goddard Laboratory for Atmospheric Sciences AGCM to show that over southeast Asia and India, dry soil conditions lead to enhanced summer precipitation. They attributed this to the increase in water vapour transport into these regions due to stronger land-ocean thermal contrast. Their studies also showed there were no precipitation in the dry-soil case over Europe and large parts of Asia. This contrast underlines the potential role of negative soil moisture-precipitation feedbacks on Indian summer monsoon rainfall, which was also hypothesised by Barnett et al. (1989). Also, Cook et al. (2006) investigated the effect of increased soil moisture on the wet season (October-March) rainfall over southern Africa using the Community Climate System Model version 3 for 1979-2000. Two cases were investigated: A control run where the soil was allowed to interact with the atmosphere, and a saturated soil moisture simulation such that evapotranspiration was not limited by soil moisture. In the moist soil experiment, precipitation was reduced compared to the control run. The reduction in rainfall occurred in two ways. First, changes in surface energy partition favoured increased latent heat flux, which led to the cooling of the surface. The cooling subsequently increased surface pressure and the vertical equivalent potential temperature gradient and reduced boundary layer height. These changes are characteristic of a more stable atmosphere. Secondly, the higher surface pressure weakened surface moisture convergence and reduced column-integrated precipitable water. In general, the results from these studies point to the varying and complex SM-ET coupling, which may alter the SM-P feedback, depending on the climatic zone. Furthermore, while observational and modelling studies continue to analyse LAC, these efforts remain challenging and uncertain, especially on how the LAC influences the northward propagation of the BSISO.

Additionally, a better representation of the SM-P feedback in models may improve the prediction skill of the monsoon on sub-seasonal timescales based on model experiments such as the Global Land-Atmosphere Coupling Experiment version 2 (GLACE2) by Koster et al. (2010, 2011). Eleven modelling systems participating in GLACE2 performed two-month forecasts using multiple boreal summer start dates for 1986-1985 to study the soil moisture contribution to sub-seasonal forecast skill. They performed two sets of simulations: (a) with realistic initialisation and (b) without land initialisation. Forecast skill of air temperature and rainfall were improved in the realistic land simulation, owing to an accurate representation of soil moisture. Guo et al. (2011) conducted similar experiments to Koster et al. (2011) using the Center for Ocean-Land-Atmosphere Studies AGCM, which was a participant in the GLACE2 experiments. Simulations with and without realistic land surface initialisation were conducted for ten start dates each spanning 25 years (1982-2006). Similar to GLACE2, better representation of the land surface initialisation improved the prediction skill of air

temperature and rainfall, associated with a long soil moisture memory and strong soil moisture-evapotranspiration coupling. However, the prediction skill is dependent on the season, with stronger skill during spring-summer. It is apparent that based on these feedbacks from previous studies, the influence of LAC is regionally-dependent and may have both positive and negative feedback on the Indian monsoon rainfall. Furthermore, it is also unclear how LAC influences the intraseasonal variability over the Indian subcontinent.

2.5 Motivation

The role of land-ocean-atmosphere coupling on the variability of the Indian monsoon was reviewed in this chapter. However, there are several gaps identified in previous studies which serve as a motivation for this thesis. Specifically, it remains unclear if the influence of both ocean-atmosphere and land-atmosphere coupling on intraseasonal time-scales are necessary for the northward propagation of the convection associated with the BSISO. Evidently, modelling studies have indeed shown that the northward propagating BSISO was better simulated in coupled GCMs, in terms of its spatial and temporal patterns compared to observations. However, simulations with uncoupled AGCMs were also able to exhibit northward propagation although weaker in magnitude, while others demonstrated only a standing oscillation signal. This suggests that the internal atmosphere dynamics in AGCMs may support northward propagation and further reveal the competition between two processes in the northward propagation: the internal atmospheric dynamics and ocean-atmosphere interaction. However, some of these studies focused on simulations in climate models. Whether or not air-sea coupling is necessary for simulating the intraseasonal variability in initialised NWP forecasts remains an open question, and is the focus of this thesis. In order to achieve this goal, it is essential to first understand the mechanism(s) governing this transition by focusing on identifying signals of ocean-atmosphere interaction, as well as the dynamics and thermodynamics during the break-to-active transition (Chapter 4). This thesis will seek to assess the physical processes over the ocean and atmosphere governing the transition over the Indian monsoon region. Secondly, in order to further interpret the influence of air-sea coupling, the break-to-active transition will also be analysed in uncoupled and coupled NWP forecasts. I will utilise a novel approach to characterise break-to-active transitions in composites (Chapter 3). The modelling study approach will assist with revealing whether air-sea coupling is necessary for northward propagation, or if it plays a supporting or even a non-negligible role during the break-to-active transition (Chapter 6).

Additionally, the role of LAC during the break-to-active transition over India will also be addressed (Chapter 5). Again, many previous studies have shown different regional ET regimes and feedbacks over India, but very few attempted to investigate the influences of

these processes on northward propagation of convection and rainfall over India. Similarly, while studies have shown that the intraseasonal rainfall over India is associated with local land-atmosphere interaction and the large-scale monsoon circulation, how land surface variability influence the transition requires further investigation. Furthermore, these process may be regionally dependent over India since LAC strength varies over the subcontinent. Therefore in order to address this gap in our understanding, the break-to-active transition over India will be critically examined by identifying how the land- and near-surface variables evolve during the break-to-active transition and the influence of these variables on local LAC as well as the large-scale circulation. These efforts will assist with providing an overview of how the LAC strength may vary on intraseasonal timescales in different regions over India.

Overall, the results from this thesis seek to improve our understanding of the coupled land-atmosphere-ocean processes and the mechanism(s) governing intraseasonal events such as the break-to-active transition over the Indian monsoon domain and by extension, the general dynamics and mechanisms governing the BSISO. Finally, with a better representation of the physical processes in models, the subseasonal-to-seasonal forecast and prediction skill of the BSISO with lead times of weeks to months may also improve, which is an essential factor for stakeholders across India.

Chapter 3:

THE BREAK-TO-ACTIVE TRANSITION OF THE INDIAN SUMMER MONSOON

3.1 Purpose of the chapter

The purpose of this chapter is to provide an overview of the intraseasonal variability of the Indian monsoon. This chapter will also discuss the indices and criteria used to identify active and break phases and includes a new objective method to identify the break-to-active transition. Additionally, composites based on this criterion will demonstrate the spatial and temporal characteristics of the northward propagation associated with the boreal summer intraseasonal oscillation (BSISO).

Many observational studies have constructed indices to define individual active and break events. An early study by Ramamurthy (1969), analysing 80 years (1888-1967) of surface pressure and circulation data, defined break conditions as when the monsoon trough migrates north to the foothills of the Himalayas, accompanied by increased rainfall and the absence of low-level easterly winds over northern India during July to August. Using the same method but for a 29-year period (1968-1997), De et al. (1998) found similar synoptic conditions during the break phase.

Others have used 850 hPa winds to define active and break events (Magana, 1996; Webster et al., 1998; Goswami and Mohan, 2001; Joseph and Sijikumar, 2004; Sudeepkumar et al., 2018). Magana (1996) and Webster et al. (1998) classified break conditions as when weakened 850 hPa zonal wind (>-3 m/s) prevail over a large region of India (10-20°N, 65-95°E). Subsequently, Goswami and Mohan (2001) defined break days using a single grid point over the northern Bay of Bengal (15°N, 90°E). Their study noted that the break phase is associated with decreased cyclonic vorticity and weaker convection. A further classification of active and break events

was suggested by Joseph and Sijikumar (2004), based on the magnitude of 850 hPa zonal winds over the region 10-20°N, 70-80°E, representing the location of the low-level jet stream. During the active phase, the core of the low-level jet passes through central India, leading to increased rainfall over the Indian subcontinent and enhance convection over the northern Bay of Bengal (NBoB). In the break phase, however, the low-level jet shifts over the southern tip of India, resulting in decrease rainfall over India and suppress convection over the NBoB.

The use of satellite-derived OLR data is also well-established in previous studies. Krishnan et al. (2000) used daily OLR anomalies for 17 years (1979-1995) during 15th June to 15th September to identify break events as when the daily OLR anomalies exceed $+10 \text{ Wm}^{-2}$ for a minimum of four consecutive days, averaged over India (18-28°N, 73-82°E). In contrast to Krishnan et al. (2000), Vecchi and Harrison (2002) calculated the difference between two regions - the Indian subcontinent (10-30°N, 65-85°E) and the equatorial Indian Ocean (10°S-5°N, 75-95°E) - using normalized, seven-day moving averaged OLR anomalies. Their choice of the region is similar to the dipole of maximum cloud zones between India and the eastern equatorial Indian Ocean (EEqIO) found by Sikka and Gadgil (1980). To retain only the intraseasonal variability, the 50-day centred mean was also removed. Active and break phases are then defined as when the index is negative and positive, respectively.

A consistent feature of the monsoon is the spatial heterogeneity of the rainfall pattern; this is the basis of a variety of rainfall-based indices. Parthasarathy et al. (1994) formulated an index using daily area-weighted averaged, all-India rainfall (AIR) from more than 306 stations, representing the whole country. The AIR was shown to be a reliable measure for active and break rainfall (Sperber et al., 2001; Annamalai and Slingo, 2001) due to its strong links to the intraseasonal (the 30-60 day) variations in 850 hPa circulation field; with cyclonic flow over India and anti-cyclonic flow to the south over the Indian Ocean. Similarly, Gadgil and Joseph (2003) also used seasonal mean of AIR to define active and break spells over western and eastern parts of the monsoon trough zone. Their study found a significantly positive correlation of 0.47 between AIR and the number of active days. In contrast, a negative correlation of -0.56 was found between AIR and the number of break days. Rainfall composites based on this index also showed positive rainfall anomalies during the break over the Himalayan foothills and southeastern India, similar to Ramamurthy (1969) and De et al. (1998). Furthermore, Mandke et al. (2007) formulated an index using normalised AIR anomalies averaged over 18-28°N, 73-82°E, a region termed as the Indian core zone in which the rainfall is spatially homogeneous. This was to ensure that their index was not biased towards regions of high mean rainfall such as the Western Ghats and the Himalayan foothills. The criterion they used for an active (break) event is when the normalised rainfall anomalies over the core zone are greater than 0.7 (-0.7) for at least three consecutive days. Clearly, there are different interpretations of these indices due to different definitions and methods applied

to observational fields: different studies have used features such as convection, rainfall or circulation over different regions and periods (during JJAS) to define active and break events. My justification and choice of the index for this thesis will be discussed in detail in §3.4.

While past studies have focused their attention on studying the active and break spells in the intraseasonal variability of the Indian monsoon, very few have attempted to study the active-to-break or break-to-active transition. Traditionally, studies have examined active and break events as a single, active or break time-lagged composite (Annamalai and Slingo, 2001; Krishnamurthy and Shukla, 2000; Rajeevan et al., 2006; Krishnamurthy and Shukla, 2007; Rajeevan et al., 2010). Many of these studies assume implicitly or explicitly that all active/break phases transition towards break/active phases after a period of time. However, it is still unclear if most break phases even transition to active phases. Attempting to understand the transition based on this assumption could lead to a misguided understanding of the mechanisms governing the transition. In addition, efforts to accurately represent the timing and magnitude of the break-to-active transitions in models would potentially be beneficial, as stakeholders (e.g., farmers and water resources management) who are impacted by these extremes in intraseasonal variability would be interested to anticipate the timing of the revival of active monsoon phase. Additionally, studying the transition is also relevant for improving predictions of the onset of an active phase or the termination of break conditions. In particular, farmers would be especially interested in forecasts of when rains will return following an extended break.

In order to characterise and understand the break-to-active phase transition of the Indian summer monsoon (ISM), it is important to construct a break-to-active composite using observations and reanalyses which capture the northward propagating signals. The composite is derived from a novel method to define break-to-active transitions and will serve as the core framework for the remainder of this thesis. This chapter is thus organised as follows: §3.2 describe the datasets used in this study. Next, the choice of active/break index is discussed in §3.3, followed by a novel criterion to identify break-to-active transitions in §3.4. The break-to-active transition is then verified using an independent BSISO index (§3.5). The propagation features of the transition is analysed in a break-to-active composite constructed in §3.6. Finally, the key conclusions are discussed in §3.7.

3.2 Datasets and methods

In our analysis, the construction of the break-to-active transition composite events uses daily rainfall and OLR datasets during JJAS for the period 1979-2015.

3.2.1 Atmospheric data

The OLR dataset in this study was provided by the National Oceanic and Atmospheric Administration (NOAA)/Earth System Research Laboratory Physical Sciences Division (ESRL PSD) from their website at <https://www.esrl.noaa.gov/psd>. The OLR observations were made using the Advanced Very High-Resolution Radiometer (AVHRR), interpolated on a $2.5^\circ \times 2.5^\circ$ global grid. The missing values were filled using the methods prescribed by Liebmann and Smith (1996).

I also analysed 850 hPa horizontal winds using the European Reanalysis (ERA)-Interim product obtained from the European Centre for Medium-Range Weather Forecasts (ECMWF, Berrisford et al. 2011; Dee et al. 2011b). Daily-mean estimates of the horizontal winds were obtained using 6-hourly reanalysis on a spatial grid of $0.75^\circ \times 0.75^\circ$. The ERA-Interim dataset was selected due to the availability of the data for the time period of this study. Furthermore, the reanalysis dataset is also reliable since the product is assimilated between observations (which is currently more abundant than pre-satellite era) and models (Dee et al., 2011a; Byun et al., 2016).

The daily all-India precipitation was estimated from the India Meteorological Department (IMD) high resolution daily gridded rainfall. The rainfall dataset was developed by Rajeevan et al. (2006, 2010) based on a fixed network of 2140 rain gauge stations over the Indian subcontinent, with a minimum data availability of 90% for the period 1951-2007. Rainfall estimates were then interpolated onto grids of $1^\circ \times 1^\circ$ resolution using the Shepard (1968) interpolation technique. A detailed explanation of the interpolation method can be found in Rajeevan et al. (2006). For this study, the dataset was extended up to 2015 by the IMD.

3.3 Choice of active-break index

As discussed in §3.1, various circulation and precipitation indices over regions with differing spatial scales have been used to examine the intraseasonal variability of the ISM. For this study, I consider that a suitable index should be derived from rainfall since it is one of the most defining features of the monsoon (Gadgil et al., 2003; Krishnamurthy and Shukla, 2000, 2007).

To account for the heterogeneity of the rainfall, which may influence the index, I focus on a rainfall-based index over central India. Over this region, active and break rainfall spells are homogeneous and remove any biases from regions with high mean rainfall (Umakanth et al., 2015). This provides better identification of active/break days. Thus, I apply the active-break index to IMD gridded rainfall dataset based on studies by Rajeevan et al. (2006) and Rajeevan et al. (2010). First, daily rainfall and its daily climatological time series were obtained by

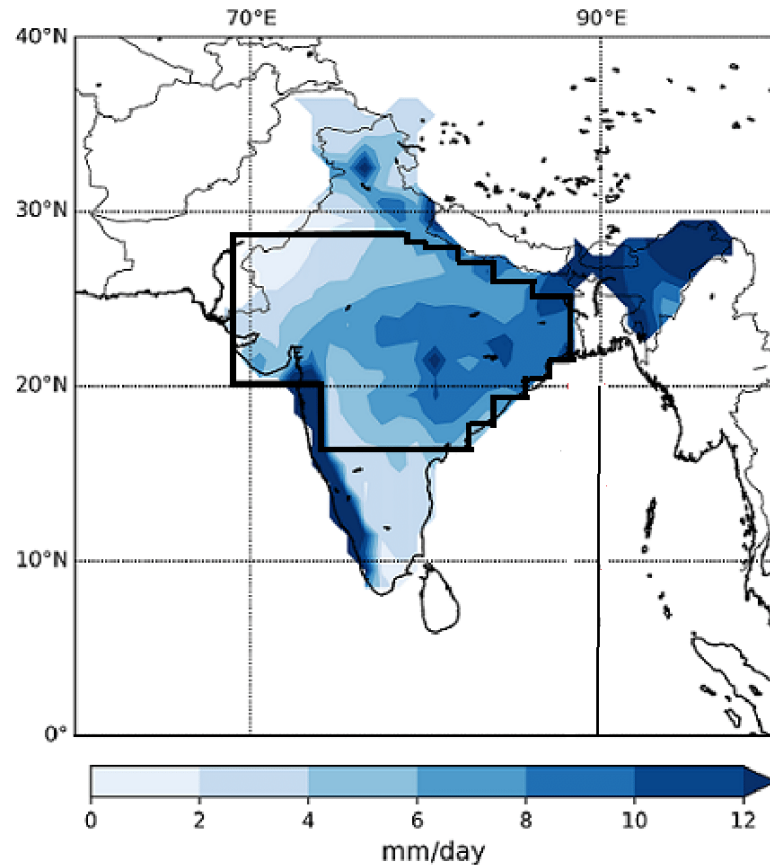


Figure 3.1: Mean 1979-2015 rainfall (mm/day) over India for JJAS. The black highlighted box is the core monsoon zone (CMZ, 65-88°E, 18-28°N) as previously defined in Mandke et al. (2007) and Rajeevan et al. (2010).

calculating the area-averaged rainfall at each grid point over the core monsoon zone (CMZ, land points within 18-28°N, 65-88°E) illustrated by the black box in Fig. 3.1, during JJAS for the period 1979-2015. Careful consideration was taken in identifying the CMZ by Rajeevan et al. (2006), so as not to include the foothills of the Himalayas, where substantial rainfall is received. Then, a 5-day running mean was applied to the daily rainfall time series to remove high-frequency variations in rainfall. Finally, for each day, the standardised rainfall anomaly (SRA) is calculated by subtracting the climatology from the daily rainfall time series and then dividing by the interannual standard deviation of rainfall.

The active and break periods are identified as days on which the standardised rainfall anomaly is greater or less than 1.0 or -1.0 respectively, provided that this condition persists for at least three consecutive days. Fig. 3.2 shows an example of the rainfall time-series during 1979: three break phases are identified by the red bars beginning on 2nd June, 2nd July and 16th August, while two active phases are illustrated by the blue bars starting on 23rd June and 2nd August.

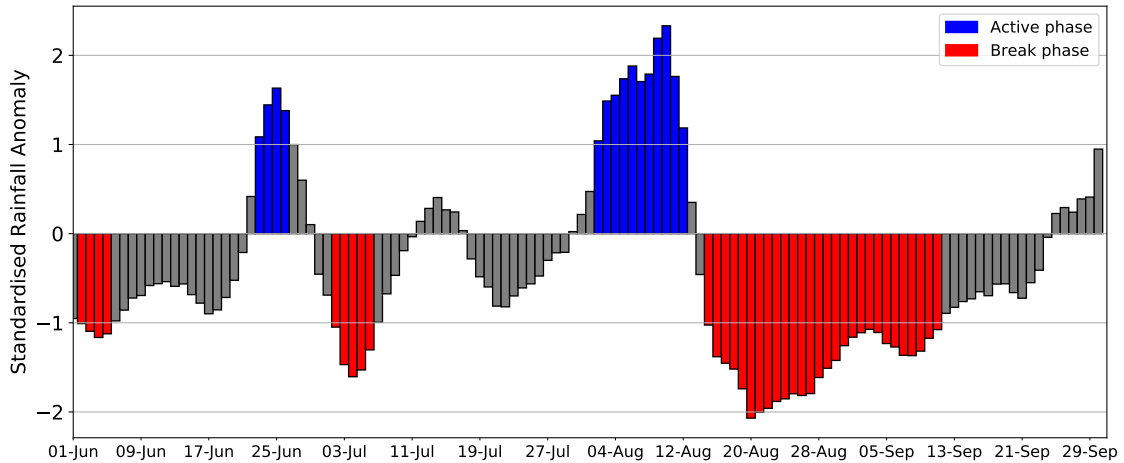


Figure 3.2: Example of the standardised rainfall anomaly during June-September 1979 averaged over the CMZ. The blue and red colour bars represent the active and break days, respectively. Active (break) days were selected when the standardised rainfall anomaly was above (below) $+1$ (-1) for at least three consecutive days. The data used are from the IMD gridded rainfall dataset.

3.4 Criteria for a break-to-active transition

Previous studies by Goswami and Xavier (2003) and Taraphdar et al. (2010) on the predictability of active and break phases of the monsoon have suggested lower predictability for a break-to-active transition compared to an active-to-break transition. Goswami and Xavier (2003) constructed an empirical model using 30-year daily summer monsoon rainfall to study the potential predictability limit of the two distinct transition regimes. Taking the active or break phase as the initial time, the predictability limit was identified when the growth of error (as measured by the variance of the ensemble members) for each transition regime, is as large as the amplitude of the ISO signal within 30 days. It was found that the error growth during a break-to-active regime is as large as the ISO signal within 8 days, while the error growth for an active-to-break transition was 20 days.

Using the high-resolution Weather Research and Forecasting (WRF) model, Taraphdar et al. (2010) found similar low predictability during the transition to an active phase. Taraphdar et al. (2010) attributed the lower predictability to the large-scale organisation of convective systems associated with the active phase over the NBoB, chiefly, lows and monsoon depressions which are more common during the active phase Gadgil et al. (2003). This is in contrast to the break phase, which is generally associated with weak convection and atmospherically-stable conditions, which lead to slower growth in error, and thus, better predictability. Their results suggest that the chaotic nature and rapid growth of error in convection make it harder to predict, especially in models. This serves as a critical motivation to focus on understanding the break-to-active transition in this thesis.

I define the transition from a break to active phase by first identifying individual break

Year	Peak break day	Peak active day	Transition length (days)
1979	4 Jun	24 Jun	20
1981	29 Aug	27 Sep	29
1987	2 Aug	26 Aug	24
1989	6 Sep	28 Sep	22
1992	3 Jul	20 Jul	17
1993	27 Aug	26 Sep	30
1995	5 Jul	19 Jul	14
1995	15 Aug	2 Sep	18
1997	16 Jul	30 Jul	14
1997	13 Aug	24 Jul	11
1998	20 Aug	14 Sep	25
1999	16 Aug	14 Sep	29
2004	17 Jul	2 Aug	16
2005	30 Aug	14 Sep	15
2006	16 Jun	3 Jul	17
2007	12 Sep	25 Sep	13
2008	18 Jul	12 Aug	25
2008	30 Aug	17 Sep	18
2009	19 Jun	18 Jul	29
2013	9 Sep	25 Sep	16
2014	2 Jul	21 Jul	19
2014	19 Aug	1 Sep	13
2015	9 Jul	26 Jul	17
2015	6 Sep	19 Sep	18
			Mean = 19.5
			Median = 18
			Std. Deviation = 5.7

Table 3.1: Dates for mid-point of break and active days, and their transition length for all 24 transition events during 1979-2015. The criterion for a break-to-active transition is that the transition must occur within 30 days. The mean, median and standard deviation of the transitions are also provided.

and active days using the methodology from §3.3. I then restrict the transition by applying a 30-day criterion such that the mid-point of the active event must occur within 30 days after the mid-point of the break. This ensures that the transitions are consistent with the nominal BSISO maximum period of 60 days (Annamalai and Slingo, 2001; Goswami et al., 2003; DeMott et al., 2014).

Based on these criteria, I identified 24 transition events (Table 3.1). For example, applying the 30-day criterion, a single break-to-active transition event was identified in 1979 (Fig. 3.2) between 4th June and 24th June, with a transition length of 20 days. It is evident from Table

3.1 that the break-to-active transition is, in fact, an uncommon occurrence, as I only identified 24 break events that transition, out of a total of 60 break phases identified between 1979-2015. This contrasts with a previous study's assumption (Rajeevan et al., 2006, 2010) that all breaks transition to an active phase (i.e., the end of a break composite is the same as the beginning of the active composite). To construct the composite, all events are averaged based on the progression through their transition period expressed as a percentage. The mid-points of the break and active phases are labelled 0% and 100% respectively, while the transition phases are categorised in steps from 12.5% to 87.5%. I represent the transition in percentage terms to standardise the varying number of transition days across the cases.

Analysis of active and break events by Rajeevan et al. (2010) and Rao et al. (2016) have suggested that break spells tend to last longer than active phases. Rao et al. (2016) reported that only 5% of the identified active spells last longer than ten days. The average life-span of the active phase is 4-5 days, comprising 70% of the total of active events. By contrast, 20-30% of the reported breaks last longer than ten days. We identified 77 active and 60 break events, respectively, between 1979-2015. The number of active and break events lasting longer than ten days were 9% and 15%, respectively, consistent with Rajeevan et al. (2010) and Rao et al. (2016).

3.5 Verification of the break-to-active transition

The active and break cycle is known to be associated with the BSISO (§2.3.1). To determine if the 24 transition events identified in §3.4 are linked to the BSISO, it is crucial to verify the results against a BSISO index. A bimodal index (Fig. 3.3) to capture the propagation features of the BSISO and MJO was developed by Kikuchi et al. (2012). This index was applied to the identified transitions. Kikuchi's bimodal index is an adaptation of an earlier multi-variate MJO index constructed by Wheeler and Hendon (2004). The BSISO spatial pattern was derived by applying an extended empirical orthogonal function (EEOF) analysis to intraseasonally-filtered OLR, 850- and 200 hPa zonal wind data in the tropics (30°S-30°N) for June-August. The BSISO index is constructed from the combination of the first two EEOF coefficients (principal components), which illustrates the strength and phase of the BSISO. The historical and real-time bimodal index are available from http://iprc.soest.hawaii.edu/users/kazuyosh/Bimodal_ISO.html.

The phase-space representation of the BSISO for all 24 transition events between 1979-2015 is illustrated in Fig. 3.3. The most striking aspect of Fig. 3.3 is that a large proportion of the identified transitions is strongly associated with strong BSISO with a northward propagation from the equatorial Indian Ocean/NBoB towards India (Rajeevan et al., 2010; DeMott et al., 2014). For example, during the 1979 break-to-active transition, a convective

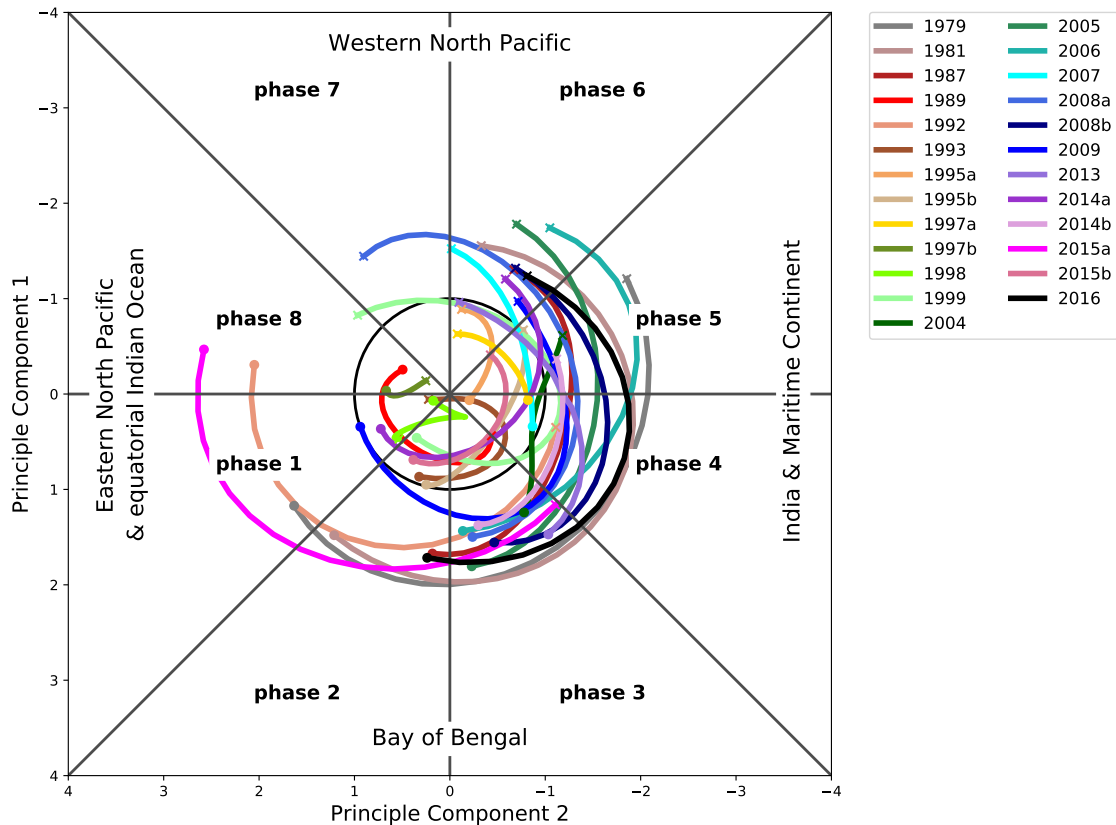


Figure 3.3: Phase space representation of the BSISO mode for all 24 transition events for 1979-2015, separated into eight defined regions. The dot represents the mid-point of the break while the cross indicates the mid-point of the active phase. Transitions within the unit circle are considered to signify weak BSISO activity. The BSISO index is based on Kikuchi et al. (2012)

anomaly appeared in the equatorial Indian Ocean (phase 1) at the mid-point of the break (grey dot) and subsequently propagated north towards India (phase 5) at the mid-point of the active phase (grey cross). Using this BSISO index enables me to associate significant BSISO events with the break-to-active transitions identified in §3.4. The results here lend credence to my method for identifying break-to-active transitions that are physically associated with the BSISO. It is noted that majority of the start of the break events are observed in phase 3. This is due to the methodology used as I have selected the mid-point of the break phase, rather than the start of the break phase.

3.6 The composite break-to-active transition

The revival of the active phase from the break is investigated using composites of rainfall, circulation and OLR, to verify that the transitions also clearly demonstrate northward-propagating signals of precipitation across the Indian monsoon region, similar to the break and active phases found in the existing literature.

In the transition composites, the mid-break and mid-active phase are represented by 0% and 100% respectively. The transition phase is marked by ranges between 12.5% and 87.5%, which represents the entire period between the mid-point of the break phase and the mid-point of the active phase. This is calculated by linearly interpolating the rainfall and OLR values on days that fall in each of the transition ranges. A one-sample Student's *t*-test was used to determine statistical significance, which tests the null hypothesis that the sample is drawn from a population with a mean of zero.

3.6.1 Rainfall

The break-to-active composite rainfall and 850 hPa wind anomalies are illustrated in Fig. 3.4. The break phase (Fig. 3.4a) over the Indian subcontinent is characterised by deficient rainfall anomalies along the west coast of India (Western Ghats), northwestern India and over the CMZ over central India. In contrast, statistically significant signals of surplus rainfall anomalies are located over the Himalayan foothills, northeastern and southern India. Moreover, the easterly anomalies over India are related to weaker background southwesterly mean monsoon winds. Another feature of the break is an anomalous anti-cyclonic circulation over northern and central India associated with the weak monsoon trough, consistent with previous studies (Gadgil and Joseph, 2003; Pai et al., 2016; Maharana and Dimri, 2016). To the south, near the southern tip of India and the equatorial Indian Ocean, an anomalous cyclonic feature is observed.

Next, the cessation of the break is marked by the weakening of easterly and northeasterly anomalies (Fig. 3.4c–e), demonstrating that the “transition” starts approximately around 25%. Concomitantly, the weakening of the wind anomalies is accompanied by the northward and westward migration of positive rainfall anomalies. During the transition phase (Fig. 3.4f), anomalous cross-equatorial, southwesterlies form, evident in the 850 hPa wind anomalies over the Western Ghats and central India.

The establishment of cross-equatorial southwesterly wind anomalies signals the initiation of an active phase over the Indian subcontinent (Webster et al., 1998; Rajeevan et al., 2010; Befort et al., 2016; Pai et al., 2016). Along with the strengthening southwesterlies over the Arabian Sea and the Bay of Bengal, the band of positive rainfall anomalies continues propagating north and northwestward (Fig. 3.4g–h). At the peak of the active phase (Fig. 3.4i), robust southwesterly anomalies are fully established. Surplus rainfall anomalies extend over the Western Ghats, CMZ and northwestern India. Meanwhile, deficient rainfall is seen over southeastern (east of the Western Ghats) and northeastern India and the Himalayan foothills (Rajeevan et al., 2010; Maharana and Dimri, 2016). In contrast to the break phase, strong cyclonic circulation anomalies are now located over central and northern India; anti-cyclonic

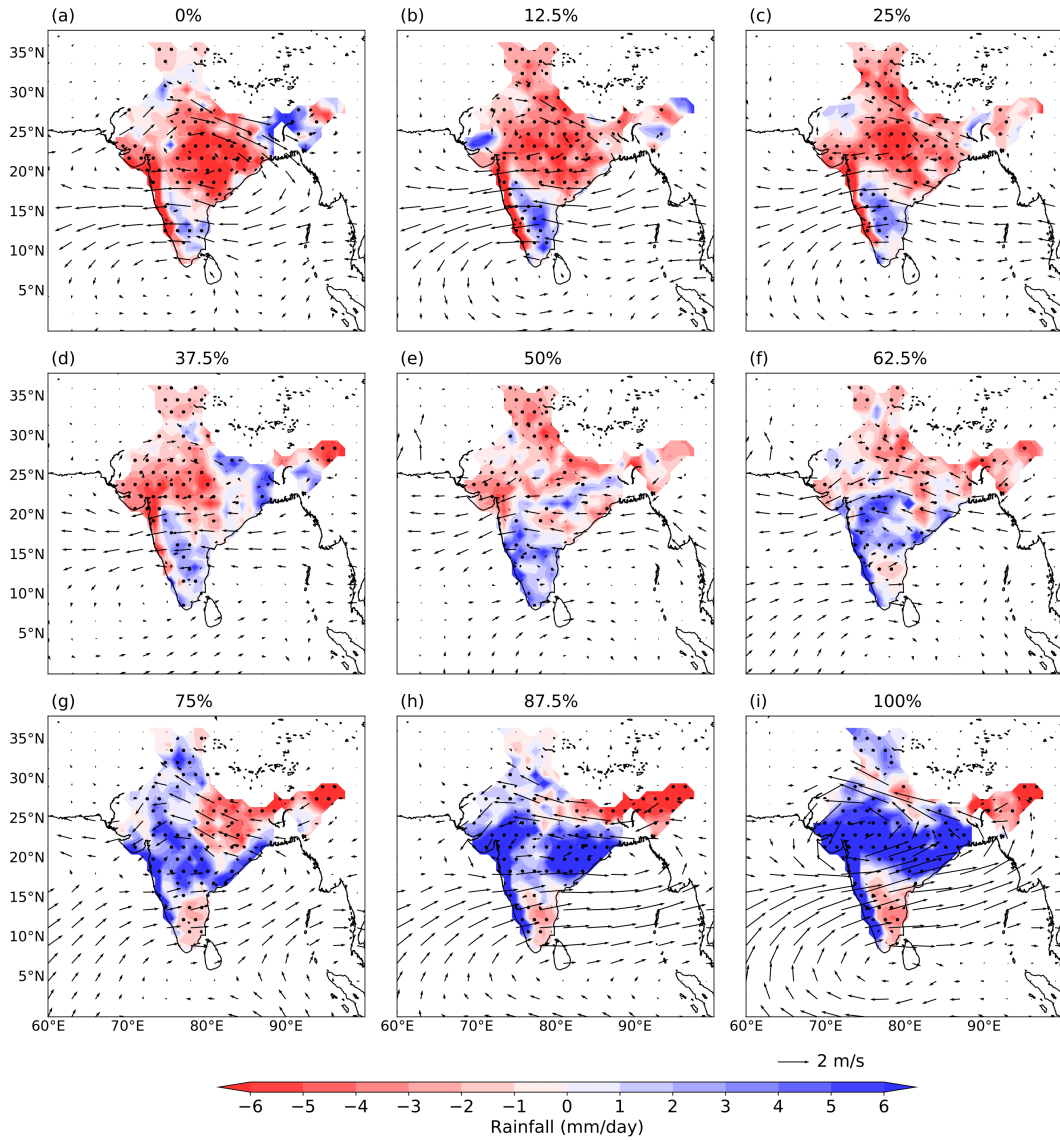


Figure 3.4: The break-to-active composite rainfall anomalies (shading, mm/day) and 850 hPa wind anomalies (vectors, m/s). The (a) 0% and (i) 100% represent the mid-points of the break and active phases, respectively, while the transition phase ranges between (b-h) 12.5% and 87.5%. The stippling represents significance at the 95% confidence level using a Student's *t*-test. The rainfall data used was obtained from the IMD gridded rainfall and wind data from ERA-Interim.

anomalies can be seen over the equatorial Indian Ocean.

The break-to-active active rainfall and wind patterns here agree with previous studies (Krishnamurthy and Shukla, 2000, 2007; Pai et al., 2016; Rao et al., 2016). These changes in rainfall anomalies are associated with the classical migration of the monsoon trough from the Himalayan foothills towards its normal position over central India, within the 30-day timescale (e.g. Annamalai and Slingo, 2001; Gadgil and Joseph, 2003; Rajeevan et al., 2010; Pai et al., 2016). The break-to-active transition is dominated by northward propagation of rainfall, similar to Krishnamurthy and Shukla (2007) and Rajeevan et al. (2010), which increases the confidence that the break-to-active criterion captures the rainfall and circulation features of

the classical break and active spells.

3.6.2 Outgoing-longwave radiation

In order to view the break-to-active transition over a wider region beyond the Indian subcontinent, Fig. 3.5 illustrates the break-to-active composite of OLR anomalies. OLR is a viable proxy for convection and rainfall in the tropics (Wang and Xu, 1997; Matsumoto and Murakami, 2000; Annamalai and Slingo, 2001) as stronger convection produces tall, cold cloud tops that reach the tropopause, resulting in lower OLR.

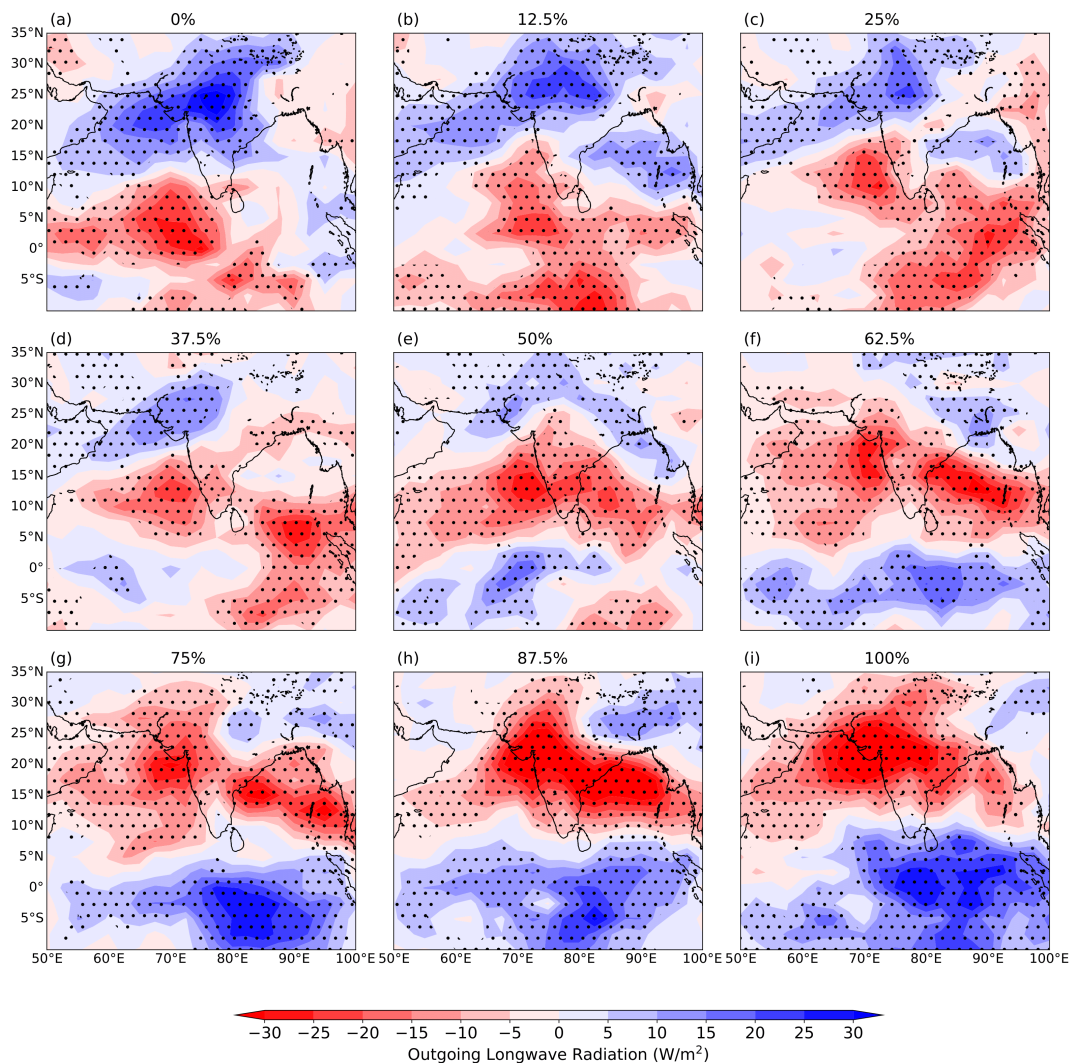


Figure 3.5: The break-to-active composite OLR anomalies (shading, W/m^2). The (a) 0% and (i) 100% represent the mid-points of the break and active phases respectively, while the transition phase ranges between (b-h) 12.5% and 87.5%. The stippling represents significance at the 95% confidence level using a Student's *t*-test. The data used were obtained from the NOAA/ESRL PSD website.

During break spells (Fig. 3.5a), a dipole pattern in OLR anomalies between India and the equatorial Indian Ocean can be seen, which is part of a larger quadrupole pattern between the

Indian and Pacific Oceans (not shown) as in Sikka and Gadgil (1980); Annamalai and Slingo (2001); Kemball-Cook and Wang (2001); Lawrence and Webster (2002); Vecchi and Harrison (2002); Klingaman et al. (2008b). The OLR pattern over India and the adjacent ocean is strongly associated with the circulation pattern: 850 hPa anti-cyclonic circulation anomalies are associated with suppressed convection over India during the break. Simultaneously, cyclonic circulation anomalies are associated with enhanced convection over the equatorial Indian Ocean during the break.

During the transition, statistically significant, negative OLR anomalies propagate northward from the EEQIO towards the Indian subcontinent. Subsequently, the dipole pattern reverses in the active phase. Significant negative anomalies ($<-30 \text{ W m}^{-2}$) can be seen over India, the Arabian Sea and NBoB, while positive anomalies ($>20 \text{ W m}^{-2}$) are located over the EEQIO. The northward and westward movement of the OLR forms the classical northwest-southeast tilt in convection and rainfall over India and the Bay of Bengal (10-25°N,70-90°E), a prime characteristic of the BSISO in both observations (Li et al., 2013; Wang et al., 2018a) and models (Fang et al., 2017b). This further confirms that the break-to-active transition in this study is strongly tied to the BSISO.

3.7 Summary and discussion

This chapter examined a novel method of studying the break-to-active transition during the Indian summer monsoon, highlighting the ability of the method to realistically represent the transition. A sensitivity test was conducted on the standard deviation threshold to define active and break days in the Rajeevan et al. (2006) index (§3.4). Besides using standardised rainfall anomalies of ± 1 , SRA values of ± 0.75 and ± 0.5 were also tested. As expected, the number of transitions increased, to 42 and 70 respectively. However, we note that the SRA of ± 1 showed a better representation of active and break phase over the CMZ compared to the lower threshold. With an SRA of ± 0.5 , the northward propagation in both rainfall and OLR composites is not coherent. In other words, lowering the threshold may lead to the inclusion of active/break events which are not physically associated with the BSISO.

Another caveat in this study is the definition of the transition phase. In §3.6, the transition phase is defined as the period between the midpoint of the break and active phase. As the results in Fig. 3.4 and Fig. 3.5 have shown, active phase conditions over the NBoB can already be observed as early as 75%, depending on the length of the active phase in each event. Likewise, break conditions are also evident in the 12.5% panel. Thus, the term “transition” used in this chapter (and in the following chapters) should not be interpreted as only the period between the end of the break and the beginning of the active phase.

Additionally, while the majority of previous studies identified individual composite active

and break events, those studies assumed that an active (break) phase is followed by a break (active) spell after a period of time. A core issue that arises from this assumption is that the time-lagged break composite is linked to active composite. However, it is shown that a break-to-active transition is uncommon since the transition only occurs for $\approx 40\%$ of the break events identified in 1979-2015.

This study also shows the strong connection between the break-active cycle and the BSISO. This link was identified based on the Kikuchi et al. (2012) bimodal BSISO index using OLR, illustrating the robust northward propagation feature of the 24 break-to-active transitions associated with the BSISO. The result in §3.5 confirms that the BSISO modulates the active/break spells on intraseasonal time-scales. Konda and Vissa (2019) applied the EEOF from the bimodal index to study different phases of the BSISO during the period 2002-2015. Their composites of rainfall and 850 hPa wind showed strong intraseasonal variability at different phases: Negative rainfall patterns and easterly wind anomalies were observed over India during phase 1-2 associated with the break phase. In contrast, a positive rainfall pattern and westerlies dominate over India in phases 4-6 associated with the active phase. Our results of the break-to-active events in Fig. 3.3 are largely consistent with Konda and Vissa (2019).

A composite break-to-active transition of rainfall, circulation and OLR anomalies was then constructed based on the 24 transition events. Our break-to-active composites represent the break and active phase accurately, similar to previous studies. With this result, the transition phase can be better represented by our composite, which individual active/break composites are unable to replicate. The composite also describes the robust northward propagating feature in rainfall and OLR from the EEQIO towards the Indian subcontinent. The active phase shows northwest-southeast tilted convection front, confirming results from Lawrence and Webster (2002). Krishnamurthy (2018) applied a multi-channel single spectrum analysis to extract intraseasonal features of precipitation and reported a similar northwest-southeast tilting rainfall band.

Finally, this chapter validates the novel transition-identification method and composites against past studies. Furthermore, it is critically important to identify the mechanism(s) modulating the northward propagation during the break-to-active transition. This effort will be undertaken in Chapter 4, which will apply reanalysis datasets to the break-to-active transition composite. Therefore, an accurate representation and mechanism(s) of the transition is essential to improve our understanding and prediction of the internal monsoon dynamics and will be undertaken in the following chapters of this thesis.

Chapter 4:

THE BREAK-TO-ACTIVE TRANSITION OVER THE NORTHERN BAY OF BENGAL IN REANALYSIS

4.1 Introduction

This chapter of the thesis attempts to answer the objectives set out in §1.2: (a) to understand the thermodynamics of the break-to-active transition over the northern Bay of Bengal (NBoB), (b) to examine the potential role of air-sea coupling associated with the intraseasonal surface turbulent fluxes and sea surface temperatures (SST) during the BSISO lifecycle and (c) to identify the sources of moisture contributing to the break-to-active transition. To undertake this effort, the break-to-active transition composite introduced in Chapter 3 will be applied to reanalysis and observed datasets.

The northward movement of convection originating from the eastern equatorial Indian Ocean (EEqIO) is one of the most robust features associated with the BSISO (Webster, 1983; Gyoswami and Shukla, 1984; Kemball-Cook and Wang, 2001; Jiang et al., 2004; Drbohlav and Wang, 2005; Bellon and Sobel, 2008a). The initiation of the active phase over the NBoB is preceded by the northward transport of moisture, energy and momentum which favours atmospheric instability and convection, indicated by observations (Bhat et al., 2001; Webster and Yang, 1992; Wang et al., 2001; Gao et al., 2019) and model simulations (Kemball-Cook and Wang, 2001; Drbohlav and Wang, 2005; Lee et al., 2013). Thus, the pre-conditioning of the planetary boundary layer by moisture transport was suggested to be a key factor for inducing deep convection and the associated poleward migration of the BSISO. Abhik et al. (2013) demonstrated using observations that shallow convection leads the active BSISO

convection in the lower troposphere to the north. The shallow convection is triggered by low-level moisture convergence leading to an unstable and moist boundary layer, which pre-conditions the environment and initiates deep convection. As the convection grows, the strong updraft within the convection transports liquid hydrometeors upward. Subsequently, the liquid hydrometeors produce precipitable ice in the middle troposphere at approximately 500 hPa. The formation of precipitable ice releases latent heat which further increases the instability and enhances the convection.

In fact, models with convective momentum transport (CMT), the vertical transport of horizontal momentum by shallow convection have been shown to improve the simulation of the northward-propagating BSISO (Kang et al., 2010; Liu et al., 2015, 2018). Liu et al. (2015) (in their Fig. 7) proposed that CMT can induce the poleward propagation of the BSISO through the barotropic vorticity effect to the north of the BSISO. Under the easterly vertical shear of the Indian summer monsoon, the CMT due to convection of the BSISO tends to accelerate the barotropic westerly wind. However, to the north, downward motion associated with the suppressed BSISO convection accelerates the barotropic easterly wind. As a result, a positive barotropic vorticity tendency can be found to the north of the BSISO convection centre. The barotropic vorticity further excites planetary boundary layer moisture convergence. Thus, the moisture pre-conditions the atmosphere and encourages the poleward migration of the convection. While a similar barotropic vorticity effect was discussed by Jiang et al. (2004) in their vertical shear mechanism, Liu et al. (2018) argues that the lower troposphere can only be moistened in the presence of shallow convection.

Additionally, Li et al. (2016) used a coupled Community Earth System Model (CESM) for the period 1981-2000 to show that the northward propagation of the BSISO was better simulated in the CESM model with the Community Atmosphere Model (CAM) version 5 atmospheric model compared to the CAM version 4 atmospheric model. CAM version 5 used improved shallow cumulus convection in the cumulus momentum transport (CMT) parameterisation scheme. This scheme better represented moistening processes by the moisture transport in the lower and middle troposphere. The shallow convection subsequently transports moisture to the mid-troposphere to the north of active convection, leading to the development of deep convection and northward propagation in the CESM with the CAM5 atmospheric model. In general, shallow convection is essential to ensure a moist lower and middle troposphere during the BSISO lifecycle. A moist atmospheric column north of active convection enhances localised deep convection in situ and induces northward propagation of the BSISO.

While these previous studies highlight the importance of atmospheric dynamics in pre-conditioning the atmosphere, the air-sea coupling effect may also be of equal importance, as discussed in Chapter 2. Since the presence of low-level moisture north of BSISO convection

is vital in pre-conditioning the atmosphere and enhancing instability, this chapter will elucidate the dominant source of moisture governing the break-to-active transition over the NBoB during the Indian summer monsoon by applying reanalysis datasets to the composite introduced in Chapter 3. Therefore, this chapter is organised as follows: §4.2 describes the datasets and the moisture budget used in this study. Additionally, §4.2.4 discusses the case study of the 2016 break-to-active transition, which serves as an out-of-sample test to compare against the 24-event composite transition derived in Chapter 3. Next, the thermodynamics of the northward propagation during the transition to an active phase will be analysed in §4.3. Furthermore, the role of the ocean surface (§4.4) as a source of moisture will also be analysed. Using a moisture-budget analysis (§4.5), I then attempt to quantify the contribution of these moisture sources during the transition. Finally, after the role of moisture is established, I conduct a case study analysis of the 2016 transition event (§4.6). The key conclusions and implications of this study are presented in §4.7.

4.2 Datasets and Methods

In this chapter, the break-to-active transition composite introduced in §3.6 will be applied to daily atmospheric, SST and surface turbulent heat fluxes datasets for JJAS spanning the years 1979 to 2015.

4.2.1 ERA-Interim

The dynamics, thermodynamics and water budget of the northward propagation are analysed using the European Reanalysis (ERA)-Interim reanalysis obtained from the European Centre for Medium-Range Weather Forecasts (Berrisford et al., 2011; Dee et al., 2011b). The surface meteorological variables used include winds (850 hPa zonal and meridional winds), precipitation, evaporation, total column water and the vertically integrated moisture flux and its divergence. Also, to study the vertical profile of the atmosphere, estimates of daily winds (zonal, meridional and vertical winds), temperature, specific humidity and relative humidity on 14 pressure levels were used. All variables are daily means based on 6-hourly temporal resolution and a spatial resolution of $0.75^{\circ} \times 0.75^{\circ}$.

4.2.2 TropFlux

The TropFlux dataset (Praveen Kumar et al., 2012) is a reanalysis-based, air-sea flux product for the tropics over the band 30°N - 30°S . Meteorological variables such as surface turbulent heat fluxes and SSTs were used in this study. These air-sea fluxes were computed using the COARE version 3 (COARE3.0) algorithm (Fairall et al., 2003) with fields from the

bias-corrected ERA-Interim datasets (Dee and Uppala, 2009) as inputs. Additionally, estimates of surface fluxes and SSTs from TropFlux are further bias- and amplitude-corrected based on in situ measurements from the Global Tropical Moored Buoy Array (McPhaden et al., 2010), which utilises the Research Moored Array for African-Asian-Australian Monsoon Analysis and Prediction (RAMA) for the Indian Ocean region. Presently, it is available on a $1^\circ \times 1^\circ$ spatial resolution from 1979 to the present.

Recently, Sanchez-Franks et al. (2018) compared SSTs and surface fluxes from five reanalysis products against the RAMA in-situ observation to study the ability of these datasets to characterise the intraseasonal air-sea fluxes over the NBoB during the southwest Indian summer monsoon. These five reanalysis products are ERA-Interim, TropFlux, the National Aeronautics and Space Administration (NASA) Modern-Era Retrospective Analysis for Research and Applications version 2 (MERRA-2), the Japan Meteorological Agency (JMA) Japanese 55-year Reanalysis (JRA-55) and the National Centers for Environmental Prediction (NCEP) Climate Forecast System Reanalysis (CFSR). It was shown that for the latent heat flux variable, TropFlux showed the smallest overestimation ($\sim 10 \text{ Wm}^{-2}$) relative to RAMA, compared to the other reanalysis products ($\sim 40 \text{ Wm}^{-2}$). Generally, TropFlux performed best at representing surface turbulent heat fluxes. Furthermore, the reanalysis products were also applied to a BSISO index (Lee et al., 2013) to examine the ability of these datasets to capture the spatial and temporal characteristics of the BSISO. Compared with the RAMA buoy, TropFlux was also able to capture the observed BSISO lifecycle across the NBoB basin unlike those from the MERRA-2, CFSR and JRA-55 product which showed weak convective signals.

4.2.3 Atmospheric moisture budget analysis

A moisture budget analysis is performed to investigate the contribution of moisture (i.e., pre-conditioning) to the break-to-active transition using reanalysis datasets. The NBoB ($85\text{-}92^\circ\text{E}$, $10\text{-}17^\circ\text{N}$) was selected as the region of interest. The NBoB was selected since deep convection and precipitation are observed during the active phase, an important characteristic of the intraseasonal monsoon as shown in §3.6.2 and in previous studies (Rajeevan et al., 2010). In fact, the intraseasonal rainfall variability accounts for approximately 80% of the total variability over the NBoB (Jongaramrungruang et al., 2017) during the summer months. Furthermore, rainfall variability in the NBoB is strongly coupled to upper ocean properties such as SSTs and latent heat flux (evaporation) as described by observations and models (Kemball-Cook and Wang, 2001; Lawrence and Webster, 2002; Vecchi and Harrison, 2002; Vialard et al., 2012). Hence, it is expected that these variables have a strong influence on NBoB rainfall. Thus the atmospheric moisture budget can be mathematically expressed through the following equation:

$$\frac{1}{g} \frac{\partial}{\partial t} \int_0^{p_s} q \, dp + \nabla \cdot \frac{1}{g} \int_0^{p_s} \vec{u} q \, dp = E - P + R \quad (4.1)$$

where $\vec{u} = (u, v)$, which represents the zonal and meridional components of the horizontal winds, respectively. The terms in Eq. (4.1) consist of the rate of change of atmospheric precipitable water, the vertically integrated moisture flux divergence (*MFD*), evaporation (*E*), precipitation (*P*) and the residual (*R*). Due to data assimilation and the lack of moisture conservation in the underlying model, ERA-Interim does not have a closed budget: $E - P$ does not balance the vertically integrated moisture divergence and precipitable water tendency. Hence, a residual term is included to close the moisture budget as suggested by Trenberth and Fasullo (2013a,b). Trenberth et al. (2011) have shown that the residual term in ERA-Interim is the smallest compared to seven other reanalysis datasets. Equally, Lorenz and Kunstmann (2012) also found that ERA-Interim offers a reasonable closure of the atmospheric moisture budget. It is noted that while studies have confirmed the small residuals in ERA-Interim, care must be taken in interpreting the moisture budget analysis as it contains uncertainties.

4.2.4 Case study: The 2016 break-to-active transition

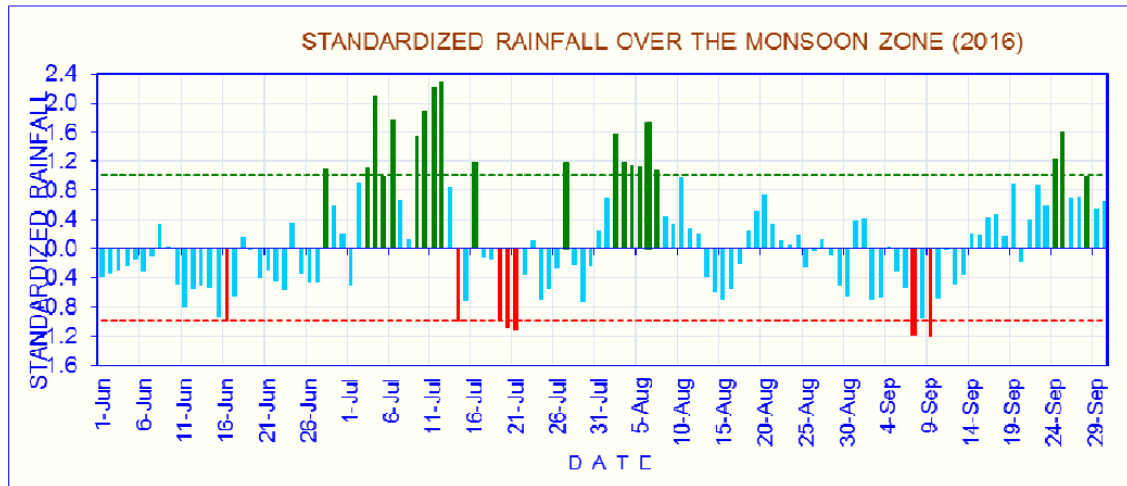


Figure 4.1: The standardised rainfall anomaly (SRA) time-series for the 2016 Indian summer monsoon season. The red and green bars denote the break and active phase, respectively. A single transition event was identified, satisfying the criteria presented in Chapter 3. The mid-point of the break phase is on 20th July, while the mid-point of the active phase is on 5th August. The length of the transition is 16 days. The time-series was obtained from the IMD website at http://www.imd.gov.in/pages/monsoon_main.php

A case study on the 2016 break-to-active transition will serve as an 'out-of-sample' test to compare the characteristics of the 2016 transition against the 1979-2015 composite transition. Similar methods used to investigate the composite transition will be extended to 2016, and the dynamics and thermodynamics of the 2016 transition will also be analysed using reanalysis. A

single break-to-active phase transition from 20th July to 5th August was identified based on the SRA released by the IMD, illustrated in Fig. 4.1. The length of this transition is approximately 16 days, satisfying our criteria. Additionally, the 2016 transition case is also captured by the BSISO index (solid black line in Fig. 3.3) as illustrated in §3.5, further confirming that the transition event is associated with the northward propagating BSISO. These dates were subsequently confirmed in the annual report of the Indian monsoon season by the India Meteorological Department (Rao, P.C.S., Pai. D. S. and Mohapatra, M., 2017).

4.3 Thermodynamics of the break-to-active transition

The thermodynamics of the break-to-active transition of the Indian summer monsoon for the period 1979-2015 are analysed. The thermodynamic variables are plotted as zonally-averaged vertical cross-sections over the 85°E-90°E longitudinal band. When calculating the anomalies, the climatology is calculated from the period 1979-2015.

4.3.1 Mixing ratio anomalies

The break-to-active composite of mixing ratio anomalies, the ratio of water vapour to dry air, are illustrated in Fig. 4.2. The break phase of the Indian monsoon (Fig. 4.2a) is characterised by a dipole structure of mixing ratio anomalies that are statistically significant at the 95% confidence level: Anomalous dry air is observed over the NBoB, with the driest anomalies located in the lower- and mid-troposphere, and moist anomalies over the EEqIO. Additionally, the vertical wind anomalies show an anomalous Hadley-type circulation between the NBoB and EEqIO. The descending branch of the circulation is co-located with the dry anomalies over the NBoB, while the ascending branch is co-located with moist anomalies over the EEqIO. This dipole pattern is consistent with observations of a convergence zone occurring alternately at Indian and equatorial latitudes during the intraseasonal oscillation (Gadgil and Joseph, 2003; Raju et al., 2005; Pathak et al., 2017).

In the transition phase (Fig. 4.2b-f), a robust and statistically significant northward propagation of moist anomalies, in excess of 0.8 g/kg, is observed in the mid-troposphere. The ascending branch of the anomalous circulation shifts northwards towards the NBoB together with the moist anomalies. Simultaneously, a wedge of anomalous dry air (<-0.8 g/kg) and descending circulation forms to the south.

The transition phase is followed by the initiation of the active phase (Fig. 4.2g-i) when the moist anomalies and ascending circulation are located over the NBoB. Since our active-break indices are based on rainfall over central India, it is expected that the active phase is initiated over the NBoB in the 75% panel in Fig. 4.2g. The deep column of moisture anomalies dominate

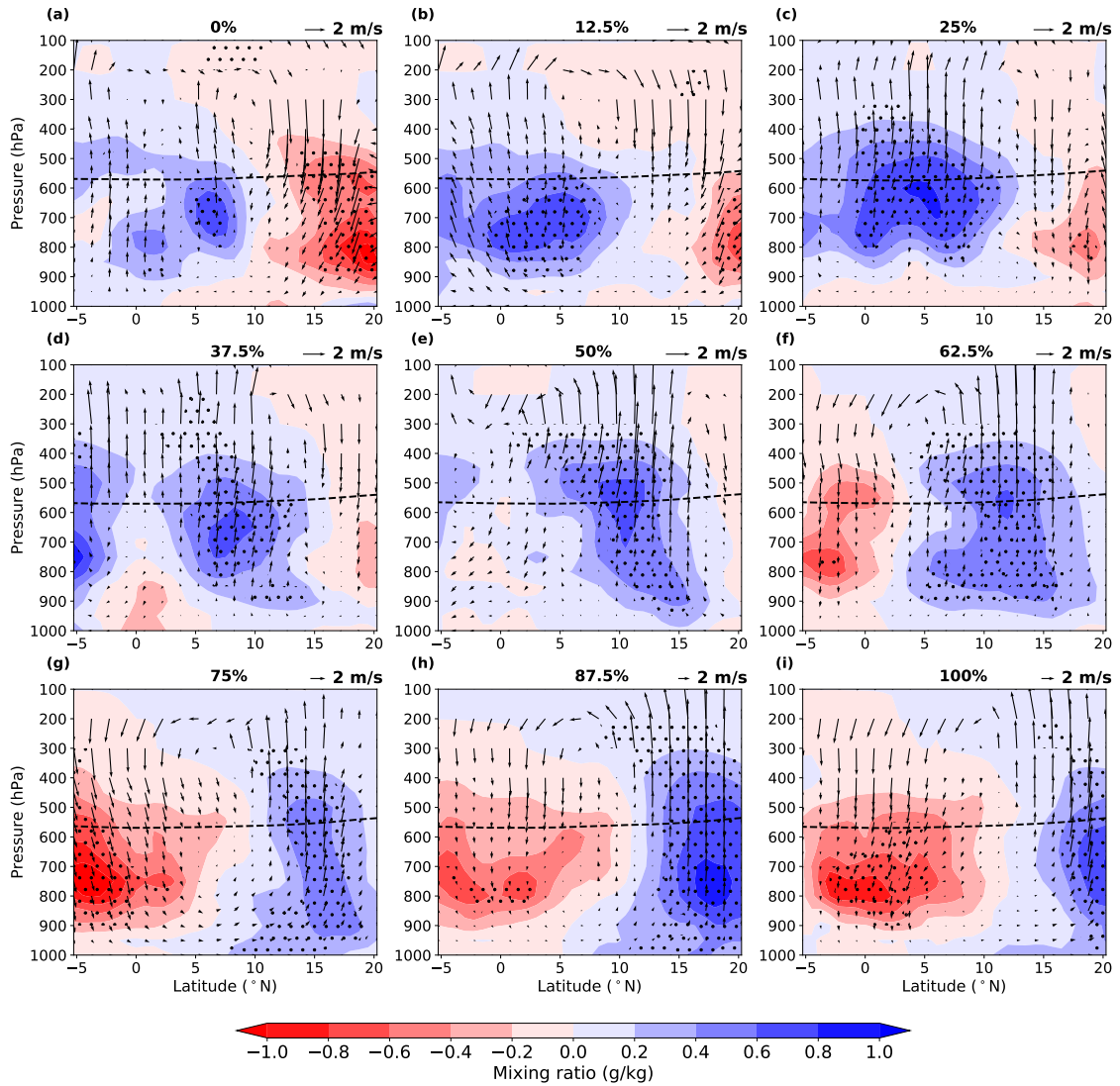


Figure 4.2: Zonally-averaged break-to-active transition composite of mixing ratio anomalies (g/kg) overlaid with vertical and meridional wind anomalies (m/s). Climatology was calculated using a 1979-2015 period. The dashed lines represents the freezing level. The stipplings represent significance at the 95% confidence level using a Student's *T*-Test. Datasets were retrieved from ERA-Interim.

over the NBoB, and maximum moist anomalies are found over the NBoB as the Hadley-type circulation reverses. It is clear from the composite that the active phase is characterised by convergence and ascent associated with convective activity in the NBoB.

An important feature in Fig. 4.2 is the location of the maximum moist anomalies in the mid-troposphere. During the northward propagation, the vertical extent of moist anomalies breaches the freezing level ($T=0^{\circ}\text{C}$ isotherm) at approximately 550 hPa. Johnson et al. (1996) proposed that detrainment of moisture from cumulus congestus clouds occurs preferentially at the freezing level. In the composite, the deepening in mixing ratio anomalies towards the active phase may be due to deeper convection and resulting in deeper detrainment. Similar patterns were also observed in Parker et al. (2016) and Menon et al. (2018), who inferred that

detrainment of moisture from cumulus clouds increases the moisture in the mid-troposphere. The release of moisture and latent heat may further destabilise the mid-troposphere. This further suggest that break-to-active transition over the NBoB is associated with the increase in deep tropospheric moist anomalies. These anomalies are vital for the revival of the active phase.

4.3.2 Equivalent potential temperature anomalies

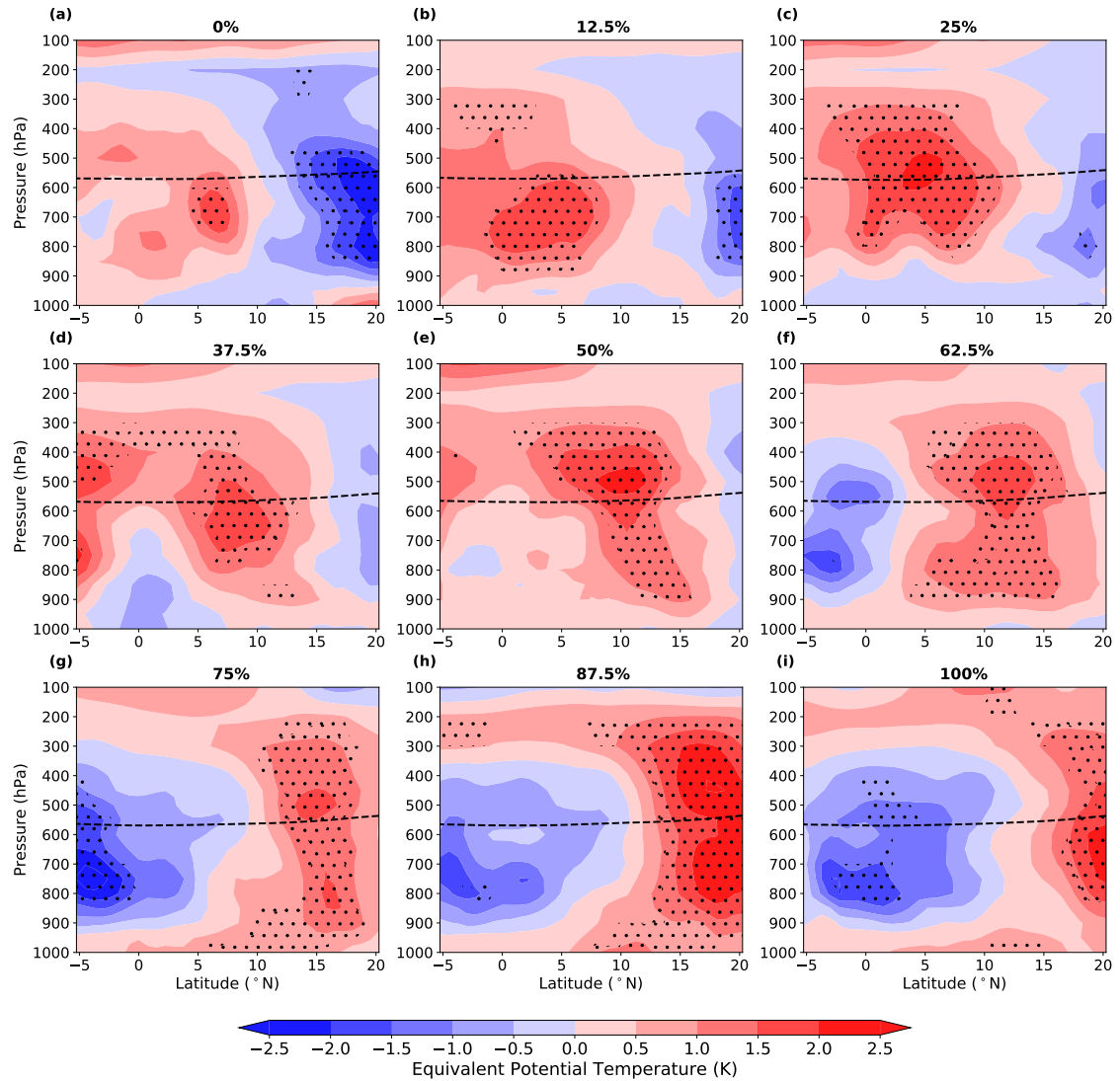


Figure 4.3: As in Fig. 4.2 but for equivalent potential temperature (θ_e) anomalies.

Next, the stability of the atmospheric column during the break-to-active transition is examined by analysing composite of equivalent potential temperature (θ_e) anomalies. The θ_e is the potential temperature a parcel would have if all its moisture were condensed and the latent heat released was used to warm the parcel and the parcel is then brought dry-adiabatically back to the surface. It is also a measure of conditional instability of a localised column of air, with positive anomalies in the vertical indicating anomalous unstable

conditions.

The most striking feature in the θ_e composites (Fig. 4.3) is the similarities in patterns to the composite of mixing ratio anomalies. In the break phase (Fig. 4.3a), the cold anomalies over the NBoB are associated with an anomalously dry atmospheric column. Thus, during break conditions, the atmospheric column is stable, and no convective activity can manifest as suggested by the subsidence in the circulation in Fig. 4.2a. Concomitantly, anomalously unstable conditions are observed to the south in the EEqIO as shown by the warm θ_e anomalies as the increase in moisture and temperature encourages convective activity.

Next, as the break transitions to an active phase, the anomalously warm and unstable atmospheric column originating from the EEqIO propagates northwards. As the moisture continues to increase towards the NBoB, the unstable layer also continues to deepen in the vertical as the negative θ_e layer is continuously eroded from below. The active phase is initiated over the NBoB due to the presence of increased moisture and warm anomalies in the mid-levels, well above the freezing level. Subsequently, the instability of the atmosphere increased, resulting in deep convection. The detrainment of moisture and release of latent heat flux through condensation at this level further feedback on the instability, and continues to strengthen the convection. The increasing instability over the NBoB during the active phase further confirms the vital role of moisture and mid-tropospheric heating in pre-conditioning the atmosphere (Abhik et al., 2013).

4.4 Air-sea turbulent fluxes and SST in the break-to-active transition

Previously, I investigated the potential role of thermodynamics in facilitating with the break-to-active transition. In this section, I consider the potential influence of SST and surface turbulent fluxes. Similarly, the climatology was calculated based on the 1979-2015 period.

4.4.1 SST

The composite of SST anomalies is shown in Fig. 4.4. In the break phase (Fig. 4.4a), warm SST anomalies are observed in the NBoB, while cold anomalies are located in the EEqIO. The SST pattern represents a distinct dipole structure between the NBoB and the EEqIO similar to previous studies (Gadgil and Joseph, 2003; Vecchi and Harrison, 2002; Klingaman et al., 2008b; Vialard et al., 2012; Roxy and Tanimoto, 2012). Furthermore, the SST anomalies do not achieve their maximum during the break. Statistically significant warm anomalies in excess of 0.3°C only manifest several days after the break (Fig. 4.4c–d). Subsequently, in the active phase (Fig. 4.4g–i), the warm anomalies gradually cool over the NBoB.

The intraseasonal SST variability during the transition is consistent with studies by

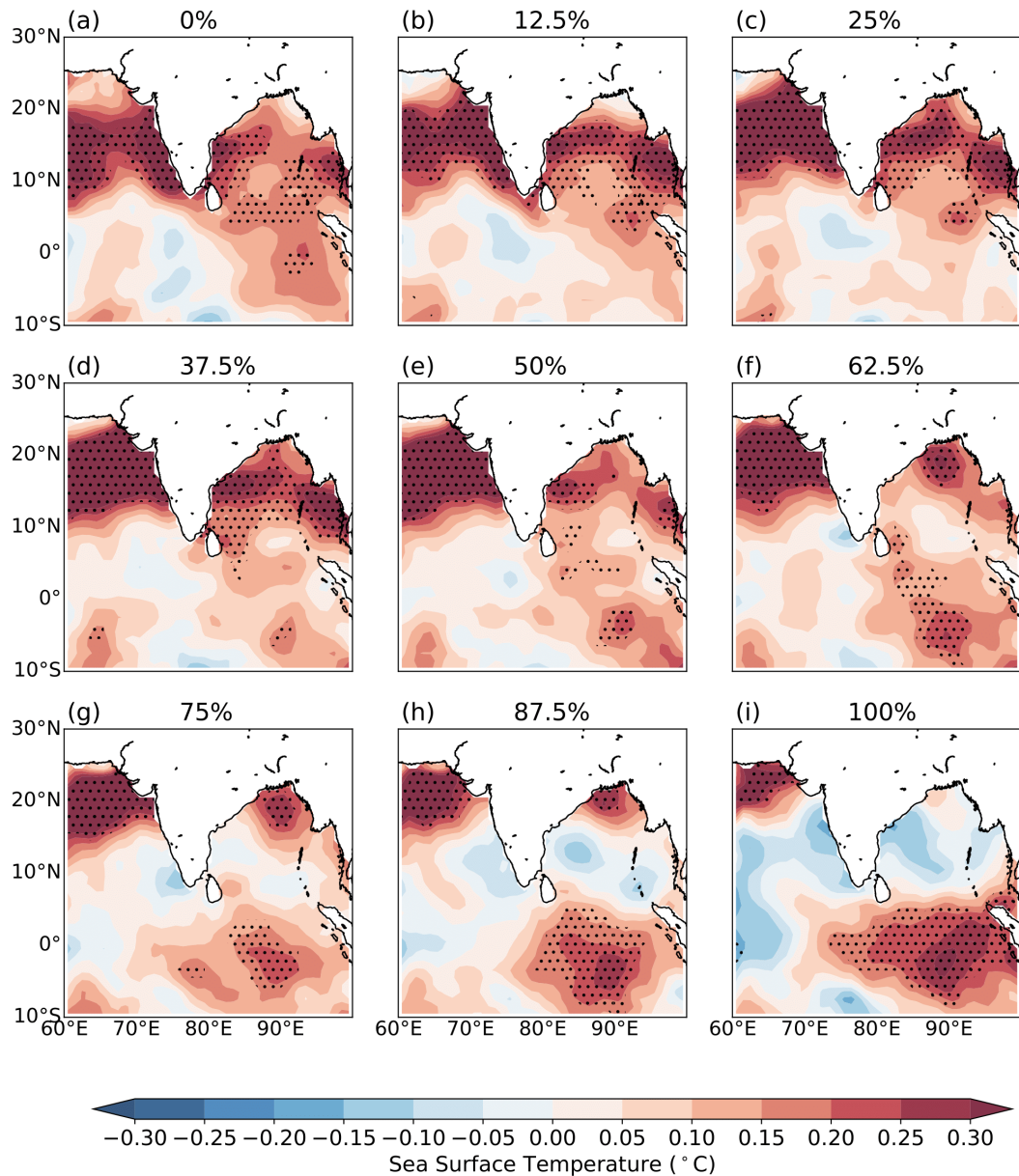


Figure 4.4: The break-to-active transition of SST anomalies ($^{\circ}\text{C}$). Data and climatology were obtained from TropFlux for the period 1979-2015. The stipplings represent significance at the 95% confidence level using a Student's T-Test.

Duvel and Vialard (2007); Roxy and Tanimoto (2007); Klingaman et al. (2008b); Wang et al. (2018b) in which the warm SST anomalies in the NBoB lead the onset of the active convection and precipitation by about ten days. During the transition to an active phase, enhanced northward-propagating convective activity cools the underlying SST anomalies by a combination of (1) a reduction in downward solar radiation and (2) enhanced wind-induced LHF anomalies (see Fig. 4.5i). However, north of the convection, warm SST anomalies form because of weak near-surface winds which reduces LHF (Fig. 4.5c-d) into the atmosphere as well as stronger incoming shortwave radiation (due to clear sky conditions) at the ocean surface, resulting in the delay in maximum SST ahead of the convection during the transition.

4.4.2 Surface turbulent fluxes

Anomalies in latent heat flux (LHF, positive into the atmosphere) are defined as enhanced (or suppressed) evaporation from the ocean surface into the atmosphere, which may influence SST anomalies and low-level moisture availability in the boundary layer.

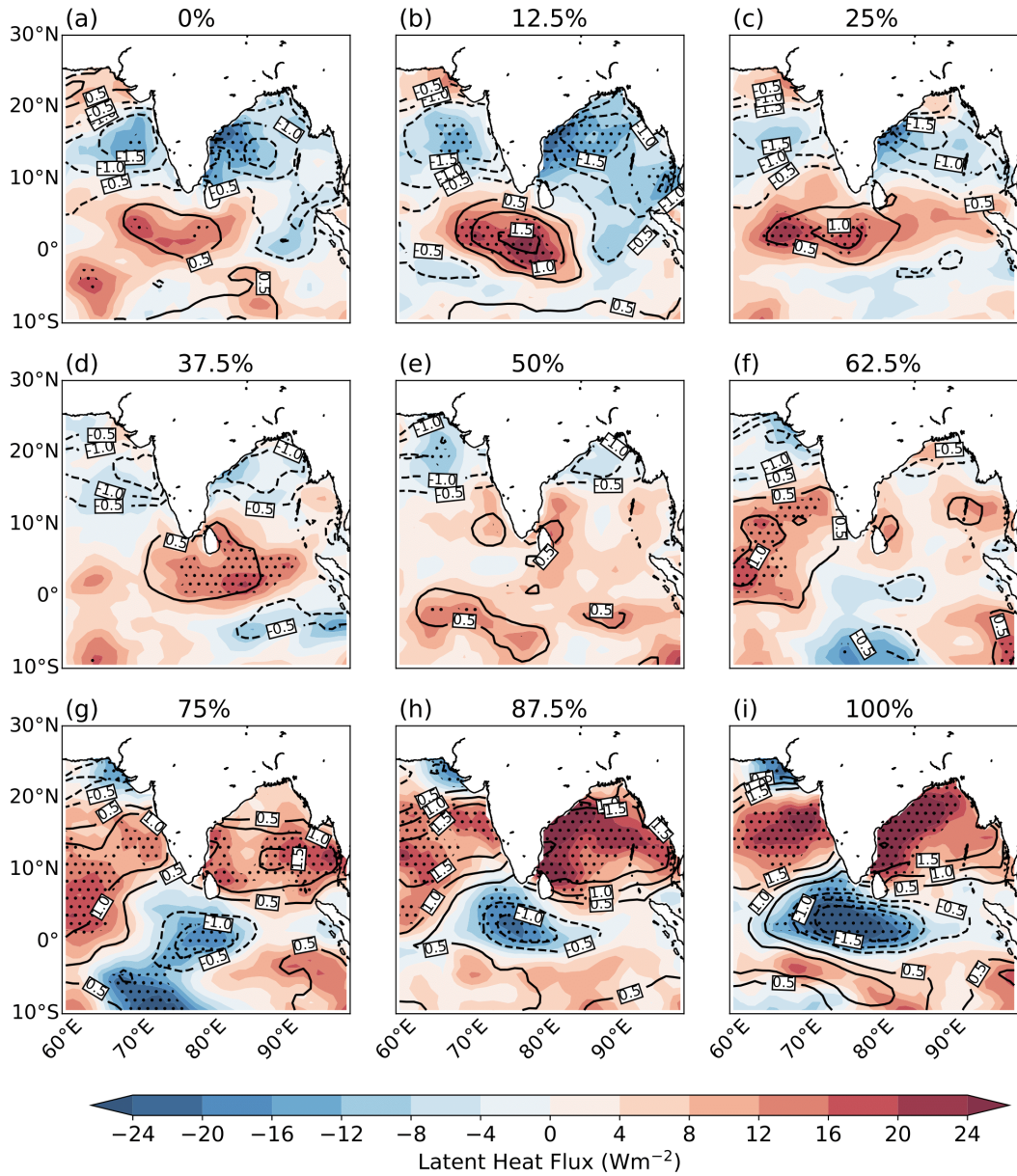


Figure 4.5: The break-to-active transition composite of surface latent heat flux anomalies (Wm^{-2}) overlaid with 10m wind speed anomalies (m/s). Data and climatology were obtained from TropFlux for the period 1979-2015. The stipplings represent significance at the 95% confidence level using a Student's T-Test. Positive values represent fluxes into the atmosphere.

During the break phase illustrated in Fig. 4.5, negative LHF anomalies are associated with weak surface wind speeds due to the weakening of the mean monsoon westerlies in the NBoB basin. Over the EEqIO, positive LHF anomalies are linked to intense surface wind speeds. The transition towards an active phase is characterised by the robust northward propagation of

LHF anomalies from the EEQIO towards the NBoB as the surface wind speeds strengthen due to the BSISO anomalies acting on the background flow (i.e., wind-driven LHF).

However, comparing the LHF composites against the OLR composites in §3.6.2, it is shown that the region of maximum wind-driven LHF anomalies is co-located with (or slightly lags) zones of maximum convection. Negative LHF anomalies are instead, found to the north of the BSISO convection during the transition phase. This suggests the wind-driven LHF may support BSISO convection but is not conducive for northward propagation, similar to that in Gao et al. (2019).

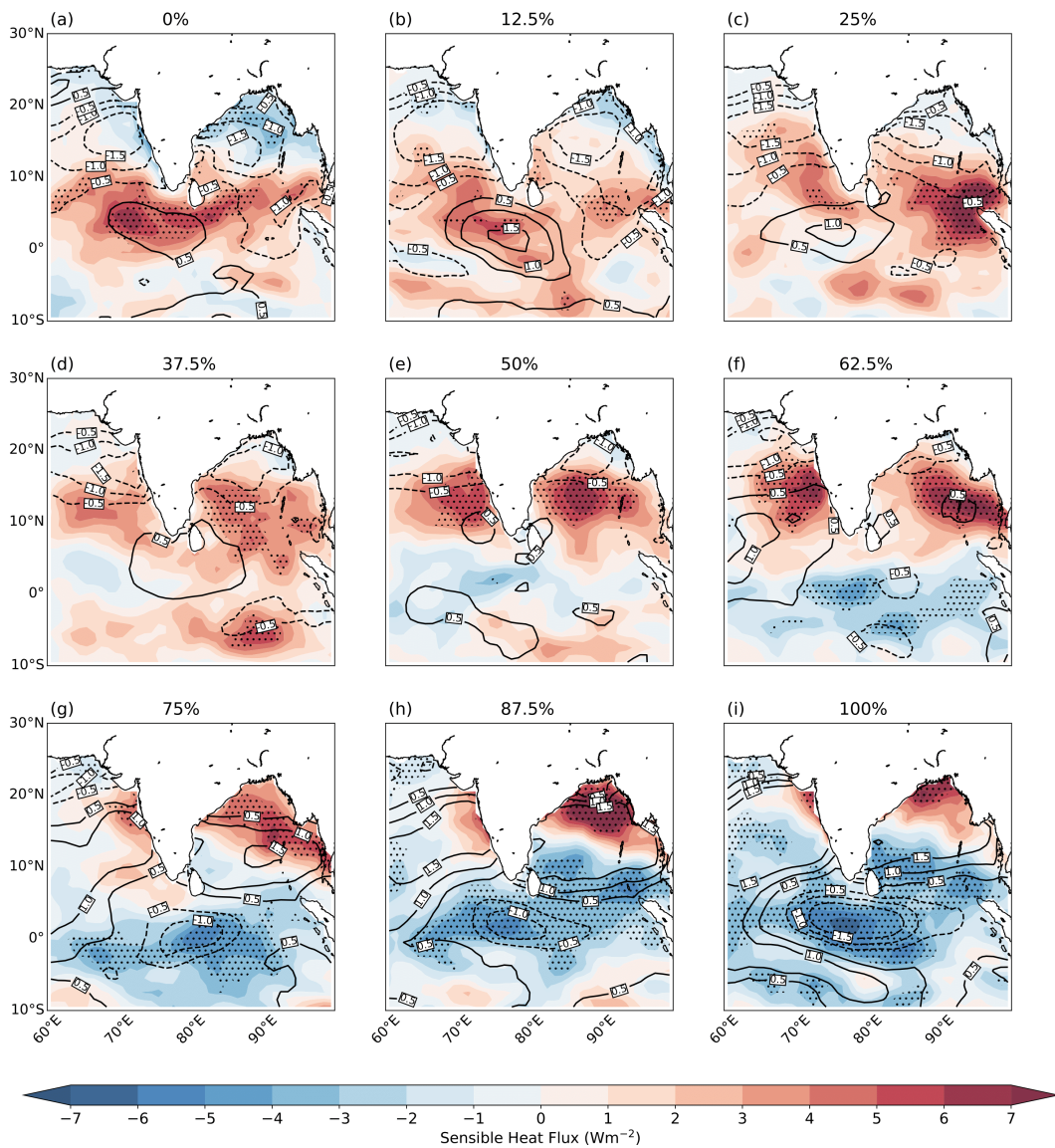


Figure 4.6: Similar to Fig. 4.5 but for surface sensible heat flux anomalies (Wm^{-2})

Next, Fig. 4.6 illustrates the composites of SHF anomalies. Similar to the LHF composites, the SHF anomalies also display poleward propagation from the equator. However, the magnitude of the anomalies is weaker (approximately three times) compared to the LHF. The weaker magnitude of SHF anomalies was also found over the NBoB Gao et al. (2019). Their

study has shown that intraseasonal SST variability has a significant influence on SHF north of 10°N by amplifying the air-sea temperature gradient. While the magnitude is smaller than LHF, positive SHF anomalies are observed to lead active BSISO convection and are generally consistent with the warmer SST which leads the convection. Therefore, the SST-modulated SHF anomalies, while small, may have a non-negligible influence on the BSISO convection (although not as large as LHF) and its propagation (Gao et al., 2019).

The results of the analysis above suggest the existence of oceanic feedback on the atmosphere during the break-to-active transition. During the break, to the north of active BSISO convection over the EEQIO, warm SST anomalies exist as a result of weak wind-induced LHF anomalies and increased shortwave radiation at the surface. As the progression continues, wind-induced LHF which is co-located with the active BSISO convection, may increase the moisture in the boundary layer and support BSISO convection, but it is not favourable for northward propagation. Concomitantly, the warmer SST over the NBoB may also increase boundary layer temperature through enhanced SHF anomalies, which may promote instability and pre-conditions the lower troposphere north of the active convection. Subsequently, this may potentially trigger shallow convection and results in the northward propagation of the BSISO convection. However, it is difficult to deduce, based on the results from our composites, if SSTs play an active role in the northward propagating ISO or is merely a passive response to atmospheric forcing. To further diagnose the SSTs and air-sea coupling, modelling studies on the break-to-active transition must be undertaken, which is the basis of Chapter 6.

4.5 Moisture budget analysis of the break-to-active transition over the northern Bay of Bengal

In this section, the potential source(s) of the moisture and their relative contributions prior to the active phase are explored. Here, I analyse the moisture budget (Fig. 4.7) terms derived in Eq. 4.1 over the NBoB. The precipitation (solid blue line) over the NBoB steadily increases from 8.04 mm/day in the mid-point of the break phase to 15.14 mm/day just before the mid-point of the active phase over the NBoB. A similar increase is observed in the moisture convergence (solid green line) term during the transition (from 4.4 mm/day to 10.26 mm/day). The evaporation (solid grey line) term shows a slight increase (4.72 mm/day to 5.84 mm/day), although the magnitude is smaller compared to the moisture convergence term. The residual term (purple line) is small, approximately 1 mm/day throughout the transition. These residual estimates agree with Trenberth et al. (2011) for ERA-Interim. The change in moisture tendency (solid black line) throughout the transition is also small, implying that

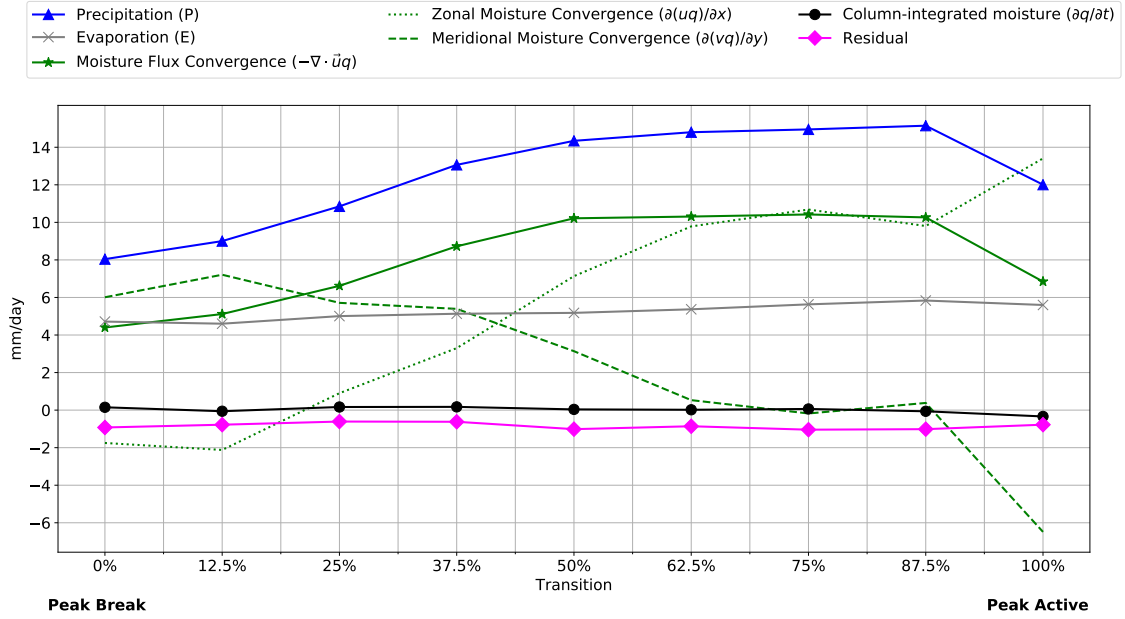


Figure 4.7: The break-to-active transition of precipitation (P), evaporation (E), vertically-integrated moisture flux divergence ($\nabla \cdot \tilde{u}q$) and its corresponding zonal ($\partial(uq)/\partial x$) and meridional ($\partial(vq)/\partial y$) components, column-integrated moisture tendency ($\partial q/\partial t$) and residual. The moisture budget was calculated using ERA-Interim reanalysis for 1979-2015 averaged over the northern Bay of Bengal ($10-17^\circ\text{N}$, $85-92^\circ\text{E}$). Units: mm/day.

over the ocean, the precipitable water is nearly constant. Furthermore, the precipitation, evaporation and moisture convergence reach their maximum at 87.5% and decrease soon after. This is expected since the active-break selection is based on rainfall over the CMZ region and not the NBoB; the active phase is established earlier over the NBoB than the CMZ.

The sources of moisture for precipitation over the NBoB based on Fig. 4.7 are associated with moisture convergence and evaporation. It is apparent that the moisture convergence term is the dominant source of moisture for precipitation, as the variations in rainfall coincide consistently with the variations in moisture convergence. The moisture convergence accounts for approximately 67% of the total rainfall contribution, with 33% from evaporation. The study by Pillai and Sahai (2014) agrees with this result as they also found that moisture convergence contributes approximately 70% of the total rainfall during the active phase, with the remainder from evaporation.

Since moisture convergence has been established as the dominant moisture contributor for precipitation, it is important to quantify the contributions from its zonal ($\partial qu/\partial x$) and meridional ($\partial qv/\partial y$) components, represented by the dotted and dashed green lines respectively. Initially, during the break phase over the NBoB, the $\partial qu/\partial x$ anomalies are negative (e.g., divergence) while those from $\partial qv/\partial y$ anomalies are positive (e.g., convergence). Progressively, the convergence contributed by the zonal component increases considerably from -1.75 mm/day to 9.80 mm/day, when the precipitation reaches its peak. In contrast,

the meridional component decreases substantially (from 6.01 mm/day to 0.38 mm/day). Clearly, the strengthening of the moisture convergence during the break-to-active transition is attributable to its zonal component.

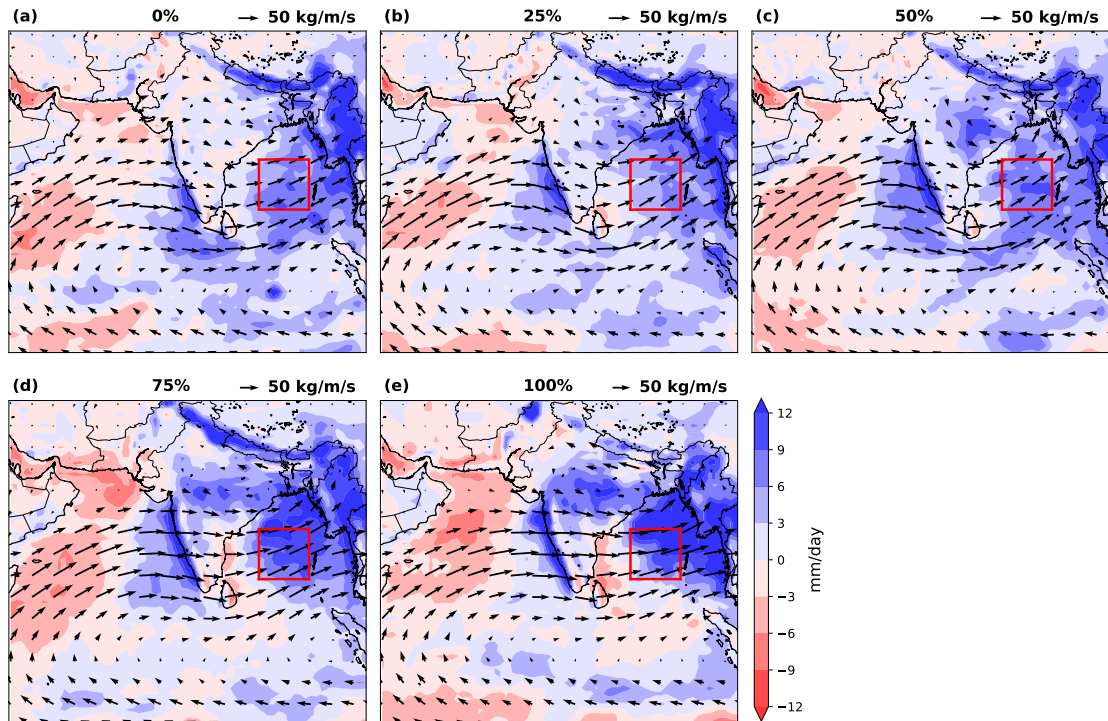


Figure 4.8: The break-to-active composite for vertically integrated moisture convergence (shading, mm/day), and vertically integrated zonal and meridional moisture flux (vectors, kg/m/s) for selected break-to-active transition panels. The red box represents the Bay of Bengal region used for the moisture budget analysis. Positive contour values represent moisture convergence.

The changes in the zonal and meridional moisture fluxes and the MFD terms are shown more clearly in Fig. 4.8. The red box illustrates the Bay of Bengal region used in the moisture budget analysis. At the mid-point of the break phase (Fig. 4.8a), the moisture convergence (contour) and the moisture flux (vectors) into the NBoB are weak. This is attributable to the weak background southwesterly/westerly mean monsoon wind typical of the break. As the active phase is established (Fig. 4.8e), the maximum convergence zone and southwesterly monsoon wind strengthen, as it shifts north towards the NBoB. As the wind strengthens, the moisture advection increases.

Therefore, the increase in moisture convergence over the NBoB, as shown in the moisture budget analysis, is due to the strengthening of both the zonal and meridional moisture convergence associated with the southwesterly monsoon winds (Raju et al., 2005; Pillai and Sahai, 2014). While the zonal component of moisture convergence is important for active phase precipitation, Gao et al. (2019) in their MSE budget analysis that the meridional component is equally important for the northward propagation of BSISO convection. Their analysis suggests that the horizontal advection of MSE over the Bay of Bengal, associated

with the northward-propagating BSISO is largely due to the meridional component of the horizontal advection. There is a contribution by the zonal component as well, but with a weaker amplitude. In our results, the meridional component may be potentially essential for northward propagation of the active phase rainfall and will be discussed in detail in §4.7. The meridional winds from the Indian subcontinent prior to the active phase may transport high-mean MSE over East Asia towards the Bay of Bengal, which may be associated with enhanced convection.

4.6 Case study: The 2016 break-to-active transition

Previously, I have analysed the break-to-active transition based on the 24-event composite. In this section, I now analyse a case study of a transition event during the 2016 Indian summer monsoon, which I compare against the 24-event composite transition event (hereafter the “composite transition”). Similar to the previous section, I analyse composites of rainfall, thermodynamics, surface turbulent fluxes and SST anomalies during the case study period to determine if the composite is consistent with a single transition. Similarly, the climatology was calculated from the period 1979-2015. The 2016 Indian monsoon was selected as it a well-observed season of interest due to the Interaction of Convective Organisation and Monsoon Precipitation, Atmosphere, Surface and Sea and the Bay of Bengal Boundary Layer Experiment field campaign organised during this period.

4.6.1 Rainfall and OLR

The rainfall overlaid with 850 hPa wind anomalies and OLR anomalies during the 2016 transition event is shown in Fig. 4.9 and 4.10, respectively. During the break phase in the case study (Fig. 4.9a), negative rainfall and easterly anomalies are dominant over much of India. Simultaneously, suppressed convection and rainfall are also observed over NBoB, while the opposite is seen over the EEqIO in Fig. 4.10a. This is very similar to the characteristics of the break phase shown in the composite transition in Fig. 3.4 and Fig. 3.5 in Chapter 3. During the transition phase, there is a clear northward propagation in BSISO convection, reaching the NBoB in Fig. 4.10b-f, prior to the active phase over the Indian subcontinent. However, a noticeable difference is seen over the Western Ghats between the case study and the composite transition: negative rainfall anomalies are observed during the active phase (Fig. 4.9g-h). This is perhaps associated with the weaker southwesterly/westerly monsoon wind during the active phase in 2016 compared to the composite transition. Additionally, a northwest-southeast tilted band of rainfall and convection, characteristic of the BSISO over the Indian region, extends towards the NBoB in both the case study and transition composite,

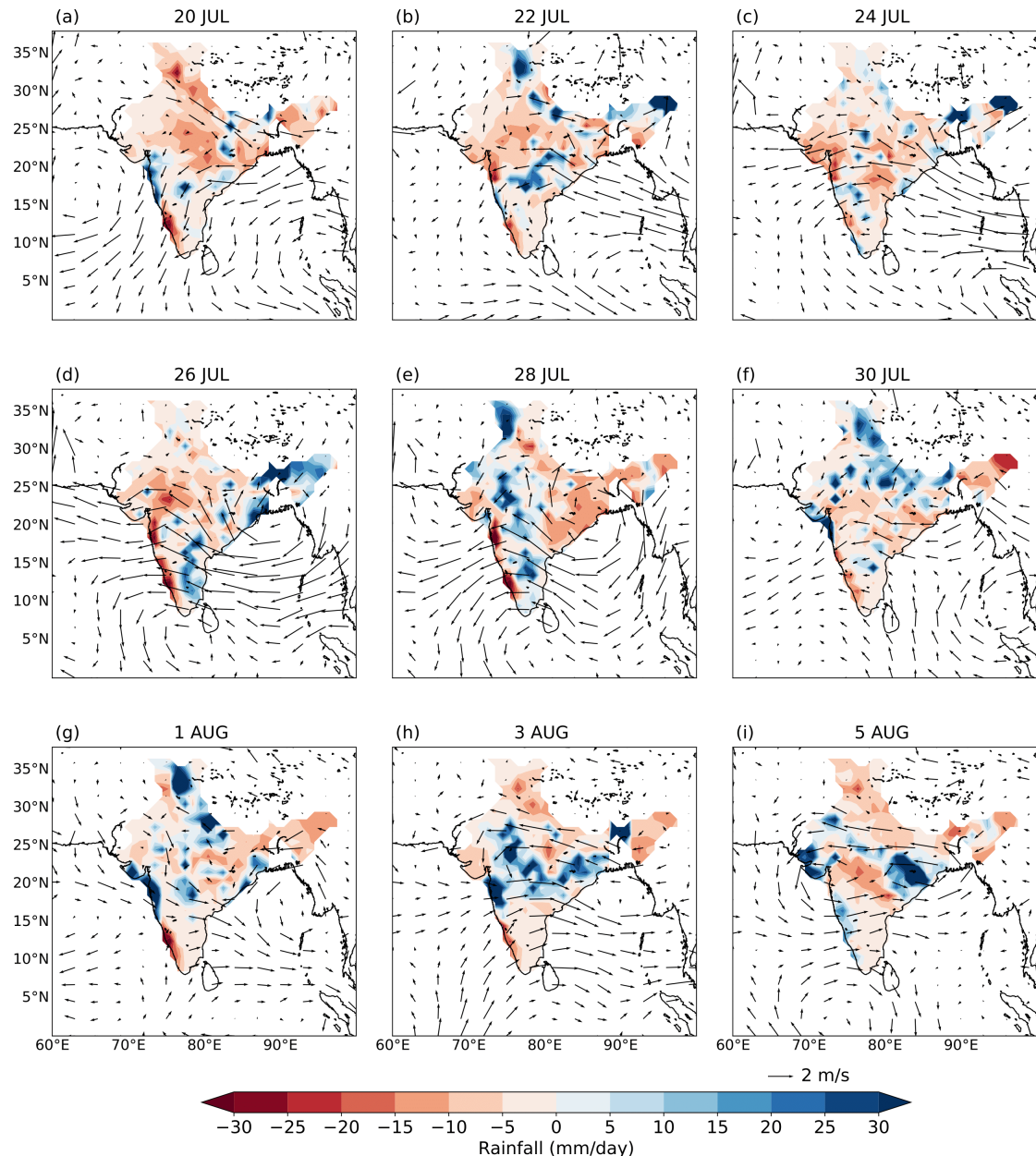


Figure 4.9: The break-to-active transition of rainfall and 850 hPa wind anomalies for the 2016 case study period. The rainfall dataset were obtained from IMD and the 850 hPa horizontal winds were retrieved from ERA-Interim. The climatology was calculated from the 1979-2015 period.

as well as in other observations by Lee et al. (2013); Fang et al. (2017a).

There are several fundamental patterns common to both the composites and case study with some variation: the shift in the anomalous wind direction from northeasterly during the break, to southwesterly during the active phase; and the anomalous low-level anticyclone indicative of suppressed conditions over the Indian continent (although more towards the west over the Arabian Sea in Fig. 4.10a) during the break phase. Low-level cyclonic anomalies and enhanced convection are present over the NBoB during the mid-point of the active phase. From these results, the rainfall pattern and propagation, along with the 850 hPa anomalies in

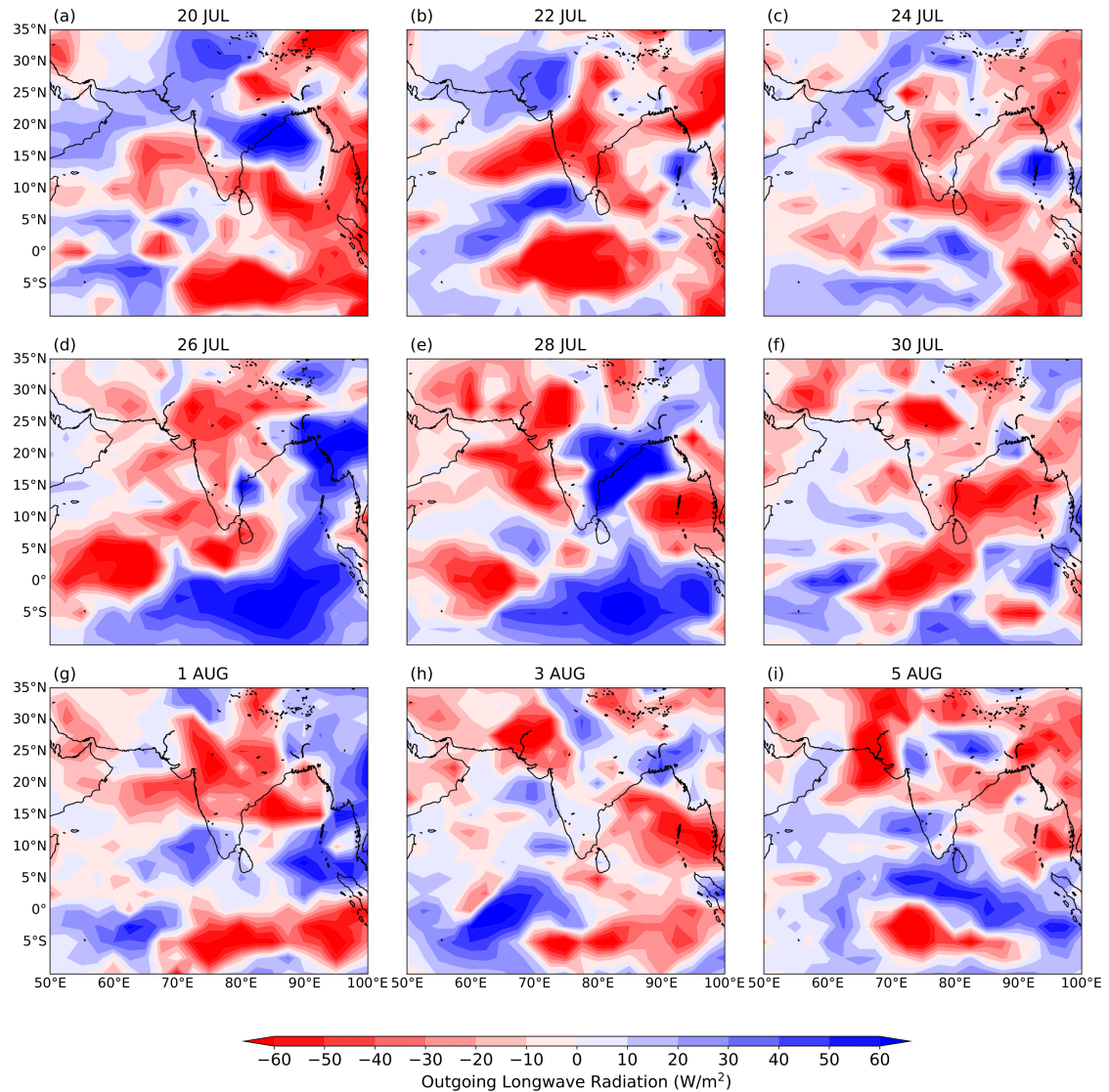


Figure 4.10: The break-to-active transition of OLR anomalies for the 2016 case study period obtained from the NOAA/ESRL PSD website. The climatology was calculated from the 1979-2015 period.

both the 2016 and composite transition have similarities with the spatial characteristics of the BSISO. Finally, the OLR is also observed to be in-phase with the active phase rainfall.

4.6.2 Thermodynamics

In this section, I analyse the thermodynamics of the 2016 break-to-active transition using the same methods applied in §4.3. I only show a selected range of panels for brevity. The composite mixing ratio anomalies for the 2016 case are shown in Fig. 4.11a-e. Similar to the composite transition, a south-to-north dipole structure of mixing ratio anomalies between the EEqIO and NBoB is observed in the case study. During the break (active) phase, moist (dry) anomalies are located over the EEqIO with dry (moist) anomalies over the NBoB. As expected, a northward propagating band of moisture associated with the BSISO is seen, especially in the

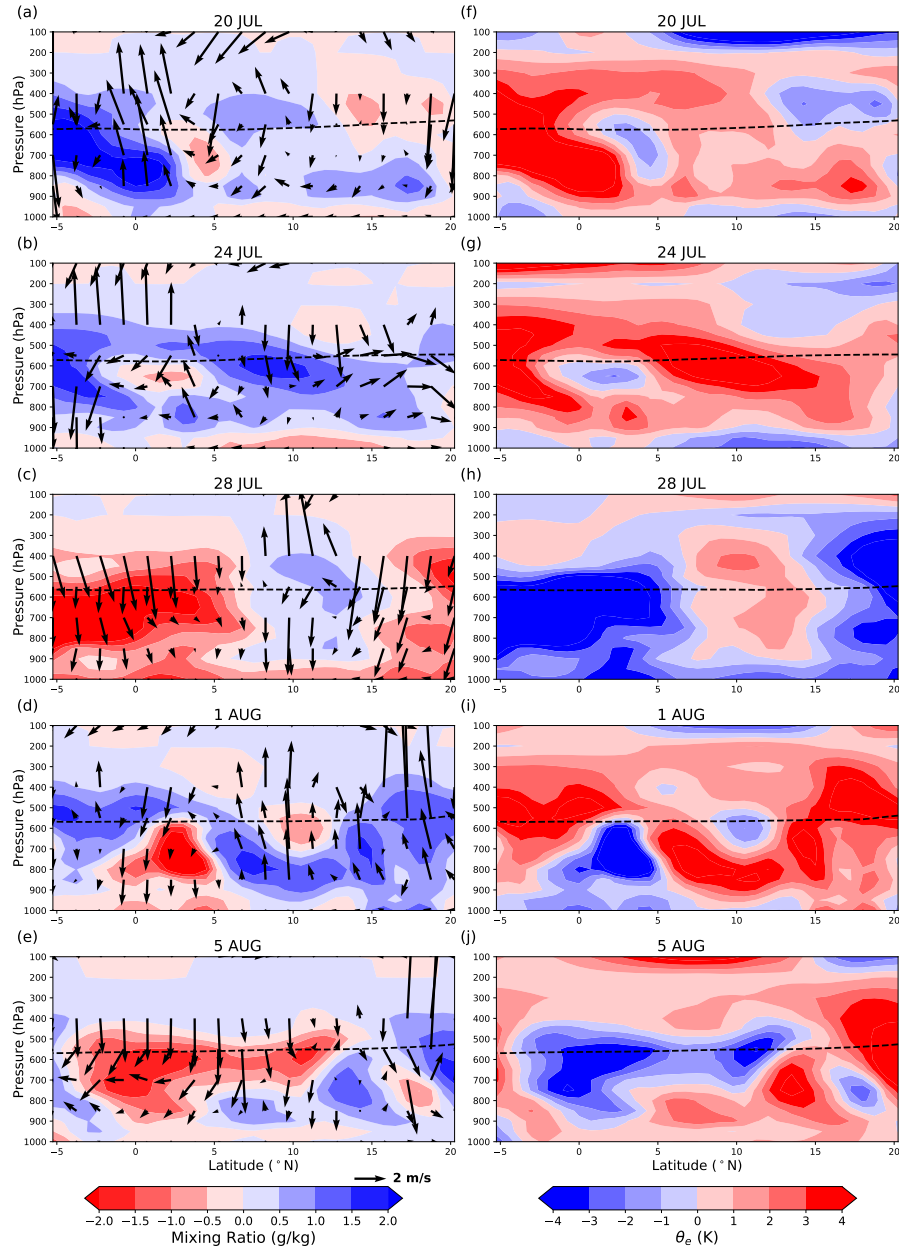


Figure 4.11: Zonally-averaged (85-90°E) break-to-active transition composites of atmospheric thermodynamic and circulation variables. The panels show (a-e) mixing ratio anomalies (g/kg) overlaid with vertical and meridional wind anomalies, (f-j) θ_e anomalies for the 2016 case study. The dashed line marks the freezing level. The stippling represents significance at the 95% confidence level using a Student's *t*-test. The data was obtained from ERA-Interim. The climatology was calculated from the 1979-2015 period.

mid-levels between 800 hPa and 500 hPa, breaching the freezing level. Concurrent with the northward-propagating moist anomalies, stronger ascent resembling the composite transition in Fig. 4.2 is also seen, which suggests an increase in convective activity and rainfall.

Furthermore, several features in the composite θ_e transition (Fig. 4.3) are well reflected in the case study (Fig. 4.11f-j). Most importantly, the northward propagation of positive θ_e anomalies associated with the moisture anomalies concentrated at mid-levels is also captured

during the case study. Again, the northward propagation of positive θ_e anomalies in the 2016 example highlights the increasing instability of the atmospheric column over the NBoB, which can lead to the transition to an active regime.

4.6.3 Air-sea fluxes and SST

Similar to §4.4, this section analyses the surface turbulent flux and SSTs during the 2016 case study period as illustrated in Fig. 4.12. Only selected panels are shown for brevity. Recall from §4.4.1 that the peak in SST warming occurs several days after the onset of the break. This intraseasonal SST pattern was also observed for 2016 on 28th July (Fig. 4.12c), which showed maximum warming occurring eight days after the break and leading BSISO convection, consistent with the composite transition and in earlier studies by Vecchi and Harrison (2002); Klingaman et al. (2008b); Vialard et al. (2012).

Next, Fig. 4.12f–j illustrates the break-to-active composite of latent heat flux and total 10m wind speed anomalies. The LHF anomalies show a distinct intraseasonal variability in the break-to-active transition. Similar to the composite transition, the anomalously negative wind speed during the break phase (< -3 m/s in Fig. 4.12a) induces negative LHF anomalies over the NBoB. It is also apparent that the weak wind-induced LHF anomalies and stronger incoming shortwave radiation lead to the warming of the SST. Furthermore, the LHF composite also show northward propagating signals, although they are weaker than the composite transition. The positive LHF anomalies associated with the enhanced surface winds are also similarly collocated with the BSISO convection. Additionally, the maximum SHF anomalies are not collocated with maximum SSTs, which suggest that SHF anomalies did not support BSISO propagation but could still support BSISO convection during 2016. This is similar with the findings in the composite transition in Fig. 4.6.

To summarise, in this section, a case study on the break-to-active transition during the 2016 Indian summer monsoon was carried out. A single transition event was identified, and the dynamics, thermodynamics and the air-sea interaction during this period were analysed. Analysis of the case study showed remarkable consistencies with results from the averaged 24-transition event case. In both the 2016 and composite transition cases, there is a clear and coherent northward propagating moisture anomalies originating from the EEQIO towards the NBoB. In both cases, the moisture anomalies may have contributed to the anomalously positive θ_e in the mid-troposphere, which pre-conditions the atmosphere by enhancing the instability of the atmospheric profile for the NBoB. However, the most significant difference between the 2016 transition and the composite transition is the role of intraseasonal SST. During the 2016 break-to-active transition, wind-driven LHF and SST-induced SHF anomalies were collocated (or even lags behind) with BSISO convection. Thus, this suggests that

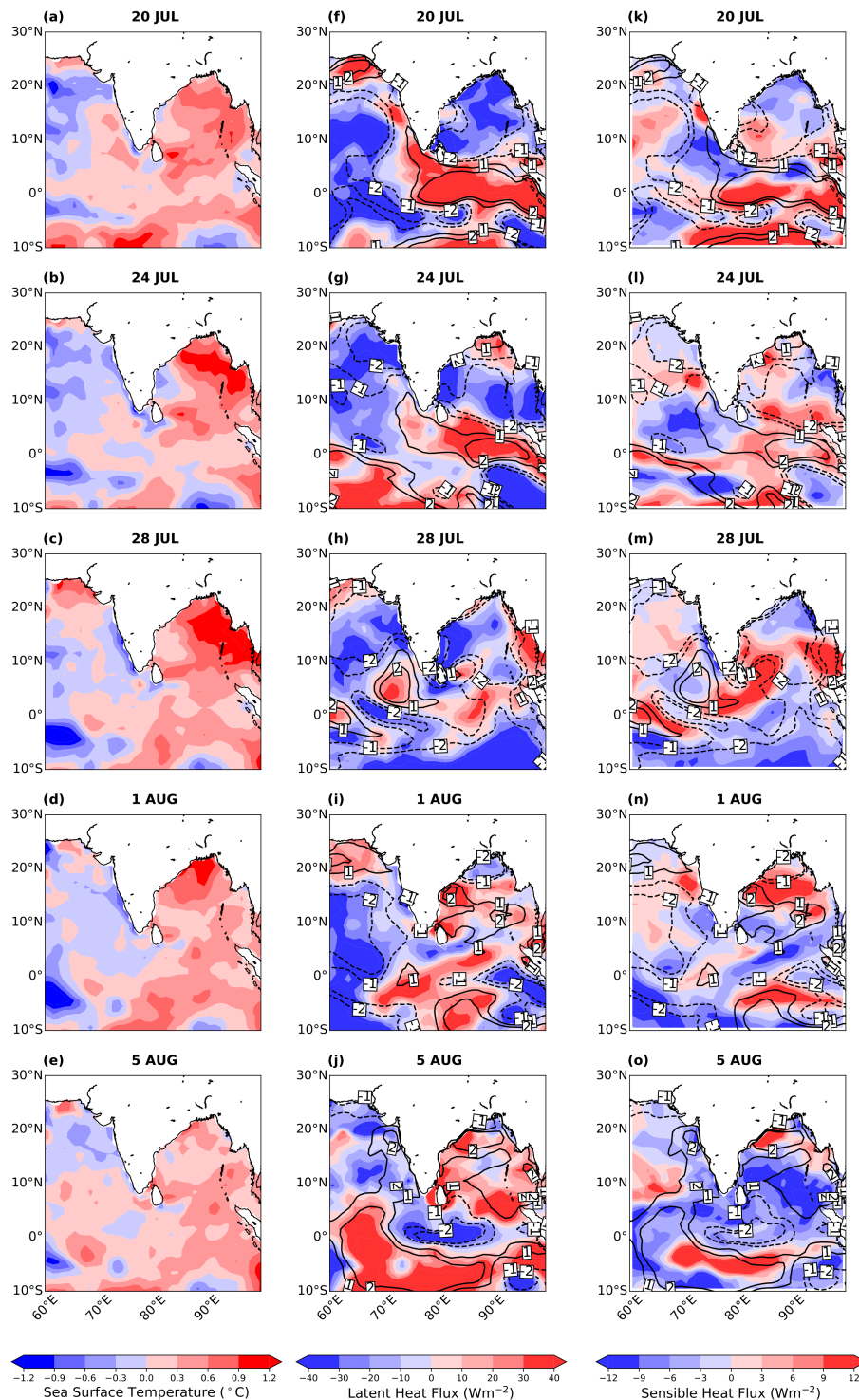


Figure 4.12: The break-to-active transition composites of (panels a-e) SST , (panels f-j) LHF (Wm^{-2}) and (panels k-o) SHF (Wm^{-2}) anomalies during the 2016. Overlaid in panels f-o are the total 10m wind speed anomalies (ms^{-1}). The solid and dashed lines represents positive and negative total wind speed anomalies respectively. Positive surface fluxes values represent upwards into the atmosphere. Data obtained from TropFlux.

fluxes associated with the SSTs may only support BSISO convection, but not its northward propagation. The results here further suggest that air-sea coupling may potentially have a weak influence on the break-to-active transition, and may be facilitated by other processes

such as internal atmospheric dynamics. Analysis of the 2016 transition in the forecast from both a coupled and uncoupled model in Chapter 6 will further assist with diagnosing the role of intraseasonal SSTs in the BSISO propagation.

4.7 Summary and Discussion

A new transition index has been used to assess the dynamics and thermodynamics of the intraseasonal variability of the Indian summer monsoon. This chapter focuses on the mechanisms governing the break-to-active transition over the northern Bay of Bengal using reanalysis. In order to identify the mechanism(s) involved, composites of the break-to-active events were constructed to study the thermodynamics of the transition. This revealed significant and robust northward propagation of atmospheric instability towards the NBoB, originating from the EEQIO, with respect to the increasing mixing ratio and θ_e anomalies in Fig. 4.3. The moist anomalies also show a deep structure extending from the surface to the mid-troposphere, which was similarly seen in Hsu et al. (2004), just above the freezing level. This is important as suggested by Parker et al. (2016) and Menon et al. (2018), since detrainment of moisture from clouds may contribute to the increased moisture in the mid-troposphere. Johnson et al. (1996) also suggested that detrainment of moisture from cumulus congestus clouds occurs preferentially at the freezing level. The case for moisture as an important ingredient for the northward propagation was further bolstered in a recent study by Liu et al. (2018) using the EHCAM4 model, which highlighted the importance of detrainment of moisture from shallow convection. It was shown that in a simulation without the influence of detrainment, the lower and middle troposphere was too dry. This prohibited the development of deep convection and consequently the northward propagation.

Composites of air-sea turbulent fluxes and sea surface temperature to consider their potential influence on the transition were then analysed. As illustrated in Fig. 4.5, positive wind-driven LHF anomalies are found to be in-phase with or slightly lags the BSISO convection, which was similarly observed in Gao et al. (2019). While, north of active convection, low-level easterly anomalies decelerates the near-surface wind speed, reducing the LHF. This results in the maximum warming of SST anomalies leading BSISO convection by approximately ten days (Vecchi and Harrison, 2002; Klingaman et al., 2008a; Roxy and Tanimoto, 2007). In turn, the warm SSTs increase SHF anomalies by amplifying the sea-air temperature gradient. This oceanic feedback acts to heat and destabilises the low-level atmosphere, triggering shallow convection and further developing into deep convection. Since enhanced wind-driven LHF anomalies are collocated with BSISO convection, it can maintain convection but is not conducive for northward propagation. Therefore, SST-modulated surface turbulent fluxes may be important for supporting the poleward shift of the BSISO

convection. While the magnitude of the SHF anomalies is small, it may still be essential in maintaining BSISO convection and propagation. In fact, Gao et al. (2019) reported that it is SST-modulated LHF, and not wind-driven LHF that is important to support northward propagation in their MSE budget. They found that more than 12% (3%) of the northward-propagating BSISO is due to SST-modulated LHF (SHF). In total, the intraseasonal SST contributes up to 20% to the northward propagation of the BSISO.

The composite analyses also showed that thermodynamics and oceanic feedbacks might contribute to break-to-active transitions through the increase of moisture. Calculation of the moisture budget in Fig. 4.7 over the NBoB revealed two sources of moisture for precipitation: moisture convergence and localised evaporation. It is clear that moisture convergence contributes more to the precipitation compared to evaporation. However, evaporation still plays a secondary role during the transition similar to the findings in previous studies (Chou and Hsueh, 2010; DeMott et al., 2013), and as such, cannot be neglected. Next, decomposing the moisture convergence also showed that the zonal component of the moisture convergence is responsible for the increased moisture over the NBoB, associated with the strengthening of the southwesterly monsoon wind. However, the meridional component is equally important during the transition phase in supporting the northward propagation of convection. Gao et al. (2019) showed that the horizontal advection of MSE contributes about 80% to the northward propagation of the BSISO. They further showed that it is the meridional advection of MSE that dominates the horizontal advection of MSE over the Bay of Bengal. The anomalous northerlies (which are observed during the break in our results) may potentially be important by transporting high-mean MSE located over the Asian monsoon region towards the EEQIO/southern Bay of Bengal, and support BSISO convection as shown in Gao et al. (2019). During the transition phase, the northward propagation of BSISO convection may be supported by the strengthening of the anomalous southerlies, which transports the enhanced MSE near the BSISO convection to the north.

Here, a mechanism by which the break-to-active transition is strongly coupled to anomalous moisture is proposed as shown in Fig. 4.13: Initially, during the break phase over India, anomalous northerlies may transport high-mean MSE towards the equator, and support BSISO convection. Subsequently, the anomalous winds become southwesterly and shift northwards towards the NBoB and India, leading to the advection on low-level moisture convergence over the NBoB, promoting local instability as illustrated by the θ_e anomalies. The enhanced wind-driven LHF anomalies may further enhance convection by promoting moisture into the boundary layer. On the other hand, warm SST anomalies leading of the active convection to the north are observed due to weaker LHF and increased incoming solar radiation due to clear sky conditions associated with suppressed convection. As the transition phase progresses, enhanced SST-modulated SHF anomalies may promote heating

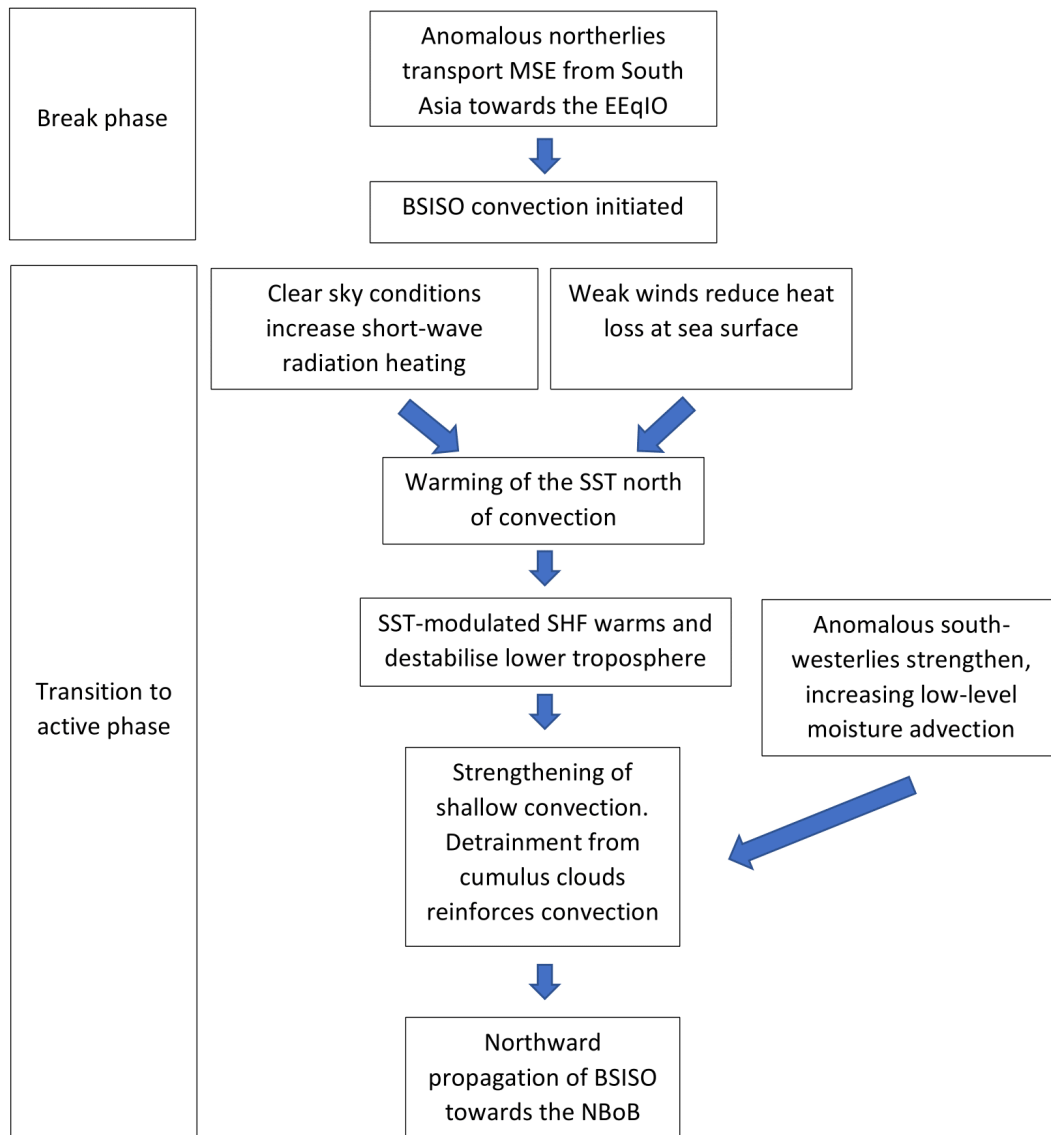


Figure 4.13: Schematic illustrating the possible mechanisms for the break-to-active transition.

of the boundary layer and by the anomalous southerlies which may also transport MSE from the BSISO convection polewards (Gao et al., 2019), which promotes instability of the boundary layer and trigger shallow convection. As the subsequent convection continues to strengthen, the clouds may increase in the vertical and breach through the freezing level. Moisture is being detrained from the cumulus clouds, further increasing the moisture and instability of the atmosphere. This could lead to the northward propagation of convection and the transition to an active phase over the NBoB. Wang et al. (2018b) have shown that intraseasonal SST may induce low-level moisture convergence and surface turbulent flux anomalies, which consequently increase heat and moisture in the boundary layer favouring northward propagation. However, the SST effect alone cannot support northward propagation as atmospheric internal dynamics is also required and is therefore essential for northward propagation as seen in our studies as well as in previous studies, with the SST effect as

a secondary mechanism (Chou and Hsueh, 2010; DeMott et al., 2013; Wang et al., 2018b; Gao et al., 2019). The secondary role of SST-modulated surface turbulent fluxes can also be further diagnosed based on the analysis of the 2016 transition event which showed that these fluxes (both LHF and SHF anomalies) are in-phase with the northward-propagating BSISO convection, in contrast to the composite transition. Thus in 2016, it appears that the surface turbulent flux anomalies supported BSISO convection, but not the propagation.

Despite these promising results, this study is not without limitations. A primary issue is the strict criteria that I have imposed for a transition. The maximum length of transition (in our case, 30 days) is somewhat arbitrary. The number of break-to-active transition cases can be increased if the criterion were extended, for example, to 45 days. This increased the number of transitions to about 31 events. However, it is my view that the 30-day criteria would be the best choice as it coincides with the 30-60 day life cycle of the BSISO. Furthermore, it is recognised that the use of the ERA-Interim reanalysis dataset for the moisture budget analysis may not be accurate since the moisture budget in ERA-Interim is not closed. In order to close the budget and to estimate the error arising from this issue, I calculated a residual term as suggested by Trenberth and Fasullo (2013a,b). It was found that the residual error is small, similar to their studies, and can adequately estimate the moisture budget over the NBoB during the break-to-active transition. However, future studies would benefit from modelling the transition in order to validate the role of air-sea coupling in the northward propagating moisture anomalies in the break-to-active transition.

The goal of this study is to identify the mechanism(s) governing the break-to-active transition. Many previous studies have offered mechanisms for the BSISO such as air-sea interactions (Kemball-Cook and Wang, 2001; Fu et al., 2003; Sharmila et al., 2013), vertical wind shear and boundary layer moisture advection (Jiang et al., 2004; DeMott et al., 2013) which is widely accepted to be important for the northward propagation of the BSISO. The results here suggest that SST-modulated surface turbulent fluxes alone may not necessarily cause, but instead, facilitates the northward propagation of the BSISO. In fact, air-sea coupling may influence the amplitude rather than the propagation speed of the BSISO (Fu et al., 2003; Lin et al., 2011). However, this role cannot be identified merely by looking at composites based on reanalysis and remains inconclusive as seen in both the composite and 2016 transition event. In order to better understand the influence of SST-modulated fluxes during the transition, analysis of the transition in an uncoupled and coupled model is required. These efforts will be undertaken in Chapter 6, which focuses on comparing the transition event in observations against outputs from an uncoupled model forced with high-resolution daily SSTs and coupled forecast NWP model for the 2016 case study. Previous modelling studies of the BSISO have shown improvements in the spatio-temporal characteristics and the SST-precipitation phase relationship of the BSISO in long-term coupled model simulations as a result of air-sea

coupling. However, the influence of coupling during the break-to-active transition requires further attention. The comparison between the models would also assist with diagnosing if the transition in the uncoupled model can occur without the influence of air-sea interaction. Finally, this may offer new insights and the opportunity to improve the forecasting skill for the intraseasonal variability of the Indian summer monsoon.

Chapter 5:

LAND-ATMOSPHERE COUPLING DURING THE BREAK-TO-ACTIVE TRANSITION OVER INDIA

5.1 Purpose of the chapter

This chapter will serve to answer the second objective of this thesis as presented in §1.2: (a) to understand the evolution of land-surface properties over India in the break-to-active transition and (b) how their variations influence local land-atmosphere coupling (LAC) and large-scale circulation on intraseasonal timescales. These efforts will be achieved by applying a LAC metric to reanalysis datasets, together with the break-to-active composites introduced in previous chapters.

It has long been understood that variations in land surface properties can modulate Indian monsoon circulation and surface hydrology by modifying the dynamics, thermodynamics and hydrological processes across varying spatial and temporal scales (Webster, 1983; Koster et al., 2000; Seneviratne et al., 2010; Koster et al., 2011; Kutty et al., 2018). For example, the impact of soil moisture on precipitation (and vice versa) is determined by a series of nonlinear processes ranging from soil moisture dynamics to planetary boundary layer (PBL) turbulence and convection. However, understanding which physical processes are important at time scales ranging from seasonal to sub-seasonal remains an open scientific question. Moreover, since soil moisture partially governs land-atmosphere feedbacks, its memory is considered a potential source of predictability for sub-seasonal to seasonal forecasts (Brown et al., 2012; Yuan et al., 2014; Zeng and Yuan, 2018b). For instance, Koster et al. (2000) used the NASA Goddard Earth Observing System-Climate atmosphere-only

general circulation model (AGCM) to show that simulations initialised with perfect soil moisture states contributed to a significant increase in prediction skill over transition zones between dry and humid climates, such as those found over the Indian subcontinent. Furthermore, in the second phase of the Global Land-Atmosphere Coupling Experiment (GLACE), (Seneviratne and Orth, 2012) found an increased in skill in regions with strong soil moisture-atmosphere coupling in multi-model experiments with realistic soil moisture initialisation during the boreal summer season. They attributed the high skill to the soil moisture memory which was found to be vital for sub-seasonal to seasonal forecasting. The persistence of soil moisture allows the soil to “remember” previous precipitation anomalies, which may then feedback into the atmosphere with memory ranging from weeks to months. The Indian monsoon is vital as a water source for agriculture and food production on which over one billion people depend. Nevertheless, the role of land surface processes in modulating the intraseasonal variability of the Indian summer monsoon is still not well understood. Therefore, it is important to consider and understand the feedbacks between the land and atmosphere, and if the feedbacks are relevant on sub-seasonal to seasonal timescales.

Understanding the physical nature of the LAC is difficult due to having several pathways and opposing feedbacks as well as being challenging to observe (Seneviratne et al., 2010). For instance, previous research identified a soil moisture-precipitation feedback, whereby soil moisture influences atmospheric processes by modulating surface latent heat fluxes (LHF), which then modify atmospheric states (e.g., lifting condensation level and planetary boundary layer height) and consequently, the precipitation. The soil moisture reinforcing precipitation, and precipitation increasing soil moisture, or decreasing soil moisture weakening precipitation and subsequently decreasing soil moisture is called a positive soil moisture-precipitation (SM-P) feedback (Pal and Eltahir, 2001).

In the positive SM-P feedback, Eltahir (1998) proposed that the wet soil moisture acts to decrease the surface albedo and Bowen ratio (the ratio between sensible and latent heat flux). Thus, wet soil moisture conditions enhance the net solar radiation received at the surface due to reduced reflectivity. Simultaneously, wet soil moisture conditions enhance net terrestrial radiation at the surface through cooling of surface temperature by the reduction of upward terrestrial radiation (in combination with the increase in atmospheric water vapour and downwards terrestrial radiation flux). Thus the decrease in both albedo and Bowen ratio over a large area enhance latent heat flux into the atmosphere and increases boundary layer moist static energy, which feeds the growth of localised convection and subsequent rainfall, further moistening the soil. Zeng and Yuan (2018b) used a combination of reanalysis and sub-seasonal reforecast datasets (obtained from the Subseasonal to Seasonal (S2S) prediction project database) to investigate LAC over East Asia. Results from the reanalysis revealed a

positive correlation between soil moisture and evapotranspiration (ET) over semiarid regions. Additionally, the SM-P feedback is also determined by the correlation between ET and lifting condensation level (LCL) over “hot spot” regions (Koster et al., 2006). A negative correlation suggests that the increase in ET lowers the LCL and is subsequently associated with a higher amount of precipitation, providing more moisture for ET.

Despite this, regions showing negative SM-P feedbacks, where dry soil conditions may amplify precipitation, were also identified by Findell and Eltahir (1997) and Taylor et al. (2012). In this case, the drier soil contributes to a higher SHF which in turn, heats the lower atmosphere and increases the instability of the PBL. As a result, convective activity can grow and subsequently increases the precipitation. Based on satellite remote sensing and ground observations, Lingbin Yang and Zhao (2018) discovered the existence of negative SM-P feedback over extreme dry and wet regions of the Indian subcontinent. However, positive SM-P feedback also occurs simultaneously in transitional regions (regions between wet and dry climate) over central and northwestern India. Physically, the sign of the SM-P feedback depends on the soil moisture-evaporation correlation. In transitional climatic zones, the relationship between ET and soil moisture is approximately linear. However, in dry regions, the changes in evapotranspiration are soil moisture-limited. In a soil moisture-limited regime, the soil moisture is positively correlated with ET, suggesting that variations of soil moisture are the controlling factor on the evaporation response. In contrast, over wet regions, energy-limited regime prevails such that ET is limited by the availability of net radiative energy at the surface.

It was discussed previously in Chapter 2 that India is located in a “hot spot” region of strong LAC, which is associated with transitional climate zones. Moreover, the intraseasonal variability of the Indian summer monsoon is influenced by the feedback between the land and atmosphere (Ferranti et al., 1999). For instance, Kutty et al. (2018) used the Weather Research and Forecast (WRF) model to study the sensitivity of convective precipitation to soil moisture during the break phase. It was found that the magnitude of precipitation over central India (CI) is enhanced over regions with anomalously high soil moisture during the break spells. The clear sky and anomalous wet soil conditions (from the previous active phase) during the break period enhanced the LAC over central India, based on the proposed mechanism by Eltahir (1998). Additionally, Asharaf et al. (2011) through a moisture budget analysis showed that the moisture for monsoon precipitation over India is contributed by localised LAC via evapotranspiration (a direct process) and by advection from external sources such as the Indian Ocean (an indirect process). Using COSMO-CLM model simulations over India, Asharaf et al. (2011) subsequently showed that the direct process is more pronounced in simulations with dry soil moisture perturbations in eastern India, while in the indirect process is more important in simulations with wet soil moisture perturbations in western India. For instance, in the wet soil simulation where soil moisture was increased by a factor of two, the surface

pressure increased due to cooling of the surface through increased LHF over northwestern India (NWI). Subsequently, the large-scale circulation over NWI weakens, and transport of moisture from the Arabian Sea is suppressed.

While there have been many studies dedicated to understanding air-sea coupling, studies on the influence of LAC on sub-seasonal northward propagation over India remain limited. The LAC is one of the most uncertain parts of the coupled climate system: while the impact of precipitation on soil moisture is clear, the return path of soil moisture affecting precipitation through modulation of ET remains controversial, especially over India due to the presence of both positive and negative SM-P feedback (Koster et al., 2004; Seneviratne et al., 2010). In addition, the link between soil moisture and atmospheric variability in the break-to-active phase transition also requires further attention. Quantifying this coupling strength will broaden our understanding of how anomalies in soil moisture may affect the atmosphere at timescales ranging from weeks to months. Thus the influence of LAC on the revival of the active phase of the Indian summer monsoon based on reanalysis will be investigated. This chapter is organised as follows: the data and methods are described in §5.2. In particular, this chapter aims to understand the variability of the land-surface properties during the transition in order to identify regions with potential LAC, which is discussed in §5.3. Next, similar to previous chapters, the thermodynamics and moisture budget during the transition are also investigated (§5.4). Subsequently, after regions with LAC are identified, the coupling strength is quantified to determine if LAC may have a potential role in the break-to-active transition, or if other factors are responsible (§5.5). The results of this study are concluded and discussed in §5.6.

5.2 Datasets and methods

In this chapter, the break-to-active transition composite will be used to study the evolution of surface variables and its link to LAC. Additionally, I used a restricted period of 1979-2010, compared to 1979-2015 in previous sections due to the availability of the ERA-Interim/Land datasets. The use of ERA-Interim/Land in assessing surface variables will be discussed in-depth in §5.2.1. The similar time period is also used to calculate the climatology. As such, only 19 events were used in the break-to-active transition composites. In addition, §5.2.2 presents the moisture budget analysis, followed by the discussion of the metrics used to quantify the LAC over India.

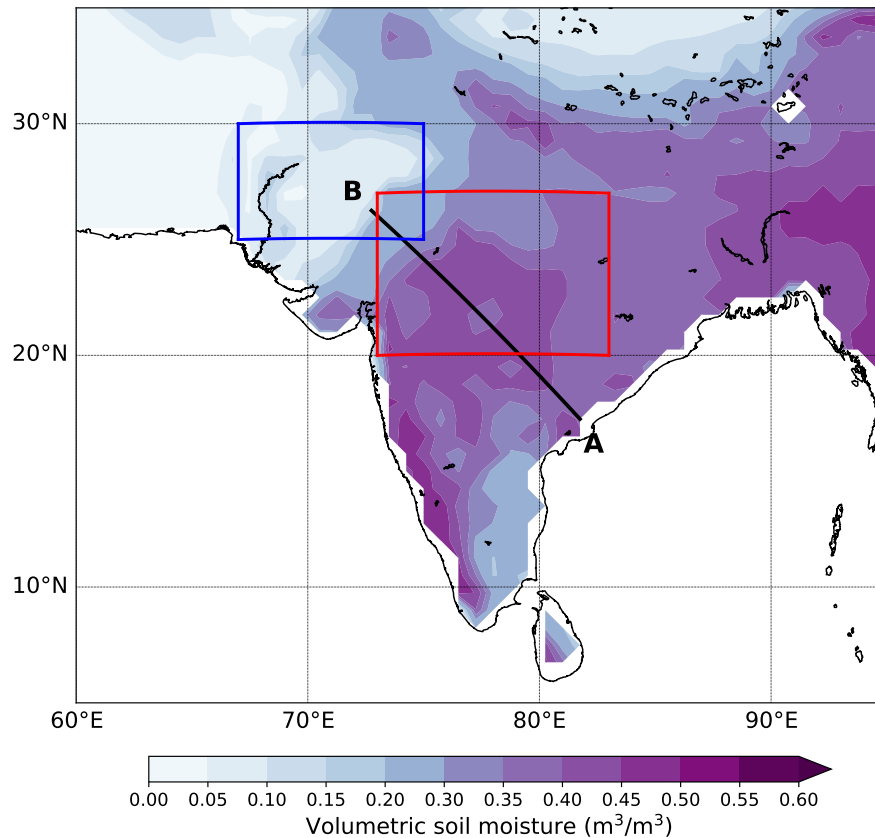


Figure 5.1: Diagram illustrating the southeast-to-northwest endpoints (black solid line), labeled as A and B respectively for the thermodynamic cross-section analysis. The red and blue boxes represent the area used in the moisture budget analysis in §5.4.3, representing central India (20-27°N, 73-83°E) and northwestern India (25-30°N, 67-75°E), respectively. The contoured lines represent the JJAS climatology (1979-2010) of volumetric soil moisture (0-7 cm) over the Indian subcontinent obtained from ERA-Interim/Land.

5.2.1 ERA-Interim and ERA-Interim/Land

In order to explore the land-atmosphere characteristics, daily surface and near-surface atmospheric variables at a horizontal resolution of $0.75^\circ \times 0.75^\circ$, derived from the ERA-Interim/Land datasets (Balsamo et al., 2015) for the period 1979-2010 were used. The surface variables include soil moisture (0m-0.07m), surface net radiative fluxes and surface turbulent fluxes (SHF and LHF). The near-surface variables used are the humidity at 2 metres, and the LCL, which is calculated from near-surface air temperature, dew-point temperature, relative humidity and surface pressure.

Additionally, the thermodynamics of the transition, similar to the composites in §4.3 will be studied using ERA-Interim (Dee et al., 2011a). Rather than averaging over a longitudinal band, I will examine the transition in a southeast-northwest transect across India, illustrated by the solid black line in Fig. 5.1, using estimates of specific humidity and equivalent potential temperature. This transect is similar to the ones used in Parker et al. (2016) and Menon et al. (2018) and was selected as it not only covers the climatologically dry and wet soil regions of

India, but also showed intraseasonal variability signals during active and break events.

The ERA-Interim/Land reanalysis is produced by using near-surface meteorological fields from ERA-Interim to force an updated version of the Hydrology-Tiled ECMWF Scheme for Surface Exchanges over Land (HTESSEL) land surface model. Some of the upgrades in HTESSEL include improved soil hydrology and bare soil evaporation as well as a new snow scheme (Balsamo et al., 2009; Dutra et al., 2010; Balsamo et al., 2011). Moreover, comparison against ERA-Interim and verification with in-situ observations have shown improvements in variables such as soil moisture and surface turbulent fluxes, attributed to the improvements made in HTESSEL (Balsamo et al., 2015). For example, comparisons of the root mean square error (RMSE) for LHF were made based on in situ flux tower observations averaged over 34 sites (in various location of the globe) against ERA-Interim/Land and ERA-Interim for the year 2004. The RMSE was computed for seasonal-to-sub-seasonal timescales using 10-day averages. It was shown that that the RMSE in ERA-Interim/Land was lower (21.8 Wm^{-2}) than ERA-Interim (26.0 Wm^{-2}). Similarly, the mean bias in the latent heat flux was reduced to 14.4 Wm^{-2} in ERA-Interim/Land, compared to 18.2 Wm^{-2} in ERA-Interim.

5.2.2 Moisture budget analysis

A moisture budget analysis similar to the method introduced in Chapter 4 will be used to study the contribution of moisture (from localised evapotranspiration and moisture convergence) for the atmospheric moistening during the transition over two distinct regions in India: (a) central India [CI, (20° - 27° N, 73° - 83° E)] and (b) northwestern India [NWI, (25° - 30° N, 67° - 75° E)] as shown by the boxes in Fig. 5.1. The motivation for selecting these regions will be discussed in §5.4. The dataset used to quantify the moisture budget is obtained from ERA-Interim.

5.2.3 Land-atmosphere coupling metrics

LAC occurs via two steps (or legs): the “terrestrial leg” in which soil moisture anomalies affect surface fluxes (LHF and SHF); and the “atmospheric leg” where variations in the surface fluxes affect near-surface parameters such as temperature, humidity and planetary boundary layer height (Seneviratne et al., 2010). Therefore the LAC can be identified through a simple correlation between soil moisture and atmospheric variables: a strong correlation between the land surface state and surface fluxes (terrestrial leg) and between surface fluxes and atmospheric states (atmospheric leg) would suggest that a physical relationship (i.e., feedback) exists between the land and atmosphere (Hirsch et al., 2016; Dirmeyer and Halder, 2017; Draper et al., 2018; Halder et al., 2018). A positive correlation between soil moisture and latent heat fluxes would indicate that soil moisture has a strong control on the fluxes, which suggests

a moisture-limited regime, as opposed to an energy-limited regime where net surface radiation controls the fluxes, as discussed previously in Chapter 2.

Halder et al. (2018) further suggests that in order to quantify the coupling strength, the correlation and variability must be accounted for since high correlation without variability may infer that while coupling exists, there is no influence on the atmosphere. The variability here is defined by the standard deviation of surface fluxes or atmospheric variables/diagnostics. The variance demonstrates the strength of the relationship. For example, over desert regions during summer months, a strong (negative) correlation between soil moisture and sensible heat flux exists. However, weak variability in the surface fluxes may limit the coupling strength despite a strong correlation. Therefore, a two-legged coupling metric will be used in this chapter to quantify the coupling strength during the break-to-active transition (Dirmeyer, 2011).

The two-legged coupling metrics are represented by the terrestrial coupling index (TCI; Dirmeyer, 2011) and atmospheric coupling index (ACI; Dirmeyer et al., 2014). These indices account for the variability (standard deviation, σ) and the correlation between the atmosphere and surface fluxes or soil moisture to quantify coupling strength. The TCI is formulated as

$$TCI = \sigma_x Corr_{xy} \quad (5.1)$$

where x represents a surface flux variable and $Corr_{xy}$ represents the correlation between those fluxes and soil moisture (represented as y). Similarly, the ACI can also be formulated as:

$$ACI = \sigma_i Corr_{ij} \quad (5.2)$$

where i represents surface flux variables or diagnostics (e.g., lifting condensation level, 2m humidity or boundary layer height), and $Corr_{ij}$ represents the correlation between the atmospheric variable and fluxes of moisture or heat. Only correlations significant at the 99% confidence level using the Kendall's Tau correlation coefficient are considered. I have opted to use the Kendall's correlation similar to Dirmeyer (2011) and Dirmeyer et al. (2014) as it is less sensitive to outliers compared to the Pearson's correlation. The break-to-active composites for the TCI and ACI are calculated by binning the percentiles of transition length into 0-20%, 21-40%, 41-60%, 61-80% and 81-100%. The percentiles were binned such that there are a larger number of samples in each bin when calculating the correlation and standard deviation, while still maintaining the intraseasonal variability of the LAC strength.

5.3 The break-to-active transition over India

The evolution of surface and near-surface variables during the break-to-active transition over India is analysed. The composites consist of 19 transition events identified during the period 1979-2010. For brevity, only selected transition panels will be shown.

5.3.1 Soil moisture and surface turbulent fluxes

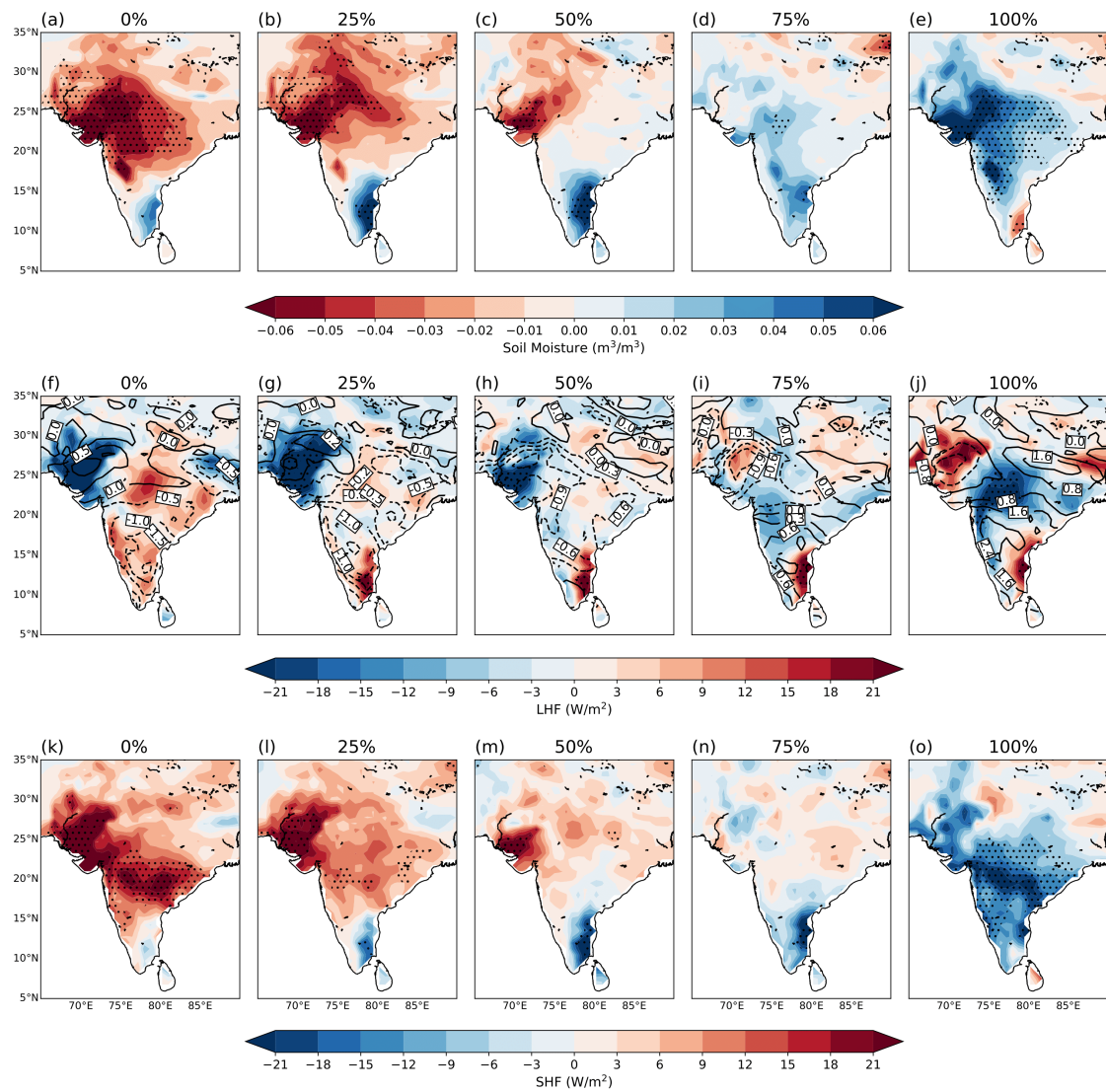


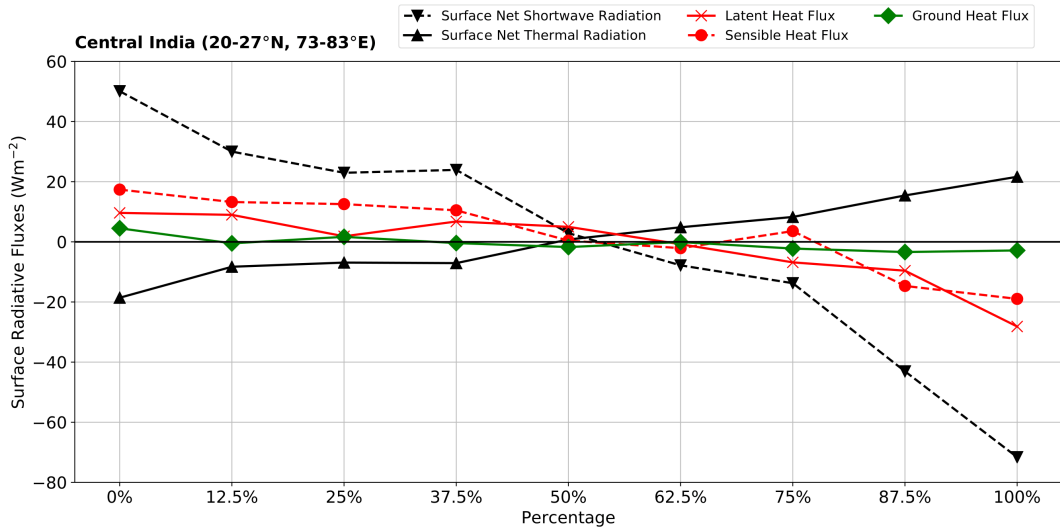
Figure 5.2: The break-to-active transition composites of (a-e) soil moisture anomalies, (f-j) latent heat flux anomalies overlaid with 10m total wind speed anomalies and (k-o) sensible heat flux anomalies. The fluxes are defined as positive upwards. The labels 0% and 100% represents the break and active phase mid-point, respectively, while labels 25%, 50% and 75% represents the transition phase. Additionally, the stippling represents significance at the 95% confidence level using a Student's T-test.

In order to understand the role of intraseasonal soil moisture variability in the break-to-active transition, it is important first to explore how basic land surface variables

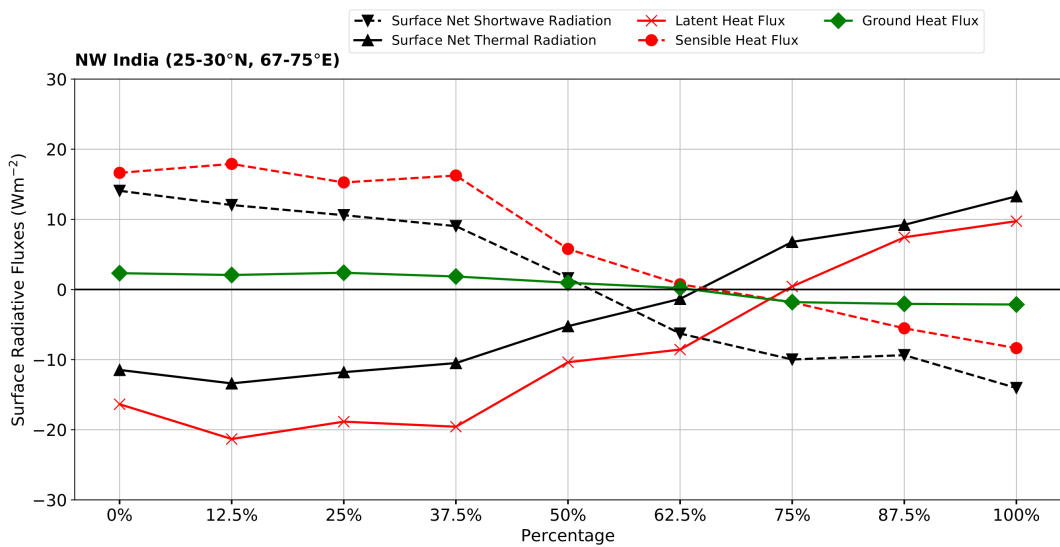
evolve during the transition, notably the relationship between soil moisture anomalies and changes in the surface turbulent fluxes. The JJAS climatology of soil moisture available for potential ET over India is illustrated in Fig. 5.1. Regions of climatologically wet soils (in the range of $0.35\text{-}0.60\text{ m}^3/\text{m}^3$) can be found over central India, the Western Ghats and northeastern India, which are associated with the distribution and progress of the summer-mean monsoon rainfall (Nayak et al., 2018; Varikoden and Revadekar, 2018). In contrast, dry summer-mean soils ($<0.15\text{ m}^3/\text{m}^3$) are located over northwestern and south India. These distributions in soil moisture are consistent with those in Nayak et al. (2018) using satellite observations, although the magnitude in this study is slightly larger by approximately $0.10\text{ m}^3/\text{m}^3$.

Next, the break-to-active composite anomalies of soil moisture, LHF and SHF are shown in Fig. 5.2. In the mid-point of the break phase, the soil moisture anomalies (Fig. 5.2a) are negative (approximately $-0.06\text{ m}^3/\text{m}^3$) throughout most of the Indian subcontinent except for southern India. The transition (Fig. 5.2b-d) is marked by the progressive increase in soil moisture content, starting from southeastern India and propagating northwest towards NWI. Subsequently, the mid-point of the active phase (Fig. 5.2e) is associated with increased soil moisture over much of India and reduced soil moisture over southern India, on the lee-side of the Western Ghats. The soil moisture pattern is consistent with the rainfall variability during the break-to-active transition shown in Chapter 3 (see Fig. 3.4) and in previous studies over India (Krishnamurthy and Goswami, 2000; Rajeevan et al., 2006). It is worth pointing out that the soil over northwestern India is climatologically dry, while the soil moisture over central India is climatologically wet (Seneviratne et al., 2010; Pangaluru et al., 2019) as shown in Fig. 5.1. As such, the large, positive soil moisture anomalies over the NWI region during the active phase could be attributed to the climatologically drier soil (i.e., saturation deficit). Conversely, the soil moisture content over CI is already high, which requires less moisture absorption before reaching saturation. Therefore, in the absolute sense, the total soil moisture over CI is considerably higher than NWI.

In Fig. 5.2f, the LHF (or ET) is characterised by negative anomalies over NWI and northeastern India along with positive anomalies over CI during the break. The LHF anomalies are associated with the variations in the net solar radiation received at the surface, as shown by the area-averaged radiation budget in Fig. 5.3. The radiation budget consists of surface net shortwave radiation (black dashed line), surface net thermal radiation (black solid line), LHF (red solid line), SHF (red dashed line) and the ground heat flux (green solid line) as residual. The LHF anomalies over CI in Fig. 5.3a are associated with strong surface net solar radiation. Combined with stronger heating at the surface and the soil being climatologically moist over this region (despite the drying anomalies), the ET from the soil is thus enhanced. The increased ET despite weakening surface wind speeds further suggests a strong control of



(a) Central India



(b) Northwestern India

Figure 5.3: The radiation budget over (a) central India (20-27°N, 73-83°E) and (b) northwestern India (25-30°N, 67-75°E) during the break-to-active transition. The radiation budget terms are surface net shortwave radiation (SSR), surface net thermal radiation (STR), surface latent heat flux (LHF), surface sensible heat flux (SHF) and the ground heat flux (G) as residual. The radiation budget was calculated using ERA-Interim/Land reanalysis for 1979-2010. The fluxes are defined as positive upwards. Units: Wm^{-2} .

ET by the available energy at the surface. Subsequently, the anomalies weakened during the transition phase (in both Fig. 5.2g-i and Fig. 5.3a), and the signs reversed at the mid-point of the active phase in Fig. 5.2f, which similarly is linked to the reduction in surface net solar radiation. Over the NWI region, the distribution of ET is associated with the soil moisture anomalies such that negative (positive) LHF anomalies are linked to dry (wet) soil during the break phase, while positive LHF anomalies are associated with wet soils during the active phase (see both Fig. 5.2g-i and Fig. 5.3b). The weak ET during the break over NWI in

the presence of strong net surface solar radiation (Fig. 5.3b) also further suggests that the availability of soil moisture governs ET and not surface energy availability.

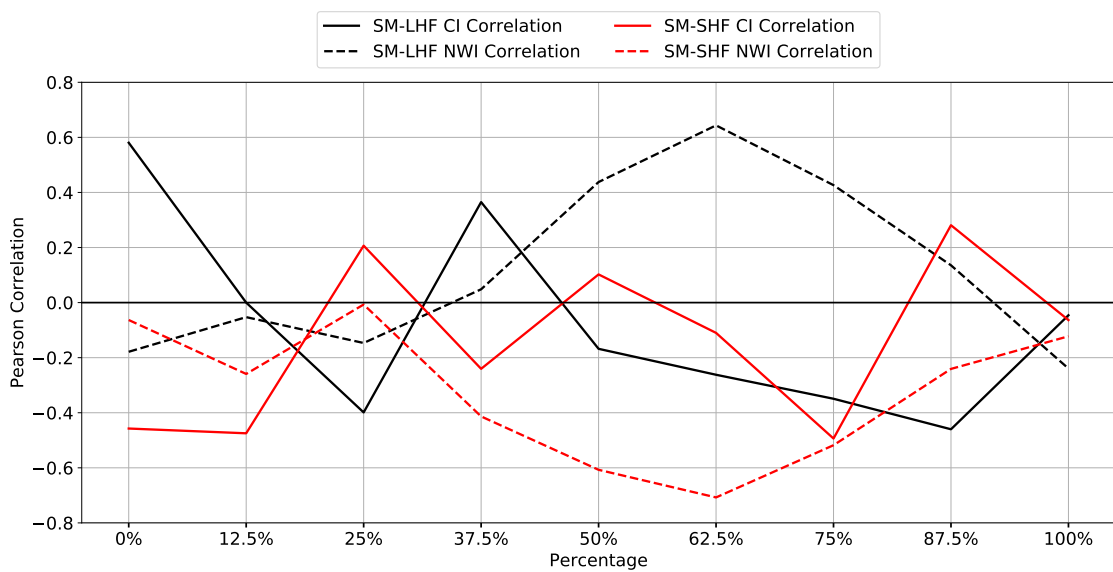


Figure 5.4: The Pearson's correlation across the 19 composite events between soil moisture and LHF (black) and between soil moisture and SHF (red) averaged over central India (solid line) and northwestern India (dashed line) in the composite break-to-active transition. The labels 0% and 100% represent the mid-point of the break and active phase, respectively, while labels 25%, 50% and 75% represent the transition phase.

Therefore it is clear that during the break-to-active transition, there are two distinct regimes over the Indian subcontinent which may influence the LAC: a moisture-limited regime over NWI and energy-limited regime over CI. It is evident that in the moisture-limited regime, ET is strongly controlled by the availability of soil moisture. These characteristics can be clearly demonstrated by the correlations between SM and LHF (black dashed line in Fig. 5.4). It is observed that the correlation is increasingly positive towards the active phase, which implies that the increase in soil moisture increases LHF. As discussed earlier, NWI is inherently a dry region; thus, the moisture received at the surface by increasing precipitation is evaporated even as the surface net solar radiation is reduced (Fig. 5.3b).

In contrast, the energy-limited regime over CI shows that reduced surface net solar radiation anomalies over CI limit ET towards the active phase (Trenberth et al., 2009). As shown by the correlation across the 19 composite event between SM and LHF over CI (solid black line in Fig. 5.4), the negative correlation towards the active phase suggests that the increase in SM is correlated with decreasing LHF at the surface. The reduction in surface radiation is likely due to the increase in cloud cover during the active phase, which can be inferred from the negative OLR anomalies over India during the active phase as previously presented in Fig 3.5. Furthermore, studies by Wang et al. (2015b) and Chakravarty et al. (2018) have shown that the active phase is dominated by convective clouds over much of CI, which reduces the amount of

incoming shortwave radiation, thereby limiting the energy available for ET.

For SHF, positive anomalies dominate during the break phase over India, especially in CI and NWI (Fig. 5.2k), where the rainfall and soil moisture anomalies are weak (Fig. 5.2f). These anomalies are also observed in the radiation budget, represented by the red dashed line in Fig. 5.3a. Subsequently, during the transition towards the active phase (Fig. 5.2o), the SHF anomalies decrease over both NWI and CI. Soil moisture may also affect SHF anomalies indirectly since it controls the partitioning of available energy between SHF and LHF. This is most apparent over the soil moisture-limited regime over NWI. For example, low precipitation during break conditions limits soil moisture availability, leading to decreased LHF and increased SHF (Seneviratne et al., 2006, 2010). Halder et al. (2018) also suggest that the negative correlation between soil moisture and SHF over NWI (red dashed line in Fig. 5.4) shows that the fluxes are strongly controlled by soil moisture variations (i.e., soil moisture-limited regime). The converse is observed during the active phase, such that the increase in soil moisture increases LHF at the expense of SHF. This contribution is observed in the energy-limited regime over CI. Subsequently, in the active phase, the SHF anomalies decrease due to the lack of surface heating due to the decrease in surface net solar energy. Therefore, the soil moisture-evapotranspiration coupling over CI and NWI discussed here are in agreement with the general findings in the GLACE experiment (Koster et al., 2004, 2006) showing that India is in a transitional zone between dry and wet climate which suggests that it is a “hot-spot” region of strong LAC.

5.4 Thermodynamics of the break-to-active transition over India

Vertical cross-sections from the northwest to the southeast region of India are examined to analyse the evolution of several thermodynamic variables during the break-to-active transition. The transect illustrated in Fig. 5.1 crosses over CI and NWI. The transect is selected based on the results from §5.3 which described strong links between soil moisture and surface turbulent fluxes. These fluxes may potentially feedback into the planetary boundary layer, leading to instability of the atmospheric layer. Additionally, the transect is chosen such that it spans several different hydro-climatic zones such as NWI and CI, but also over southeast India which is climatologically dry, but the signs of rainfall anomaly between active and break events is different to the rest of India.

5.4.1 Mixing ratio anomalies

The vertical sections of mixing ratio anomalies are shown in Fig. 5.5. In the break phase (Fig. 5.5a), a wedge of dry anomalies (<-2.0 g/kg) near the 700 hPa level is seen in

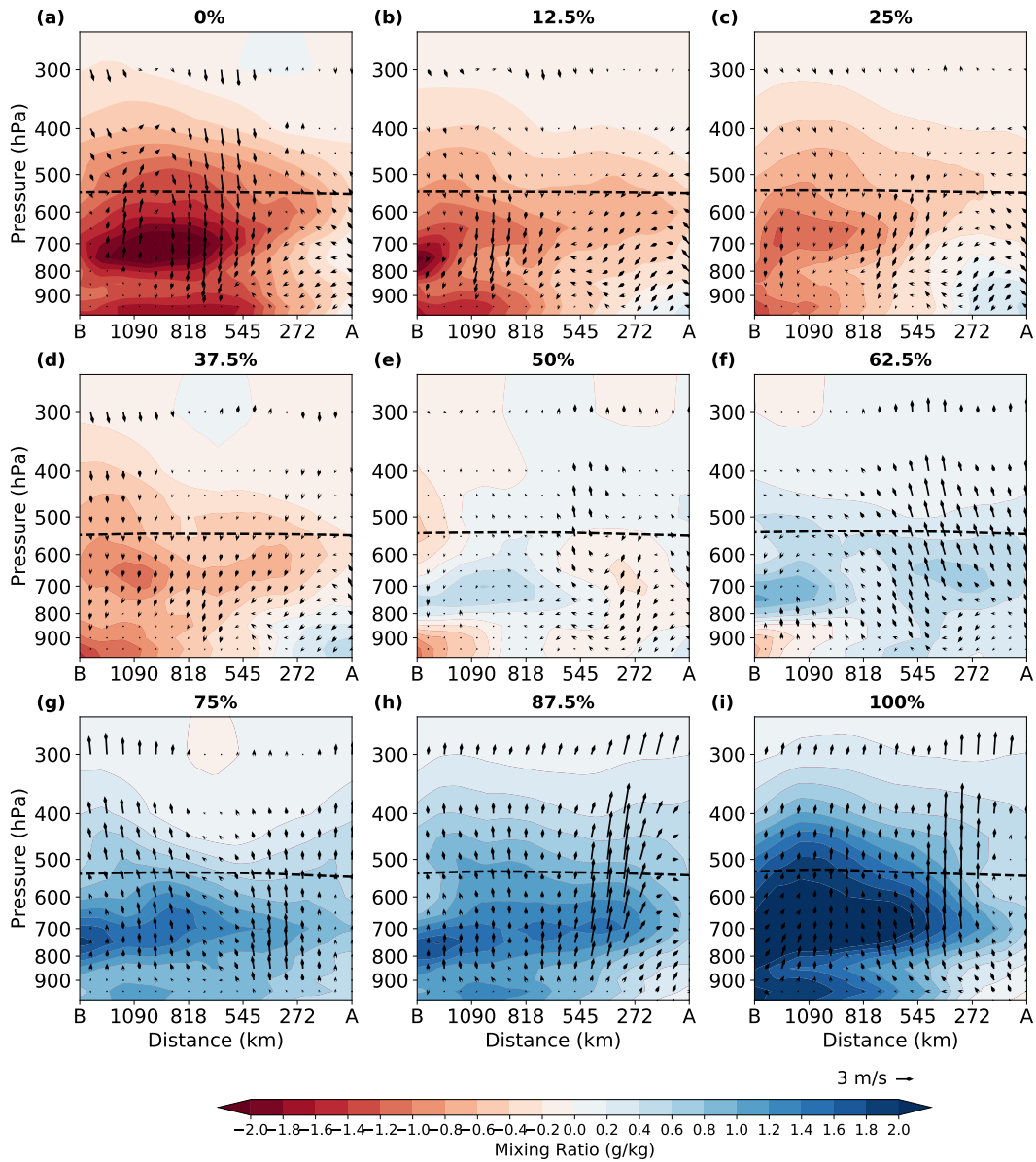


Figure 5.5: The northwest (B) to southeast (A) vertical cross-section of mixing ratio anomalies (g/kg) and wind anomalies (m/s) during the break-to-active transition. Data were obtained from ERA-Interim reanalysis for the period 1979-2010. The wind vectors represent horizontal winds relative to the transect line shown on Fig. 5.1, such that a horizontal vector represents flow parallel to the transect. The dashed lines marks the freezing level, $T=0^{\circ}\text{C}$.

the northwest and weakens at all levels towards the southeast. This is consistent with the deficient rainfall over CI and NWI at the break phase. As the break transitions, the dry anomalies in the southeast are being eroded and replaced by moist anomalies (≈ 0.4 g/kg) from below as seen in Fig. 5.5b-c. These moist anomalies increase towards central India in the northwestward/northward direction, especially at low-levels. Prior to the active phase (Fig. 5.5f-g), the dry anomalies in NWI are additionally being eroded by the moisture anomalies. As the active phase is initiated over India Fig. 5.5g-i, the moist anomalies over NWI deepens in the vertical, breaching the freezing level at approximately 500 hPa. Furthermore, the

moist anomalies (>2.0 g/kg) extend further inland towards central and southeastern India. The increase in moist anomalies is generally accompanied by stronger vertical winds, which indicate enhanced convective activity during the transition to the active phase. The moisture variations in Fig. 5.5 resembles the mixing ratio composites in Fig. 4.2, such that the initiation of the active phase and the subsequent rainfall is associated with the increase in moisture anomalies.

5.4.2 Equivalent potential temperature anomalies

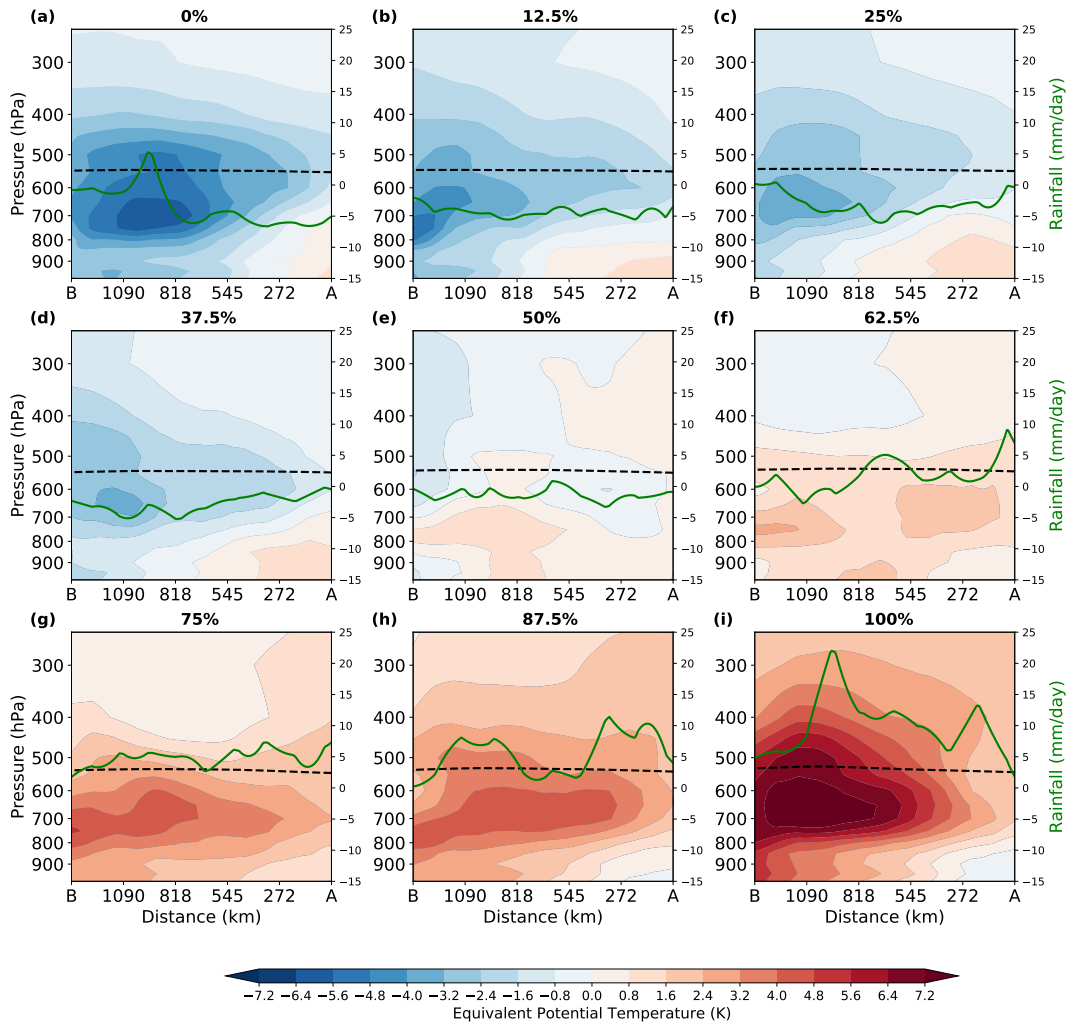


Figure 5.6: Similar to Fig. 5.5 but for equivalent potential temperature anomalies. The green line represents the rainfall anomalies obtained from the IMD gridded rainfall dataset.

Next, the composite equivalent potential temperature (θ_e) anomalies are shown in Fig. 5.6. Evidence of anomalous low-level instability associated with the increase in moisture over southeast India after the break phase (Fig. 5.6b-c) is observed. However, these anomalous instabilities are weak and do not suggest the presence of strong convective activity as inferred from the vertical wind vectors in Fig. 5.5b-c and by the rainfall anomalies (solid green line) in

Fig. 5.6.

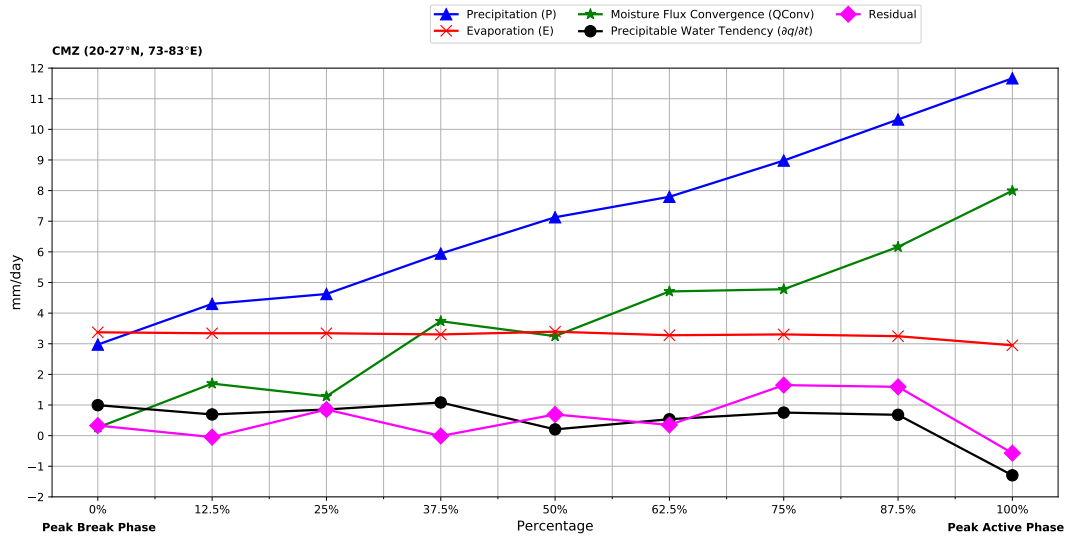
During the transition to the active phase, the layer of cooler and drier air is continuously eroded from below by moist anomalies over southeastern India (Fig.5.6b-e). However, this erosion and the increase in maximum θ_e anomalies (Fig.5.6d) are only limited to the southeast over a shallow depth (surface to 800 hPa) early in the transition. As a result, any further growth of instability over southeastern India may be inhibited by the lack of moisture at the boundary layer and the anomalous weak stable layer in the upper-troposphere (Fig.5.6d). In addition, an anomalous warm and unstable layer forms over NWI at low-levels (surface up to 700 hPa) as shown in Fig.5.6e-f. Following this, the cooler θ_e are completely replaced by the anomalous unstable layer in the vertical, and the enhanced rainfall anomalies appear first over southeastern India and subsequently throughout CI and NWI. The positive rainfall anomalies are stronger over CI compared to NWI. Thus, it is apparent here that moisture and instability are associated with the growth of instability and convective activity, which leads to the revival of the active phase, similar to those chapter 4 (Fig. 4.2 and Fig. 4.3).

In Chapter 4, it was discussed that the moisture anomalies breaching the freezing level are important for inducing additional instability in the mid-troposphere over the NBoB. A similar distribution of the moisture anomalies over the Indian subcontinent are also observed (Fig. 5.5e-f) at approximately 550 hPa. The detrainment of moisture from convective clouds occurs preferentially at the freezing level (Johnson et al., 1996). In the composite, the deepening in mixing ratio anomalies towards the active phase may be due to deeper convection, as supported by the vertical wind vectors and rainfall anomalies, resulting in deeper detrainment and further instability. Results from Parker et al. (2016) using reanalysis dataset and Menon et al. (2018) using model simulations further supports this result.

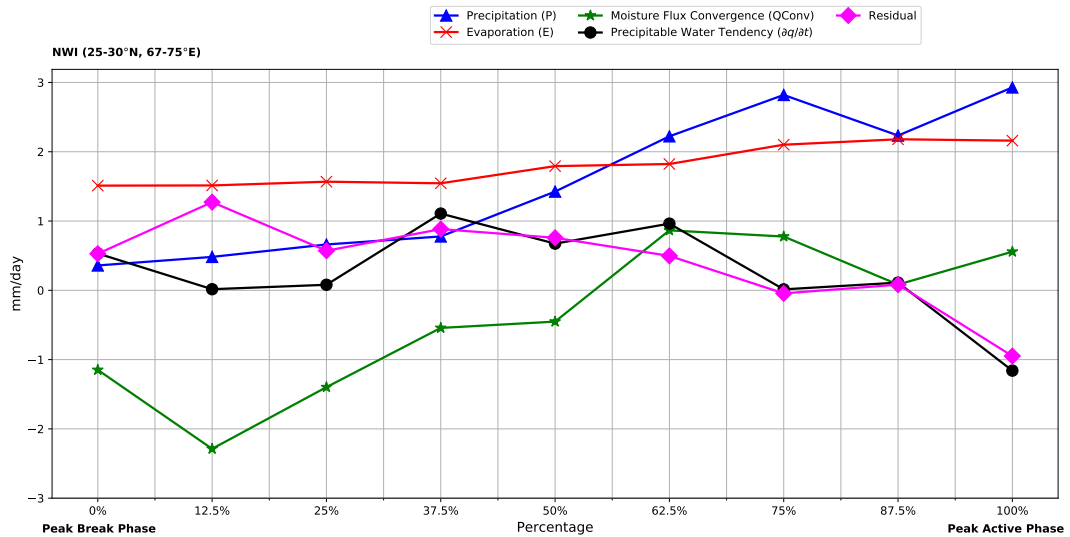
5.4.3 Moisture budget

In the previous section, the thermodynamics of the break-to-active transition were analysed. The composites revealed that the transition to the active phase is associated with increased moisture and instability anomalies over India. In this section, the moisture budget in regions where these significant moisture anomalies were observed is investigated to further identify the potential source(s). In Fig. 5.7, the moisture budget over (a) CI and (b) NWI are shown.

Quantitatively over CI (Fig. 5.7a) during the break phase, the area-averaged precipitation (solid blue line) is approximately 2.9 mm/day, and the moisture convergence (solid green line) is approximately 0.6 mm/day, while the evaporation (solid red line) is 3.4 mm/day. The weak convergence and rainfall over CI are characteristic of the break phase and consistent with previous observations. Towards the active phase, the significant increase in precipitation (11.6



(a) Central India



(b) Northwestern India

Figure 5.7: The moisture budget over (a) central India (20-27°N, 73-83°E) and (b) northwestern India (25-30°N, 67-75°E) during the break-to-active transition. The moisture budget terms are precipitation (P), evaporation (E), vertically-integrated moisture flux divergence ($\nabla \cdot \bar{u}q$), column-integrated moisture tendency ($\partial q/\partial t$) and the residual. The moisture budget was calculated using ERA-Interim reanalysis for 1979-2010. Note the difference in magnitude of the moisture budget between central India and northwestern India. Units: mm/day.

mm/day) is supplied by the strengthening of moisture convergence (8.0 mm/day).

In contrast, the evaporation does not appear to be important in determining the changes in precipitation as it remains relatively constant throughout the break-to-active transition. In short, the changes rainfall is strictly associated with the changes in moisture convergence. However, in terms of the northward/northwestward propagation of rainfall, evaporation is equally important as moisture convergence, but only up to the mid-transition phase. The contribution by evaporation is larger than (at 12.5% and 25%) or equals to (at 37.5% and

50%) the contribution from moisture convergence during the transition phase. Thus, over CI, evaporation is stronger than and equals the contribution from moisture convergence up till the mid-transition.

Therefore, moisture convergence is essential for the increase in rainfall during the transition such that it accounts for about 69% of the maximum active phase rainfall (at the mid-point of the active phase) and the remainder from evaporation. But in the context of the supply of moisture for the transition to the active phase, which was identified in §5.4, evaporation contributes similarly to moisture convergence over central India. The stronger evaporation in the early stages of the transition is consistent with the energy-limited regime over CI, such that strong heating at the surface, enhances evaporation as depicted in Fig. 5.2f–h.

In contrast to CI, the moisture budget terms over NWI (Fig. 5.7b) are weaker. For instance, the magnitude of precipitation and evaporation are 0.4 mm/day and 1.5 mm/day during the break, respectively. Additionally, moisture divergence (-1.1 mm/day) dominates during the break through the mid-transition phase over NWI.

The results for NWI reveal that the atmospheric moisture in the transition to the active phase is mainly supported by evaporation, as it is consistently larger than moisture convergence. In fact, evaporation increases towards the active phase, which is consistent with LHF composites in Fig. 5.2i–j, affirming that NWI is in a moisture-limited regime. The increase in precipitation enhances the soil moisture and correspondingly strengthens evaporation. The evaporation subsequently feeds the precipitation, suggesting positive feedback between soil moisture and precipitation over NWI.

Unlike evaporation, moisture convergence is only observed over NWI just before the mid-point of the active phase at 62.5%, in contrast to CI, which showed significant moisture convergence after the break (12.5%). This indicates that moisture convergence contributes to precipitation in the later stages of the transition, but is still far less critical as a moisture source than evaporation. Furthermore, the decrease in moisture divergence between from the break to 62.5% may also strengthen the atmospheric moistening and thus contributing to the precipitation.

In conclusion, evaporation contributes about 75% to the maximum active phase rainfall, while moisture convergence contributes only up to 25%. The results suggest that evaporation is the dominant contributor of moisture for the northward/northwestward propagation of rainfall during the break-to-active transition over NWI. The contribution of moisture convergence becomes increasingly important but only after the mid-point transition. In contrast, evaporation and moisture convergence contribute similarly over CI.

5.5 Land-atmosphere coupling strength

In previous sections, we have shown a strong relationship between SM and ET during the break-to-active transition over India (§5.3.1). It was revealed that NWI is in a soil moisture-limited regime, whereby the availability of SM controls ET. In contrast, CI is in an energy-limited regime such that net surface energy limits ET. While it was shown that there is evidence of feedback between the surface and atmosphere, it is important to quantify the coupling to demonstrate the LAC strength. Dirmeyer (2011) suggested that a positive correlation in the surface state (terrestrial leg), for example, between soil moisture and evaporation, as shown in Fig. 5.4 is a necessary, but insufficient condition for the land surface to influence the atmosphere. The LAC may break down if the atmospheric leg of the link is weak. With respect to the strength of the coupling, a significant correlation between soil moisture and surface fluxes can exist in regions where the impact of LAC is, in fact, weak, due to small surface flux changes across a significant variation in soil moisture. Thus, these limitations are addressed by quantifying the LAC strength based on the TCI and ACI presented in §5.2.3 by taking into account the correlation and the variability (i.e., standard deviation).

The TCI, representing the variations of LHF to SM during the break-to-active transition, is shown in Fig. 5.8a–e. The evolution of the TCI shows similarities with the pattern of “hot spots” of strong LAC from Koster et al. (2004, 2006). This is indicated by regions of large positive values, specifically over NW India ($> 25 \text{ W/m}^2$) associated with a significant positive correlation between soil moisture and LHF, and the large variability of LHF. This is expected since NWI is located in a transitional zone between dry and wet climates. Additionally, the positive TCI suggests that the ET is sensitive to soil moisture variations (i.e., a soil moisture-limited regime). The coupling remains strong throughout the transition, although a slight weakening in TCI is observed in Fig. 5.8d ($8\text{--}10 \text{ W/m}^2$) just before the active phase due to weaker correlations.

In contrast, the TCI over most of CI is negative, except for patches of positive TCI over southeastern India. The negative coupling over CI is due to the negative correlation between soil moisture and ET, resulting in negative feedback. The negative feedback indicates that an increase in soil moisture leads to a decrease in ET. This result infers that it is not soil moisture, but other factors such as net surface radiation (i.e., energy-limited regime as shown in Fig. 5.3) or atmospheric moisture that limits ET over CI. The revival of the active phase is linked with strong convection and increasing cloudy conditions which limit the available energy at the surface. Thus, during the break-to-active transition, NWI is continuously within a soil-moisture limited regime while CI is predominantly in an energy-limited regime; these regimes do not substantially change during the break-to-active transition.

The corresponding ACI showing the variations of latent heat flux to 2m specific humidity

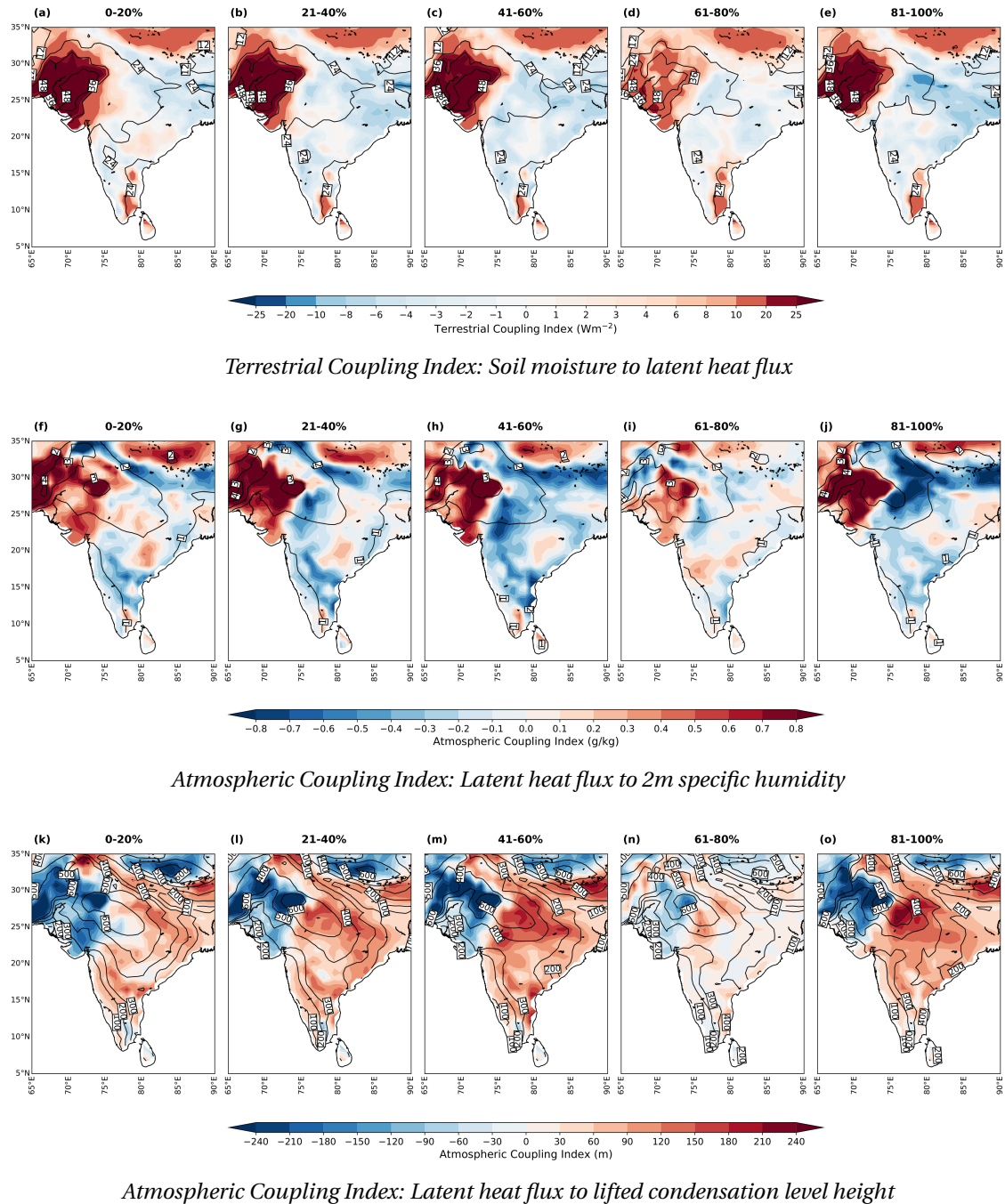


Figure 5.8: (a-e) Terrestrial coupling index (TCI) for soil moisture and latent heat flux (LHF), with positive LHF values representing upward fluxes and (f-j) the corresponding atmospheric coupling index (ACI) based on latent heat flux to 2m specific humidity (2mQ) during the break-to-active transition. Panel (k-o) shows the ACI for lifted condensation level height (LCL). Units are in Wm^{-2} , g/kg and m , respectively. The numbered contour line shows the standard deviation of LHF, 2mQ and LCL respectively.

(2mQ) is illustrated in Fig. 5.8f–j. The ACI over CI shows a direct relationship between LHF and 2mQ, similar to its TCI counter-part. The increase in LHF over NWI is associated with the increase in 2mQ, suggesting strong feedback during the break-to-active transition. However, a weakly negative correlation dominates over CI which suggests that the evaporation is being counteracted by horizontal moisture convergence, which was shown to be strong over CI in the

moisture budget analysis (Fig. 5.7a). Additionally, the negative correlation may also be limited by available surface energy, as shown by the TCI composites. Thus, the weak correlation suggests that over the CI, near-surface humidity does not control LCL height.

Next, the ACI between LHF and LCL height is analysed. A negative correlation between ET and LCL is indicative of positive feedback: the increase in ET results in a decrease in LCL height. Subsequently, a lower LCL height suggests higher precipitation, and thus, providing more water for ET. For example, the negative correlation between ET and LCL is observed over NWI during the break-to-active transition (Fig. 5.8k–o). The results suggest that the increase in LHF (as shown by the LHF composites in Fig. 5.2) is associated with a decrease in LCL height. Additionally, the strong negative correlation, combined with large variability over NWI suggest a strong LAC coupling over NWI. This is consistent with the availability of moisture over NWI (i.e., soil moisture-limited regime), which may increase evaporation which lowers the LCL. In contrast, the correlation is positive over CI. It is possible that the positive ET–LCL correlation may be attributed to weaker ET and the subsequent higher LCL due to reduced surface solar radiation at the surface to support ET. Furthermore, the negative correlation between LHF and 2mQ may also increase the LCL height.

Collectively, the TCI and ACI in Fig. 5.8 revealed two crucial aspects of the LAC over India during the break-to-active transition: Firstly, over NWI, strong coupling exists between the land surface and the atmosphere. In the terrestrial segment (TCI), the soil moisture-limited regime implies that moisture is readily evaporated, as shown by the positive correlation between soil moisture and LHF. As the LHF increases, 2mQ increases which lower the LCL height. The link between the terrestrial and the atmospheric segment suggest that LAC plays a role in supporting the transition towards the active phase over NWI.

Secondly, the TCI and ACI reveal the lack of strong LAC over CI. In the terrestrial segment, a significant portion of CI shows negative TCI during the transition, which is associated with the negative correlation between soil moisture and LHF. Soil moisture is plentiful over CI, but the evaporation is limited by reduced net surface radiation due to increasingly cloudy conditions towards an active phase. As a consequence, evaporation is suppressed and does not influence the variability of 2mQ and LCL. Therefore, the land surface state over CI may have a weak effect on the atmosphere during the break-to-active transition. This suggests that other external factors may also be responsible for the revival of the active phase over CI. The results from the moisture budget analysis confirm that moisture convergence is strong during the transition phase; however, ET still does play a role. Thus, ET may play a supporting role, together with moisture convergence in contributing to the atmospheric moistening in the break-to-active transition.

5.6 Summary and Discussion

In this chapter, I have examined the break-to-active transition over the Indian subcontinent to understand the evolution of the land surface state, thermodynamics and strength of LAC in the revival of the active phase. The results show two distinctive regions; CI and NWI, which showed different land surface properties during the break-to-active transition. I also found that the transition over CI and NWI is governed by different mechanisms at the surface.

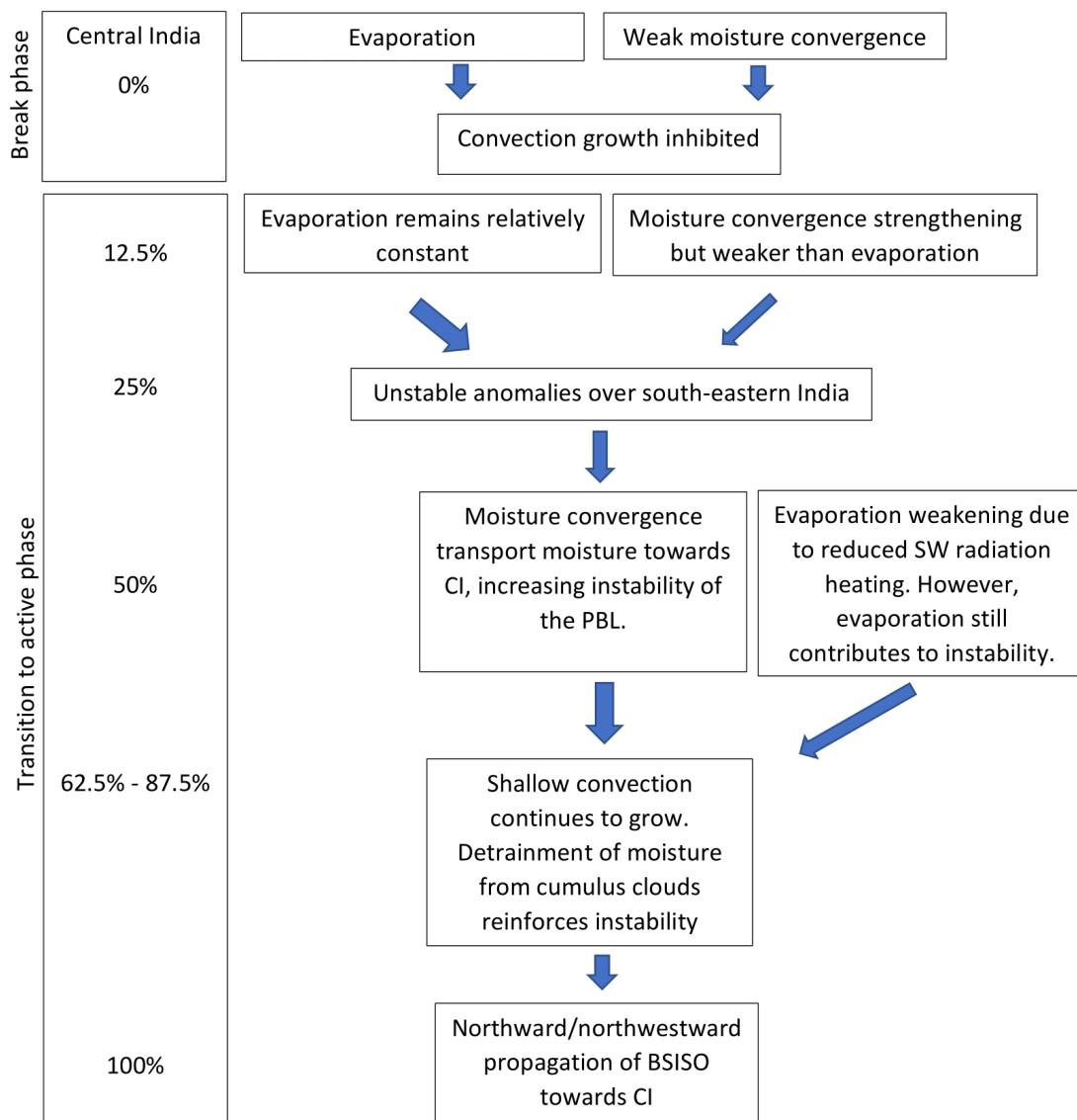


Figure 5.9: Schematic for the break-to-active transition mechanisms over central India based on the results in this chapter. Size of the arrows depicts the strength of mechanism.

By combining the results in this chapter, we may now infer and summarise a possible mechanism to explain the evolution of the break-to-active transition over India based on the schematics in Fig. 5.9 and Fig. 5.10 for both CI and NWI respectively. In the mid-point of the break and early stages of the transition, ET is strong over central India and southeastern

India which are in an energy-limited. In contrast, ET is weak over NWI and is located in a soil moisture-limited regime. Initially, the strong ET over northwestern India provides moisture for atmospheric moistening. However, this moistening is not sufficient to create instability and convection. Furthermore, weak low-level convection over southeastern India prevents any vertical advection of moisture. Subsequently, the moisture convergence increases, which transports moisture from the NBoB towards the Indian subcontinent and further moistens the lower troposphere. The increase in low-level moisture (Fig. 5.5) by both evaporation and moisture convergence is thus associated with enhanced instability (Fig. 5.6). The instability results in the formation of convection during the mid-transition phase, and further deepening of the positive θ_e anomalies in the vertical. Additionally, the formation of clouds breaching the freezing level may also cause moisture detrainment from the cloud (Johnson et al., 1996), and enhancing mid-level moisture and subsequently, convection. This detrainment process was also hypothesised in Parker et al. (2016) and Menon et al. (2018) in their studies of the advancing monsoon onset.

Subsequently, the enhanced evaporation ahead of the active convection over CI further increases the moisture anomalies and instability towards the northwest. The atmosphere destabilises, and the active convection propagates northwestward/northward. The evaporation from the land surface over CI then becomes limited, despite the availability of soil moisture due to low surface net radiation availability (Fig. 5.3), as the strengthening convection reduces surface solar radiation. Thus, the local LAC over central India is perhaps more significant early in the transition but becomes weaker thereafter. The northwestward/northward propagation of convection and precipitation over CI is then supported by the strengthening of moisture convergence.

Next, evaporation of moisture from the surface is enhanced over NWI, possibly, due to antecedent soil moisture availability (from the previous active phase). As the convection progresses, the enhanced precipitation feeds back to the surface, increasing soil moisture and subsequently enhancing ET. LAC over NWI plays an important role during this period, as the positive feedback between evaporation and near-surface humidity leads to an increase in moisture and instability in the planetary boundary layer. This is noted in the TCI and ACI in Fig. 5.8. Unlike CI in which the break-to-active transition is influenced by moisture convergence with the support of LAC, my results suggest that the break-to-active transition over NWI is associated with strong LAC which is in agreement with Webster (1983).

Over NWI, a "hot-spot" region showed a positive feedback between soil moisture and precipitation (Pal and Eltahir, 2001). Despite NWI being climatically dry, antecedent soil moisture from the previous active phase provides the moisture necessary for evaporation during the transition from the break (Webster, 1983). My analysis of the LAC metrics shows that soil moisture-evaporation and evaporation-LCL coupling are the key processes that

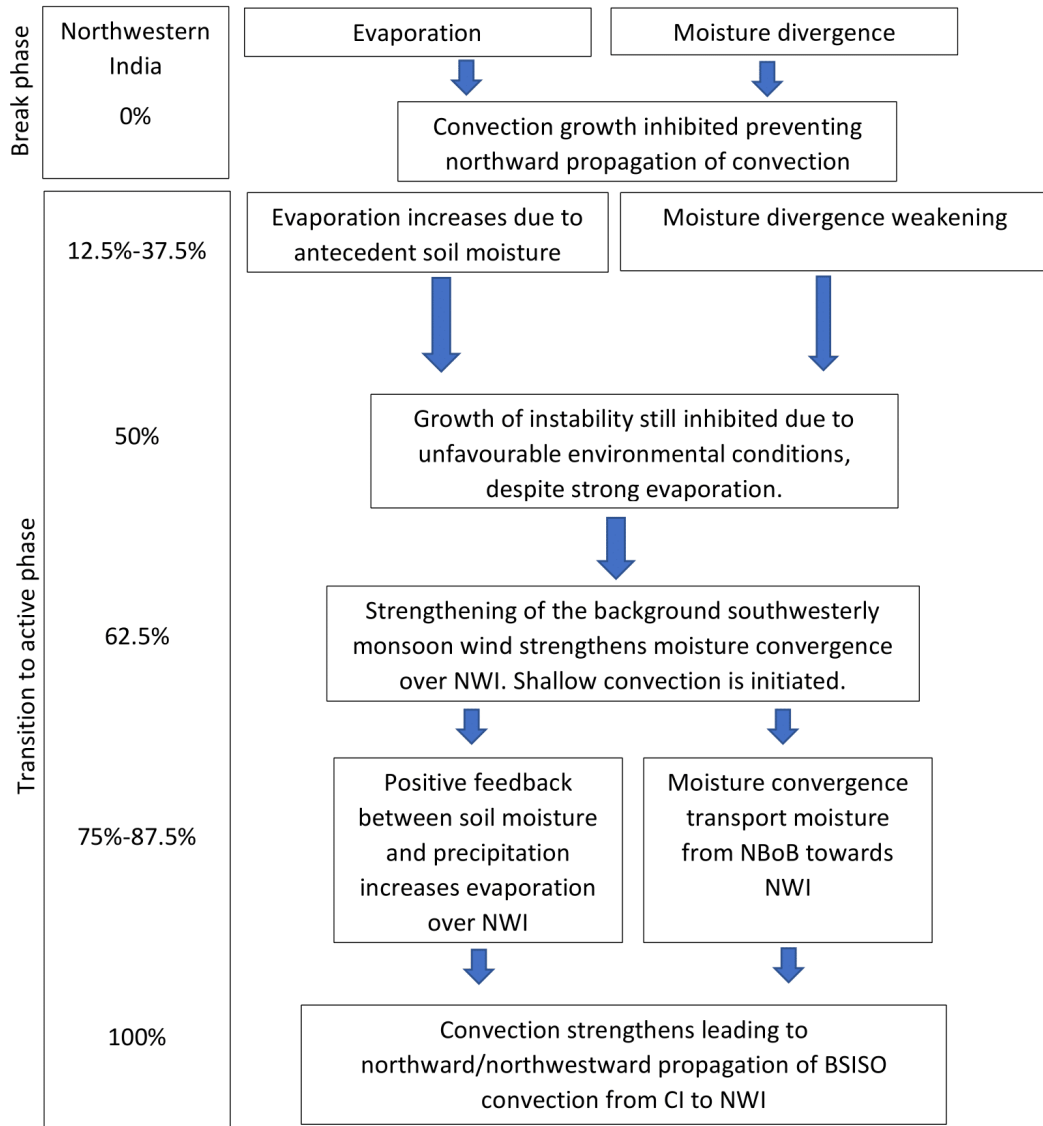


Figure 5.10: Similar to Fig. 5.9 but over north-western India.

determine the soil moisture-precipitation coupling. Zhu et al. (2009) investigated the role of antecedent soil moisture on the North American monsoon in a coupled land-surface model and found that wet pre-monsoon soil moisture leads to an increase in monsoon precipitation. They attributed their results to modulation of large-scale circulation and localised LAC by the soil moisture-precipitation feedback. Furthermore, Kutty et al. (2018) studied the role of soil moisture on influencing convective precipitation during the break phase using a WRF model. Their results showed that positive antecedent soil moisture anomalies lead to increased precipitation, highlighting the role of local LAC and similar to my results. One significant difference, however, is that their results suggest strong LAC over central India can influence rainfall. This is in contrast with my finding, which showed no significant LAC over CI based on reanalysis. Thus, the difference in results highlights the difficulty of their model to correctly represent LAC in the intraseasonal variability of the ISM. In addition, I have used

ERA-Interim/Land reanalysis to compute the LAC strength, which assimilates model outputs and observations. ERA-Interim/Land may be constrained by the availability of observations which may lead to uncertainties in my results.

Although this study has described the evolution of the break-to-active transition in terms of thermodynamics and LAC, there are still gaps in our understanding that needs to be answered. In particular, further understanding of the soil moisture-precipitation coupling in different soil moisture states is needed. For example, how does a drier (or wetter) than normal soil moisture over India during the break influence the LAC and SM-P feedback? These efforts would reveal how the speed or intensity of the northward propagation and the subsequent active phase varies with antecedent soil moisture during the break. This is important knowledge to have as stakeholders such as farmers are dependent on the timing of the active-phase rainfall. Moreover, future work should also identify how vegetation types; an important factor that influences the atmosphere and has been shown to have strong interaction with soil moisture, may influence the northward propagation (Mahmood et al., 2011). In addition, forecast of the intraseasonal variability over India should include irrigation effects as India is one of the most heavily irrigated regions in South Asia. Approximately 80-90% of the groundwater extracted is used for irrigation (Lee et al., 2009). Devanand et al. (2019) used the WRF model coupled to the Community Land Model version 4 to demonstrate that the intensity of rainfall over CI was associated with the increase in irrigation. They stress the importance of realistically representing irrigation practices in models in simulating the Indian monsoon as irrigation influences the terrestrial moisture transport through variations in the dynamic and thermodynamic feedbacks that subsequently influences the precipitation over India. Therefore, these efforts can be achieved by testing the sensitivity of the break-to-active transition (in terms of its timing and magnitude) in forecast models concurrently by modifying soil moisture, irrigation effect and vegetation-type. A better understanding of these processes may then improve the quality of seasonal-to-subseasonal forecasts in numerical models which depend strongly on model initialisation (Asharaf et al., 2011).

Chapter 6:

FORECASTING THE 2016 BREAK-TO-ACTIVE TRANSITION - THE ROLE OF AIR-SEA COUPLING

6.1 Purpose of the chapter

This chapter aims to respond to the final objectives of this thesis outlined in §1.2: (a) to identify the performance of the northward-propagating BSISO signal in numerical weather prediction (NWP) forecasts of the 2016 break-to-active transition in an uncoupled and coupled models and (b) if air-sea coupling improves the forecast of this event. In Chapter 4, it was shown through reanalysis datasets that there is variability in surface turbulent heat fluxes which may affect the break-to-active transition, associated with the northward propagating BSISO. These sea surface temperature-modulated fluxes precede the active phase and may influence low-level atmospheric stability and thus, the intraseasonal variability of convection. Furthermore, the sea surface temperature (SST) and rainfall showed a quadrature phase relationship, such that warm SST anomalies lead active phase rainfall by approximately 10 days. The SST variability suggests that atmosphere-ocean feedbacks exist during the break-to-active transition. However, the cause-and-effect relationship is impossible to diagnose based on observations alone; hence, modelling studies are required to reveal the importance of air-sea coupling. It was discussed in §2.3.2.3 that in previous studies, adding air-sea coupled processes in general circulation models (GCMs) improved the spatial and temporal patterns of the BSISO, as well as exhibiting a correct SST-rainfall phase relationship compared to uncoupled model simulations.

As discussed in Chapter 2, the northward-propagating BSISO over the tropics was initially

studied using atmosphere-only general circulation models (AGCMs) (Kemball-Cook et al., 2002; Waliser et al., 2003; Fu and Wang, 2004a; Klingaman et al., 2008a; Mandke et al., 2013). While the AGCMs in these studies demonstrated some form of northward propagation, the signals are usually weak and inconsistent. In practice, simulations in AGCMs are typically forced using SSTs derived from observations (satellite-derived and in situ) or forced by SSTs from their coupled model counterparts (Fu and Wang, 2004b; Ham et al., 2014). In AGCMs forced with observations, for instance, Klingaman et al. (2008a) showed that simulations using high-frequency daily SST variability demonstrated stronger intraseasonal variability of convection compared to those with 5-day means and monthly mean SST forcing. The improvements were attributed to a more realistic SST intraseasonal variability. However, the northward propagating signal was weak in the AGCM (except in the daily SST run), and it also failed to simulate the SST-rainfall phase relationship. Nevertheless, the weak northward-propagating signal in their study is not ascribed to the inaccurate SST-rainfall phase relation, but to the weaker magnitude of the SST variability forcing on monthly and sub-seasonal timescales. Meanwhile, in studies using coupled-model SSTs to force AGCM simulations, Fu and Wang (2004b) found better intraseasonal variability in rainfall anomalies when the AGCMs were forced with daily SSTs instead of the monthly mean. While the spatiotemporal evolution of the BSISO in the uncoupled simulations was comparable to the coupled simulation and observations, the amplitude, however, was approximately 20%-25% weaker. Yet, the fact that AGCMs are still able to simulate northward-propagating signals, albeit weaker compared to observations, suggests that the basic nature of the BSISO such as its oscillation and northward propagation may have its origins in the internal atmospheric variability (Jiang et al., 2004).

Given the inherent inaccuracy in simulating the spatio-temporal northward-propagating BSISO in AGCMs, previous studies have suggested that coupled models may improve the errors exhibited by these AGCMs (Kemball-Cook et al., 2002; Roxy and Tanimoto, 2007; Wang et al., 2009; Sharmila et al., 2013). For example, Fu and Wang (2004a) showed improvements in the three-dimensional (vertical and horizontal) structure of water vapour, as well as the strength and propagation characteristics associated with the BSISO. Additionally, coupled models were able to demonstrate a realistic SST-rainfall phase relationship between SST and precipitation, such that SST leads rainfall by about 10 days. Zheng et al. (2004) suggest that the improved phase relationship in coupled models lead to the improved simulations of the intraseasonal northward propagation. Better simulations in the coupled model can be traced to atmosphere-ocean coupling, leading to a better representation of the SST and LHF variability, which is connected to atmospheric variability. In turn, the atmosphere can then drive oceanic variability and influence the SSTs. These results suggest that air-sea coupling improves the simulation of the BSISO and that it is essential to generate a robust

northward-propagating signal, which is otherwise weak in AGCMs with low-frequency SST forcing (e.g., monthly means) (Rajendran et al., 2004; Fu and Wang, 2004b).

While air-sea coupling improves the simulations of the BSISO, it is still unclear if it is an essential mechanism driving northward propagation, since it has been demonstrated that AGCMs with high-frequency daily SSTs may also simulate the characteristics of the BSISO. Implicitly, this suggests that the northward propagation of the BSISO may have an internal atmospheric dynamics origin. Instead, air-sea interaction may be important in controlling the amplitude and frequency of the BSISO. Furthermore, most of the previous studies have designed their experiments to examine the BSISO in longer-term climate models. In fact, very few have studied the active and break phases, specifically, the transition from one phase to another on intraseasonal timescales. Therefore, it is crucial to understand the influence that air-sea coupling has on governing the transition to an active or break phase.

In this study, the forecasts of the 2016 break-to-active transition case study, identified in Chapter 3, from three different configurations of the Met Office NWP model at high horizontal resolution are analysed. The three models consist of a single uncoupled model and two coupled models. The primary interest is to determine the role of air-sea coupling in influencing the forecast performance of the break-to-active transition at varying forecast lead times. Thus, by comparing the uncoupled and coupled models, this analysis will assist with determining whether air-sea coupling is an important mechanism in improving the prediction skill of short-scale processes such as the break-to-active transition, and in general the northward propagating BSISO, or if it plays (if any) a supporting role. Therefore, this chapter is organised as follows. The three models and observational data are described in §6.2. In order to verify the transition event, the rainfall during the break-to-active transition from the models is compared against observations (§6.3). Subsequently, northward propagation in the models is examined (§6.4). Next, the role of air-sea coupling in the prediction of the 2016 transition event is diagnosed in §6.5. The thermodynamics of the transition in the forecasts are then evaluated in §6.6. In §6.7, the key findings and conclusions are summarised.

6.2 Model and data

6.2.1 Model description

Three configurations of the Met Office atmosphere-only model are summarised in Table 6.1. Further description of each model is presented in the following subsection.

Model	Type	Atmospheric component	Oceanic component
NWP	Atmosphere-only	GA6.1	x
KPP	Coupled	GA6.1	MC-KPP
NEMO	Coupled	GA6.1	NEMO

Table 6.1: The forecast models used for the 2016 break-to-active transition prediction. GA6.1 = Met Office Global Atmosphere 6.1; NEMO = Nucleus for European Modelling of the Oceans; MC-KPP = Multi-Column K Profile Parameterisation.

6.2.1.1 The atmosphere-only model

The atmosphere-only forecast is based on the Met Office Global Atmosphere 6.1 numerical weather prediction model (GA6.1, hereafter “NWP”) configured on the N768 horizontal grid (0.23°x 0.16°). The Even Newer Dynamics for General atmosphere modelling of the environment dynamical core is employed in GA6.1, which has an improved representation of tropical variability. A full description of GA6.1 is presented in Walters et al. (2017). Additionally, observed daily SSTs and sea ice distribution retrieved from the Operational Sea-surface Temperature and sea ice Analysis (OSTIA, Donlon et al. 2012) are used as initial conditions for the NWP model. The OSTIA dataset was derived from a combination of satellite-derived SSTs from the Group for High-Resolution Sea Surface Temperature project and in-situ observations. These SSTs and ice are persisted over the seven-day forecast.

6.2.1.2 The coupled model

6.2.1.2.1 The mixed layer MC-KPP model

The atmospheric component of this coupled model is the GA6.1 NWP model. The ocean component of the coupled model is the Multi-Column K Profile Parameterization (MC-KPP) one-dimensional ocean mixed-layer model (hereafter “KPP”) with a horizontal resolution identical to GA6.1. GA6.1 exchanges information with MC-KPP hourly via the Ocean Atmosphere Sea Ice Soil (OASIS, Craig et al. 2017) coupler. In order to simulate vertical mixing, the scheme of Large et al. (1994) is used, consisting of 100 points in a 1000 m column, with 70 points in the top 300m and a top layer thickness of 1m. Due to a lack of sea-ice module, the initial sea ice is persisted over the forecast period. GA6.1 and MC-KPP ocean model are coupled between 25°S and 35°N at all longitudes to reduce computational cost. Outside these regions, the initial SSTs are persisted following the NWP model.

Bernie et al. (2005) demonstrated that the intraseasonal variability of daily mean SST increases when the diurnal cycle is represented in the MC-KPP model. It was found that in the absence of the diurnal cycle, the intraseasonal SST was underestimated by about 0.34 °C

when compared against in-situ observations from moored buoys (0.86 °C). This resulted in a weaker influence on the atmosphere from intraseasonal SST by about 40%. The diurnal SST is influenced by the coupling frequency and the thickness of the upper-layer in the model. For example, when a top layer thickness of 10 m was used, MC-KPP was unable to simulate the observed magnitude of diurnal SST variability. Therefore, to capture 90% of the diurnal variability of SST, which accounts for 95% of the intraseasonal variability of SST, a coupling frequency of 3 hours or less, in combination with a vertical resolution with an upper-layer thickness of 1 m is required.

6.2.1.2.2 The fully dynamic NEMO model

In this model, GA6.1 is coupled to the NEMO dynamical ocean model (hereafter "NEMO", Megann et al. 2014). Unlike the MC-KPP ocean model, NEMO includes horizontal and vertical ocean dynamics. Additionally, NEMO is also coupled to the Los Alamos sea ice (CICE) model, which predicts sea ice extent and depth. NEMO uses a tri-polar horizontal grid of approximately 0.25° resolution, with 75 vertical levels and 1 m vertical resolution in the top 10 m and is coupled hourly to GA6.1 via the OASIS coupler.

Therefore, there are several key differences between NEMO and MC-KPP. The NEMO model represents ocean dynamics in horizontal and vertical advection and utilises the Turbulent Kinetic Energy vertical mixing scheme. In contrast, MC-KPP only simulates vertical mixing and the surface current is set to zero since the model does not simulate ocean dynamics. Aside from differing vertical resolution and the representation of sea ice, the coupling region is also different.

6.2.2 Model experiment design

The atmospheric initial conditions for all forecasts come from the Met Office operational analyses, while the ocean initial conditions for coupled KPP and NEMO forecasts come from the operational Met Office Forecast Ocean Assimilation Model (FOAM, Martin et al. 2007; Waters et al. 2015) system. In contrast to OSTIA, the FOAM dataset is produced by assimilating in-situ and satellite SST data, satellite altimeters, sea-level anomaly data, satellite sea-ice concentration data, and temperature and salinity profile data (Storkey et al., 2010).

Simulations for the three configurations for 2016 are performed for the period 15 May to 30 September 2016. The uncoupled NWP model is a 7-day deterministic forecast while the coupled KPP and NEMO models are 15-day deterministic forecasts. Both NWP and coupled KPP are initialised twice a day (00 and 12 UTC), while coupled NEMO is initialised once a day (00UTC). In order to maintain consistency, the forecast output for the first seven days initialised at 00 UTC will be analysed.

6.2.3 Observation and reanalysis data

To validate the model output, only observational and reanalysis datasets for 2016 will be utilised. The daily merged satellite-gauge rainfall dataset (Mitra et al., 2009) at a $1^\circ \times 1^\circ$ horizontal grid over the Indian monsoon domain is used to verify the rainfall predictions. Furthermore, OLR dataset retrieved from the NOAA ESRL-PSD (§3.2) with a $2.5^\circ \times 2.5^\circ$ spatial grid is used to verify the OLR output from the model. Finally, the ECMWF ERA-Interim reanalysis will be used to verify the atmospheric vertical and horizontal structure. The horizontal grid of ERA-Interim is $0.75^\circ \times 0.75^\circ$. Lastly, the Tropflux dataset is also utilised to verify surface fluxes and SST predictions at a $1^\circ \times 1^\circ$ spatial resolution. The predicted fields from the models are also regridded to the respective observational and reanalysis horizontal grid for comparison.

6.3 Verification of the 2016 break-to-active rainfall in forecasts

To provide brevity and clarity to the results of the 2016 break-to-active transition in both observations and models, only panels representing the break, transition and active phase will be presented. Each phase is organised in triads: the break phase represents the mean of 19th-21st July, the transition phase represents the mean of 27th-29th July, and the active phase represents the mean of 4th-6th August. The mid-point of the break and mid-point of the active phase occurred on 20th July and 5th August respectively. Additionally, only forecast lead day of +1, +4 and +7 will be shown. To account for model drift, the anomalies are calculated based on a July 2016 climatology only for each forecast lead time. I have chosen to use July to provide a reference climatology against which to measure the intraseasonal variability.

6.3.1 Observations

The results from the observations are discussed here first. In the break phase (Fig. 6.1a), positive rainfall anomalies (>15 mm/day) are observed over the eastern equatorial Indian Ocean (EEqIO) compared to the negative anomalies (<-10 mm/day) over the northern Bay of Bengal (NBoB). The 850 hPa wind patterns show easterly anomalies over NBoB and central India, which weakens the climatological southwesterly/westerly winds. Over the Indian subcontinent, the easterly anomalies are associated with drier conditions across central India and the coastal regions of the Western Ghats. Towards the northeast, stronger wet signatures are observed near the foothills of the Himalayas. Since the southwesterly/westerly mean monsoon wind is weaker during the break, the amount of moisture for precipitation evaporating from the adjacent oceans is greatly reduced (Pathak et al., 2017).

In the transition phase (Fig. 6.1b), enhanced precipitation shifts northwards from the

EEqIO (>10 mm/day) towards the NBoB. The positive anomalies over the EEqIO during the break are subsequently replaced by drier anomalies. Additionally, wet conditions are now observed over the southern tip of India and parts of central India, consistent with the northward propagation of rainfall. Similar to the break, the easterly anomalies persist over the Indian monsoon domain.

Towards the active phase, further northward propagation of enhanced rainfall towards the Indian subcontinent is observed, with the maximum positive rainfall anomalies now located over the NBoB (>35 mm/day). Additionally, the rainfall is also enhanced along the Western Ghats and northwestern India. In contrast, suppressed rainfall anomalies are observed in southern India, due to the rain shadow effect. While the rainfall anomalies over central India is quite mixed, generally, the increase in rainfall over the Western Ghats (and some of central India) is associated with the stronger westerly anomalies over the Indian subcontinent and the NBoB during the active phase.

6.3.2 NWP model

The forecasts from NWP with leads of 1, 4 and 7 days are shown in Figs. 6.1d–f, g–i and j–l respectively for each phases. In general, NWP is able to capture the spatial pattern of the break phase precipitation anomalies at all lead times, albeit with varying magnitude. The model forecasts stronger positive rainfall anomalies over the foothills of the Himalayas and weaker negative anomalies over central India and the NBoB. This is clearly seen in the forecast at +1 (Fig. 6.1d) and +4 (Fig. 6.1g) days. Additionally, the negative rainfall anomalies over the Indian subcontinent are more spatially extensive during the break. In the +7 day forecast (Fig. 6.1j), larger negative rainfall anomalies over the Western Ghats are observed, compared to the observations and in the +1 and +4 day forecasts. Next, the spatial pattern of the winds during the break phase is generally well captured in the NWP forecasts for +1 and +4 days. The easterly anomalies over central India at +7 day are much stronger, which further weakens the climatological winds, and are associated with the larger negative rainfall anomalies over the region, especially in the Western Ghats. Overall, NWP is able to forecast the general pattern of the break phase rainfall; however, the magnitudes over the anomalies are underestimated over India and NBoB, but is overestimated over northeastern India. The wind anomalies are also stronger at longer forecast lead times.

Next, the transition phase in NWP is evaluated. The general pattern of the rainfall was also simulated, although, errors in the magnitude are seen. In the +1 day forecast (Fig. 6.1e), the rainfall anomalies are generally well captured, especially over the NBoB and central India. However, the dry conditions over the EEqIO are much weaker. In addition, in both the +4 (Fig. 6.1h) and +7 (Fig. 6.1k) day forecasts, the negative rainfall anomalies over the

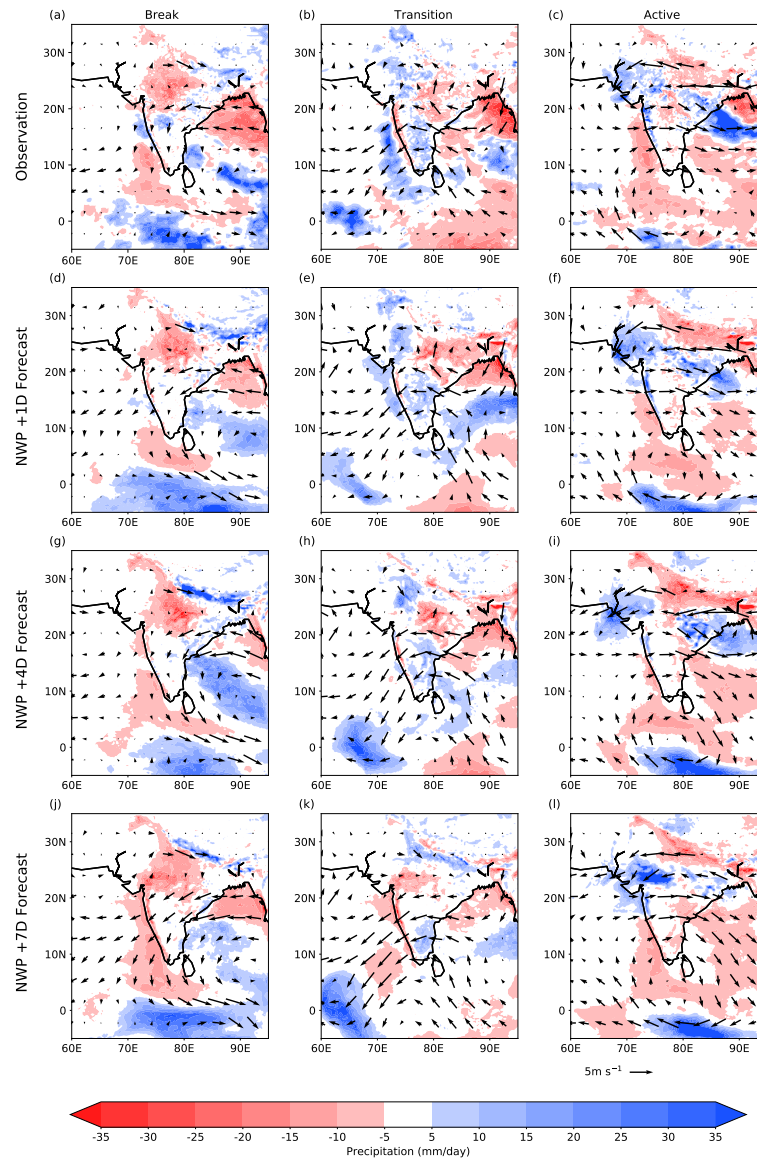


Figure 6.1: The 2016 break-to-active precipitation anomalies from observations (panels a-c) and NWP at forecast lead day of +1 (panels d-f), +4 (panels g-i) and +7 (panels j-l). The panels on the left and right represent the active and break phase, while the middle panels indicate the transition phase. Overlaid in each panels are the 850 hPa horizontal wind anomalies obtained from ERA-Interim (panels a-c) and from the NWP (panels d-l).

NBoB and the positive rainfall anomalies to the south are underestimated. Additionally, the positive rainfall anomalies over the western part of central India are weaker in the model at longer lead times. The wind patterns, while consistent with observations, are stronger with increasing forecast lead time. Despite this, the northward migration of rainfall over the NBoB, an important feature during the transition phase, is reproduced by the model. However, the northward propagation appears to be weaker in the +4 the +7 day forecast, as the positive rainfall between 10°-15°N is weak. Therefore, while the patterns remain consistent in NWP,

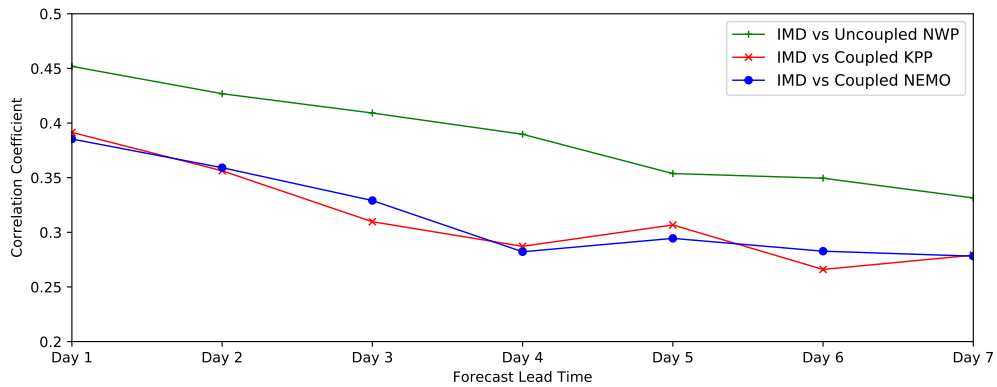
the magnitude of the rainfall deteriorates, especially at longer lead days (e.g., +4 and +7 days). The weaker rainfall anomalies over the NBoB, central India and EEqIO in NWP model are most apparent. For example, at forecast lead day of +7, the rainfall deficit over both NBoB and India is approximately -5 mm/day.

Lastly, the active phase in the NWP is analysed. The locations of active phase rainfall and the westerly winds in the model are similar to the observations but only for the +1 and +4 day lead times (Fig. 6.1f and i, respectively). In the +7 day forecast, however, there is no northward-propagating signal or the subsequent active phase rainfall seen over the NBoB. The analysis of the active phase in NWP indicates that while the northward propagation is simulated, the signal is weak and deteriorates at longer lead times. The positive rainfall anomalies are weaker than the observations, especially over NBoB region, even at +1 day (Fig. 6.1f). Over the Western Ghats, however, dry conditions are seen, especially at +7 day, compared to the observed wet conditions. The weaker active phase rainfall over the Western Ghats may be associated with the weaker westerly anomalies in the model. In contrast, the negative rainfall anomalies along the foothills of the Himalayas are much stronger in the forecast. This could be associated with the anomalous low-level anti-cyclonic winds south of the NBoB which are stronger in the model.

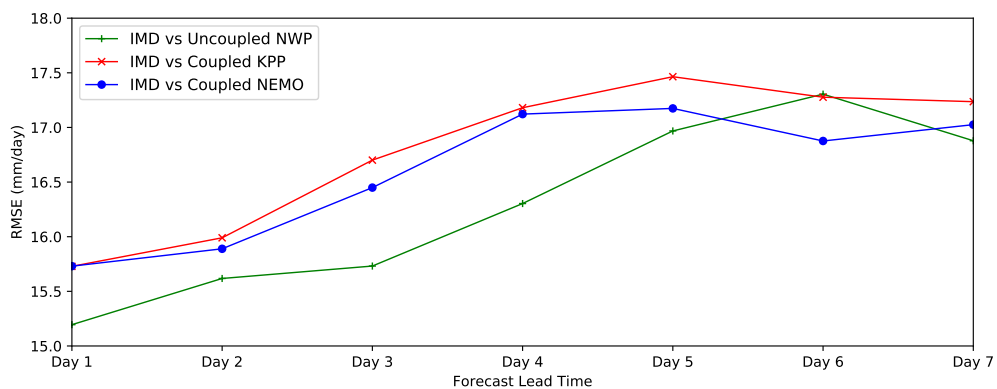
The model performance of the 2016 break-to-active transition for NWP is further shown in Fig. 6.2. The pattern correlation coefficient and root-mean-square error are computed for the precipitation over the Indian monsoon domain (5°S-35°N, 60°E-95°E) at different lead times. Analysis of the results shows that NWP achieves the highest correlations (solid green line in Fig. 6.2a) and smallest forecast errors (solid green line in Fig. 6.2b) when compared against the coupled models, which will be discussed in the next subsection. In the day +1 forecast, for instance, the correlation is approximately 0.45, with an RMSE of 15.2 mm/day. Subsequently, the performance of NWP deteriorates with lead time (e.g., $r=0.35$ at +7 day lead) consistent with the weakening of the northward propagating signal over the Indian monsoon domain. In general, it is clear from the results that NWP can reproduce the northward propagation over the NBoB but only for short forecast lead times (1-4 days). Furthermore, a significant issue that arises with NWP is the rainfall magnitude, with an increasingly weaker active phase rainfall (dry bias) at longer-range forecast. This error in magnitude suggests a weaker magnitude of the northward propagating BSISO in NWP.

6.3.3 KPP

In KPP, the break-to-active rainfall and 850 hPa wind patterns (Fig. 6.3) are very similar to the observations (Fig. 6.1), and comparable to NWP. However, similar issues in the magnitude of the rainfall and wind anomalies are inherent in KPP. In the break phase, for example, the



(a) Pattern correlation coefficient



(b) Root-mean-square error

Figure 6.2: (a) Pattern correlation coefficient (PCC) and (b) root-mean-square error (RMSE) of the 2016 break-to-active transition between the observation and three different configurations of the NWP model at different forecast lead time. The three configurations are: the uncoupled NWP (green line), the coupled KPP (red line) and the coupled NEMO (blue line). The observation used is the IMD merged satellite-gauge dataset. The correlations and RMSE were calculated by taking the mean from each day during the 2016 break-to-active transition (e.g., 20th July - 5th August 2016) over the domain 5°S-35°N, 60°E-95°E.

negative rainfall anomalies over the NBoB are weaker in KPP at all lead times, similar to those seen in NWP. Furthermore, KPP tends to forecast larger positive rainfall anomalies south of the NBoB, especially at +7 day lead (Fig. 6.3j), which are not seen in NWP and observations. Thus, the break phase over NBoB and India appears to be weaker in KPP at longer leads.

In the transition phase, the suppressed rainfall over the NBoB is much weaker compared to both observations and NWP, most evident in the +4 (Fig. 6.3h) and +7 (Fig. 6.3k) day forecasts. A similar error is also seen over central India, such that the negative anomalies over central India are not simulated (Fig. 6.3k). Although the rainfall magnitudes are not well represented, northward propagation of rainfall from the EEQIO towards the NBoB is observed.

The northward propagation associated with the active phase in KPP is also simulated; however, the magnitude reduces with lead time relative to both observations and NWP. This

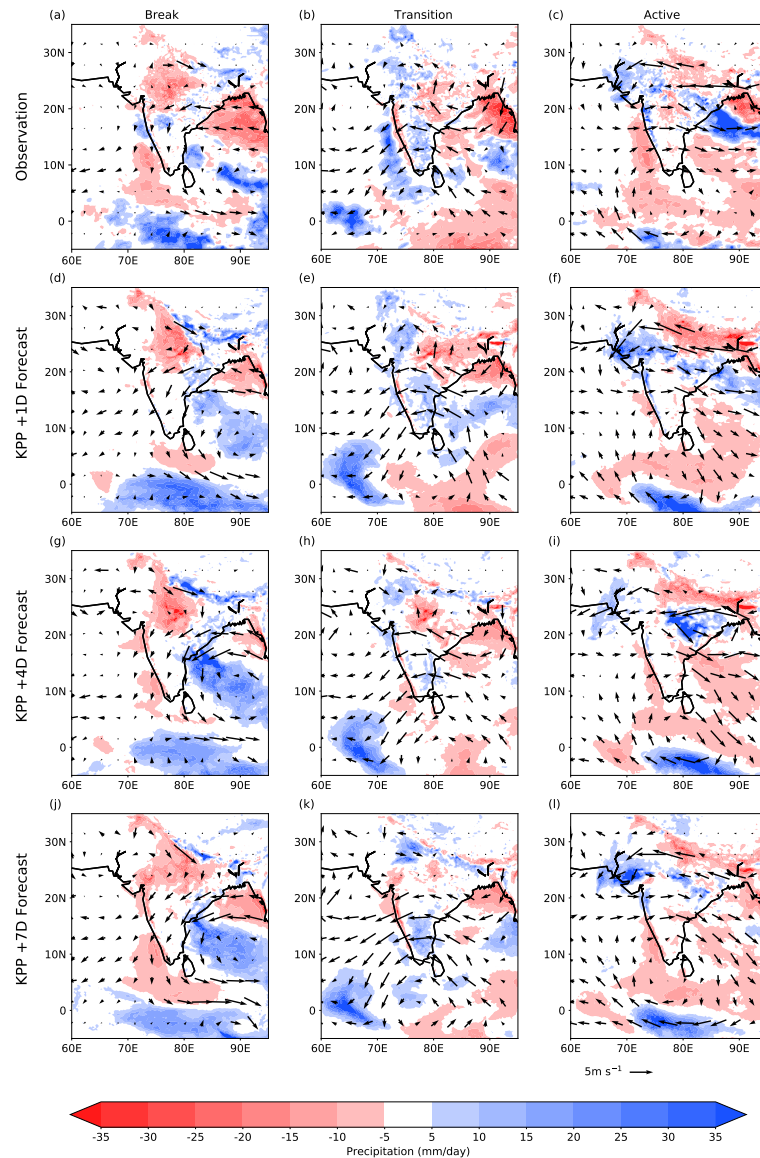


Figure 6.3: Similar to Fig. 6.1, but for the coupled KPP.

is most obvious in the +1 day forecast in Fig. 6.3f. The rainfall over NBoB is also extended further north, as seen in NWP, consistent with the anomalous cyclonic circulation simulated in KPP, which is not present in the observations. A significant issue with KPP is that the active phase rainfall signal is weak in the +4 day forecast (Fig. 6.3i) and disappears completely in the +7 day forecast (Fig. 6.3l), such that there is no active phase over NBoB. Next, over the Indian subcontinent, the negative rainfall near the Himalayan foothills is stronger, similar to that in NWP. In contrast, over central and eastern India, the rainfall anomalies are weaker and stronger, respectively, with longer forecast lead time.

In terms of model performance, the correlation of the break-to-active rainfall in KPP is consistently smaller than NWP at all lead times, as discussed previously. For instance, at +1

forecast lead day, the correlation (solid red line in Fig. 6.2a) is approximately 0.39, compared to 0.45 in NWP. Subsequently, in the +7 day lead, the correlation decreases to 0.3 in KPP compared to 0.35 in NWP. Additionally, the RMSE in KPP is also consistently larger than NWP at all forecast lead days. The smaller correlation and higher RMSE in KPP as compared to NWP is consistent with the precipitation anomalies in Fig 6.3: the northward propagation during the break-to-active transition is much weaker than NWP even at +1 day forecast lead, and worsens at longer lead days. It is worth noting that given that I have only analysed one forecast (2016 season) from each model, these difference in correlation are not statistically significant. Furthermore, the active phase associated with the northward-propagating BSISO is not seen in the +4 day forecast in KPP, unlike that in NWP. However, it is difficult to identify the role of air-sea coupling in Fig. 6.3. The results here suggest that there is no improvement in the forecast of the 2016 break-to-active transition with coupling, especially at longer forecast lead times, when compared to the NWP model. Although the general spatial pattern of the rainfall and wind anomalies are simulated, the magnitudes are incorrect. In fact, the results also suggest that the active phase rainfall, specifically those over the NBoB and central India, is weaker in the coupled model forecast, compared to the uncoupled model.

6.3.4 NEMO

In this section, the precipitation and wind anomalies from the NEMO model are analysed. Overall, the break-to-active transition in NEMO is very similar to that in KPP. This is evident in Fig. 6.2a such that the correlation of NEMO (solid blue line) is similar to KPP at all forecast lead times. Perhaps one difference that can be seen is that the RMSE in NEMO (solid blue line in Fig. 6.2b) is slightly smaller than KPP, but in general, the representation of the three-dimensional ocean model in NEMO did not show any statistically significant improvement to the forecast performance. Thus, due to their similarities, the difference between NEMO and KPP is analysed in Fig. 6.4. The composites show that there is no significant difference in rainfall and 850 hPa wind anomalies during the break-to-active transition at all lead times. Therefore, the inclusion of ocean dynamics in the NEMO model did not show any significant improvement when simulating the rainfall break-to-active transition, compared to observations.

Overall, statistical analysis suggests that the inclusion of air-sea coupling did not improve the prediction skill of the 2016 transition event. In fact, the uncoupled NWP model showed better correlations and smaller forecast errors, especially at shorter forecast lead times, than the coupled models. However, at longer lead times, the correlations significantly reduced, and there are larger errors in the forecasts in all models.

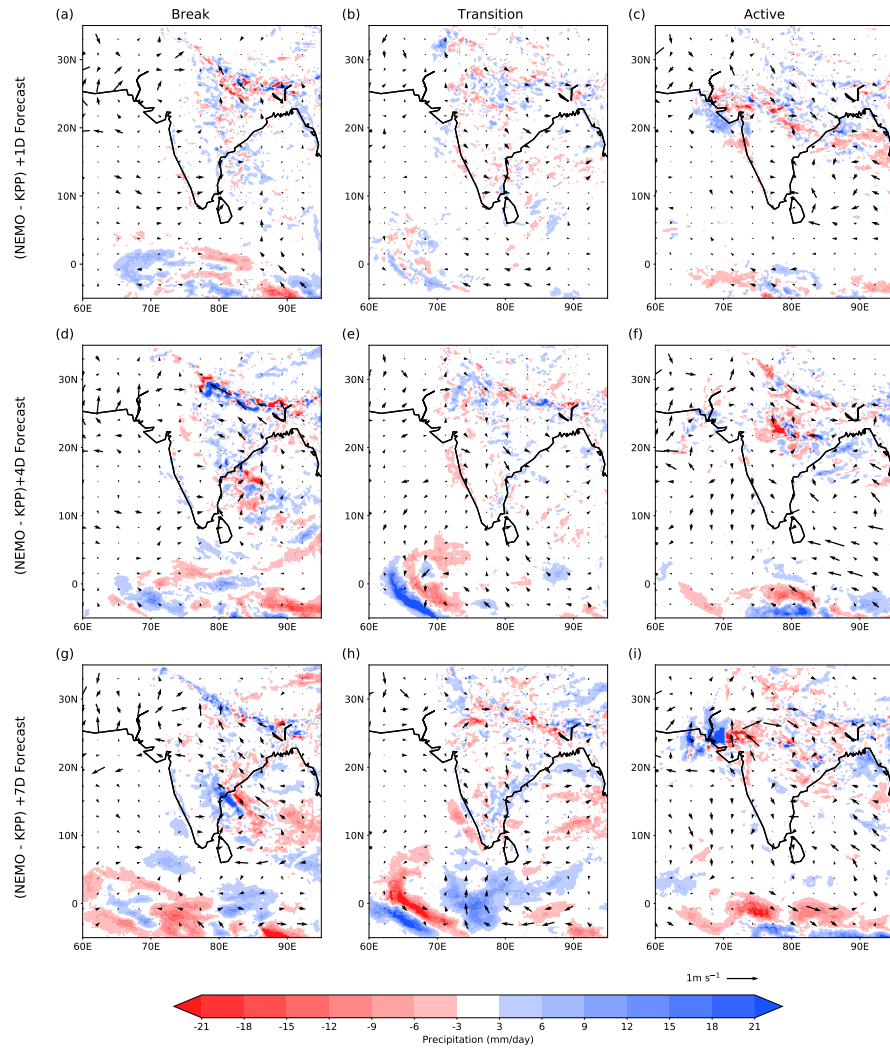


Figure 6.4: Difference between NEMO and KPP at forecast lead day of +1 (panels a-c), +4 (panels d-f) and +7 (panels g-i).

6.4 Northward propagation in the forecasts

In the previous §6.3, it was shown that the northward propagation in the uncoupled and both coupled models were simulated but for shorter forecast lead times. Furthermore, the precipitation anomalies in all three models are weaker, and the duration of the active phase is shorter at longer lead times. In this section, Hovmöller diagrams of OLR anomalies averaged between 80°E-90°E for observations, and the three configurations of the NWP model are shown in Fig. 6.5. Analysis of this diagram will assist with revealing the speed and magnitude of the enhanced active phase convection associated with the northward propagation. For the forecast models, lead times of +1, +4 and +7 days are provided.

In the observations, the active spell manifests as a track of negative OLR anomalies propagating northwards with time. The enhanced convection associated with the active phase

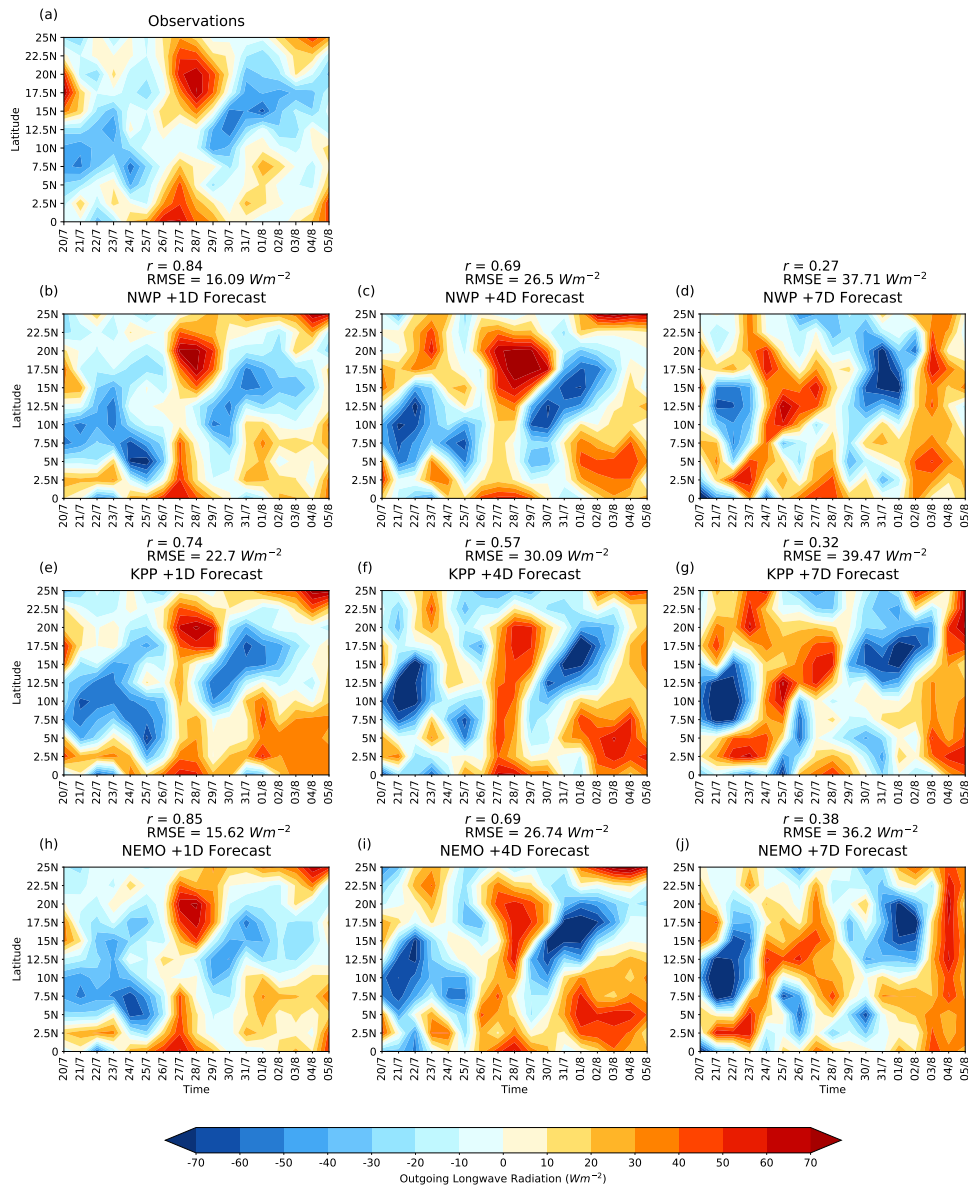


Figure 6.5: Time-latitude Hovmöller plots of OLR anomalies for (a) observations, (b-d) NWP, (e-g) KPP and (h-j) NEMO during the 2016 break-to-active transition averaged between 80° and 90°E. Only forecasts with a lead day of +1, +4 and +7 are shown for brevity. The black solid line represents the northward propagation of active phase convection. The pattern correlation and root-mean square error against the observations for each models are also shown. Observations are the Uninterpolated OLR data provided by the NOAA/OAR/ESRL PSD, Boulder, Colorado, USA, from their website at <https://www.esrl.noaa.gov/psd/>.

appears at 10°N on 28th July (OLR anomalies $< -40 \text{ Wm}^{-2}$), eight days after the peak-break phase. Subsequently, the convection reaches the NBoB (to about 20°N) between 31st July and 1st August, with a propagation speed of approximately $3.33^\circ \text{ day}^{-1}$. Over the EEQIO, OLR anomalies are positive, indicating suppressed convection, which is associated with weaker rainfall over the equator during the active phase. This pattern is similar to the OLR dipole

between NBoB and EEqIO, as shown in Chapter 3 and from previous studies (Yasunari, 1980; Li et al., 2013). A slight weakening of the convection is observed in the middle of the transition between 7.5°N and 10°N, on 26th July, and strengthens again by 29th July. In general, the observed propagation of the OLR is consistent with the observed rainfall shown earlier in Fig. 6.1a.

The forecasts for all three configurations of the NWP model with leads of +1, +4 and +7 days are shown in Fig. 6.5b–j, respectively. The northward propagation, as expected, is observed in all models at +1 day. Furthermore, enhanced convection anomalies in the models (Fig. 6.5b,e,h) manifest over 10°N on 28th July and move towards the NBoB with phase speeds similar to observations. Thus, propagation speed in the +1 day forecast in all models is comparable to observations. The weakening of the enhanced convection prior to the mid-transition phase is also seen. In general, the OLR pattern in the +1 day forecast from all three models is comparable to observations as shown by their high correlations, although, the correlation in KPP is the lowest compared to NEMO and NWP. Furthermore, the RMSE in KPP is also highest amongst the three models.

In the +4 day forecast, all three models are also able to simulate the northward propagation originating from 10°N towards the NBoB. The propagation speed of the enhanced convection is comparable to observations and the +1 day forecast. A significant difference, however, is that the active phase is shorter and weaker in all models. For instance, weak active phase signals are seen over NBOB during the peak-active phase on 5th August in NWP and NEMO. In KPP however, suppressed convection at 20°N associated with break-like conditions are seen by 4th August over the NBoB. Therefore, compared to the other models, KPP appears to underestimate the active phase convection. This is further evident by the lower correlation ($r=0.57$) and higher RMSE (30.09 Wm^{-2}), compared to NWP and NEMO which have similar magnitudes in correlations and RMSE.

This weakening of the active phase convection is more apparent and further worsens in the +7 day forecast. In addition, the enhanced active phase convection is also delayed. In all models, the convection only appears on 30th at 12.5°N and reaches the NBoB on 1st August which translates to a propagation speed of about $2.5^\circ \text{ day}^{-1}$. This is in contrast to the convection manifesting on 29th July at 10°N in the +1 and +4 day forecast. Furthermore, the active phase over the NBoB terminates much earlier on 3rd August in the NWP model and on 4th August in both the coupled models, such that the duration of the active phase is about three days. This is in contrast to a duration of 5 days in both observations and the +1 day forecasts. Positive OLR anomalies ($>30 \text{ Wm}^{-2}$) indicating suppressed convection are observed over the NBoB between 3rd and 5th August in the models, although, in the observations, convection is still evident during this period. Therefore, the rainfall over the NBoB during the active phase is much weaker and persists for a much shorter duration compared to the observations (see Fig

6.11 and Fig 6.3l). In general, the northward propagation in all the models was well simulated but worsened at longer lead times. The spatio-temporal pattern at +1 day lead resembles the observation well. Interestingly, the propagation speed of the convection associated with the BSISO during 2016 (2° day^{-1}) is in contrast with previous studies. Jiang et al. (2004) used OLR data obtained from the NOAA ESRL-PSD for the period 1980-2001 and found a BSISO propagation speed between 0°N - 20°N of about 1° day^{-1} . The results from this section suggest that the propagation speed of the BSISO for 2016 is faster than the climatological speed. However, as depicted by the OLR anomalies in the models, the propagation speed in the +1 and +4 day forecast is consistent with observations and is overestimated in the +7 day forecast. Additionally, the active phase convection is delayed, and its duration over the NBoB is shorter, which suggest that the magnitude of BSISO is weaker at increasing forecast lead time.

6.5 Role of air-sea coupling in forecasts

In this section, the relationship between sea surface temperature and surface latent heat fluxes during the 2016 break-to-active transition in the forecasts is analysed.

6.5.1 Hovmöller diagram of SST and LHF

The Hovmöller diagram in Fig. 6.6a illustrates the SST and LHF anomalies in observations during the 2016 break-to-active. In the break phase, warm SST anomalies over the NBoB and cooler SST anomalies to the south are observed. The warm SST persists from the break through the transition phase till 30th July and subsequently cools as the active phase initiates over the NBoB. The warm SST anomalies leading enhanced convection by about eight days are consistent with previous studies (Vecchi and Harrison, 2002; Klingaman et al., 2008a). The warming of the SSTs may also be due to strong incoming solar radiation at the surface, together with clear sky conditions and weaker evaporation as shown by the negative LHF anomalies (solid black contour lines). Subsequently, after the active phase, the cooling of SSTs is associated with the increase in wind-induced evaporation (positive LHF anomalies) which will be discussed in §6.5.2. The reduction in incoming solar radiation also enhances this cooling.

The SST and LHF anomalies for the NWP model at +1, +4 and +7 forecast lead days are illustrated in Fig. 6.6b-d. The diagram illustrates the daily SSTs obtained from OSTIA used as initial conditions for NWP. The OSTIA dataset is produced from observations and satellite-derived SST. As expected, the SST anomalies for the +1 day forecast look similar to that of the observations but significantly differ at longer forecast lead day. For example, warm SST leads the active phase convection over the NBoB by approximately 10 days, similar

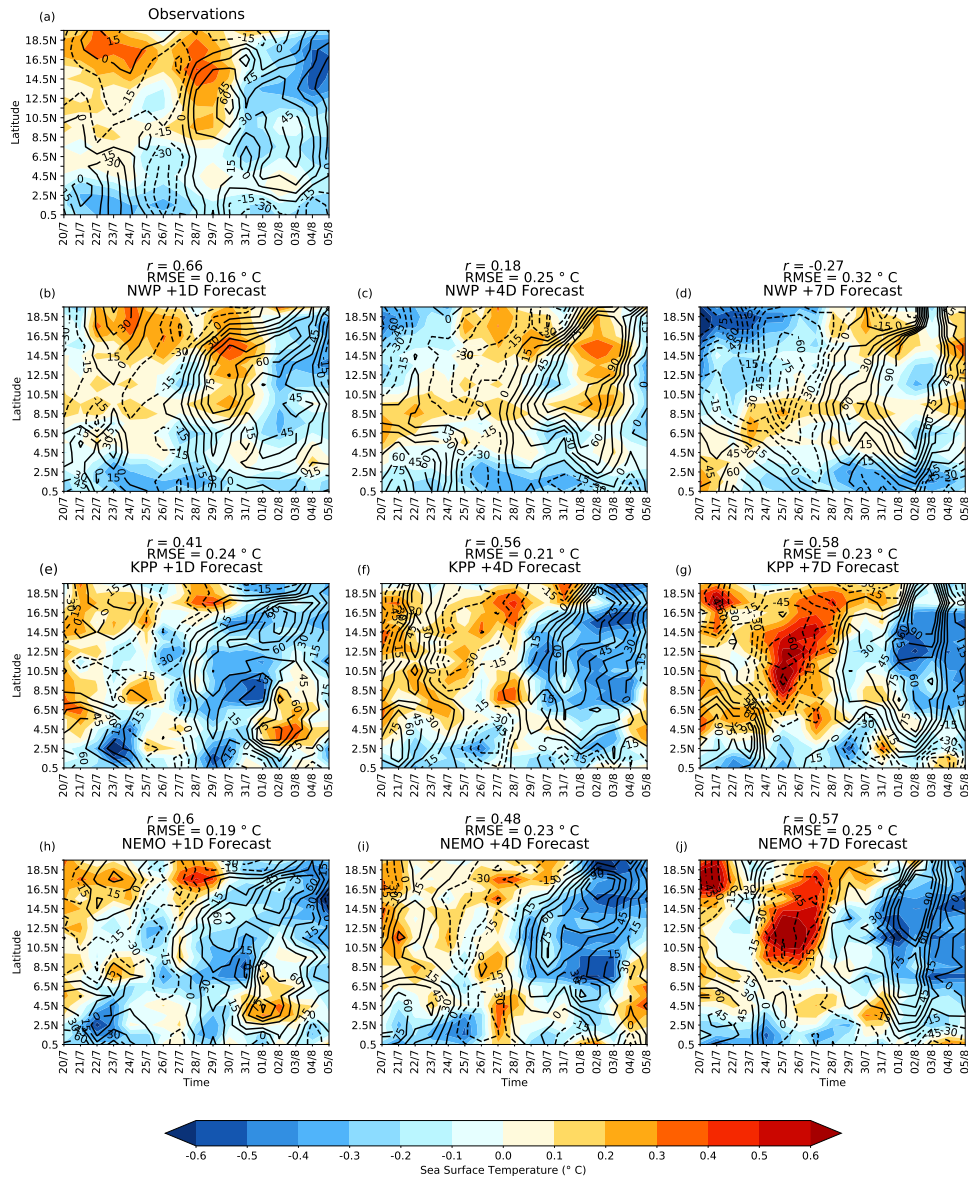


Figure 6.6: Time-latitude Hovmöller plots of sea surface temperature (shading, °C) and surface latent heat flux (contour, Wm^{-2}) anomalies for (a) observations, (b–d) NWP, (e–g) KPP and (h–j) NEMO during the 2016 break-to-active transition averaged between 85° and 95°E. Only forecasts with a lead day of +1, +4 and +7 are shown for brevity. The pattern correlation and root-mean square error for each models against the observations are also shown. The observations were obtained from TropFlux for both sea surface temperature and latent heat flux.

to observations. This similarity is further shown by the correlation in the +1 day forecast of 0.6, with an RMSE of 0.16°C. However, in the +4 and +7 day forecasts, the warm SST anomalies leading the break phase are replaced by cold SST anomalies. Furthermore, warm SST anomalies are dominant over the NBoB at the active phase. As a result, a significant decrease in correlation is seen in the +4 and +7 day forecast, with a r value of 0.16 and -0.27, respectively. There is also a significant increase in RMSE, which is two times larger in the +7

day forecast (0.32°C) compared to the +1 day forecast. As for the LHF anomalies, the spatial pattern resembles the observations, but the magnitude is significantly overestimated in NWP at longer forecast lead times.

Next, Fig. 6.6e–g shows the forecast of SST and LHF anomalies from KPP. In the +1 day forecast (Fig. 6.6e), the maximum warming over the NBoB eight days after the break is also seen, indicating that KPP is able to simulate the observed intraseasonal SST variability. However, the spatial pattern of the anomalies differs from observations. For example, the magnitude of this warming is much weaker and is confined to a smaller region compared to the observations. In the observations, the warming (on 29th July) extends between 8°–20°N, but in KPP, the warming is confined to 16.5°–20°N. The incorrect spatial pattern of SST anomalies is further supported by the correlation in KPP ($r=0.41$) and RMSE (0.24°C). At longer lead times, larger correlations of SST anomalies in KPP are seen. For instance, the correlations at +4 and +7 day lead times are 0.56 and 0.58, respectively. Furthermore, the maximum SST anomalies during the transition phase over the NBoB persist much longer, up till 1st August and 2nd August in the +4 and +7 day forecast, respectively (Fig. 6.6f–g). The SST pattern may be associated with negative LHF anomalies which may prevent cooling of the SST anomalies. The warm SST extending further south during the mid-transition is also simulated in KPP at longer leads, which was not seen in the +1 day forecast. Thus at longer lead times, the spatial pattern of the SST anomalies is better simulated. Similarly, the SST anomalies in NEMO resembles KPP, although the correlation ($r=0.6$) in the +1 day forecast is initially higher. By +7 day forecast lead time, the correlation decreases to 0.57 and is comparable to that of KPP. It is noted that since I am only analysing a single forecast, the statistics here are not robust. The key point in this section is that the inclusion of air-sea coupling in the coupled models is to maintain the observed SST patterns.

In general, towards the transition of the active phase, the magnitudes of LHF anomalies are significantly stronger in all models at longer leads. The large LHF magnitude in all the models may be attributed to the stronger surface wind speeds, which will be discussed in the next section. Moreover, the results from the NEMO are very similar to KPP, which suggests that the ocean dynamics in the coupled NEMO model did not have any significant influence on the intraseasonal variability of SST and LHF anomalies, and the overall model performance. More importantly, the inclusion of the air-sea coupling processes in the coupled model acts to maintain the spatio-temporal pattern of the SST (as shown by the correlations). Furthermore, the addition of air-sea coupling also preserves the warming of the SSTs after the peak-break phase, such that the warming leads active phase convection by approximately eight days. This warming is not seen in NWP at longer leads. Despite this, northward propagation of convection and rainfall are still observed in all three configurations of the NWP models with a similar level of performance, which may suggest that air-sea coupling did

not improve the northward propagation of the BSISO. The fact that northward propagation is seen in the atmosphere-only NWP model suggests that other mechanisms such as the internal atmospheric dynamics may also be essential for the poleward propagation of the BSISO, at least for the 2016 season (Jiang et al., 2004; Gao et al., 2019).

6.5.2 NBoB area-average

In order to further verify the role of air-sea coupling in the models, anomalies of rainfall, SSTs, LHF and total wind speeds averaged over the NBoB domain (15°-23°N, 80°-95°E). This will assist with evaluating the possible role of air-sea coupling in producing a correct phase relationship between SST and rainfall as seen in previous studies (Vecchi and Harrison, 2002; Roxy and Tanimoto, 2007; Klingaman et al., 2008b; Vialard et al., 2012).

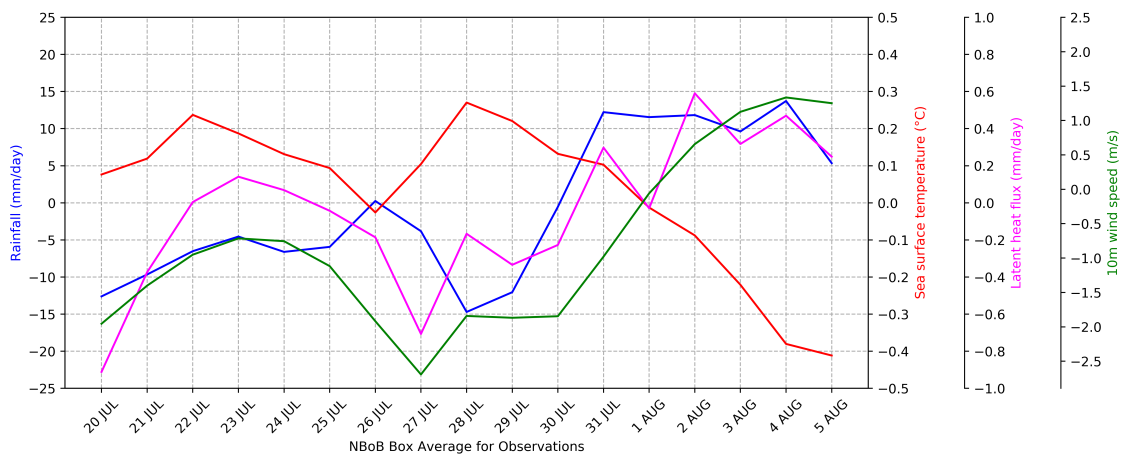


Figure 6.7: The area-average of the 2016 break-to-active transition anomalies of rainfall (blue line, mm/day), SSTs (red line, °C), LHF (magenta line, mm/day), 10m wind speeds (green, m/s) averaged over the NBoB domain (15°-23°N, 80°-95°E) in observations.

The NBoB area-average for observations are shown in Fig. 6.7. An important feature in the observations is the SST-rainfall quadrature phase relationship: the warm SSTs anomalies over the NBoB maximised at around eight days after the break, such that warm SSTs precede active convection, confirming the results in Fig. 6.6a. Furthermore, as the response to the preexisting break phase, the weak wind speeds and reduced LHF may increase the SST anomalies over the NBoB. Furthermore, stronger shortwave radiation at the surface may also be responsible for the warming. Additionally, the cooling of the SSTs is observed after the active phase onsets over the NBoB. Also, during the active phase, enhanced evaporation is in phase with the increase in positive rainfall anomalies. The increase in evaporation is associated with the strengthening of the surface wind speeds. Thus, the results from Fig. 6.7 are consistent with those shown in the previous sections. Based on the observations, however, wind-induced LHF anomalies cannot support the northward propagation of the BSISO as it slightly leads or is in-phase with active phase rainfall.

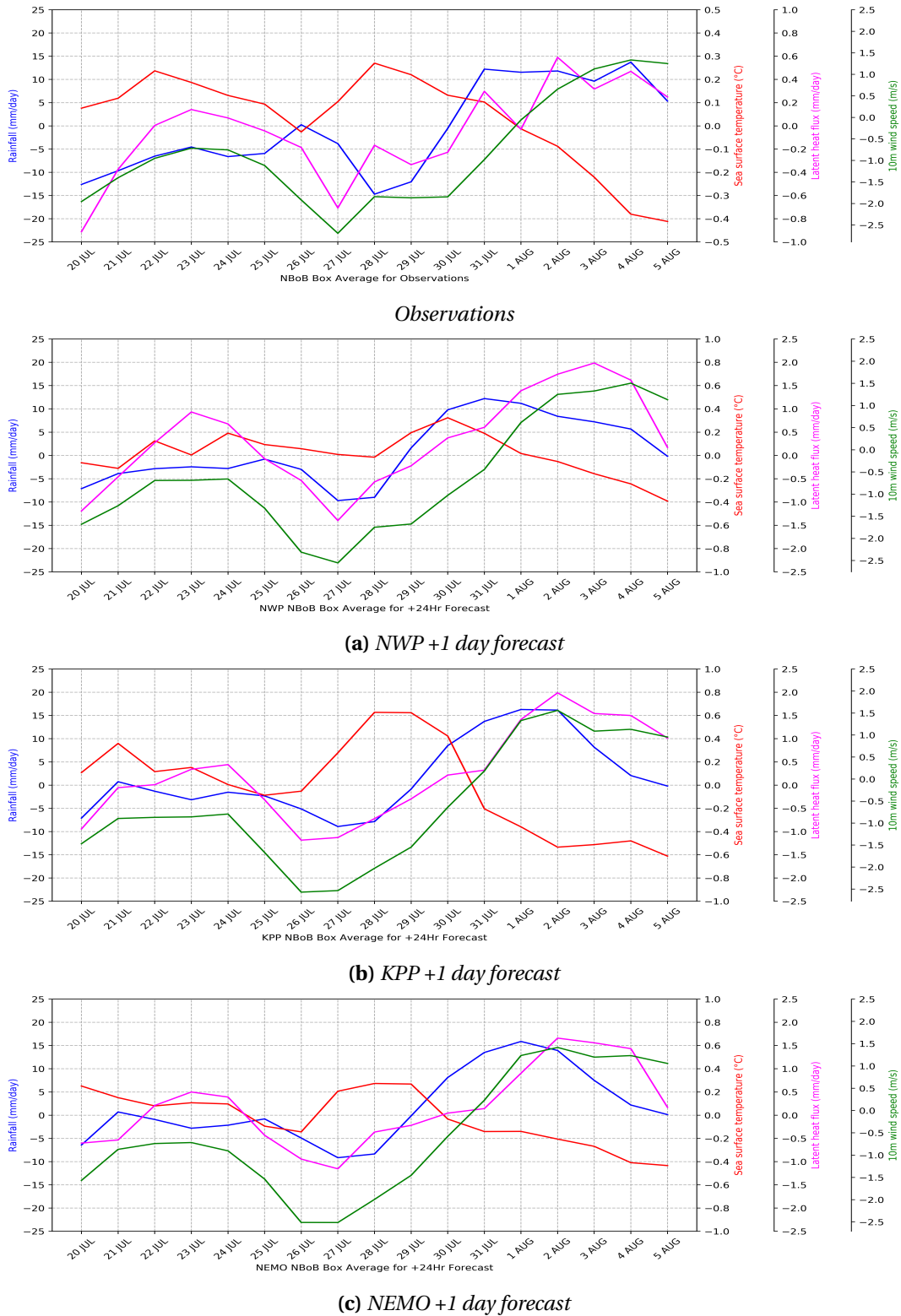


Figure 6.8: Similar to Fig. 6.7 but for the +1 day forecast for (a) NWP, (b) KPP and (c) NEMO. The top most panel illustrates the observations.

Next, the NBoB area-average in the +1 day forecast for all three models is illustrated in Fig. 6.8a-c. The rainfall anomalies over the NBoB during the active phase in NWP (Fig. 6.8a) are slightly larger than observations. This is consistent with the active phase rainfall over the

NBoB being too far north in the model (see Fig. 6.1f). Furthermore, the quadrature SST-rainfall relationship associated with the BSISO is seen; however, the maximum SST anomalies form 10 days after the break, instead of eight days as in the observations. While the LHF anomalies are larger, the magnitude of total surface wind speeds in the NWP model is comparable to observations. For example, the maximum positive LHF anomalies in NWP are approximately 2.0 mm/day compared to 0.6 mm/day in the observations during the active phase. This may suggest that the air-sea humidity gradient in the model is larger, such that the lower atmosphere is drier in the model compared to observations.

The SST-rainfall phase relationship is also simulated in both KPP (Fig. 6.8b) and NEMO models (Fig. 6.8c) in the +1 day forecast. In fact, the phase relationship in both the coupled models resembles the observations more closely than those found in the NWP. The SST anomalies achieve their maximum about eight days after the break. Unsurprisingly, larger LHF anomalies during the transition to the active phase are inherent in both coupled models, despite surface wind speed anomalies being similar to observations. This may suggest a drier lower atmosphere in both coupled models over the NBoB during the active phase, which may strengthen the evaporation from the oceanic surface or that the model simulates warmer SSTs. Furthermore, in all models, the active phase represented by the large positive rainfall anomalies is initiated on 31st July similar to observations. However, subsequently, there is a decrease in the rainfall, confirming the weaker active phase rainfall in the +1 day forecast as shown previously in §6.3. In observations, large rainfall anomalies persist throughout the active phase.

In contrast, the day +7 forecast shown in Fig. 6.9 is dissimilar to the observations and the +1 day forecast. Notably, in the NWP model (Fig. 6.9a), the SST-rainfall relationship is almost in-phase, such that the maximum SST anomalies are associated with the maximum active phase rainfall. Another significant difference in NWP at longer forecast lead time is that the magnitude of the wind speeds over the NBoB is much stronger (approximately two times stronger), which results in the magnitude of the positive LHF anomalies being twice as large, compared to the +1 day forecast. Additionally, the wind-induced LHF also lags BSISO convection in NWP, especially at longer lead times.

Interestingly in the +7 day forecast in both KPP (Fig. 6.9b) and NEMO (Fig. 6.9c) model, there is a large peak in maximum SST anomalies (>1 °C) a day after the break on 21st July, compared to those seen in observations. This peak may be due to much stronger negative LHF anomalies (reduced evaporation) or by stronger heating at the surface by shortwave radiation, thereby warming the SSTs. However, even in the +7 day forecast, the coupled models still showed a SST-rainfall phase relationship in contrast to the NWP model. Therefore, the role of air-sea coupling is to maintain the observed relationship between SST and rainfall. Furthermore, the surface wind speeds are almost twice as large compared to both observations

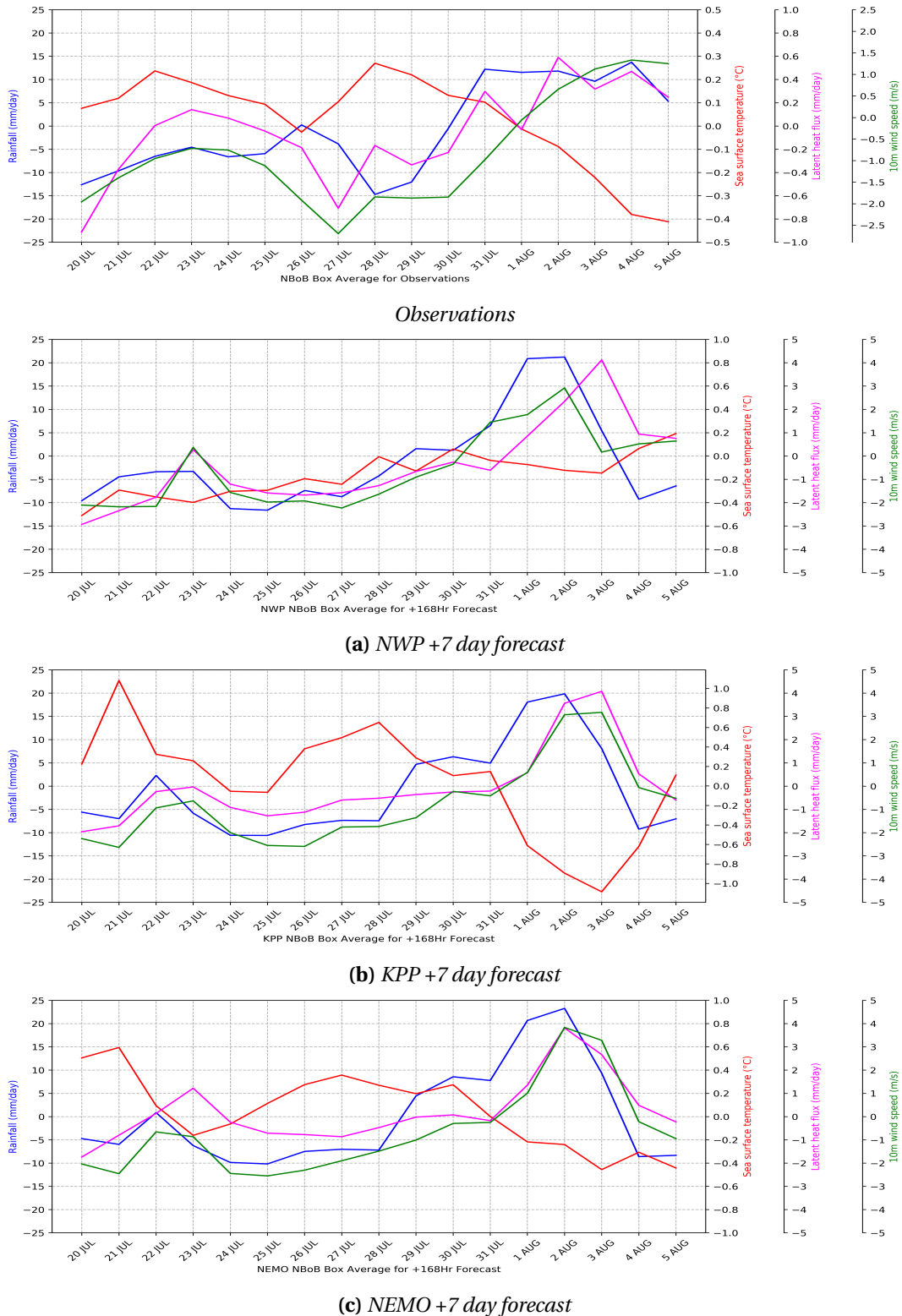


Figure 6.9: Similar to Fig. 6.7 but for the +7 day forecast for (a) NWP, (b) KPP and (c) NEMO. The top most panel illustrates the observations.

and +1 day forecast, leading to stronger LHF anomalies over the NBoB during the active phase. Interestingly, the SST anomalies in the KPP model at +7 day forecast showed a significantly quicker cooling, followed by warming of the SSTs during the transition phase. This pattern

in the SST anomalies is not seen in NEMO, which instead, showed a gradual cooling similar to observations. The results here suggest that the representation of ocean dynamics or the difference in the vertical mixing scheme in NEMO is important in improving SST simulations.

In general, as discussed in §6.4, the NBoB area-averaged results in Fig. 6.8 showed distinct northward propagation in convection and rainfall, but only for the +1 day forecast. Distinct errors in all the models are that: 1) the break phase persists much longer, 2) the duration of the active phase is shorter and 3) the start of the active phase is delayed. For example, in the +7 day forecast, the start of the active phase is delayed by about one day and two days in the NWP, and both coupled models, respectively. Additionally, in the observations, the active phase initiated on 31st July and persisted through 5th July. However, in the models, the active phase weakens 1-2 days after the onset of the active phase. This error becomes larger at longer forecast lead times in all the models. This suggests that the northward propagating BSISO significantly weakens after the active phase, at longer lead compared to observations. Therefore, based on these results, the role of air-sea coupling in the coupled model is to maintain the intraseasonal SST-rainfall quadrature relationship but does not improve the forecast performance of the active-to-break transition. The atmosphere-only NWP model forced with observed daily high-resolution SSTs is capable of simulating northward propagation. Still, the timing and duration of the break-to-active transition are significantly misrepresented at the longer lead, similar to both coupled models.

6.6 Thermodynamics of the break-to-active transition in forecasts

It has been discussed that the active phase in the models is delayed and persists much shorter (i.e., weaker) compared to observations. In this section, the moisture anomalies of the break-to-active transition in the models are evaluated over the NBoB.

The composites of specific humidity anomalies in the observations, and in the +1, +4 and +7 day lead forecasts in NWP are shown in Fig. 6.10. The composites were obtained by averaging between 85°-95°E longitude. In the observations, there is a robust northward propagation of moisture anomalies from the EEQIO towards the NBoB. Furthermore, in the active phase, the weak positive moisture anomalies (1.0–1.5 mm/day) extend deep in the vertical between 925 hPa and 200 hPa. This suggests that positive moisture anomalies may be able to support and sustain active phase convection. The +1 and +4 day forecasts show similarities with the observations, such that the northward propagation is simulated, although the magnitude of the moisture anomalies is smaller compared to observations. Interestingly, in the +4 day forecast, the layer of dry air in the upper atmosphere (400 hPa) intrudes further north in the active phase. The dry layer may stabilise the atmosphere over the NBoB and weaken the enhanced convection. Now, in the +7 day forecast, the northward propagating

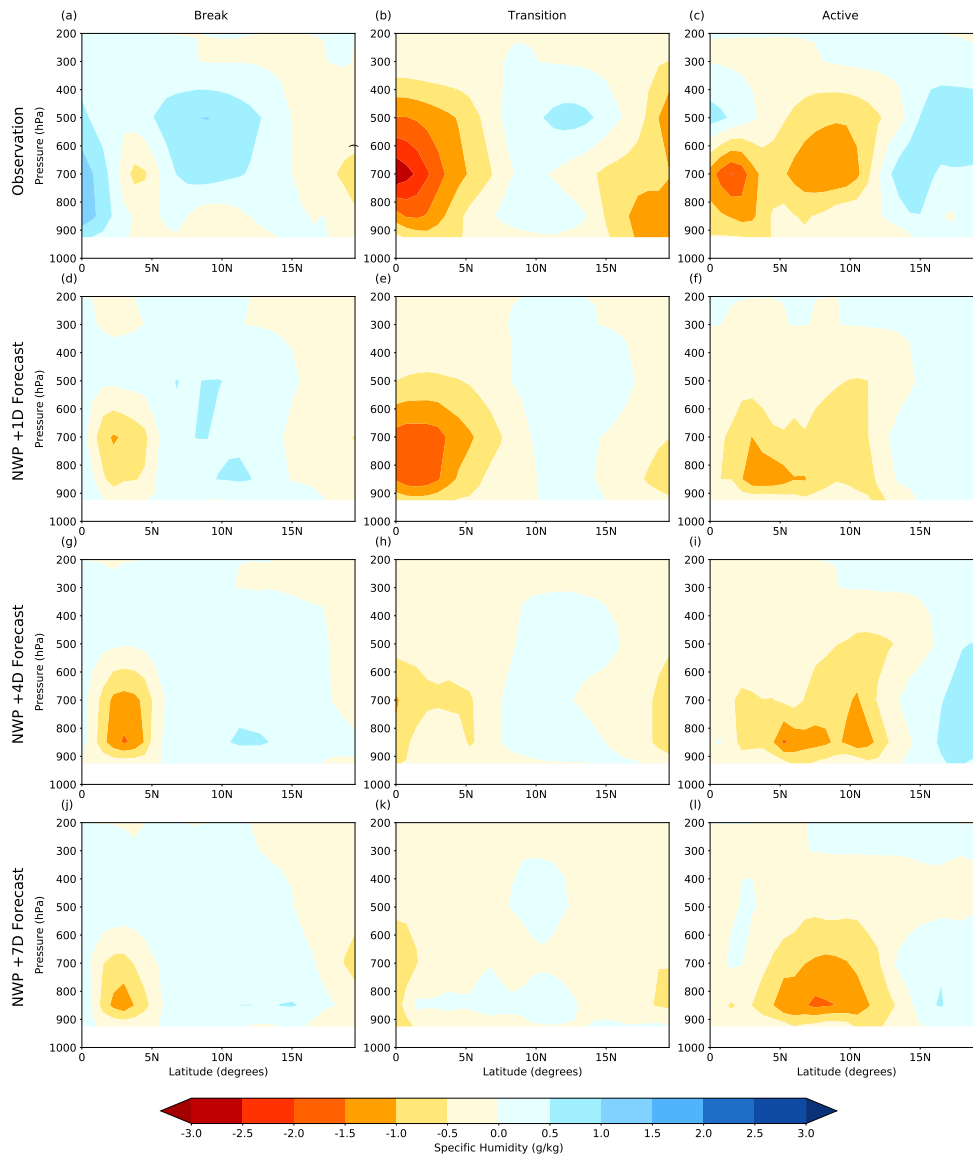


Figure 6.10: The pressure-latitude composite specific humidity anomalies (g/kg) averaged between 85°–95°E in (a–c) observations and in NWP at (d–f) +1 day, (g–i) +4 day and (j–l) +7 day forecast. Observations were obtained from ERA-Interim.

moisture anomalies in the transition and active phases are significantly weaker compared to the +1 and +4 day forecasts. The anomalies in the transition phase are also shifted to the south compared to observations. Additionally, the wedge of mid-level dry anomalies seen in the +4 day forecast (Fig. 6.10i) now extends further north over the NBoB between 500 hPa and 300 hPa (Fig. 6.10l) during the active phase. Therefore, in the long-range forecast, the combination of smaller moisture anomalies and the dry layer above may be associated with a more stable atmosphere and weaker convection. Subsequently, this decreases the predicted duration of the active phase.

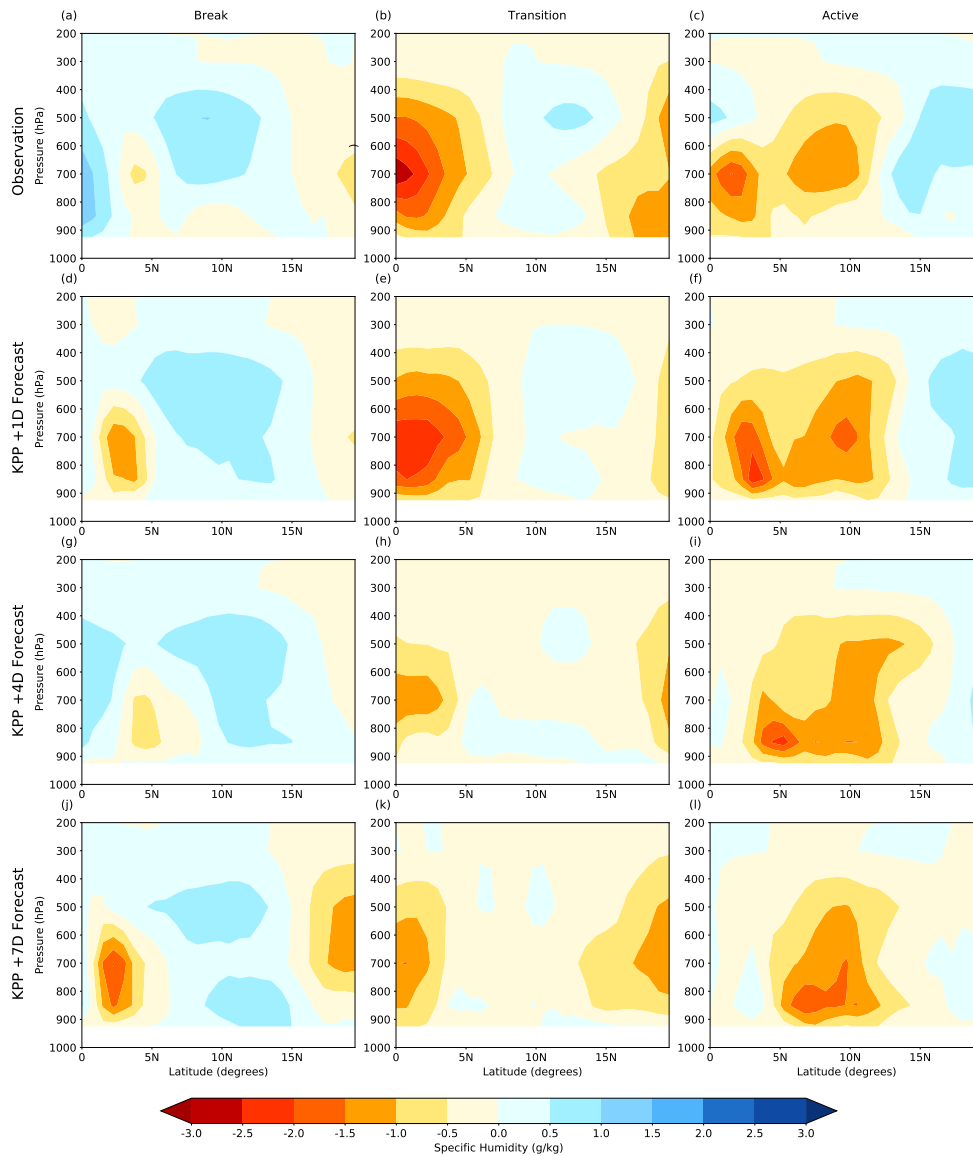


Figure 6.11: The pressure-latitude composite specific humidity anomalies (g/kg) averaged between 85°-95°E in (a–c) observations and in the KPP at (d–f) +1 day, (g–i) +4 day and (j–l) +7 day forecast. Observations were obtained from ERA-Interim.

Next, Fig. 6.11 illustrate the composites of specific humidity anomalies from the KPP. Due to similarities between NEMO and KPP, only composites from the KPP model are shown. Similar to the NWP model, while the northward propagation of moisture anomalies are simulated, its magnitude and speed significantly deteriorate at longer leads. Likewise, the moisture anomalies during the active phase over the NBoB gradually decreases at longer forecast lead time, including the intrusion of mid-level dry air over the NBoB from the south. Generally, the results from the coupled models suggest that the moisture anomalies, especially in KPP, are stronger and deeper, compared to NWP. However, in all three models at increasing

forecast lead times, the simulated northward propagation is weaker. More importantly, the enhanced convection associated with the active phase over the NBoB is also weaker, which is associated with predominantly dry mid-level air. Consequently, this is association with a stabilised atmosphere, preventing further growth of the convection.

Importantly, the results from the coupled models further suggest that air-sea coupling does not improve the spatio-temporal pattern of the simulated northward propagating BSISO during the 2016 break-to-active transition. In the transition towards the active phase, the errors, such as weaker moisture anomalies and mid-level dry intrusion extending further north over the NBoB in all the models are very similar. This may indicate that the break-to-active transition is rooted (or is mostly attributed) to the internal atmospheric processes, rather than air-sea coupling. Also, this suggests that the models have difficulty in simulating convective activity associated with the active phase.

6.7 Summary and discussion

Accurate and skilful prediction of the ISM rainfall on intraseasonal time scales is vital for the agricultural and socio-economic sectors of India. The main objective of this chapter is to evaluate the representation of the 2016 break-to-active transition and its associated northward propagation in an uncoupled and coupled models, at varying forecast lead times. By comparing the models, the role of air-sea coupling processes during the transition can be diagnosed. Additionally, the role of ocean dynamics is also studied by comparing two coupled models. In order to achieve this, three different configurations of the NWP model are used: (1) the uncoupled Met Office GA6.1 model (2) the GA6.1 model coupled to MC-KPP and (3) The GA6.1 model coupled to NEMO. In order to maintain the consistency in the results, only forecasts for the first seven days initialised at 00 UTC were utilised. During the break-to-active transition in observations, a distinct northward propagation of enhanced convection and rainfall is observed from the equator to NBoB/central India. Furthermore, large-amplitude SST anomalies precede active phase rainfall by about eight days during the 2016 transition event, which may contribute to the intensification of the convection. Furthermore, wind-induced positive LHF anomalies are observed to slightly lag or even be in-phase with BSISO convection and are therefore not conducive for the northward propagation.

The forecasts at +1, +4 and +7 day leads in all three models were examined to evaluate the ability of the models to simulate the break-to-active transition. Verification of the models was undertaken by comparing the forecasts of rainfall and OLR anomalies. Both coupled and uncoupled models are capable of simulating the northward propagation of convection and rainfall from the eastern equatorial Indian Ocean towards the NBoB. However, while the

northward propagation is simulated at all forecast times, a significant error in the models is that the active phase onset over the NBoB is delayed. The simulated active phase initiates 1-2 days later than observed. Additionally, the duration of the active phase in the model is much shorter as well, as it tends to weaken within 1-2 days after its initiation. The results here are consistent with Li et al. (2018); however, their studies used the CFSv2 to forecast 28 active events during 1999-2010. Their study also found that the (1) rainfall anomalies are weaker, and (2) the northward propagation is delayed compared to observations. However, unlike their results which found prolonged active events, our results instead showed shorter active phases at longer forecast lead times. They also showed significantly lower correlations due to higher forecast errors when compared to break events.

In order to further verify the results from the rainfall composite, the correlations and RMSEs of the rainfall were examined. The results showed that the uncoupled NWP model achieves higher correlations compared to the coupled models. This is in contrast with previous studies of Kemball-Cook and Wang (2001) and Shukla and Zhu (2014), which suggest that air-sea coupling is essential to simulate realistic intraseasonal variability in rainfall. Furthermore, Fu et al. (2003) showed that the magnitude of the northward propagating BSISO is 30% stronger in the coupled model, compared to its uncoupled counterpart. They also showed that the spatio-temporal pattern of the BSISO is improved in the coupled model. However, the results in this chapter suggest otherwise, in fact, the uncoupled NWP model showed better performance in predicting the 2016 transition event than in the coupled model. Additionally, the RMSE in the uncoupled model is lower than the coupled model, which suggest that air-sea coupling did not improve the forecast performance of the 2016 transition event. It is worth noting, however, that our study only analyses the forecast for a single transition in 2016, whereas Fu et al. (2003) studied the BSISO for 16 years in a climate model. Thus, air-sea coupling may be less important for shorter weather-scale forecasts such as those analysed in this chapter.

While the correlations from NWP are higher than the both KPP and NEMO model, the correlation values, in general, are small. This is consistent with results from Abhilash et al. (2014), which suggest difficulties in the models to realistically represent strong northward propagating BSISO events. More importantly, I have only analysed a single event during the 2016 season. Thus the statistical analysis may not be robust. Furthermore, Goswami and Xavier (2003) and Abhilash et al. (2014) further suggest that the prediction skill of the active phase is much lower than the break phase, and attributed this to the chaotic nature of the active phase (i.e., convective systems such as low-pressure systems and cyclones) which are more difficult to predict. Generally, the results in this study suggest that the uncoupled NWP model using persisted initial SSTs can better simulate the break-to-active transition compared to the coupled KPP and NEMO models. However, an inherent error in all the models is the

weaker BSISO, as well as a shorter duration of the active phase. Besides, it is also difficult to infer if the models used in this chapter display a weak performance in forecasting the active phase as I have not analysed and compared the model's performance in simulating the active-to-break transition. It could also be that the performance of the Met Office NWP model may be as low during the break, as with the active phase. Future work should also focus on analysing the active-to-break transition in order to verify the ability of the model in forecasting the intraseasonal variability of the Indian monsoon.

To further understand the role of air-sea coupling, evaluation of the SST and LHF anomalies further showed that the coupled model was able to reproduce the maximum SST anomalies leading the active phase in the northern Bay of Bengal, as well as the quadrature SST-rainfall phase relationship at all forecast lead times. However, there are errors in the magnitude of the SSTs, for example, in the +7 day forecast of the KPP model, the cooling (warming) over the NBoB during the active (break) phase is much stronger than in observations. The NEMO model, however, at the +1 day forecast lead time showed an improved representation of the SSTs compared to the KPP as shown by the larger correlations. However, at longer lead times, the correlations between NEMO and KPP were almost comparable. In contrast, the quadrature-phase relationship is not evident in NWP, as the maximum rainfall and SST anomalies are in phase especially at longer leads. Thus, air-sea coupling is an important process in coupled models to maintain the correct relationship between SST and rainfall.

An interesting result which is inherent in all models (and at all lead times) is the considerably larger magnitude of the LHF anomalies compared to observations. In the +1 day forecast for all models, the positive LHF anomalies during the active phase are approximately twice as large as observations; however, the surface wind speed anomalies are almost comparable. This may be associated with a drier lower atmosphere over the NBoB, which may increase the air-sea humidity gradient and thus the LHF anomalies or that the SSTs are warmer in the models. At longer leads, the LHF anomalies are even higher, and the surface winds are significantly stronger. As such, stronger 10m wind speeds combined with larger air-sea humidity gradient may lead to the positive LHF anomalies. Furthermore, it is clear that SST anomalies respond to LHF in the models as warm (cool) SSTs are associated with negative (positive) LHF anomalies.

Additionally, the relationship between rainfall and LHF could explain the weaker magnitude of the BSISO, such that LHF anomalies can maintain BSISO convection (Gao et al., 2019). In the result so far, it is evident that the active phase in the models is shorter than in observations. In all three models, after the active phase manifests over the NBoB, there is a decrease in LHF anomalies which could be associated with the weakening of the surface winds. Thus, the shorter duration of large-scale surface winds reduces the magnitude of LHF

over the NBoB are not able to maintain active phase convection and thus leading to a much shorter and weaker active phase. Alternatively, the weaker convection could be associated with weaker winds (convergence) and hence, weaker LHF. Generally, as the model error grows at longer lead times, the characteristics of the northward propagating BSISO based on its initial conditions gradually adjusts towards the inherent characteristics of the models (Li et al., 2018). The errors in the coupled model also suggest that the air-sea coupling processes are misrepresented which not only lead to a weaker BSISO and consequently, to a delayed active phase, but also a shorter duration of the active phase. This means that the period of the BSISO is, therefore, shorter than in observations.

The strength of the convection is also further diagnosed based on composites of specific humidity anomalies. In the composites at longer forecast lead times, the specific humidity anomalies tend to be weaker than in observations. Furthermore, in all models at the +7 day forecast, a wedge of dry mid-level air extends further north over the NBoB which was not seen in observations. The anomalously drier air may stabilise the atmosphere over the NBoB and may weaken the convection to as well. Previous observational studies showed that dry mid-level air inhibits the growth of convection (Bhat et al., 2001; Parker et al., 2016; Menon et al., 2018). Overall, the errors in forecasting the 2016 break-to-active transition reflect the uncertainties in the models in representing the atmospheric convection and its associated moisture processes.

The findings in this chapter further support the conclusions in Gao et al. (2019) that intraseasonal SST variability associated with the air-sea coupling alone could not drive northward propagation. Our results suggest that air-sea coupling has no effect on the propagation, at least for the 2016 event. However, this study also stresses the importance of local air-sea coupling in the BSISO forecast. The coupling maintains a realistic SST-rainfall phase relationship in the coupled model, which was otherwise, not seen in the uncoupled model. The results for the forecast of the 2016 break-to-active transition event are clear: all three models were able to simulate northward propagation; however, significant errors in the models are evident at longer forecast leads. The delayed onset and shorter period of the active phase are the most significant issues in terms of the forecast performance of the event. Furthermore, the results also showed that the uncoupled NWP model forced with realistic daily SSTs achieved better performance at predicting the intraseasonal rainfall variability compared to both coupled model. It is important to note, however, that these conclusions are based on the forecasts of a single transition event. Thus, it can be suggested that 2016 break-to-active transition may have an internal atmospheric dynamics origin. Alternatively, the results may also indicate that the models used in this chapter perform poorly in forecasting this event.

Chapter 7:

CONCLUSIONS

This thesis has presented a detailed analysis of the break-to-active transition in the northward-propagating boreal summer intraseasonal oscillation (BSISO) of the Indian summer monsoon. §7.1 provides a review of the conclusions of this thesis in the context of the aims and objectives in §1.2. Limitations faced in this thesis are presented in §7.2. §7.3 discusses avenues to expand the research on the intraseasonal variability of the Indian summer monsoon.

7.1 Summary of key findings

7.1.1 A novel method for identifying break-to-active transition

In §1.2, the first objectives of this thesis were to determine the evolution of the break-to-active transition over the northern Bay of Bengal (NBoB), as well as to explain the physical mechanism(s) governing this transition. To achieve this, chapter 3 introduced a novel criterion to distinguish the break-to-active transition using the IMD gridded rainfall dataset.

Individual active and break phase dates were found by applying to the IMD gridded rainfall datasets an index based on Rajeevan et al. (2010). The criterion for the break-to-active transition required that the transition from a break to an active phase occur within 30 days (§3.4). The 30-day criterion was chosen to ensure that the transitions were physically associated with the northward-propagating BSISO. Of the 60 breaks identified, only 24 transitioned to an active phase. This suggests that a break-to-active transition is an uncommon event, which is in contrast to previous studies which assumed that most breaks transition to the active phase. Furthermore, the transition dates identified were validated against a Bimodal BSISO index of Kikuchi et al. (2012) which confirmed that a majority of the transitions were associated with the BSISO (§3.5).

Next, the rainfall and OLR anomalies were composited to illustrate their evolution during

the break-to-active transition (§3.6). In the rainfall composite, the break phase was associated with dry anomalies over central India (CI) and the Western Ghats, while increased rainfall anomalies were seen near the Himalayan foothills. The reduced westerly anomalies over CI and the Western Ghats reduced the amount of moisture (originating from the adjacent oceans) available for precipitation. In the active phase, opposite signs of rainfall anomalies were seen along with the strengthening of the southwesterly monsoon winds. The characteristics of the break and active rainfall and wind anomalies are comparable to previous studies (Krishnamurthy and Shukla, 2000; Rajeevan et al., 2006, 2010).

Furthermore, the composite of OLR anomalies showed a distinct dipole between the Indian subcontinent/NBoB and the eastern equatorial Indian Ocean (EEqIO), similar to the maximum cloud zones over these latitudes in Sikka and Gadgil (1980). A robust northward propagation of enhanced convection from the EEqIO towards the NBoB was also seen during the transition to the active phase. The success of the criterion and the composites to capture the northward-propagating signals associated with the BSISO further motivated the use of the composites to understand the mechanism(s) governing the transition.

7.1.2 Possible mechanism(s) for the break-to-active transition

To identify the mechanism(s), the thermodynamic properties of the transition were analysed (§4.3) using ERA-Interim reanalysis. Composite mixing ratio anomalies (§4.3.1) reveal that the transition to the active phase was associated with northward-propagating moisture anomalies, statistically significant at the 95% confidence level, from the EEqIO towards the NBoB. Regions of large moisture anomalies were also associated with strong vertical winds, which suggests anomalous convection. To confirm this, composites of equivalent potential temperature anomalies showed anomalous instability in regions with positive moisture anomalies (§4.3.2). Thus, the transition to an active phase is linked to the poleward movement of equatorial moisture and convection anomalies towards the NBoB.

Previous studies have suggested that air-sea coupling may support the northward-propagating BSISO. Thus, the moisture for precipitation during the break-to-active transition may originate from the evaporation of moisture from the ocean surface. For this to be possible, oceanic surface variables must show intraseasonal variability during the transition. Thus, the composite of sea surface temperature (SST) anomalies showed SST variability during the transition (§4.4.1). During the mid-break phase, warm and cold SST anomalies were observed over the NBoB and EEqIO, respectively. However, the maximum warming over the NBoB only manifested several days after mid-break, consistent with previous studies which showed a lag of approximately 10 days (Vecchi and Harrison, 2002; Klingaman et al., 2008a; Vialard et al., 2012). This relationship has also been found using

coupled global circulation models (CGCMs, e.g., Fu and Wang, 2004a).

Furthermore, surface turbulent fluxes may also influence the atmospheric stability and formation of convection. Composites of latent heat flux (LHF) and sensible heat flux (SHF) anomalies showed intraseasonal variability (§4.4.2). The LHF anomalies were negative over the NBoB during the mid-break associated with the weak surface wind speed anomalies, which contributed to the warming NBoB SSTs. Subsequently, the LHF anomalies increased with stronger surface wind speeds towards the active phase. The stronger LHF anomalies over the NBoB during the transition are not able to support the northward propagation of the BSISO convection, as the positive LHF anomalies are collocated with or even slightly lagged the enhanced convection.

Next, the SHF anomalies over the NBoB during the break are negative, perhaps due to the warm SST anomalies increasing the ocean-atmosphere temperature gradient. As the transition progresses towards the active phase, the SHF anomalies become positive, which slightly leads convection. The magnitude of SHF anomalies is much smaller than those of LHF. However, the influence of SHF on the northward propagation should not be discounted, as the SHF anomalies heat the boundary layer north of the active convection, thereby favouring the northward propagation of convection. Although it is difficult to show causality from observations alone, the results suggest that intraseasonal variability of SST-induced sensible heat fluxes, not wind-induced LHF, may feedback onto enhanced atmospheric convection in accordance with the objectives in (§1.2).

A moisture budget analysis over the NBoB (§4.5) was conducted to confirm the origins of the moisture during the break-to-active transition. Both moisture convergence and evaporation increase during the transition. While the contribution by moisture convergence (67%) is more substantial than evaporation (33%), the influence of evaporation cannot be ignored as it may support the northward propagation. The SST-induced LHF may enhance the evaporation and boundary layer heating north of the convection (Gao et al., 2019). Decomposing the moisture convergence (Fig. 4.8) revealed that the zonal component of the moisture convergence dominated. However, the meridional component may also support northward propagation, based on a recent study by Gao et al. (2019). Their study suggests that the northerlies during the break transport large area mean moist static energy (MSE) over the Asian monsoon region towards the southern Bay of Bengal, which may support the generation of BSISO convection. Subsequently, the northward propagation of MSE, associated with the propagation of BSISO convection, is dominated by the zonal advection of MSE, which confirms the large contribution of the zonal component. Gao et al. (2019) also suggest that the SST-induced surface fluxes supports the propagation of MSE and offsets the impact of wind-induced LHF, which weakens the northward propagation. Lastly, thermodynamic-induced SHF may support both the generation and maintenance

of the convection. In general, the results showed the presence of intraseasonal SSTs and surface turbulent heat fluxes, and thus, air-sea coupling may support the northward propagation. However, the cause-and-effect from air-sea coupling cannot be diagnosed through observations alone. The results do, however, support the conclusions of Gao et al. (2019) that while air-sea coupling may support the northward propagation, it alone cannot drive the propagation. Internal atmospheric dynamics is required as it drives a large proportion of the propagation (Woolnough et al., 2000).

7.1.3 Variability of land-atmosphere coupling in the break-to-active transition

The second objective of this thesis was to determine how the land-atmosphere coupling may influence the northward-propagation of the BSISO over the Indian subcontinent (§1.2). Chapter 5 addressed this by applying ERA-Interim/Land reanalysis datasets to the break-to-active transition composite. Analysis of the soil moisture anomalies (§5.3.1) showed that the soil conditions are drier over most over the Indian subcontinent during the break. The soil moisture subsequently increases from southeastern India towards northwestern India (NWI) in a northwestward direction associated with the rainfall anomalies towards the active phase. It should be noted, however, that central India (CI) is located in a climatological wet soil region while NWI is situated in a climatologically dry soil zone.

The relationship between soil moisture and SHF over India is straightforward: dry soil is associated with positive SHF, while wet soil is associated with negative SHF anomalies. However, the LHF anomalies revealed interesting characteristics of the land surface over India during the break-to-active transition. In the mid-break phase, negative LHF anomalies or weak evapotranspiration (ET) were observed over NWI. Enhanced ET, however, was observed over CI. Towards the active phase, the sign of the anomalies reverses with weak ET now located over CI and strong ET over NWI. The variability of the ET revealed two distinct regimes over the Indian subcontinent: (1) a soil moisture-limited regime over NWI and (2) an energy-limited regime over CI.

In the moisture-limited regime, ET is actively controlled by the availability of soil moisture. In the energy-limited regime, soil moisture is abundant, but ET is controlled by the availability of energy at the surface. Thus, in the break phase, stable atmospheric and cloudless sky conditions increased surface insolation. Since CI has climatologically wet soil, ET is increased due to the available surface energy. ET over NWI is suppressed due to the lack of soil moisture. Now, in the active phase, increased convection and cloudy sky conditions reduced the amount of solar radiation at the surface. This was subsequently shown in the net surface radiation budget for both CI and NWI (Fig. 5.3). As a result, ET decreases over CI and increases over NWI as the ET. The stronger ET over NWI is supported by the wetter soil due to increasing

precipitation. Similar results were found using 12 AGCMs in the GLACE experiment showing “hot-spot” regions of strong land-atmosphere coupling especially in regions of transitional climate zones between dry and wet climates (Koster et al., 2004).

In addition to the land surface variability, the thermodynamics of the atmosphere over India, similar to Chapter 4 was also investigated (§5.4). The results showed that the northward/northwestward propagation of the active phase rainfall was associated with anomalies in moisture and atmospheric stability. Moisture budget analysis over CI and NWI was further conducted to establish the mechanism(s) for the break-to-active transition over India. As previous results from the analysis of surface turbulent heat fluxes have indicated, land surface variability exists during the break-to-active transition. The moisture budget will reveal whether land-atmosphere coupling may be present during the break-to-active transition. Over CI, evaporation was larger than moisture convergence during the mid-break and early transition phase. Subsequently, moisture convergence dominates. Thus, the results suggest that evaporation increase the moisture in the boundary-layer and support the transition, followed later on by moisture convergence. Additionally, the spatiotemporal pattern of the moisture convergence coincides with precipitation; thus, moisture convergence is responsible for supplying the moisture for precipitation. In contrast, evaporation is always dominant over moisture convergence for the northward propagation over NWI. However, the support from moisture convergence is only apparent and important after the mid-point of the transition.

It is clear that land-atmosphere coupling may be important for the break-to-active transition. A metric for land-atmosphere coupling was computed with reanalysis datasets to quantify the coupling strength over India. Land-atmosphere coupling influences the atmosphere through soil moisture affecting surface fluxes (terrestrial leg) and the surface fluxes influencing near-surface variability such as the boundary layer and lifting condensation level height (the atmospheric leg). The terrestrial coupling index (TCI) and atmospheric coupling index (ACI) based on Dirmeyer and Halder (2017) were used.

Over NWI, a positive correlation between soil moisture and LHF implies that soil moisture is readily evaporated. As the LHF increases, $2mQ$ increases which lower the lifting condensation level (LCL) height. The link between the terrestrial and the atmospheric leg suggest that land-atmosphere coupling is necessary over NWI. In contrast, the land-atmosphere coupling is less important over CI. The negative correlation between soil moisture and LHF suggests that the moisture availability at the lower-level is limited by radiation and may not influence the instability, as shown by the correlation of the 2m specific humidity and the LCL. As a result, land-atmosphere coupling over CI is weak and may not influence the break-to-active transition over India. Thus other external factors such as the moisture convergence may be more critical over CI rather than evaporation, especially during

the later stages of the transition.

7.1.4 Unraveling the role of air-sea coupling during the break-to-active transition in models

The final objective from (§1.2) of this thesis is addressed in Chapter 6. The results from that chapter suggested that including of air-sea coupling did not improve the forecast performance of the break-to-active transition. Three configurations of the Met Office Global Atmosphere 6.1 (GA6.1) numerical weather prediction (NWP) model were used: (1) the atmosphere-only GA6.1 model forced with high-resolution daily SSTs (hereafter “NWP”), (2) the GA6.1 coupled to the Multi-Column K Profile Parameterization (MC-KPP) one-dimensional ocean mixed-layer model (hereafter “KPP”) and the (3) the GA6.1 coupled to the Nucleus for European Modelling of the Oceans fully dynamic ocean model (hereafter “NEMO”). The main difference between NEMO and KPP is that NEMO represents ocean dynamics (horizontal and vertical advection) and utilises the Turbulent Kinetic Energy vertical mixing scheme. In contrast, KPP simulates only vertical mixing. Simulations for all three models for 2016 were performed for the period 15th May to 30th September 2016. To maintain consistency, only daily forecast output for the first seven days initialised at 00UTC was utilised.

During the 2016 Indian monsoon season, the India Meteorological Department reported a single break-to-active transition as discussed in their annual report on the Indian monsoon. The peak-break occurred on 20th July, while the peak-active phase was initiated on 5th August. The length of the transition was 16 days which satisfied the criterion for a break-to-active transition. Furthermore, the break-to-active transition for 2016 was validated with the Bimodal ISO Index (Kikuchi et al., 2012) in Fig. 3.3, which confirmed that a robust BSISO signal was associated with those dates.

To verify the break-to-active transition in the models, centred-time mean of rainfall anomalies during the peak-break, mid-transition and peak-active phases were shown for the +1, +4 and +7 day forecasts (§6.3). The most striking feature in the +1 day forecast is that the rainfall anomalies during the break-to-active transition were comparable to observations. The NWP performs the better than the coupled models for the +1 day forecast with a correlation of 0.45 and an RMSE of 15.3 mm/day. The correlations for KPP and NEMO were comparable with a correlation of approximately 0.39 and an RMSE of 15.8 mm/day. However, it was found that the magnitude of the active phase rainfall over the NBoB was underestimated in all models even for the +1 day forecasts, which suggests that the active phase is weaker in the models. At longer forecast lead times, the forecast performance of the active phase deteriorated significantly, for example, in the +7 day forecasts there is no signal of active phase rainfall. This was further reflected in the lower correlations in the +7 day forecasts for all three

models. Despite this, NWP still outperforms both coupled models.

All models performed well at forecasting the northward-propagating OLR convection anomalies originating near the equator towards the NBoB in the +1 day forecasts, with high correlations. However, similar issues to the rainfall anomalies were seen especially at longer lead times. In both the +4 and +7 day forecasts, the initiation of the active phase was delayed by about 1-2 days. Furthermore, the duration of the active phase was also shorter by about 2-3 days. The late initiation and shorter duration of the active phase contributed to the weak active phase rainfall over the NBoB. Despite these findings, it is interesting that the atmospheric-only NWP model (and both coupled models) managed to forecast robust northward-propagating BSISO signals at 1-3 days lead times. Similarly, this further suggests that air-sea coupling did not improve the forecast of the convection anomalies during the break-to-active transition.

To diagnose the influence of air-sea coupling, the SST anomalies during the break-to-active transition in the models were analysed. The +1 day forecasts from models showed high correlations against observations. The warm SST anomalies led enhanced convection by approximately 9-10 days, similar to observations and previous studies (Klingaman et al., 2008a; Vialard et al., 2012). However, the warm SSTs leading convection were misrepresented in NWP, especially at longer forecast lead times as evident by the weak correlation. In the +7 day forecast, for instance, cold SST anomalies were leading SST convection instead. In contrast, for both coupled models, the inclusion of air-sea coupling was responsible for maintaining the phase relationship between SSTs and convection events at longer forecast lead times. This is further supported by the large correlations in KPP and NEMO, which were approximately 0.58 for the +7 day forecast when compared against Tropflux, in contrast to a correlation of -0.27 in NWP. Previous studies (Fu and Wang, 2004b; Klingaman et al., 2008a; Liu et al., 2018) also confirmed the role of air-sea coupling in correcting the SST-convection relationship in coupled model simulations.

To further understand the failure of the models to forecast the transition of the active phase at longer lead times, composites of mixing ratio anomalies were shown. As discussed previously, the northward propagation of enhanced convection was associated with moisture anomalies deep in the vertical. With increasing lead times, the moisture anomalies were considerably weaker than observations over the NBoB. Furthermore, the weak moisture anomalies were restricted to between the surface and 600 hPa. Dry anomalies were also found above the moist anomalies, which may inhibit anomalous instability and thus weakened the enhanced convection and rainfall associated with the active phase.

Therefore, analysis of the rainfall anomalies suggests three significant findings: (1) the atmosphere-only GA6.1 NWP model was able to forecast the break-to-active transition but, performing better than both coupled models but only shorter forecast lead times (1-3 days lead). Air-sea coupling did not improve the forecasts for this event. (2) The NEMO and

KPP model forecasts of the rainfall anomalies were comparable, which suggests that the representation of a three-dimensional ocean dynamics in NEMO also did not improve the forecasts. (3) The BSISO weakens in all models with lead time as all three models failed to forecast the active phase at longer leads. These findings suggest that the atmosphere-only NWP model was able to forecast the transition to the active phase for the 2016 season. In fact, the NWP model performed better than both coupled models, especially at shorter forecast lead times of about 1-3 days. However, the forecasts in all models deteriorated significantly at longer lead times such that the active phase was delayed and its duration was shortened by 2-3 days. Thus, air-sea coupling did not improve the seven-day forecast of the break-to-active transition, but it is essential to maintain the SST-convection phase relationship. Additionally, the inclusion of ocean dynamics in the NEMO model did not result in any improvements compared to the KPP model. Therefore, other mechanisms may be more dominant during the 2016 season, for instance, the internal atmospheric dynamics which were suggested by Jiang et al. (2004) as a possible mechanism for the northward-propagating BSISO. On the other hand, the results may also suggest the deficiency in the models to forecast the break-to-active transition. This deficiency may be attributed to the inability of the Met Office GA6.1 model to accurately represent physical processes associated with the BSISO such as the convection. This may point to the convection scheme used in GA6.1 that may have misrepresented low-level moisture processes (i.e., cumulus momentum transport) that is important for convection. Furthermore, this study reveals the competition between the internal atmosphere dynamics and air-sea coupling, which may vary between seasons.

According to Webster and Hoyos (2004), the stakeholders of the agricultural sector requires socio-economically relevant forecasts with 14-21 days lead time in order to maintain their crops. In observations, the warm SST anomalies associated with the BSISO showed persistence of approximate 10 days. This is a possible reason as to why the NWP model was able to forecast the northward propagation at shorter leads since this study only analysed forecast of the NWP with a 7-day persisted SST. Thus, it is difficult to suggest if the atmosphere-only NWP model can produce improved and relevant forecasts of the break-to-active transition beyond seven days. It can be hypothesised that the northward propagation in the NWP beyond seven days will be much weaker or even disappear completely since the warm SSTs cannot be maintained. Thus, in order to provide beneficial forecast for the stakeholders, coupled models may be required.

7.2 Limitations and caveats

Due to the limited availability of observational and reanalysis datasets, only active and break events in the period 1979-2016 were analysed. This limited the number of active,

break and transition events that were identified. Furthermore, the break-to-active transition was selected based on a 30-day criterion. This criterion is arbitrary, and the number of break-to-active events may be increased if the criterion was extended to 40 days. I also did not apply a minimum transition time; for example, some transition may have a maximum period of 10 days. Thus the samples may include transitions associated with the 10-20 day variability modes which are in contrast to the 30-60 day mode linked to the BSISO. Therefore, this may significantly reduce the robustness and statistical significance of the events as it may also include transitions that are not physically associated with the BSISO. In addition, the active and break events selected are influenced by interannual variability such as El Niño and La Niña conditions. As discussed in Chapter 2, El Niño conditions favour break phases while La Niña conditions favour active phases. My transition events may be skewed to one condition over the other due to the limited number of samples. It is possible that these composites of the break-to-active transition would differ if a larger sample of the events has been used.

Next, the use of reanalysis datasets to analyse the dynamics, thermodynamics and oceanic surface variables associated with BSISO may result in inaccuracies. This is most apparent in the assessment of the moisture and radiation budget in reanalysis. For example, ERA-Interim does not have a closed moisture budget, and thus, may misrepresent the evaporation and precipitation term. However, a residual term was calculated as in Trenberth and Fasullo (2013a) and showed small residual values. However, analysis of the moisture budget in Chapter 4 and 5 should be taken with careful consideration of this issue. Reanalysis datasets are produced by assimilating observations and model simulations which may vary depending on the location, time period, and variable considered which may affect its reliability. Furthermore, biases in observations and models may introduce spurious variability in the reanalysis output. For instance, large biases, especially in surface fluxes variables, arises due to inconsistent forcing data of the model simulations, and imperfect parameterisations. In order to mitigate this issue, I used ERA-Interim/Land variables in Chapter 5 when analysing the soil moisture and surface turbulent fluxes due to the application of the Hydrology-Tiled ECMWF Scheme for Surface Exchanges over Land. It was shown by Balsamo et al. (2011) that the latent and sensible heat fluxes were improved by 8% (based on the root-mean square error) compared to ERA-Interim. Nevertheless, the use of reanalysis datasets provides the best method to study the break-to-active transition.

While a more extended period of the IMD gridded rainfall datasets is available (1950 to present), which would overcome the issue of small active, break and transitions events sample size, I am limited by the availability of the reanalysis dataset. The ERA-Interim dataset only spans for the period 1979-2019. Therefore, a longer period and thus larger number of transition events could not be analysed. Recently, the ECMWF's next-generation reanalysis dataset, the ERA5 (Hersbach et al., 2019; Hoffmann et al., 2019) provides a new opportunity

to overcome this limitation. At the time of writing, the production of ERA5 is complete for the period 1979 to present. However, by early 2020, ERA5 will provide a detailed record of the global atmosphere and land surface parameters from 1950 onwards. In addition, ERA5 consists of a 10-member ensemble of data assimilations which provides information on uncertainties in the dataset and their changes over space and time. Despite this, several datasets will still be limited, for example, the outgoing-longwave radiation (from the National Oceanic and Atmospheric Administration) and sea surface temperature (from Tropflux) as the datasets are only constrained for 1979 to present.

In Chapter 6, I have discussed that the models were unable to accurately forecast the 2016 transition at longer lead times such that the active phase showed a late initiation and shorter period. I have related this to the poor quality of the model in forecasting this event. I am limited to the use of a single model, the Met Office GA6.1 model, and its different configurations in this thesis. Furthermore, I have only analysed the forecast for a single transition. Therefore, it is difficult to determine the statistical significance and the performance of the model in forecasting the break-to-active transition based on a single event. Similarly, the role of air-sea coupling in forecasting the break-to-active transition is also challenging to determine since I have only analysed 7-day forecast output. While the inclusion of air-sea coupling did not improve the performance in a 7-day forecast, it could be important for longer forecast lead times, for example in a 20-day forecast. Analysis of a longer-range forecast in the models would be inefficient since the coupled models failed to forecast the transition even in a 7-day forecast. In addition, analysing several transition event would also reveal whether forecast of the break-to-active transition in an atmosphere-only NWP model has better performance and skill compared to coupled NWP models.

In order to overcome this limitation, alternative datasets such as the Subseasonal-to-Seasonal (S2S) Prediction project (Vitart et al., 2017) can be used. The S2S project contains an extensive database containing sub-seasonal forecasts and reforecasts from 11 institutions ranging from 32 to 60 days. Furthermore, some models have a reforecast period exceeding 30 years. Therefore, the S2S datasets will allow me to analyse multiple break-to-active transitions with longer forecast lead times which was not possible in this thesis. The predictability of the break-to-active transition can also be studied and can be compared in multiple models. Jie et al. (2017) used the S2S dataset for period May to October 1999–2010 to study the BSISO and showed that the skill of a single model forecast is around 6–17.5 days. However, when adopting a multimodel ensemble mean approach, some models, for example, the European Centre for Medium-Range Weather Forecast model showed an increase in their forecast skills of approximately 10–24.5 days. However, a drawback of using the S2S datasets is that the role of coupling cannot be diagnosed since most of the models (7 out of 11) participating in the S2S project uses coupled models.

7.3 Future work

The results from this thesis provide a new avenue for future research of the break-to-active transition and the intraseasonal variability of the Indian monsoon associated with the BSISO. In chapter 4, the break-to-active transition was shown to be associated with northward-propagating moisture anomalies originating from the equatorial Indian Ocean. While this was observed in reanalysis datasets, a sensitivity experiment can be conducted to determine whether northward-propagating moisture anomalies are a requirement for a transition. Future work on simulating the break-to-active transition may focus on using models with modified moisture anomalies. For example, what would the representation of the break-to-active transition be if the moisture anomalies in the atmosphere are drier or wetter? If moisture anomalies were necessary for transition, then the northward propagation and thus the transition would not occur in simulations with a drier atmosphere.

In chapter 5, the influence of land-atmosphere coupling on the break-to-active transition is regionally dependent as there are different regimes (soil moisture-limited and energy-limited regime) over India. Since modelling studies over the Indian subcontinent during the break-to-active transition were not conducted in Chapter 5, future work on forecasting the transition in simulations with different soil moisture states. Notably, how land-atmosphere coupling may affect the northward propagation of the BSISO over the Indian subcontinent under a drier (or wetter) than normal soil moisture during the break. This may also be potentially important in the future to understand how irrigation for agricultural purposes may influence the intraseasonal variability of the Indian monsoon. These efforts can be achieved by testing the sensitivity of the break-to-active transition in forecast models by using differing land-surface initialisation and modifying initial soil moisture. The impact on the timing and magnitude of the active phase under these scenarios would be relevant for stakeholders such as farmers and water management agencies.

Perhaps the most significant finding of this thesis is the suggestion that the uncoupled NWP forecast model was able to simulate a robust northward propagating signal with lead times of 1–3 days. An equally significant result is that air-sea coupling in the coupled models did not improve the forecast. While this study suggests that air-sea coupling may not be necessary for forecasting short-scale processes such as the active-to-break transition, extending the forecast analysis beyond seven days such that there are changes in the SST variability should be undertaken to verify this hypothesis. Furthermore, this study would also benefit from a sensitivity experiment on the NWP model. It would be interesting to understand the improvements (if any) in the performance of the NWP model when forced with SSTs obtained from the coupled model. Fu and Wang (2004a) had shown that the northward signal of the BSISO was improved in terms of its magnitude and spatial pattern when

the atmospheric general circulation model was forced with SSTs from their coupled model counter-part. However, it is worth noting that their study was based on climate simulations and not initialised forecasts. More importantly, the northward propagation in their coupled model was better than the atmosphere-only model. The role of air-sea coupling in the forecast of the break-to-active transition can only be achieved by extending the forecast beyond seven days and for multiple events in models that better simulated the northward-propagating BSISO.

Previous studies (Goswami and Xavier, 2003; Abhilash et al., 2014; Krishnamurthy and Sharma, 2017) have shown weaker prediction skill during the break-to-active transition, with a predictability limit of about 10-12 days. The lower skill in the prediction of the break-to-active transition was attributed to the substantial and quick growth in errors due to fast-growing convective instability which is difficult to predict. Furthermore, this assessment is based on a single event only, and the statistical significance and the robustness of the event in the model questionable. However, the low performance of the three models used to forecast the break-to-active transition remains inconclusive as the results were not compared against active-to-break convection for the 2016 season. It may be that the performance of the model in forecasting the active-to-break transition is equally weak. Future work on the forecast of the active-to-break transition using the S2S database as discussed in the previous section should be conducted to determine this hypothesis and, if air-sea coupling may impact the forecast of this transition. It may be that the forecast of the intraseasonal variability in the Met Office GA6.1 model is limited. Applying the methods in this thesis to the S2S database as discussed in the previous section will assist with overcoming the 1) the small sample size of transition, 2) the limited length of the forecast period and 3) the use of a single model to forecast the break-to-active transition. However, as previously discussed, the role of air-sea coupling cannot be determined from the S2S database.

REFERENCES

- Abhik, S., M. Halder, P. Mukhopadhyay, X. Jiang, and B. N. Goswami, 2013: A possible new mechanism for northward propagation of boreal summer intraseasonal oscillations based on TRMM and MERRA reanalysis. *Climate Dynamics*, **40** (7), 1611–1624, doi:10.1007/s00382-012-1425-x.
- Abhilash, S., A. K. Sahai, N. Borah, R. Chattopadhyay, S. Joseph, S. Sharmila, S. De, B. N. Goswami, and A. Kumar, 2014: Prediction and monitoring of monsoon intraseasonal oscillations over Indian monsoon region in an ensemble prediction system using CFSv2. *Climate Dynamics*, **42** (9), 2801–2815.
- Adam, O., T. Bischoff, and T. Schneider, 2016: Seasonal and Interannual Variations of the Energy Flux Equator and ITCZ. Part I: Zonally Averaged ITCZ Position. *Journal of Climate*, **29** (9), 3219–3230, doi:10.1175/JCLI-D-15-0512.1.
- Adler, R. F., G. J. Huffman, A. Chang, R. Ferraro, P.-P. Xie, J. Janowiak, B. Rudolf, U. Schneider, S. Curtis, D. Bolvin, A. Gruber, J. Susskind, P. Arkin, and E. Nelkin, 2003: The Version-2 Global Precipitation Climatology Project (GPCP) Monthly Precipitation Analysis (1979-Present). *Journal of Hydrometeorology*, **4** (6), 1147–1167, doi:10.1175/1525-7541(2003)004<1147:TVGPCP>2.0.CO;2.
- Allan, R., D. Chambers, W. Drosowsky, H. Hendon, M. Latif, N. Nicholls, I. Smith, R. C. Stone, and Y. Tourre, 2001: Is there an Indian Ocean dipole and is it independent of the El Niño-Southern Oscillation? *CLIVAR Exchanges*, **6**.
- Aneesh, S., and S. Sijikumar, 2018: Changes in the La Niña teleconnection to the Indian summer monsoon during recent period. *Journal of Atmospheric and Solar-Terrestrial Physics*, **167**, 74–79, doi:10.1016/j.jastp.2017.11.009.
- Annamalai, H., and J. M. Slingo, 2001: Active/break cycles: diagnosis of the intraseasonal variability of the Asian Summer Monsoon. *Climate Dynamics*, **18** (1), 85–102, doi:10.1007/s003820100161.
- Annamalai, H., and K. R. Sperber, 2005: Regional Heat Sources and the Active and Break Phases of Boreal Summer Intraseasonal (30-50 Day) Variability. *Journal of the Atmospheric Sciences*, **62** (8), 2726–2748, doi:10.1175/JAS3504.1.
- Asharaf, S., A. Dobler, and B. Ahrens, 2011: Soil moisture initialization effects in the Indian monsoon system. *Advances in Science and Research*, **6** (1), 161–165, doi:10.5194/asr-6-161-2011.
- Asharaf, S., A. Dobler, and B. Ahrens, 2012: Soil Moisture-Precipitation Feedback Processes in the Indian Summer Monsoon Season. *Journal of Hydrometeorology*, **13** (5), 1461–1474, doi:10.1175/JHM-D-12-06.1.
- Ashfaq, M., D. Rastogi, R. Mei, D. Touma, and L. Ruby Leung, 2017: Sources of errors in the simulation of south Asian summer monsoon in the CMIP5 GCMs. *Climate Dynamics*, **49** (1).
- Ashok, K., S. K. Behera, S. A. Rao, H. Weng, and T. Yamagata, 2007: El Niño Modoki and its possible teleconnection. *Journal of Geophysical Research: Oceans*, **112** (C11), doi:10.1029/2006JC003798.
- Ashok, K., Z. Guan, N. H. Saji, and T. Yamagata, 2004: Individual and combined influences of enso and the indian ocean dipole on the indian summer monsoon. *Journal of Climate*, **17** (16), 3141–3155, doi:10.1175/1520-0442(2004)017<3141:IACIOE>2.0.CO;2.

REFERENCES

- Ashok, K., Z. Guan, and T. Yamagata, 2003: A Look at the Relationship between the ENSO and the Indian Ocean Dipole. *Journal of the Meteorological Society of Japan. Ser. II*, **81** (1), 41–56, doi:10.2151/jmsj.81.41.
- Balsamo, G., A. Beljaars, K. Scipal, P. Viterbo, B. van den Hurk, M. Hirschi, and A. K. Betts, 2009: A Revised Hydrology for the ECMWF Model: Verification from Field Site to Terrestrial Water Storage and Impact in the Integrated Forecast System. *Journal of Hydrometeorology*, **10** (3), 623–643, doi:10.1175/2008JHM1068.1.
- Balsamo, G., S. Boussetta, E. Dutra, A. Beljaars, P. Viterbo, and B. van den Hurk, 2011: Evolution of land-surface processes in the IFS. 17–22, doi:10.21957/x1j3i7bz, URL <https://www.ecmwf.int/node/17444>.
- Balsamo, G., C. Albergel, A. Beljaars, S. Boussetta, E. Brun, H. Cloke, D. Dee, E. Dutra, J. Muñoz Sabater, F. Pappenberger, P. de Rosnay, T. Stockdale, and F. Vitart, 2015: ERA-Interim/Land: a global land surface reanalysis data set. *Hydrology and Earth System Sciences*, **19** (1), 389–407, doi:10.5194/hess-19-389-2015.
- Baquero-Bernal, A., M. Latif, and S. Legutke, 2002: On Dipolelike Variability of Sea Surface Temperature in the Tropical Indian Ocean. *Journal of Climate*, **15** (11), 1358–1368, doi:10.1175/1520-0442(2002)015<1358:ODVOSS>2.0.CO;2.
- Barimalala, R., A. Bracco, and F. Kucharski, 2012: The representation of the South Tropical Atlantic teleconnection to the Indian Ocean in the AR4 coupled models. *Climate Dynamics*, **38** (5), 1147–1166, doi:10.1007/s00382-011-1082-5.
- Barnett, T. P., L. Dümenil, U. Schlese, E. Roeckner, and M. Latif, 1989: The Effect of Eurasian Snow Cover on Regional and Global Climate Variations. *Journal of the Atmospheric Sciences*, **46** (5), 661–686.
- Barton, E. J., C. M. Taylor, D. J. Parker, A. G. Turner, D. Belusic, S. J. Böing, J. K. Brooke, R. C. Harlow, P. P. Harris, K. Hunt, A. Jayakumar, and A. K. Mitra, 2019: A case-study of land-atmosphere coupling during monsoon onset in northern India. *Quarterly Journal of the Royal Meteorological Society*, 1–15, doi:10.1002/qj.3538.
- Basu, B. K., 2007: Diurnal variation in precipitation over India during the summer monsoon season: Observed and model predicted. *Monthly Weather Review*, **135** (6), 2155–2167, doi:10.1175/MWR3355.1.
- Befort, D. J., G. C. Leckebusch, and U. Cubasch, 2016: Intraseasonal variability of the indian summer monsoon: wet and dry events in cosmo-clm. *Climate Dynamics*, **47** (7), 2635–2651, doi:10.1007/s00382-016-2989-7.
- Beljaars, A. C. M., P. Viterbo, M. J. Miller, and A. K. Betts, 1996: The Anomalous Rainfall over the United States during July 1993: Sensitivity to Land Surface Parameterization and Soil Moisture Anomalies. *Monthly Weather Review*, **124** (3), 362–383, doi:10.1175/1520-0493(1996)124<0362:TAROTU>2.0.CO;2.
- Bellon, G., 2011: Monsoon intraseasonal oscillation and land-atmosphere interaction in an idealized model. *Climate Dynamics*, **37** (5), 1081–1096, doi:10.1007/s00382-010-0893-0.
- Bellon, G., and A. Sobel, 2008a: Poleward-Propagating Intraseasonal Monsoon Disturbances in an Intermediate-Complexity Axisymmetric Model. *Journal of the Atmospheric Sciences*, **65** (2), 470–489, doi:10.1175/2007JAS2339.1.

REFERENCES

- Bellon, G., and A. H. Sobel, 2008b: Instability of the axisymmetric monsoon flow and intraseasonal oscillation. *Journal of Geophysical Research: Atmospheres*, **113** (D7), 1–11, doi:10.1029/2007JD009291, d07108.
- Bernie, D. J., S. J. Woolnough, J. M. Slingo, and E. Guilyardi, 2005: Modeling diurnal and intraseasonal variability of the ocean mixed layer. *Journal of Climate*, **18** (8), 1190–1202, doi:10.1175/JCLI3319.1.
- Berrisford, P., P. Kållberg, S. Kobayashi, D. Dee, S. Uppala, A. J. Simmons, P. Poli, and H. Sato, 2011: Atmospheric conservation properties in ERA-Interim. *Quarterly Journal of the Royal Meteorological Society*, **137** (659), 1381–1399, doi:10.1002/qj.864.
- Betts, A. K., J. H. Ball, A. C. M. Beljaars, M. J. Miller, and P. A. Viterbo, 1996: The land surface-atmosphere interaction: A review based on observational and global modeling perspectives. *Journal of Geophysical Research: Atmospheres*, **101** (D3), 7209–7225, doi:10.1029/95JD02135.
- Bhat, G. S., 2006: The Indian drought of 2002 - a sub-seasonal phenomenon? *Quarterly Journal of the Royal Meteorological Society*, **132** (621), 2583–2602, doi:10.1256/qj.05.13.
- Bhat, G. S., S. Gadgil, P. V. H. Kumar, S. R. Kalsi, P. Madhusoodanan, V. S. N. Murty, C. V. K. P. Rao, V. R. Babu, L. V. G. Rao, R. R. Rao, M. Ravichandran, K. G. Reddy, P. S. Rao, D. Sengupta, D. R. Sikka, J. Swain, and P. N. Vinayachandran, 2001: BOBMEX: The Bay of Bengal Monsoon Experiment. *Bulletin of the American Meteorological Society*, **82** (10), 2217–2243, doi:10.1175/1520-0477(2001)082<2217:BTBOBM>2.3.CO;2.
- Bjerknes, J., 1969: Atmospheric Teleconnections from the Equatorial Pacific. *Monthly Weather Review*, **97** (3), 163–172, doi:10.1175/1520-0493(1969)097<0163:ATFTEP>2.3.CO;2.
- Blanford, H. F., 1884: On the connexion of the himalaya snowfall with dry winds and seasons of drought in india. *Proceedings of the Royal Society of London*, **37** (232-234), 3–22, doi:10.1098/rspl.1884.0003.
- Bracco, A., F. Kucharski, F. Molteni, W. Hazeleger, and C. Severijns, 2007: A recipe for simulating the interannual variability of the Asian summer monsoon and its relation with ENSO. *Climate Dynamics*, **28** (5), 441–460.
- Brown, A., S. Milton, M. Cullen, B. Golding, J. Mitchell, and A. Shelly, 2012: Unified Modeling and Prediction of Weather and Climate: A 25-Year Journey. *Bulletin of the American Meteorological Society*, **93** (12), 1865–1877, doi:10.1175/BAMS-D-12-00018.1.
- Budyko, M. I., 1963: *Evaporation Under Natural Conditions*. Israel Program for Scientific Translations.
- Byun, J.-K., J.-H. Son, and K.-N. Ko, 2016: Reliability assessment of ERA-Interim/MERRA reanalysis data for the offshore wind resource assessment. *Journal of the Korea Society For Power System Engineering*, **20**, 44–51, doi:10.9726/kspse.2016.20.4.044.
- Chakravarty, K., S. Pokhrel, M. Kalshetti, A. K. M. Nair, M. C. R. Kalapureddy, S. M. Deshpande, S. K. Das, G. Pandithurai, and B. N. Goswami, 2018: Unraveling of cloud types during phases of monsoon intra-seasonal oscillations by a Ka-band Doppler weather radar. *Atmospheric Science Letters*, **19** (9), e847, doi:10.1002/asl.847.
- Chang, C.-P., and T. Li, 2000: A Theory for the Tropical Tropospheric Biennial Oscillation. *Journal of the Atmospheric Sciences*, **57** (14), 2209–2224, doi:10.1175/1520-0469(2000)057<2209:ATFTTT>2.0.CO;2.

- Charney, J., and J. Shukla, 1981: Monsoon Dynamics: Predictability of Monsoons, edited by: Lighthill, J. and Pearce, R. Cambridge University Press, Cambridge, UK.
- Chevuturi, A., A. G. Turner, S. J. Woolnough, G. M. Martin, and C. MacLachlan, 2019: Indian summer monsoon onset forecast skill in the UK Met Office initialized coupled seasonal forecasting system (GloSea5-GC2). *Climate Dynamics*, **52** (11), 6599–6617, doi:10.1007/s00382-018-4536-1.
- Chou, C., and Y.-C. Hsueh, 2010: Mechanisms of Northward-Propagating Intraseasonal Oscillation—A Comparison between the Indian Ocean and the Western North Pacific. *Journal of Climate*, **23** (24), 6624–6640, doi:10.1175/2010JCLI3596.1.
- Christensen, J., K. Krishna Kumar, E. Aldrian, S.-I. An, I. Cavalcanti, M. de Castro, W. Dong, P. Goswami, A. Hall, J. Kanyanga, A. Kitoh, J. Kossin, N.-C. Lau, J. Renwick, D. Stephenson, S.-P. Xie, and T. Zhou, 2013: Climate phenomena and their relevance for future regional climate change. Cambridge University Press, Cambridge, United Kingdom and New York, NY, USA, URL www.climatechange2013.org, 1217–1308 pp., doi:10.1017/CBO9781107415324.028.
- Cook, B. I., G. B. Bonan, and S. Levis, 2006: Soil Moisture Feedbacks to Precipitation in Southern Africa. *Journal of Climate*, **19** (17), 4198–4206, doi:10.1175/JCLI3856.1.
- Craig, A., S. Valcke, and L. Coquart, 2017: Development and performance of a new version of the OASIS coupler, OASIS3-MCT_3.0. *Geoscientific Model Development*, **10** (9), 3297–3308, doi:10.5194/gmd-10-3297-2017.
- Dandi, R. A., J. S. Chowdary, P. A. Pillai, S. Sidhan N. S., K. K., and R. S.S.V.S., 2019: Impact of el niño modoki on indian summer monsoon rainfall: Role of western north pacific circulation in observations and cmip5 models. *International Journal of Climatology*, **n/a** (n/a), doi:10.1002/joc.6322.
- De, U. S., R. R. Lele, and J. C. Natu, 1998: Breaks in southwest monsoon. Tech. Rep. 1998/3, Indian Meteorological Department.
- Dee, D. P., and S. Uppala, 2009: Variational bias correction of satellite radiance data in the ERA-Interim reanalysis. *Quarterly Journal of the Royal Meteorological Society*, **135** (644), 1830–1841, doi:10.1002/qj.493.
- Dee, D. P., S. M. Uppala, A. J. Simmons, P. Berrisford, P. Poli, S. Kobayashi, U. Andrae, M. A. Balmaseda, G. Balsamo, P. Bauer, P. Bechtold, A. C. M. Beljaars, L. van de Berg, J. Bidlot, N. Bormann, C. Delsol, R. Dragani, M. Fuentes, A. J. Geer, L. Haimberger, S. B. Healy, H. Hersbach, E. V. Hólm, L. Isaksen, P. Kållberg, M. Köhler, M. Matricardi, A. P. McNally, B. M. Monge-Sanz, J.-J. Morcrette, B.-K. Park, C. Peubey, P. de Rosnay, C. Tavolato, J.-N. Thépaut, and F. Vitart, 2011a: The ERA-Interim reanalysis: configuration and performance of the data assimilation system. *Quarterly Journal of the Royal Meteorological Society*, **137** (656), 553–597, doi:10.1002/qj.828.
- Dee, D. P., S. M. Uppala, A. J. Simmons, P. Berrisford, P. Poli, S. Kobayashi, U. Andrae, M. A. Balmaseda, G. Balsamo, P. Bauer, P. Bechtold, A. C. M. Beljaars, L. van de Berg, J. Bidlot, N. Bormann, C. Delsol, R. Dragani, M. Fuentes, A. J. Geer, L. Haimberger, S. B. Healy, H. Hersbach, E. V. Hólm, L. Isaksen, P. Kållberg, M. Köhler, M. Matricardi, A. P. McNally, B. M. Monge-Sanz, J.-J. Morcrette, B.-K. Park, C. Peubey, P. de Rosnay, C. Tavolato, J.-N. Thépaut, and F. Vitart, 2011b: The ERA-Interim reanalysis: configuration and performance of the data assimilation system. *Quarterly Journal of the Royal Meteorological Society*, **137** (656), 553–597, doi:10.1002/qj.828.

- DeMott, C. A., J. J. Benedict, N. P. Klingaman, S. J. Woolnough, and D. A. Randall, 2016: Diagnosing ocean feedbacks to the MJO: SST-modulated surface fluxes and the moist static energy budget. *Journal of Geophysical Research: Atmospheres*, **121** (14), 8350–8373, doi:10.1002/2016JD025098.
- DeMott, C. A., C. Stan, and D. A. Randall, 2013: Northward Propagation Mechanisms of the Boreal Summer Intraseasonal Oscillation in the ERA-Interim and SP-CCSM. *Journal of Climate*, **26** (6), 1973–1992, doi:10.1175/JCLI-D-12-00191.1.
- DeMott, C. A., C. Stan, D. A. Randall, and M. D. Branson, 2014: Intraseasonal Variability in Coupled GCMs: The Roles of Ocean Feedbacks and Model Physics. *Journal of Climate*, **27** (13), 4970–4995, doi:10.1175/JCLI-D-13-00760.1.
- Devanand, A., M. Huang, M. Ashfaq, B. Barik, and S. Ghosh, 2019: Choice of Irrigation Water Management Practice Affects Indian Summer Monsoon Rainfall and Its Extremes. *Geophysical Research Letters*, **46** (15), 9126–9135, doi:10.1029/2019GL083875.
- Dirmeyer, P. A., 2006: The Hydrologic Feedback Pathway for Land-Climate Coupling. *Journal of Hydrometeorology*, **7** (5), 857–867, doi:10.1175/JHM526.1.
- Dirmeyer, P. A., 2011: The terrestrial segment of soil moisture-climate coupling. *Geophysical Research Letters*, **38** (16), doi:10.1029/2011GL048268.
- Dirmeyer, P. A., and S. Halder, 2017: Application of the Land-Atmosphere Coupling Paradigm to the Operational Coupled Forecast System, Version 2 (CFSv2). *Journal of Hydrometeorology*, **18** (1), 85–108, doi:10.1175/JHM-D-16-0064.1.
- Dirmeyer, P. A., Z. Wang, M. J. Mbulu, and H. E. Norton, 2014: Intensified land surface control on boundary layer growth in a changing climate. *Geophysical Research Letters*, **41** (4), 1290–1294, doi:10.1002/2013GL058826.
- D’Odorico, P., and A. Porporato, 2004: Preferential states in soil moisture and climate dynamics. *Proceedings of the National Academy of Sciences*, **101** (24), 8848–8851, doi:10.1073/pnas.0401428101.
- Donlon, C. J., M. Martin, J. Stark, J. Roberts-Jones, E. Fiedler, and W. Wimmer, 2012: The Operational Sea Surface Temperature and Sea Ice Analysis (OSTIA) system. *Remote Sensing of Environment*, **116**, 140 – 158, doi:https://doi.org/10.1016/j.rse.2010.10.017, advanced Along Track Scanning Radiometer(AATSR) Special Issue.
- Douville, H., F. Chauvin, and H. Broqua, 2001: Influence of Soil Moisture on the Asian and African Monsoons. Part I: Mean Monsoon and Daily Precipitation. *Journal of Climate*, **14** (11), 2381–2403, doi:10.1175/1520-0442(2001)014<2381:IOSMOT>2.0.CO;2.
- Draper, C. S., R. H. Reichle, and R. D. Koster, 2018: Assessment of MERRA-2 Land Surface Energy Flux Estimates. *Journal of Climate*, **31** (2), 671–691, doi:10.1175/JCLI-D-17-0121.1.
- Drbohlav, H.-K. L., and B. Wang, 2005: Mechanism of the Northward-Propagating Intraseasonal Oscillation: Insights from a Zonally Symmetric Model. *Journal of Climate*, **18** (7), 952–972.
- Dutra, E., G. Balsamo, P. Viterbo, P. M. A. Miranda, A. Beljaars, C. Schär, and K. Elder, 2010: An Improved Snow Scheme for the ECMWF Land Surface Model: Description and Offline Validation. *Journal of Hydrometeorology*, **11** (4), 899–916, doi:10.1175/2010JHM1249.1.
- Duvel, J. P., and J. Vialard, 2007: Indo-Pacific Sea Surface Temperature Perturbations Associated with Intraseasonal Oscillations of Tropical Convection. *Journal of Climate*, **20** (13), 3056–3082, doi:10.1175/JCLI4144.1.

REFERENCES

- Eltahir, E. A. B., 1998: A Soil Moisture-Rainfall Feedback Mechanism: 1. Theory and observations. *Water Resources Research*, **34** (4), 765–776, doi:10.1029/97WR03499.
- Fairall, C. W., E. F. Bradley, J. E. Hare, A. A. Grachev, and J. B. Edson, 2003: Bulk Parameterization of Air-Sea Fluxes: Updates and Verification for the COARE Algorithm. *Journal of Climate*, **16** (4), 571–591, doi:10.1175/1520-0442(2003)016<0571:BPOASF>2.0.CO;2.
- Fang, Y., P. Wu, M. Mizieliński, M. Roberts, B. Li, X. Xin, and X. Liu, 2017a: Monsoon intra-seasonal variability in a high-resolution version of Met Office Global Coupled model. *Tellus A: Dynamic Meteorology and Oceanography*, **69** (1), 1354 661, doi:10.1080/16000870.2017.1354661.
- Fang, Y., P. Wu, T. Wu, Z. Wang, L. Zhang, X. Liu, X. Xin, and A. Huang, 2017b: An evaluation of boreal summer intra-seasonal oscillation simulated by BCC_AGCM2.2. *Climate Dynamics*, **48** (9), 3409–3423, doi:10.1007/s00382-016-3275-4.
- Fang, Y., P. Wu, M. S. Mizieliński, M. J. Roberts, T. Wu, B. Li, P. L. Vidale, M.-E. Demory, and R. Schiemann, 2017c: High-resolution simulation of the boreal summer intraseasonal oscillation in Met Office Unified Model. *Quarterly Journal of the Royal Meteorological Society*, **143** (702), 362–373, doi:10.1002/qj.2927.
- Fasullo, J., 2004: A Stratified Diagnosis of the Indian Monsoon-Eurasian Snow Cover Relationship. *Journal of Climate*, **17** (5), 1110–1122, doi:10.1175/1520-0442(2004)017<1110:ASDOTI>2.0.CO;2.
- Ferranti, L., J. M. Slingo, T. N. Palmer, and B. J. Hoskins, 1999: The effect of land-surface feedbacks on the monsoon circulation. *Quarterly Journal of the Royal Meteorological Society*, **125** (557), 1527–1550, doi:10.1002/qj.49712555704.
- Findell, K. L., and E. A. B. Eltahir, 1997: An analysis of soil moisture-rainfall feedback, based on direct observations from Illinois. *Water Resources Research*, **33** (4), 725–735, doi:10.1029/96WR03756.
- Frye, J. D., and T. L. Mote, 2010a: Convection Initiation along Soil Moisture Boundaries in the Southern Great Plains. *Monthly Weather Review*, **138** (4), 1140–1151, doi:10.1175/2009MWR2865.1.
- Frye, J. D., and T. L. Mote, 2010b: The Synergistic Relationship between Soil Moisture and the Low-Level Jet and Its Role on the Prestorm Environment in the Southern Great Plains. *Journal of Applied Meteorology and Climatology*, **49** (4), 775–791.
- Fu, X., and B. Wang, 2004a: Differences of Boreal Summer Intraseasonal Oscillations Simulated in an Atmosphere-Ocean Coupled Model and an Atmosphere-Only Model. *Journal of Climate*, **17** (6), 1263–1271, doi:10.1175/1520-0442(2004)017<1263:DOBSIO>2.0.CO;2.
- Fu, X., and B. Wang, 2004b: The Boreal-Summer Intraseasonal Oscillations Simulated in a Hybrid Coupled Atmosphere-Ocean Model. *Monthly Weather Review*, **132** (11), 2628–2649, doi:10.1175/MWR2811.1.
- Fu, X., B. Wang, T. Li, and J. P. McCreary, 2003: Coupling between Northward-Propagating, Intraseasonal Oscillations and Sea Surface Temperature in the Indian Ocean. *Journal of the Atmospheric Sciences*, **60** (15), 1733–1753, doi:10.1175/1520-0469(2003)060<1733:CBNIOA>2.0.CO;2.
- Gadgil, S., 1990: Poleward propagation of the ITCZ: Observations and theory. *Muwasam*, **41** (1), 285–290.

REFERENCES

- Gadgil, S., 2003: The indian monsoon and its variability. *Annual Review of Earth and Planetary Sciences*, **31** (1), 429–467, doi:10.1146/annurev.earth.31.100901.141251.
- Gadgil, S., 2018: The monsoon system: Land–sea breeze or the itcz? *Journal of Earth System Science*, **127** (1), 1–29, doi:10.1007/s12040-017-0916-x.
- Gadgil, S., and P. V. Joseph, 2003: On breaks of the Indian monsoon. *Journal of Earth System Science*, **112** (4), 529–558, doi:10.1007/BF02709778.
- Gadgil, S., and J. Srinivasan, 2011: Seasonal prediction of the indian monsoon. *Curr. Sci.*, **100**.
- Gadgil, S., P. N. Vinayachandran, and P. A. Francis, 2003: Droughts of the Indian summer monsoon: Role of clouds over the Indian Ocean. *Current Science*, **85** (12), 1713–1719.
- Gadgil, S., P. N. Vinayachandran, P. A. Francis, and S. Gadgil, 2004: Extremes of the Indian summer monsoon rainfall, ENSO and equatorial Indian Ocean oscillation. *Geophysical Research Letters*, **31** (12), 1–4, doi:10.1029/2004GL019733.
- Gao, Y., N. P. Klingaman, C. A. DeMott, and P.-C. Hsu, 2019: Diagnosing Ocean Feedbacks to the BSISO: SST-Modulated Surface Fluxes and the Moist Static Energy Budget. *Journal of Geophysical Research: Atmospheres*, **124** (1), 146–170, doi:10.1029/2018JD029303.
- Gates, W. L., J. S. Boyle, C. Covey, C. G. Dease, C. M. Doutriaux, R. S. Drach, M. Fiorino, P. J. Gleckler, J. J. Hnilo, S. M. Marlais, T. J. Phillips, G. L. Potter, B. D. Santer, K. R. Sperber, K. E. Taylor, and D. N. Williams, 1999: An Overview of the Results of the Atmospheric Model Intercomparison Project (AMIP I). *Bulletin of the American Meteorological Society*, **80** (1), 29–56, doi:10.1175/1520-0477(1999)080<0029:AOOTRO>2.0.CO;2.
- Goddard, L., S. J. Mason, S. E. Zebiak, C. F. Ropelewski, R. Basher, and M. A. Cane, 2001: Current approaches to seasonal to interannual climate predictions. *International Journal of Climatology: A Journal of the Royal Meteorological Society*, **21** (9), 1111–1152.
- Goswami, B. N., R. S. Ajayamohan, P. K. Xavier, and D. Sengupta, 2003: Clustering of synoptic activity by Indian summer monsoon intraseasonal oscillations. *Geophysical Research Letters*, **30** (8), 1–4, doi:10.1029/2002GL016734, 1431.
- Goswami, B. N., and R. S. A. M. Mohan, 2001: Intraseasonal Oscillations and Interannual Variability of the Indian Summer Monsoon. *Journal of Climate*, **14** (6), 1180–1198, doi:10.1175/1520-0442(2001)014<1180:IOAIVO>2.0.CO;2.
- Goswami, B. N., V. Venugopal, D. Sengupta, M. S. Madhusoodanan, and P. K. Xavier, 2006: Increasing Trend of Extreme Rain Events Over India in a Warming Environment. *Science*, **314** (5804), 1442–1445, doi:10.1126/science.1132027, URL <https://science.sciencemag.org/content/314/5804/1442>, <https://science.sciencemag.org/content/314/5804/1442.full.pdf>.
- Goswami, B. N., and P. K. Xavier, 2003: Potential predictability and extended range prediction of Indian summer monsoon breaks. *Geophysical Research Letters*, **30** (18), 1–4, doi:10.1029/2003GL017810.
- Govardhan, D., V. B. Rao, and K. Ashok, 2017: Understanding the revival of the indian summer monsoon after breaks. *Journal of the Atmospheric Sciences*, **74** (5), 1417–1429, doi:10.1175/JAS-D-16-0325.1.
- Guo, Z., P. A. Dirmeyer, and T. DelSole, 2011: Land surface impacts on subseasonal and seasonal predictability. *Geophysical Research Letters*, **38** (24), doi:10.1029/2011GL049945.

REFERENCES

- Gyoswami, B. N., and J. Shukla, 1984: Quasi-Periodic Oscillations in a Symmetric General Circulation Model. *Journal of the Atmospheric Sciences*, **41** (1), 20–37, doi:10.1175/1520-0469(1984)041<0020:QPOIAS>2.0.CO;2.
- Halder, S., and P. A. Dirmeyer, 2017: Relation of eurasian snow cover and indian summer monsoon rainfall: Importance of the delayed hydrological effect. *Journal of Climate*, **30** (4), 1273–1289, doi:10.1175/JCLI-D-16-0033.1.
- Halder, S., P. A. Dirmeyer, L. Marx, and J. L. Kinter, 2018: Impact of Land Surface Initialization and Land-Atmosphere Coupling on the Prediction of the Indian Summer Monsoon with the CFSv2. *Frontiers in Environmental Science*, **5**, 92, doi:10.3389/fenvs.2017.00092.
- Ham, S., S.-Y. Hong, and S. Park, 2014: A study on air-sea interaction on the simulated seasonal climate in an ocean-atmosphere coupled model. *Climate Dynamics*, **42** (5), 1175–1187, doi:10.1007/s00382-013-1847-0.
- Hameed, S., B. N. Goswami, P. Vinayachandran, and T. Yamagata, 1999: A dipole mode in the Tropical Indian Ocean. *Nature*, **401**, 360–3, doi:10.1038/43854.
- Hersbach, H., W. Bell, P. Berrisford, A. Horányi, M.-S. J., J. Nicolas, R. Radu, D. Schepers, A. Simmons, C. Soci, and D. Dee, 2019: Global reanalysis: goodbye ERA-Interim, hello ERA5. 17–24, doi:10.21957/vf291hehd7, URL <https://www.ecmwf.int/node/19027>.
- Hirsch, A. L., A. J. Pitman, and V. Haverd, 2016: Evaluating Land-Atmosphere Coupling Using a Resistance Pathway Framework. *Journal of Hydrometeorology*, **17** (10), 2615–2630, doi:10.1175/JHM-D-15-0204.1.
- Hoffmann, L., G. Günther, D. Li, O. Stein, X. Wu, S. Griessbach, Y. Heng, P. Konopka, R. Müller, B. Vogel, and J. S. Wright, 2019: From ERA-Interim to ERA5: the considerable impact of ECMWF's next-generation reanalysis on Lagrangian transport simulations. *Atmospheric Chemistry and Physics*, **19** (5), 3097–3124, doi:10.5194/acp-19-3097-2019.
- Hsu, H.-H., C.-H. Weng, and C.-H. Wu, 2004: Contrasting Characteristics between the Northward and Eastward Propagation of the Intraseasonal Oscillation during the Boreal Summer. *Journal of Climate*, **17** (4), 727–743, doi:10.1175/1520-0442(2004)017<0727:CCBTNA>2.0.CO;2.
- Huffman, G. J., R. F. Adler, D. T. Bolvin, and G. Gu, 2009: Improving the global precipitation record: GPCP Version 2.1. *Geophysical Research Letters*, **36** (17), doi:10.1029/2009GL040000.
- International Hydropower Association, 2018: 2018 Hydropower Status Report: sector trends and insights. Tech. rep., International Hydropower Association, 1-53 pp. URL https://www.hydropower.org/sites/default/files/publications-docs/iha_2018_hydropower_status_report_4.pdf.
- Jiang, X., T. Li, and B. Wang, 2004: Structures and Mechanisms of the Northward Propagating Boreal Summer Intraseasonal Oscillation. *Journal of Climate*, **17** (5), 1022–1039, doi:10.1175/1520-0442(2004)017<1022:SAMOTN>2.0.CO;2.
- Jie, W., F. Vitart, T. Wu, and X. Liu, 2017: Simulations of the Asian summer monsoon in the sub-seasonal to seasonal prediction project (S2S) database. *Quarterly Journal of the Royal Meteorological Society*, **143** (706), 2282–2295, doi:10.1002/qj.3085.
- Johnson, R. H., P. E. Ciesielski, and K. A. Hart, 1996: Tropical Inversions near the 0°C Level. *Journal of the Atmospheric Sciences*, **53** (13), 1838–1855, doi:10.1175/1520-0469(1996)053<1838:TINTL>2.0.CO;2.

REFERENCES

- Johnson, S. J., A. Turner, S. Woolnough, G. Martin, and C. MacLachlan, 2017: An assessment of Indian monsoon seasonal forecasts and mechanisms underlying monsoon interannual variability in the Met Office GloSea5-GC2 system. *Climate Dynamics*, **48** (5), 1447–1465, doi:10.1007/s00382-016-3151-2, URL <https://doi.org/10.1007/s00382-016-3151-2>.
- Jongaramrungruang, S., H. Seo, and C. C. Ummenhofer, 2017: Intraseasonal rainfall variability in the Bay of Bengal during the Summer Monsoon: coupling with the ocean and modulation by the Indian Ocean Dipole. *Atmospheric Science Letters*, **18** (2), 88–95, doi:10.1002/asl.729.
- Joseph, P. V., and S. Sijikumar, 2004: Intraseasonal Variability of the Low-Level Jet Stream of the Asian Summer Monsoon. *Journal of Climate*, **17** (7), 1449–1458, doi:10.1175/1520-0442(2004)017<1449:IVOTLJ>2.0.CO;2.
- Joseph, P. V., K. P. Sooraj, and C. K. RAJAN, 2006: The summer monsoon onset process over South Asia and an objective method for the date of monsoon onset over Kerala. *International Journal of Climatology*, **26** (13), 1871–1893, doi:10.1002/joc.1340.
- Joseph, S., A. K. Sahai, and B. N. Goswami, 2009: Eastward propagating MJO during boreal summer and Indian monsoon droughts. *Climate Dynamics*, **32** (7), 1139–1153, doi:10.1007/s00382-008-0412-8.
- Ju, J., and J. Slingo, 1995: The asian summer monsoon and ENSO. *Quarterly Journal of the Royal Meteorological Society*, **121** (525), 1133–1168, doi:10.1002/qj.49712152509.
- Kang, I.-S., D. Kim, and J.-S. Kug, 2010: Mechanism for northward propagation of boreal summer intraseasonal oscillation: Convective momentum transport. *Geophysical Research Letters*, **37** (24), n/a–n/a, doi:10.1029/2010GL045072, l24804.
- Kemball-Cook, S., and B. Wang, 2001: Equatorial Waves and Air-Sea Interaction in the Boreal Summer Intraseasonal Oscillation. *Journal of Climate*, **14** (13), 2923–2942, doi:10.1175/1520-0442(2001)014<2923:EWAASI>2.0.CO;2.
- Kemball-Cook, S., B. Wang, and X. Fu, 2002: Simulation of the Intraseasonal Oscillation in the ECHAM-4 Model: The Impact of Coupling with an Ocean Model. *Journal of the Atmospheric Sciences*, **59** (9), 1433–1453, doi:10.1175/1520-0469(2002)059<1433:SOTIOI>2.0.CO;2.
- Kikuchi, K., B. Wang, and Y. Kajikawa, 2012: Bimodal representation of the tropical intraseasonal oscillation. *Climate Dynamics*, **38** (9), 1989–2000, doi:10.1007/s00382-011-1159-1.
- Kim, H.-M., and I.-S. Kang, 2008: The impact of ocean-atmosphere coupling on the predictability of boreal summer intraseasonal oscillation. *Climate Dynamics*, **31** (7), 859, doi:10.1007/s00382-008-0409-3.
- Klingaman, N. P., 2008: The intraseasonal oscillation of the Indian summer monsoon: Air-sea interactions and the potential for predictability. Ph.D. thesis, University of Reading.
- Klingaman, N. P., P. M. Inness, H. Weller, and J. M. Slingo, 2008a: The Importance of High-Frequency Sea Surface Temperature Variability to the Intraseasonal Oscillation of Indian Monsoon Rainfall. *Journal of Climate*, **21** (23), 6119–6140, doi:10.1175/2008JCLI2329.1.
- Klingaman, N. P., H. Weller, J. M. Slingo, and P. M. Inness, 2008b: The Intraseasonal Variability of the Indian Summer Monsoon Using TMI Sea Surface Temperatures and ECMWF Reanalysis. *Journal of Climate*, **21** (11), 2519–2539, doi:10.1175/2007JCLI1850.1.

REFERENCES

- Konda, G., and N. K. Vissa, 2019: Intraseasonal Convection and Air-Sea Fluxes Over the Indian Monsoon Region Revealed from the Bimodal ISO Index. *Pure and Applied Geophysics*, doi:10.1007/s00024-019-02119-1.
- Koster, R. D., and M. J. Suarez, 2004: Suggestions in the Observational Record of Land-Atmosphere Feedback Operating at Seasonal Time Scales. *Journal of Hydrometeorology*, **5** (3), 567–572.
- Koster, R. D., M. J. Suarez, and M. Heiser, 2000: Variance and Predictability of Precipitation at Seasonal-to-Interannual Timescales. *Journal of Hydrometeorology*, **1** (1), 26–46, doi:10.1175/1525-7541(2000)001<0026:VAPOPA>2.0.CO;2.
- Koster, R. D., P. A. Dirmeyer, Z. Guo, G. Bonan, E. Chan, P. Cox, C. T. Gordon, S. Kanae, E. Kowalczyk, D. Lawrence, P. Liu, C.-H. Lu, S. Malyshev, B. McAvaney, K. Mitchell, D. Mocko, T. Oki, K. Oleson, A. Pitman, Y. C. Sud, C. M. Taylor, D. Verseghy, R. Vasic, Y. Xue, and T. Yamada, 2004: Regions of Strong Coupling Between Soil Moisture and Precipitation. *Science*, **305** (5687), 1138–1140, doi:10.1126/science.1100217.
- Koster, R. D., Y. C. Sud, Z. Guo, P. A. Dirmeyer, G. Bonan, K. W. Oleson, E. Chan, D. Verseghy, P. Cox, H. Davies, E. Kowalczyk, C. T. Gordon, S. Kanae, D. Lawrence, P. Liu, D. Mocko, C.-H. Lu, K. Mitchell, S. Malyshev, B. McAvaney, T. Oki, T. Yamada, A. Pitman, C. M. Taylor, R. Vasic, and Y. Xue, 2006: GLACE: The Global Land-Atmosphere Coupling Experiment. Part I: Overview. *Journal of Hydrometeorology*, **7** (4), 590–610, doi:10.1175/JHM510.1.
- Koster, R. D., S. P. P. Mahanama, T. J. Yamada, G. Balsamo, A. A. Berg, M. Boisserie, P. A. Dirmeyer, F. J. Doblas-Reyes, G. Drewitt, C. T. Gordon, Z. Guo, J.-H. Jeong, D. M. Lawrence, W.-S. Lee, Z. Li, L. Luo, S. Malyshev, W. J. Merryfield, S. I. Seneviratne, T. Stanelle, B. J. J. M. van den Hurk, F. Vitart, and E. F. Wood, 2010: Contribution of land surface initialization to subseasonal forecast skill: First results from a multi-model experiment. *Geophysical Research Letters*, **37** (2), doi:10.1029/2009GL041677.
- Koster, R. D., S. P. P. Mahanama, T. J. Yamada, G. Balsamo, A. A. Berg, M. Boisserie, P. A. Dirmeyer, F. J. Doblas-Reyes, G. Drewitt, C. T. Gordon, Z. Guo, J.-H. Jeong, W.-S. Lee, Z. Li, L. Luo, S. Malyshev, W. J. Merryfield, S. I. Seneviratne, T. Stanelle, B. J. J. M. van den Hurk, F. Vitart, and E. F. Wood, 2011: The Second Phase of the Global Land-Atmosphere Coupling Experiment: Soil Moisture Contributions to Subseasonal Forecast Skill. *Journal of Hydrometeorology*, **12** (5), 805–822, doi:10.1175/2011JHM1365.1.
- Kothawale, D. R., and K. Rupa Kumar, 2002: Tropospheric temperature variation over India and links with the Indian summer monsoon: 1971-2000. *Mausam*, **53** (3), 289–308.
- Krishna Kumar, K., M. Hoerling, and B. Rajagopalan, 2005: Advancing dynamical prediction of Indian monsoon rainfall. *Geophysical Research Letters*, **32** (8), doi:10.1029/2004GL021979.
- Krishnamurthy, V., 2018: Intraseasonal oscillations in East Asian and South Asian monsoons. *Climate Dynamics*, **51** (11), 4185–4205, doi:10.1007/s00382-016-3466-z.
- Krishnamurthy, V., and D. Achuthavari, 2012: Intraseasonal oscillations of the monsoon circulation over South Asia. *Climate Dynamics*, **38** (11), 2335–2353, doi:10.1007/s00382-011-1153-7.
- Krishnamurthy, V., and B. N. Goswami, 2000: Indian monsoon-ENSO relationship on interdecadal timescale. *Journal of Climate*, **13** (3), 579–595, doi:10.1175/1520-0442(2000)013<0579:IMEROI>2.0.CO;2.
- Krishnamurthy, V., and A. S. Sharma, 2017: Predictability at intraseasonal time scale. *Geophysical Research Letters*, **44** (16), 8530–8537, doi:10.1002/2017GL074984.

REFERENCES

- Krishnamurthy, V., and J. Shukla, 2000: Intraseasonal and Interannual Variability of Rainfall over India. *Journal of Climate*, **13** (24), 4366–4377, doi:10.1175/1520-0442(2000)013<0001:IAIVOR>2.0.CO;2.
- Krishnamurthy, V., and J. Shukla, 2007: Intraseasonal and Seasonally Persisting Patterns of Indian Monsoon Rainfall. *Journal of Climate*, **20** (1), 3–20, doi:10.1175/JCLI3981.1.
- Krishnamurthy, V. and Shukla, J., 2011: Predictability of the Indian monsoon in coupled general circulation models. Tech. rep., The Center for Ocean-Land-Atmosphere Studies, 1-46 pp. URL ftp://cola.gmu.edu/pub/ctr/CTR313_ms.pdf.
- Krishnamurti, T. N., D. K. Oosterhof, and A. V. Mehta, 1988: Air-Sea Interaction on the Time Scale of 30 to 50 Days. *Journal of the Atmospheric Sciences*, **45** (8), 1304–1322, doi:10.1175/1520-0469(1988)045<1304:AIOTTS>2.0.CO;2.
- Krishnamurti, T. N., A. Simon, A. Thomas, A. Mishra, D. Sikka, D. Niyogi, A. Chakraborty, and L. Li, 2012: Modeling of Forecast Sensitivity on the March of Monsoon Isochrones from Kerala to New Delhi: The First 25 Days. *Journal of the Atmospheric Sciences*, **69** (8), 2465–2487, doi:10.1175/JAS-D-11-0170.1.
- Krishnamurti, T. N., A. Thomas, A. Simon, and V. Kumar, 2010: Desert Air Incursions, an Overlooked Aspect, for the Dry Spells of the Indian Summer Monsoon. *Journal of the Atmospheric Sciences*, **67** (10), 3423–3441, doi:10.1175/2010JAS3440.1.
- Krishnan, R., V. Kumar, M. Sugi, and J. Yoshimura, 2009: Internal Feedbacks from Monsoon-Midlatitude Interactions during Droughts in the Indian Summer Monsoon. *Journal of the Atmospheric Sciences*, **66** (3), 553–578, doi:10.1175/2008JAS2723.1.
- Krishnan, R., C. Venkatesan, and R. N. Keshavamurty, 1998: Dynamics of upper tropospheric stationary wave anomalies induced by ENSO during the northern summer: A GCM study. *Indian Academy of Sciences Proceedings: Earth and Planetary Sciences*, **107** (1), 65–90, doi:10.1007/BF02842261.
- Krishnan, R., C. Zhang, and M. Sugi, 2000: Dynamics of Breaks in the Indian Summer Monsoon. *Journal of the Atmospheric Sciences*, **57** (9), 1354–1372, doi:10.1175/1520-0469(2000)057<1354:DOBITI>2.0.CO;2.
- Kucharski, F., and M. A. Abid, 2017: Interannual Variability of the Indian Monsoon and Its Link to ENSO. *Oxford Encyclopedia of Climate Science*, 1–23, doi:10.1093/acrefore/9780190228620.013.615.
- Kumar, K. K., B. Rajagopalan, M. Hoerling, G. Bates, and M. Cane, 2006a: Unraveling the Mystery of Indian Monsoon Failure During El Niño. *Science*, **314** (5796), 115–119, doi:10.1126/science.1131152.
- Kumar, K. K., B. Rajagopalan, M. Hoerling, G. Bates, and M. Cane, 2006b: Unraveling the mystery of indian monsoon failure during el niño. *Science*, **314** (5796), 115–119, doi:10.1126/science.1131152.
- Kutty, G., S. Sandeep, Vinodkumar, and S. Nhaloor, 2018: Sensitivity of convective precipitation to soil moisture and vegetation during break spell of Indian summer monsoon. *Theoretical and Applied Climatology*, **133** (3), 957–972, doi:10.1007/s00704-017-2228-0.
- Large, W. G., J. C. McWilliams, and S. C. Doney, 1994: Oceanic vertical mixing: A review and a model with a nonlocal boundary layer parameterization. *Reviews of Geophysics*, **32** (4), 363–403, doi:10.1029/94RG01872.

REFERENCES

- Larkin, N. K., and D. E. Harrison, 2005: On the definition of El Niño and associated seasonal average U.S. weather anomalies. *Geophysical Research Letters*, **32** (13), doi:10.1029/2005GL022738.
- Lau, W. K. M., D. E. Waliser, and B. N. Goswami, 2012: South asian monsoon. *Intraseasonal Variability in the Atmosphere-Ocean Climate System*, Springer Berlin Heidelberg, Berlin, Heidelberg, chap. 2, 21–72.
- Lawrence, D. M., and J. M. Slingo, 2005: Weak Land-Atmosphere Coupling Strength in HadAM3: The Role of Soil Moisture Variability. *Journal of Hydrometeorology*, **6** (5), 670–680, doi:10.1175/JHM445.1.
- Lawrence, D. M., and P. J. Webster, 2002: The boreal summer intraseasonal oscillation: Relationship between northward and eastward movement of convection. *Journal of the Atmospheric Sciences*, **59** (9), 1593–1606, doi:10.1175/1520-0469(2002)059<1593:TBSIOR>2.0.CO;2.
- Lee, E., T. N. Chase, B. Rajagopalan, R. G. Barry, T. W. Biggs, and P. J. Lawrence, 2009: Effects of irrigation and vegetation activity on early Indian summer monsoon variability. *International Journal of Climatology*, **29** (4), 573–581, doi:10.1002/joc.1721.
- Lee, J.-Y., B. Wang, M. C. Wheeler, X. Fu, D. E. Waliser, and I.-S. Kang, 2013: Real-time multivariate indices for the boreal summer intraseasonal oscillation over the Asian summer monsoon region. *Climate Dynamics*, **40** (1), 493–509, doi:10.1007/s00382-012-1544-4.
- Lee, S.-S., B. Wang, D. E. Waliser, J. M. Neena, and J.-Y. Lee, 2015: Predictability and prediction skill of the boreal summer intraseasonal oscillation in the intraseasonal variability hindcast experiment. *Climate Dynamics*, **45** (7), 2123–2135, doi:10.1007/s00382-014-2461-5.
- Li, C., and M. Yanai, 1996: The Onset and Interannual Variability of the Asian Summer Monsoon in Relation to Land-Sea Thermal Contrast. *Journal of Climate*, **9** (2), 358–375, doi:10.1175/1520-0442(1996)009<0358:TOAIVO>2.0.CO;2.
- Li, K., W. Yu, T. Li, V. S. N. Murty, S. Khokiattiwong, T. R. Adi, and S. Budi, 2013: Structures and mechanisms of the first-branch northward-propagating intraseasonal oscillation over the tropical Indian Ocean. *Climate Dynamics*, **40** (7), 1707–1720, doi:10.1007/s00382-012-1492-z.
- Li, T., P. Liu, X. Fu, B. Wang, and G. A. Meehl, 2006: Spatiotemporal Structures and Mechanisms of the Tropospheric Biennial Oscillation in the Indo-Pacific Warm Ocean Regions. *Journal of Climate*, **19** (13), 3070–3087, doi:10.1175/JCLI3736.1.
- Li, X., Y. Tang, L. Zhou, D. Chen, Z. Yao, and S. U. Islam, 2016: Assessment of Madden-Julian oscillation simulations with various configurations of CESM. *Climate Dynamics*, **47** (7), 2667–2690.
- Li, Y., W. Han, W. Wang, L. Zhang, and M. Ravichandran, 2018: The Indian Summer Monsoon Intraseasonal Oscillations in CFSv2 Forecasts: Biases and Importance of Improving Air-Sea Interaction Processes. *Journal of Climate*, **31** (14), 5351–5370, doi:10.1175/JCLI-D-17-0623.1.
- Liebmann, B., and C. A. Smith, 1996: Description of a complete (interpolated) outgoing longwave radiation dataset. *Bulletin of the American Meteorological Society*, **77**, 1275–1277, doi:10.1175/1520-0477(2001)082<2217:BTBOBM>2.3.CO;2.

REFERENCES

- Lin, A., T. Li, X. Fu, J.-J. Luo, and Y. Masumoto, 2011: Effects of air-sea coupling on the boreal summer intraseasonal oscillations over the tropical Indian Ocean. *Climate Dynamics*, **37** (11), 2303–2322, doi:10.1007/s00382-010-0943-7.
- Lingbin Yang, L. Z., Guoqing Sun, and J. Zhao, 2018: Negative soil moisture-precipitation feedback in dry and wet-regions. *Scientific Reports*, **8** (4026), 1–9, doi:10.1038/s41598-018-22394-7.
- Liu, F., B. Wang, and I.-S. Kang, 2015: Roles of Barotropic Convective Momentum Transport in the Intraseasonal Oscillation. *Journal of Climate*, **28** (12), 4908–4920, doi:10.1175/JCLI-D-14-00575.1.
- Liu, F., J. Zhao, X. Fu, and G. Huang, 2018: The role of shallow convection in promoting the northward propagation of boreal summer intraseasonal oscillation. *Theoretical and Applied Climatology*, **131** (3), 1387–1395, doi:10.1007/s00704-017-2064-2.
- Lorenz, C., and H. Kunstmann, 2012: The Hydrological Cycle in Three State-of-the-Art Reanalyses: Intercomparison and Performance Analysis. *Journal of Hydrometeorology*, **13** (5), 1397–1420, doi:10.1175/JHM-D-11-088.1.
- Lorenz, R., A. J. Pitman, A. L. Hirsch, and J. Srbinovsky, 2015: Intraseasonal versus Interannual Measures of Land-Atmosphere Coupling Strength in a Global Climate Model: GLACE-1 versus GLACE-CMIP5 Experiments in ACCESS1.3b. *Journal of Hydrometeorology*, **16** (5), 2276–2295, doi:10.1175/JHM-D-14-0206.1.
- Madden, R. A., and P. R. Julian, 1971: Detection of a 40-50 Day Oscillation in the Zonal Wind in the Tropical Pacific. *Journal of the Atmospheric Sciences*, **28** (5), 702–708, doi:10.1175/1520-0469(1971)028<0702:DOADOI>2.0.CO;2.
- Madden, R. A., and P. R. Julian, 1972: Description of Global-Scale Circulation Cells in the Tropics with a 40-50 Day Period. *Journal of the Atmospheric Sciences*, **29** (6), 1109–1123, doi:10.1175/1520-0469(1972)029<1109:DOGSCC>2.0.CO;2.
- Magana, V., 1996: Atmospheric circulations during active and break periods of the asian monsoon. *Preprints of the Eighth Conference on the Global Ocean-Atmosphere-Land System (GOALS), Atlanta, GA., Jan 28-Feb 2, 1996*, Amer. Meteorol. Soc.
- Maharana, P., and A. P. Dimri, 2016: Study of intraseasonal variability of Indian summer monsoon using a regional climate model. *Climate Dynamics*, **46** (3), 1043–1064, doi:10.1007/s00382-015-2631-0.
- Mahmood, R., R. Leeper, and A. I. Quintanar, 2011: Sensitivity of planetary boundary layer atmosphere to historical and future changes of land use/land cover, vegetation fraction, and soil moisture in Western Kentucky, USA. *Global and Planetary Change*, **78** (1), 36 – 53, doi:https://doi.org/10.1016/j.gloplacha.2011.05.007.
- Maity, R., and D. Nagesh Kumar, 2006: Bayesian dynamic modeling for monthly indian summer monsoon rainfall using el niño–southern oscillation (enso) and equatorial indian ocean oscillation (equinoo). *Journal of Geophysical Research: Atmospheres*, **111** (D7), doi:10.1029/2005JD006539.
- Mandke, S. K., A. K. Sahai, M. A. Shinde, S. Joseph, and R. Chattopadhyay, 2007: Simulated changes in active/break spells during the Indian summer monsoon due to enhanced CO₂ concentrations: Assessment from selected coupled atmosphere–ocean global climate models. *International Journal of Climatology*, **27** (7), 837–859, doi:10.1002/joc.1440.

REFERENCES

- Mandke, S. K., M. A. Shinde, and A. K. Sahai, 2013: The Importance of Coupled Sea Surface Temperature to the Northward Propagation of Summer Monsoon Intraseasonal Oscillation. 1–26, URL <https://www.tropmet.res.in/~lip/Publication/RR-pdf/RR-129.pdf>.
- Martin, M. J., A. Hines, and M. J. Bell, 2007: Data assimilation in the FOAM operational short-range ocean forecasting system: a description of the scheme and its impact. *Quarterly Journal of the Royal Meteorological Society*, **133** (625), 981–995, doi:10.1002/qj.74.
- Matsumoto, J., and T. Murakami, 2000: Annual changes of tropical convective activities as revealed from equatorially symmetric olr data. *Journal of the Meteorological Society of Japan. Ser. II*, **78** (5), 543–561, doi:10.2151/jmsj1965.78.5_543.
- McPhaden, M. J., K. Ando, B. Bourles, H. Freitag, R. Lumpkin, Y. Masumoto, V. Murty, P. Nobre, M. Ravichandran, J. Vialard, and Coauthors, 2010: The global tropical moored buoy array. *Proceedings of Ocean Obs*, **9**, 668–682.
- Meehl, G. A., 1987: The Annual Cycle and Interannual Variability in the Tropical Pacific and Indian Ocean Regions. *Monthly Weather Review*, **115** (1), 27–50, doi:10.1175/1520-0493(1987)115<0027:TACAIV>2.0.CO;2.
- Meehl, G. A., 1994: Coupled Land-Ocean-Atmosphere Processes and South Asian Monsoon Variability. *Science*, **266** (5183), 263–267, doi:10.1126/science.266.5183.263.
- Meehl, G. A., and J. M. Arblaster, 2002a: Indian Monsoon GCM Sensitivity Experiments Testing Tropospheric Biennial Oscillation Transition Conditions. *Journal of Climate*, **15** (9), 923–944, doi:10.1175/1520-0442(2002)015<0923:IMGSET>2.0.CO;2.
- Meehl, G. A., and J. M. Arblaster, 2002b: The Tropospheric Biennial Oscillation and Asian-Australian Monsoon Rainfall. *Journal of Climate*, **15** (7), 722–744, doi:10.1175/1520-0442(2002)015<0722:TTBOAA>2.0.CO;2.
- Meehl, G. A., J. M. Arblaster, and J. Loschnigg, 2003: Coupled Ocean-Atmosphere Dynamical Processes in the Tropical Indian and Pacific Oceans and the TBO. *Journal of Climate*, **16** (13), 2138–2158, doi:10.1175/2767.1.
- Megann, A., D. Storkey, Y. Aksenov, S. Alderson, D. Calvert, T. Graham, P. Hyder, J. Siddorn, and B. Sinha, 2014: GO5.0: the joint NERC-Met office NEMO global ocean model for use in coupled and forced applications. *Geoscientific Model Development*, **7** (3), 1069–1092, doi:10.5194/gmd-7-1069-2014.
- Menon, A., A. G. Turner, G. M. Martin, and C. MacLachlan, 2018: Modelling the moistening of the free troposphere during the northwestward progression of Indian monsoon onset. *Quarterly Journal of the Royal Meteorological Society*, **144** (713), 1152–1168, doi:10.1002/qj.3281.
- Mitra, A. K., A. K. Bohra, M. N. Rajeevan, and T. N. Krishnamurti, 2009: Daily Indian Precipitation Analysis Formed from a Merge of Rain-Gauge Data with the TRMM TMPA Satellite-Derived Rainfall Estimates. *Journal of the Meteorological Society of Japan. Ser. II*, **87A**, 265–279, doi:10.2151/jmsj.87A.265.
- Mooley, D. A., and B. Parthasarathy, 1984: Fluctuations in All-India summer monsoon rainfall during 1871–1978. *Climatic Change*, **6** (3), 287–301, doi:10.1007/BF00142477.
- Moron, V., and A. W. Robertson, 2014: Interannual variability of Indian summer monsoon rainfall onset date at local scale. *International Journal of Climatology*, **34** (4), 1050–1061, doi:10.1002/joc.3745.

- Nayak, H., K. Osuri, P. Sinha, R. R. Nadimpalli, U. C. Mohanty, F. Chen, M. Rajeevan, and D. Niyogi, 2018: High-resolution gridded soil moisture and soil temperature datasets for the Indian monsoon region. *Scientific Data*, **5**, 180 264, doi:10.1038/sdata.2018.264.
- Neena, J. M., E. Suhas, and B. N. Goswami, 2011: Leading role of internal dynamics in the 2009 Indian summer monsoon drought. *Journal of Geophysical Research: Atmospheres*, **116** (D13), doi:10.1029/2010JD015328.
- Pai, D. S., and R. M. Nair, 2009: Summer monsoon onset over Kerala: New definition and prediction. *Journal of Earth System Science*, **118** (2), 123–135.
- Pai, D. S., L. Sridhar, and M. R. Ramesh Kumar, 2016: Active and break events of Indian summer monsoon during 1901–2014. *Climate Dynamics*, **46** (11), 3921–3939, doi:10.1007/s00382-015-2813-9.
- Pal, J. S., and E. A. B. Eltahir, 2001: Pathways Relating Soil Moisture Conditions to Future Summer Rainfall within a Model of the Land-Atmosphere System. *Journal of Climate*, **14** (6), 1227–1242, doi:10.1175/1520-0442(2001)014<1227:PRSMCT>2.0.CO;2.
- Palmer, T. N., A. Alessandri, U. Andersen, P. Cantelaube, M. Davey, P. Délecluse, M. Déqué, E. Díez, F. J. Doblas-Reyes, H. Feddersen, R. Graham, S. Gualdi, J.-F. Guérémy, R. Hagedorn, M. Hoshen, N. Keenlyside, M. Latif, A. Lazar, E. Maisonnavé, V. Marletto, A. P. Morse, B. Orfila, P. Rogel, J.-M. Terres, and M. C. Thomson, 2004: Development Of a European Multimodel Ensemble System for Seasonal-to-Interannual Prediction (DEMETER). *Bulletin of the American Meteorological Society*, **85** (6), 853–872, doi:10.1175/BAMS-85-6-853.
- Pangaluru, K., I. Velicogna, G. A. Y. Mohajerani, E. Ciraci, S. Charakola, G. Basha, and S. V. B. Rao, 2019: Soil Moisture Variability in India: Relationship of Land Surface-Atmosphere Fields Using Maximum Covariance Analysis. *Remote Sensing*, **11** (3), doi:10.3390/rs11030335.
- Parker, D. J., P. Willetts, C. Birch, A. G. Turner, J. H. Marsham, C. M. Taylor, S. Kolusu, and G. M. Martin, 2016: The interaction of moist convection and mid-level dry air in the advance of the onset of the Indian monsoon. *Quarterly Journal of the Royal Meteorological Society*, **142** (699), 2256–2272, doi:10.1002/qj.2815.
- Parthasarathy, B., A. A. Munot, and D. R. Kothawale, 1994: All-India monthly and seasonal rainfall series: 1871–1993. *Theoretical and Applied Climatology*, **49** (4), 217–224, doi:10.1007/BF00867461.
- Patel, K., 2019: Water Shortages in India. URL <https://earthobservatory.nasa.gov/images/145242/water-shortages-in-india>, Accessed: 2019-09-10.
- Pathak, A., S. Ghosh, J. A. Martinez, F. Dominguez, and P. Kumar, 2017: Role of Oceanic and Land Moisture Sources and Transport in the Seasonal and Interannual Variability of Summer Monsoon in India. *Journal of Climate*, **30** (5), 1839–1859, doi:10.1175/JCLI-D-16-0156.1.
- Pillai, P. A., and J. S. Chowdary, 2016: Indian summer monsoon intra-seasonal oscillation associated with the developing and decaying phase of El Niño. *International Journal of Climatology*, **36** (4), 1846–1862, doi:10.1002/joc.4464.
- Pillai, P. A., and A. K. Sahai, 2014: Moist dynamics of active/break cycle of Indian summer monsoon rainfall from NCEP2 and MERRA reanalysis. *International Journal of Climatology*, **34** (5), 1429–1444, doi:10.1002/joc.3774.

REFERENCES

- Praveen Kumar, B., J. Vialard, M. Lengaigne, V. S. N. Murty, and M. J. McPhaden, 2012: TropFlux: air-sea fluxes for the global tropical oceans—description and evaluation. *Climate Dynamics*, **38** (7), 1521–1543, doi:10.1007/s00382-011-1115-0.
- Premkumar, K., M. Ravichandran, S. R. Kalsi, D. Sengupta, and S. Gadgil, 2000: First results from a new observational system over the Indian seas. *Current Science*, **78** (3), 323–330.
- Qi, Y., R. Zhang, X. Rong, J. Li, and L. Li, 2019: Boreal Summer Intraseasonal Oscillation in the Asian-Pacific Monsoon Region Simulated in CAMS-CSM. *Journal of Meteorological Research*, **33** (1), 66–79.
- Rajeevan, M., J. Bhate, J. D. Kale, and B. Lal, 2006: High resolution daily gridded rainfall data for the Indian region: Analysis of break and active monsoon spells. *Current Science*, **91** (3), 296–306.
- Rajeevan, M., S. Gadgil, and J. Bhate, 2010: Active and break spells of the Indian summer monsoon. *Journal of Earth System Science*, **119** (3), 229–247, doi:10.1007/s12040-010-0019-4.
- Rajeevan, M., D. S. Pai, R. Anil Kumar, and B. Lal, 2007: New statistical models for long-range forecasting of southwest monsoon rainfall over India. *Climate Dynamics*, **28** (7), 813–828.
- Rajeevan, M., C. K. Unnikrishnan, and B. Preethi, 2012: Evaluation of the ENSEMBLES multi-model seasonal forecasts of Indian summer monsoon variability. *Climate Dynamics*, **38** (11), 2257–2274, doi:10.1007/s00382-011-1061-x.
- Rajendran, K., A. Kitoh, and O. Arakawa, 2004: Monsoon low-frequency intraseasonal oscillation and ocean-atmosphere coupling over the Indian Ocean. *Geophysical Research Letters*, **31** (2), doi:10.1029/2003GL019031.
- Raju, P. V. S., U. C. Mohanty, and R. Bhatla, 2005: Onset characteristics of the southwest monsoon over India. *International Journal of Climatology*, **25** (2), 167–182, doi:10.1002/joc.1121.
- Ramamurthy, K., 1969: Monsoons of India: Some aspects of the ‘break’ in the south west monsoon during July–August. *Forecasting Manual IV-18.3*, 1–57.
- Rao, T. N., K. Saikranthi, B. Radhakrishna, and S. V. B. Rao, 2016: Differences in the Climatological Characteristics of Precipitation between Active and Break Spells of the Indian Summer Monsoon. *Journal of Climate*, **29** (21), 7797–7814, doi:10.1175/JCLI-D-16-0028.1.
- Rao, P.C.S., Pai. D. S. and Mohapatra, M., 2017: Benchmark Report 2017 - India. Tech. rep., India Meteorological Department, 1-368 pp. URL http://www.imd.gov.in/pages/monsoon_main.php.
- Reddy, V. R., and G. J. Syme, 2015: Chapter 1 - Introduction. *Integrated Assessment of Scale Impacts of Watershed Intervention*, V. R. Reddy, and G. J. Syme, Eds., Elsevier, Boston, 3 – 21, doi:<https://doi.org/10.1016/B978-0-12-800067-0.00001-3>, URL <http://www.sciencedirect.com/science/article/pii/B9780128000670000013>.
- Roxy, M., and Y. Tanimoto, 2007: Role of SST over the Indian Ocean in Influencing the Intraseasonal Variability of the Indian Summer Monsoon. *Journal of the Meteorological Society of Japan. Ser. II*, **85** (3), 349–358, doi:10.2151/jmsj.85.349.
- Roxy, M., and Y. Tanimoto, 2012: Influence of sea surface temperature on the intraseasonal variability of the South China Sea summer monsoon. *Climate Dynamics*, **39** (5), 1209–1218, doi:10.1007/s00382-011-1118-x.

REFERENCES

- Roy, I., R. G. Tedeschi, and M. Collins, 2019: ENSO teleconnections to the Indian summer monsoon under changing climate. *International Journal of Climatology*, **39** (6), 3031–3042, doi:10.1002/joc.5999.
- Sabeerali, C. T., A. Ramu Dandi, A. Dhakate, K. Salunke, S. Mahapatra, and S. A. Rao, 2013: Simulation of boreal summer intraseasonal oscillations in the latest CMIP5 coupled GCMs. *Journal of Geophysical Research: Atmospheres*, **118** (10), 4401–4420, doi:10.1002/jgrd.50403.
- Saha, S., S. Pokhrel, and H. Chaudhari, 2013: Influence of Eurasian snow on Indian summer monsoon in NCEP CFSv2 freerun. *Climate Dynamics*, **41**, doi:10.1007/s00382-012-1617-4.
- Saha, S. K., S. Pokhrel, K. Salunke, A. Dhakate, H. S. Chaudhari, H. Rahaman, K. Sujith, A. Hazra, and D. R. Sikka, 2016: Potential predictability of Indian summer monsoon rainfall in NCEP CFSv2. *Journal of Advances in Modeling Earth Systems*, **8** (1), 96–120.
- Sahai, A. K., R. Chattopadhyay, and B. N. Goswami, 2008: A SST based large multi-model ensemble forecasting system for Indian summer monsoon rainfall. *Geophysical Research Letters*, **35** (19).
- Salby, M. L., and H. H. Hendon, 1994: Intraseasonal Behavior of Clouds, Temperature, and Motion in the Tropics. *Journal of the Atmospheric Sciences*, **51** (15), 2207–2224, doi:10.1175/1520-0469(1994)051<2207:IBOCTA>2.0.CO;2.
- Sanchez-Franks, A., E. C. Kent, A. J. Matthews, B. G. M. Webber, S. C. Peatman, and P. N. Vinayachandran, 2018: Intraseasonal Variability of Air-Sea Fluxes over the Bay of Bengal during the Southwest Monsoon. *Journal of Climate*, **31** (17), 7087–7109, doi:10.1175/JCLI-D-17-0652.1.
- Schneider, T., T. Bischoff, and G. Haug, 2014: Migrations and dynamics of the Intertropical Convergence Zone. *Nature*, **513**, 45–53, doi:10.1038/nature13636.
- Seneviratne, M. B. K. R. D., S. I., and R. Orth, 2012: Role of soil moisture for (sub-)seasonal. *ECMWF Seminar on Seasonal Prediction*, European Centre for Medium-Range Weather Forecasts.
- Seneviratne, S. I., T. Corti, E. L. Davin, M. Hirschi, E. B. Jaeger, I. Lehner, B. Orlowsky, and A. J. Teuling, 2010: Investigating soil moisture-climate interactions in a changing climate: A review. *Earth-Science Reviews*, **99** (3), 125 – 161, doi:https://doi.org/10.1016/j.earscirev.2010.02.004.
- Seneviratne, S. I., D. Lüthi, M. Litschi, and C. Schaer, 2006: Land-atmosphere coupling and climate change in Europe. *Nature*, **443**, 205–209.
- Sengupta, D., and M. Ravichandran, 2001: Oscillations of Bay of Bengal sea surface temperature during the 1998 Summer Monsoon. *Geophysical Research Letters*, **28** (10), 2033–2036, doi:10.1029/2000GL012548.
- Sharmila, S., P. A. Pillai, S. Joseph, M. Roxy, R. P. M. Krishna, R. Chattopadhyay, S. Abhilash, A. K. Sahai, and B. N. Goswami, 2013: Role of ocean–atmosphere interaction on northward propagation of Indian summer monsoon intra-seasonal oscillations (MISO). *Climate Dynamics*, **41** (5), 1651–1669, doi:10.1007/s00382-013-1854-1.
- Shepard, D., 1968: A two-dimensional interpolation function for irregularly-spaced data. *Proceedings of the 1968 23rd ACM National Conference*, ACM, New York, NY, USA, 517–524, ACM '68, doi:10.1145/800186.810616, URL <http://doi.acm.org/10.1145/800186.810616>.

- Shukla, J., and Y. Mintz, 1982: Influence of Land-Surface Evapotranspiration on the Earth's Climate. *Science*, **215** (4539), 1498–1501.
- Shukla, R. P., and B. Huang, 2016: Interannual variability of the Indian summer monsoon associated with the air-sea feedback in the northern Indian Ocean. *Climate Dynamics*, **46** (5), 1977–1990, doi:10.1007/s00382-015-2687-x, URL <https://doi.org/10.1007/s00382-015-2687-x>.
- Shukla, R. P., and J. Zhu, 2014: Simulations of Boreal Summer Intraseasonal Oscillations with the Climate Forecast System, version 2, over India and the Western Pacific: Role of Air–Sea Coupling. *Atmosphere-Ocean*, **52** (4), 321–330, doi:10.1080/07055900.2014.939575.
- Sikka, D. R., and S. Gadgil, 1980: On the Maximum Cloud Zone and the ITCZ over Indian, Longitudes during the Southwest Monsoon. *Monthly Weather Review*, **108** (11), 1840–1853, doi:10.1175/1520-0493(1980)108<1840:OTMCZA>2.0.CO;2.
- Sperber, K. R., and H. Annamalai, 2008: Coupled model simulations of boreal summer intraseasonal (30–50 day) variability, Part 1: Systematic errors and caution on use of metrics. *Climate Dynamics*, **31** (2), 345–372, doi:10.1007/s00382-008-0367-9.
- Sperber, K. R., C. Brankovic, M. Déqué, C. S. Frederiksen, R. Graham, A. Kitoh, C. Kobayashi, T. Palmer, K. Puri, W. Tennant, and E. Volodin, 2001: Dynamical Seasonal Predictability of the Asian Summer Monsoon. *Monthly Weather Review*, **129** (9), 2226–2248, doi:10.1175/1520-0493(2001)129<2226:DSPOTA>2.0.CO;2.
- Sreelekha, P. N., and C. A. Babu, 2019: Is the negative IOD during 2016 the reason for monsoon failure over southwest peninsular India? *Meteorology and Atmospheric Physics*, **131** (3), 413–420, doi:10.1007/s00703-017-0574-1.
- Storkey, D., E. W. Blockley, R. Furner, C. Guiavarc'h, D. Lea, M. J. Martin, R. M. Barciela, A. Hines, P. Hyder, and J. R. Siddorn, 2010: Forecasting the ocean state using NEMO: The new FOAM system. *Journal of Operational Oceanography*, **3** (1), 3–15, doi:10.1080/1755876X.2010.11020109.
- Sudeepkumar, B., C. Babu, and H. Varikoden, 2018: Future projections of active-break spells of Indian summer monsoon in a climate change perspective. *Global and Planetary Change*, **161**, 222 – 230.
- Sun, S., J. Lan, Y. Fang, Tana, and X. Gao, 2015: A Triggering Mechanism for the Indian Ocean Dipoles Independent of ENSO. *Journal of Climate*, **28** (13), 5063–5076, doi:10.1175/JCLI-D-14-00580.1.
- Taraphdar, S., P. Mukhopadhyay, and B. N. Goswami, 2010: Predictability of Indian summer monsoon weather during active and break phases using a high resolution regional model. *Geophysical Research Letters*, **37** (21), 1–6.
- Taylor, C., R. de Jeu, F. Guichard, P. Harris, and W. Dorigo, 2012: Afternoon rain more likely over drier soils. *Nature*, **489**, 423–6, doi:10.1038/nature11377.
- Taylor, C. M., 2008: Intraseasonal Land-Atmosphere coupling in the West African monsoon. *Journal of Climate*, **21** (24), 6636–6648, doi:10.1175/2008JCLI2475.1.
- Trenberth, K. E., and J. T. Fasullo, 2013a: North American water and energy cycles. *Geophysical Research Letters*, **40** (2), 365–369, doi:10.1002/grl.50107.
- Trenberth, K. E., and J. T. Fasullo, 2013b: Regional Energy and Water Cycles: Transports from Ocean to Land. *Journal of Climate*, **26** (20), 7837–7851, doi:10.1175/JCLI-D-13-00008.1.

REFERENCES

- Trenberth, K. E., J. T. Fasullo, and J. Kiehl, 2009: Earth's global energy budget. *Bulletin of the American Meteorological Society*, **90** (3), 311–324.
- Trenberth, K. E., J. T. Fasullo, and J. Mackaro, 2011: Atmospheric Moisture Transports from Ocean to Land and Global Energy Flows in Reanalyses. *Journal of Climate*, **24** (18), 4907–4924, doi:10.1175/2011JCLI4171.1.
- Trenberth, K. E., D. P. Stepaniak, and J. M. Caron, 2000: The Global Monsoon as Seen through the Divergent Atmospheric Circulation. *Journal of Climate*, **13** (22), 3969–3993, doi:10.1175/1520-0442(2000)013<3969:TGMAST>2.0.CO;2.
- Tuinenburg, O. A., R. W. A. Hutjes, C. M. J. Jacobs, and P. Kabat, 2011: Diagnosis of Local Land-Atmosphere Feedbacks in India. *Journal of Climate*, **24** (1), 251–266, doi:10.1175/2010JCLI3779.1.
- Turner, A., P. Inness, and J. M. Slingo, 2007: The effect of doubled CO₂ and model basic state biases on the monsoon-ENSO system. I: Mean response and interannual variability. *Quarterly Journal of the Royal Meteorological Society*, **133**, 1143 – 1157.
- Turner, A. G., and A. Hannachi, 2010: Is there regime behavior in monsoon convection in the late 20th century? *Geophysical Research Letters*, **37** (16), doi:10.1029/2010GL044159.
- Turner, A. G., P. M. Inness, and J. M. Slingo, 2005: The role of the basic state in the ENSO-monsoon relationship and implications for predictability. *Quarterly Journal of the Royal Meteorological Society*, **131** (607), 781–804, doi:10.1256/qj.04.70.
- Turner, A. G., and J. M. Slingo, 2011: Using idealized snow forcing to test teleconnections with the Indian summer monsoon in the Hadley Centre GCM. *Climate Dynamics*, **36** (9), 1717–1735.
- Turner, A. G., G. S. Bhat, G. M. Martin, D. J. Parker, C. M. Taylor, A. K. Mitra, S. N. Tripathi, S. Milton, E. N. Rajagopal, J. G. Evans, R. Morrison, S. Pattnaik, M. Sekhar, B. K. Bhattacharya, R. Madan, M. Govindankutty, J. K. Fletcher, P. D. Willetts, A. Menon, J. H. Marsham, the INCOMPASS team, K. M. R. Hunt, T. Chakraborty, G. George, M. Krishnan, C. Sarangi, D. Belušić, L. Garcia-Carreras, M. Brooks, S. Webster, J. K. Brooke, C. Fox, R. C. Harlow, J. M. Langridge, A. Jayakumar, S. J. Böing, O. Halliday, J. Bowles, J. Kent, D. O'Sullivan, A. Wilson, C. Woods, S. Rogers, R. Smout-Day, D. Tiddeman, D. Desai, R. Nigam, S. Paleri, A. Sattar, M. Smith, D. Anderson, S. Bauguitte, R. Carling, C. Chan, S. Devereau, G. Gratton, D. MacLeod, G. Nott, M. Pickering, H. Price, S. Rastall, C. Reed, J. Trembath, A. Woolley, A. Volonté, and B. New, 2019: Interaction of Convective Organisation with Monsoon Precipitation, Atmosphere, Surface and Sea: the 2016 INCOMPASS field campaign in India. *Quarterly Journal of the Royal Meteorological Society*, doi:10.1002/qj.3633.
- Umakanth, U., A. P. Kesarkar, T. N. Rao, and S. V. B. Rao, 2015: An objective criterion for the identification of breaks in Indian summer monsoon rainfall. *Atmospheric Science Letters*, **16** (3), 193–198, doi:10.1002/asl2.536.
- Varikoden, H., and J. V. Revadekar, 2018: Relation Between the Rainfall and Soil Moisture During Different Phases of Indian Monsoon. *Pure and Applied Geophysics*, **175** (3), 1187–1196.
- Vecchi, G. A., and D. E. Harrison, 2002: Monsoon Breaks and Subseasonal Sea Surface Temperature Variability in the Bay of Bengal. *Journal of Climate*, **15** (12), 1485–1493.
- Vialard, J., A. Jayakumar, C. Gnanaseelan, M. Lengaigne, D. Sengupta, and B. N. Goswami, 2012: Processes of 30–90 days sea surface temperature variability in the northern

- Indian Ocean during boreal summer. *Climate Dynamics*, **38** (9), 1901–1916, doi:10.1007/s00382-011-1015-3.
- Vinayachandran, P. N., A. J. Matthews, K. V. Kumar, A. Sanchez-Franks, V. Thushara, J. George, V. Vijith, B. G. M. Webber, B. Y. Queste, R. Roy, A. Sarkar, D. B. Baranowski, G. S. Bhat, N. P. Klingaman, S. C. Peatman, C. Parida, K. J. Heywood, R. Hall, B. King, E. C. Kent, A. A. Nayak, C. P. Neema, P. Amol, A. Lotliker, A. Kankonkar, D. G. Gracias, S. Vernekar, A. C. D. Souza, G. Valluvan, S. M. Pargaonkar, K. Dinesh, J. Giddings, and M. Joshi, 2018: BoBBLE (Bay of Bengal Boundary Layer Experiment): Ocean-atmosphere interaction and its impact on the South Asian monsoon. *Bulletin of the American Meteorological Society*, **99** (8), 1569–1587.
- Vishnu, S., P. A. Francis, S. S. V. S. Ramakrishna, and S. S. C. Shenoi, 2019: On the relationship between the Indian summer monsoon rainfall and the EQUINOO in the CFSv2. *Climate Dynamics*, **52** (1), 1263–1281, doi:10.1007/s00382-018-4190-7.
- Vitart, F., C. Ardilouze, A. Bonet, A. Brookshaw, M. Chen, C. Codorean, M. Déqué, L. Ferranti, E. Fucile, M. Fuentes, H. Hendon, J. Hodgson, H.-S. Kang, A. Kumar, H. Lin, G. Liu, X. Liu, P. Malguzzi, I. Mallas, M. Manoussakis, D. Mastrangelo, C. MacLachlan, P. McLean, A. Minami, R. Mladek, T. Nakazawa, S. Najm, Y. Nie, M. Rixen, A. W. Robertson, P. Ruti, C. Sun, Y. Takaya, M. Tolstykh, F. Venuti, D. Waliser, S. Woolnough, T. Wu, D.-J. Won, H. Xiao, R. Zaripov, and L. Zhang, 2017: The Subseasonal to Seasonal (S2S) Prediction Project Database. *Bulletin of the American Meteorological Society*, **98** (1), 163–173, doi:10.1175/BAMS-D-16-0017.1.
- Waliser, D. E., K. Jin, I.-S. Kang, W. F. Stern, S. D. Schubert, M. L. C. Wu, K.-M. Lau, M.-I. Lee, V. Krishnamurthy, A. Kitoh, G. A. Meehl, V. Y. Galin, V. Satyan, S. K. Mandke, G. Wu, Y. Liu, and C.-K. Park, 2003: AGCM simulations of intraseasonal variability associated with the Asian summer monsoon. *Climate Dynamics*, **21** (5), 423–446, doi:10.1007/s00382-003-0337-1.
- Walker, G. T., 1910: Correlations in seasonal variations of weather. II. *Memoirs of India Meteorological Department*, **21**, 22–45.
- Walker, G. T., 1923: Correlation in seasonal variation of weather. VIII: A preliminary study of world weather. *Memoirs of India Meteorological Department*, **24**, 75–131.
- Walker, G. T., 1924: Correlations in seasonal variations of weather. I. A further study of world weather. *Memoirs of India Meteorological Department*, **24**, 275–332.
- Walters, D., I. Boutle, M. Brooks, T. Melvin, R. Stratton, S. Vosper, H. Wells, K. Williams, N. Wood, T. Allen, A. Bushell, D. Copey, P. Earnshaw, J. Edwards, M. Gross, S. Hardiman, C. Harris, J. Heming, N. Klingaman, R. Levine, J. Manners, G. Martin, S. Milton, M. Mittermaier, C. Morcrette, T. Riddick, M. Roberts, C. Sanchez, P. Selwood, A. Stirling, C. Smith, D. Suri, W. Tennant, P. L. Vidale, J. Wilkinson, M. Willett, S. Woolnough, and P. Xavier, 2017: The Met Office Unified Model Global Atmosphere 6.0/6.1 and JULES Global Land 6.0/6.1 configurations. *Geoscientific Model Development*, **10** (4), 1487–1520, doi:10.5194/gmd-10-1487-2017.
- Wang, B., Q. Ding, X. Fu, I.-S. Kang, K. Jin, J. Shukla, and F. Doblas-Reyes, 2005a: Fundamental challenge in simulation and prediction of summer monsoon rainfall. *Geophysical Research Letters*, **32** (15), doi:10.1029/2005GL022734.
- Wang, B., T. Li, and P. Chang, 1995: An Intermediate Model of the Tropical Pacific Ocean. *Journal of Physical Oceanography*, **25** (7), 1599–1616, doi:10.1175/1520-0485(1995)025<1599:AIMOTT>2.0.CO;2.

REFERENCES

- Wang, B., and H. Rui, 1990: Synoptic climatology of transient tropical intraseasonal convection anomalies: 1975–1985. *Meteorology and Atmospheric Physics*, **44** (1), 43–61, doi:10.1007/BF01026810.
- Wang, B., P. J. Webster, and H. Teng, 2005b: Antecedents and self-induction of active-break south Asian monsoon unraveled by satellites. *Geophysical Research Letters*, **32** (4), 1–4, doi:10.1029/2004GL020996, l04704.
- Wang, B., R. Wu, and K.-M. Lau, 2001: Interannual Variability of the Asian Summer Monsoon: Contrasts between the Indian and the Western North Pacific–East Asian Monsoons. *Journal of Climate*, **14** (20), 4073–4090, doi:10.1175/1520-0442(2001)014<4073:IVOTAS>2.0.CO;2.
- Wang, B., B. Xiang, J. Li, P. Webster, M. Rajeevan, J. Liu, and K.-J. Ha, 2015a: Corrigendum: Rethinking Indian monsoon rainfall prediction in the context of recent global warming. *Nature Communications*, **6**, 7154, doi:10.1038/ncomms8154.
- Wang, B., and X. Xie, 1997: A Model for the Boreal Summer Intraseasonal Oscillation. *Journal of the Atmospheric Sciences*, **54** (1), 72–86, doi:10.1175/1520-0469(1997)054<0072:AMFTBS>2.0.CO;2.
- Wang, B., and X. Xu, 1997: Northern Hemisphere Summer Monsoon Singularities and Climatological Intraseasonal Oscillation. *Journal of Climate*, **10** (5), 1071–1085, doi:10.1175/1520-0442(1997)010<1071:NHMSMA>2.0.CO;2.
- Wang, L., and J.-Y. Yu, 2018: A Recent Shift in the Monsoon Centers Associated with the Tropospheric Biennial Oscillation. *Journal of Climate*, **31** (1), 325–340, doi:10.1175/JCLI-D-17-0349.1.
- Wang, T., S. Wong, and E. J. Fetzer, 2015b: Cloud regime evolution in the Indian monsoon intraseasonal oscillation: Connection to large-scale dynamical conditions and the atmospheric water budget. *Geophysical Research Letters*, **42** (21), 9465–9472, doi:10.1002/2015GL066353.
- Wang, T., X.-Q. Yang, J. Fang, X. Sun, and X. Ren, 2018a: Role of Air–Sea Interaction in the 30–60-Day Boreal Summer Intraseasonal Oscillation over the Western North Pacific. *Journal of Climate*, **31** (4), 1653–1680, doi:10.1175/JCLI-D-17-0109.1.
- Wang, T., X.-Q. Yang, J. Fang, X. Sun, and X. Ren, 2018b: Role of Air–Sea Interaction in the 30–60-Day Boreal Summer Intraseasonal Oscillation over the Western North Pacific. *Journal of Climate*, **31** (4), 1653–1680, doi:10.1175/JCLI-D-17-0109.1.
- Wang, W., M. Chen, and A. Kumar, 2009: Impacts of Ocean Surface on the Northward Propagation of the Boreal Summer Intraseasonal Oscillation in the NCEP Climate Forecast System. *Journal of Climate*, **22** (24), 6561–6576.
- Wang, X., and C. Wang, 2014: Different impacts of various El Niño events on the Indian Ocean Dipole. *Climate Dynamics*, **42** (3), 991–1005.
- Waters, J., D. J. Lea, M. J. Martin, I. Mirouze, A. Weaver, and J. While, 2015: Implementing a variational data assimilation system in an operational 1/4 degree global ocean model. *Quarterly Journal of the Royal Meteorological Society*, **141** (687), 333–349, doi:10.1002/qj.2388.
- Webster, P., A. M. Moore, J. P. Loschnigg, and R. Leben, 1999: Coupled ocean-atmosphere dynamics in the Indian Ocean during 1997–98. *Nature*, **401**, 356–60, doi:10.1038/43848.

REFERENCES

- Webster, P. J., 1983: Mechanisms of Monsoon Low-Frequency Variability: Surface Hydrological Effects. *Journal of the Atmospheric Sciences*, **40** (9), 2110–2124, doi:10.1175/1520-0469(1983)040<2110:MOMLFV>2.0.CO;2.
- Webster, P. J., and C. Hoyos, 2004: Prediction of Monsoon Rainfall and River Discharge on 15-30-Day Time Scales. *Bulletin of the American Meteorological Society*, **85** (11), 1745–1766, doi:10.1175/BAMS-85-11-1745.
- Webster, P. J., V. O. Magaña, T. N. Palmer, J. Shukla, R. A. Tomas, M. Yanai, and T. Yasunari, 1998: Monsoons: Processes, predictability, and the prospects for prediction. *Journal of Geophysical Research: Oceans*, **103** (C7), 14 451–14 510, doi:10.1029/97JC02719.
- Webster, P. J., and S. Yang, 1992: Monsoon and ENSO: Selectively Interactive Systems. *Quart. J. Roy. Meteor. Soc.*, **118** (507), 877–926, doi:10.1002/qj.49711850705.
- Webster, P. J., E. F. Bradley, C. W. Fairall, J. S. Godfrey, P. Hacker, R. A. Houze, R. Lukas, Y. Serra, J. M. Hummon, T. D. M. Lawrence, C. A. Russell, M. N. Ryan, K. Sahami, and P. Zuidema, 2002: The JASMINE Pilot Study. *Bulletin of the American Meteorological Society*, **83** (11), 1603–1630, doi:10.1175/BAMS-83-11-1603.
- Wheeler, M. C., and H. H. Hendon, 2004: An all-season real-time multivariate mjo index: Development of an index for monitoring and prediction. *Monthly Weather Review*, **132** (8), 1917–1932, doi:10.1175/1520-0493(2004)132<1917:AARMMI>2.0.CO;2.
- Woolnough, S. J., J. M. Slingo, and B. J. Hoskins, 2000: The Relationship between Convection and Sea Surface Temperature on Intraseasonal Timescales. *Journal of Climate*, **13** (12), 2086–2104, doi:10.1175/1520-0442(2000)013<2086:TRBCAS>2.0.CO;2.
- World Travel & Tourism Council, 2017: Benchmark Report 2017 - India. Tech. rep., World Travel & Tourism Council, 1-7 pp. URL <https://www.wttc.org/-/media/files/reports/benchmark-reports/country-reports-2017/india.pdf>.
- Yamagata, T., S. K. Behera, J.-J. Luo, S. Masson, M. R. Jury, and S. A. Rao, 2013: *Coupled Ocean-Atmosphere Variability in the Tropical Indian Ocean*, 189–211. American Geophysical Union (AGU), doi:10.1029/147GM12.
- Yamagata, T., S. K. Behera, S. A. Rao, Z. Guan, K. Ashok, and H. N. Saji, 2003: Comments on “Dipoles, Temperature Gradients, and Tropical Climate Anomalies. *Bulletin of the American Meteorological Society*, **84** (10), 1418–1422.
- Yang, Y., S.-P. Xie, L. Wu, Y. Kosaka, N.-C. Lau, and G. A. Vecchi, 2015: Seasonality and Predictability of the Indian Ocean Dipole Mode: ENSO Forcing and Internal Variability. *Journal of Climate*, **28** (20), 8021–8036, doi:10.1175/JCLI-D-15-0078.1.
- Yasunari, T., 1979: Cloudiness fluctuations associated with the northern hemisphere summer monsoon. *J. Meteor. Soc. Japan*, 227–242.
- Yasunari, T., 1980: A Quasi-Stationary Appearance of 30 to 40 Day Period in the Cloudiness Fluctuations during the Summer Monsoon over India. *Journal of the Meteorological Society of Japan. Ser. II*, **58** (3), 225–229, doi:10.2151/jmsj1965.58.3_225.
- Yu, J.-Y., and H.-Y. Kao, 2007: Decadal changes of ENSO persistence barrier in SST and ocean heat content indices: 1958–2001. *Journal of Geophysical Research: Atmospheres*, **112** (D13), doi:10.1029/2006JD007654.
- Yu, J.-Y., and K. M. Lau, 2005: Contrasting Indian Ocean SST variability with and without ENSO influence: A coupled atmosphere-ocean GCM study. *Meteorology and Atmospheric Physics*, **90** (3), 179–191.

REFERENCES

- Yuan, X., E. F. Wood, and M. Liang, 2014: Integrating weather and climate prediction: Toward seamless hydrologic forecasting. *Geophysical Research Letters*, **41** (16), 5891–5896, doi:10.1002/2014GL061076.
- Yun, K.-S., B. Ren, K.-J. Ha, J. Chan, and J.-G. Jhun, 2008: The 30-60-day oscillation in the East Asian summer monsoon and its time-dependent association with the ENSO. *Tellus A: Dynamic Meteorology and Oceanography*, **61** (5), 565–578, doi:10.1111/j.1600-0870.2009.00410.x.
- Yun, K.-S., K.-H. Seo, and K.-J. Ha, 2010: Interdecadal Change in the Relationship between ENSO and the Intraseasonal Oscillation in East Asia. *Journal of Climate*, **23** (13), 3599–3612, doi:10.1175/2010JCLI3431.1.
- Zeng, D., and X. Yuan, 2018a: Multiscale Land-Atmosphere Coupling and Its Application in Assessing Subseasonal Forecasts over East Asia. *Journal of Hydrometeorology*, **19** (5), 745–760, doi:10.1175/JHM-D-17-0215.1.
- Zeng, D., and X. Yuan, 2018b: Multiscale Land-Atmosphere Coupling and Its Application in Assessing Subseasonal Forecasts over East Asia. *Journal of Hydrometeorology*, **19** (5), 745–760, doi:10.1175/JHM-D-17-0215.1.
- Zhang, T., T. Wang, G. Krinner, X. Wang, T. Gasser, S. Peng, S. Piao, and T. Yao, 2019: The weakening relationship between Eurasian spring snow cover and Indian summer monsoon rainfall. *Science Advances*, **5** (3), doi:10.1126/sciadv.aau8932.
- Zheng, B., D. Gu, A. Lin, and C. Li, 2008: Spatial patterns of Tropospheric Biennial Oscillation and its numerical simulation. *Advances in Atmospheric Sciences*, **25** (5), 815–823.
- Zheng, Y., D. E. Waliser, W. F. Stern, and C. Jones, 2004: The role of coupled sea surface temperatures in the simulation of the tropical intraseasonal oscillation. *Journal of Climate*, **17** (21), 4109–4134, doi:10.1175/JCLI3202.1.
- Zhu, C., L. R. Leung, D. Gochis, Y. Qian, and D. P. Lettenmaier, 2009: Evaluating the Influence of Antecedent Soil Moisture on Variability of the North American Monsoon Precipitation in the Coupled MM5/VIC Modeling System. *Journal of Advances in Modeling Earth Systems*, **1** (4), 1–22, doi:10.3894/JAMES.2009.1.13.